

## Advanced Light Management in Thin-Film Solar Cells

Vismara, R.

**DOI**

[10.4233/uuid:f3f07a75-223a-43be-9da4-d063bee67f56](https://doi.org/10.4233/uuid:f3f07a75-223a-43be-9da4-d063bee67f56)

**Publication date**

2020

**Document Version**

Final published version

**Citation (APA)**

Vismara, R. (2020). *Advanced Light Management in Thin-Film Solar Cells*. [Dissertation (TU Delft), Delft University of Technology]. <https://doi.org/10.4233/uuid:f3f07a75-223a-43be-9da4-d063bee67f56>

**Important note**

To cite this publication, please use the final published version (if applicable).  
Please check the document version above.

**Copyright**

Other than for strictly personal use, it is not permitted to download, forward or distribute the text or part of it, without the consent of the author(s) and/or copyright holder(s), unless the work is under an open content license such as Creative Commons.

**Takedown policy**

Please contact us and provide details if you believe this document breaches copyrights.  
We will remove access to the work immediately and investigate your claim.

# ADVANCED LIGHT MANAGEMENT IN THIN-FILM SOLAR CELLS



ROBIN VISMARA



# **Advanced Light Management in Thin-Film Solar Cells**

## **Proefschrift**

ter verkrijging van de graad van doctor  
aan de Technische Universiteit Delft,  
op gezag van de Rector Magnificus Prof. dr. ir. T.H.J.J. van der Hagen  
voorzitter van het College voor Promoties,  
in het openbaar te verdedigen op  
maandag 16 november 2020 om 10:00 uur

door

**Robin VISMARA**

Ingenieur in Sustainable Energy Technology  
Technische Universiteit Delft, Nederland  
geboren te Torre de' Roveri, Italië

Dit proefschrift is goedgekeurd door de promotoren.

Samenstelling promotiecommissie bestaat uit:

Rector Magnificus,	voorzitter
Prof. dr. M. Zeman,	Technische Universiteit Delft, promotor
Dr. O. Isabella,	Technische Universiteit Delft, promotor

*Onafhankelijke leden:*

Prof. dr. L.C. Andreani	Università di Pavia, Italië
Prof. dr. C. Becker	Helmholtz Zentrum Berlin, Duitsland
Prof.dr. A. Polman	AMOLF, Amsterdam
Prof. dr. E. Eisemann,	Technische Universiteit Delft
Dr. B. Bläsi	Fraunhofer ISE, Duitsland
Prof. dr. P. Palenski,	Technische Universiteit Delft, reservelid

The research leading to these results has received funding from the European Union's Seventh Framework Program FP7/2007-2013 under grant agreement nr. 261901.



Typed using L<sup>A</sup>T<sub>E</sub>X. Template originally developed by dr. K. Jäger.

Cover design "Solar Cell / Bergamo" by D. Vismara, M.Sc.

Printed by Ipskamp Printing, Enschede.

ISBN: 978-94-6421-111-5

Copyright © 2020 R. Vismara

All rights reserved. No part of this publication may be reproduced, stored in a retrieval system, or transmitted in any form or by any means without the prior written permission of the copyright owner.

A digital copy of this thesis is available at <http://repository.tudelft.nl>

---

# Summary

The coming years will see humanity facing significant challenges to ensure its continued survival. The threat of global warming to humans and the environment – exacerbated by rapidly growing population and energy demand – requires quick and decisive actions. Among them, increasing the generation of electricity from renewable resources is paramount to mitigate the effects of climate change. Photovoltaic (PV) energy conversion can be one of main technologies that propels the transition from fossil fuels towards a more sustainable future. In recent years, the deployment of photovoltaic systems has increased at an astounding pace, with more than  $100\text{GW}_p$  of power installed during each of the last three years. However, further expansion of PV installations cannot solely rely on increasing industrial production, but should also be supported by research aimed at increasing the efficiency of PV devices and reduce their manufacturing costs.

One of the key aspects of photovoltaic energy conversion is absorption of light. By increasing the amount of solar energy that is absorbed inside PV devices, the efficiency of solar cells can be boosted. This is particularly true for thin-film structures, which due to their limited thickness struggle to effectively absorb photons. *Light management* indicates all the techniques aimed at maximising light absorption inside photovoltaic devices and is the main topic of this manuscript. The goal of this work is to investigate and optimise light management approaches – based on periodic structures – applied to different thin-film device technologies, and through this analysis provide guidelines for the design of photovoltaic devices and gain an insight into their optical performance.

After describing the theoretical background in **chapter 1** and the methodology in **chapter 2**, **chapter 3** begins the study of light management approaches by investigating nanowire arrays applied to thin-film nano-crystalline silicon solar cells. A proof-of-concept device was manufactured to ensure the feasibility of the proposed novel approach. Then, simulations were used to optimise the nanowire array structure. Results showed the good anti-reflective and scattering properties of nanowires, which are able to significantly boost absorption in the nano-crystalline silicon active layer.

In **chapter 4**, the analysis shifts to periodic metasurfaces and the achievement

of perfect absorption in amorphous silicon solar cells. By tuning the size and arrangement of the dielectric nanostructures that make up the metasurface, near 100% absorption can be achieved in the spectral region where amorphous silicon struggles to efficiently absorb incident photons. With respect to flat devices the performance is significantly increased, despite a reduction of used material of more than 50%.

In **chapter 5**, a thorough investigation of periodic gratings for Cu(In,Ga)Se<sub>2</sub> solar cells (CIGS) is carried out, complete with the selection of appropriate supporting materials to reduce the device thickness with a minimal sacrifice in performance. The accuracy of 3-dimensional rigorous modelling in predicting the performance of real CIGS devices was demonstrated for the first time. Then, a full study of 1-D and 2-D gratings was conducted – together with an analysis of device architectures that employ more transparent materials at the front and highly reflective metals at the back side. Results showed a marked increase in light absorption, mostly owing to a lower device reflectance and to reduced parasitic absorption in all supporting layers. The high optical performance was maintained when the thickness of the CIGS layer was reduced by 60%, which is crucial to reduce the utilisation of indium in the device and of the costs associated with it.

In **chapter 6**, the concept of front/back pyramidal textures with different geometries is introduced and fully explored. Its application to (nano-)crystalline silicon absorbers or to supporting layers is compared, showing a preference for the former. After careful study of the decoupled texture geometry, an optimised optical performance beyond the traditional Lambertian scattering limit was achieved.

In **chapter 7** the concept of double front and back textures is analysed further, by applying it to cheap and abundant barium silicide (BaSi<sub>2</sub>). The optical potential of this novel PV material was first characterised with spectroscopy measurements, then assessed in both single- and multi-junction configurations with the aid of rigorous optical simulations. Results showed that BaSi<sub>2</sub> outperforms thin-film silicon absorbers, owing to its higher absorption coefficient. This highlights the promise of this novel material, which can be an ideal candidate for both single- and double-junction thin-film devices.

---

# Samenvatting

*Dutch translation by dr. Rudi Santbergen*

De komende jaren zal de mensheid voor een grote uitdaging staan om haar voortbestaan te verzekeren. De dreiging van opwarming van de aarde voor mens en milieu - verergerd door de snel groeiende bevolking en de vraag naar energie - vereist snelle en doortastende maatregelen. Het vergroten van de opwekking van elektriciteit uit hernieuwbare bronnen is van cruciaal belang om de effecten van klimaatverandering te verzachten. Fotovoltaïsche (PV) energie-omzetting kan én van de belangrijkste technologieën zijn die de overgang van fossiele brandstoffen naar een duurzamere toekomst bewerkstelligt. In de afgelopen jaren is de installatie van fotovoltaïsche systemen in een verbazingwekkend tempo toegenomen, met in de afgelopen drie jaar een geïnstalleerde capaciteit van meer dan 100 GWp per jaar. Verdere uitbreiding van PV-installaties kan echter niet alleen steunen op een toenemende industriële productie, maar moet ook worden ondersteund door onderzoek dat gericht is op het verhogen van de efficiëntie van zonnecellen en het verlagen van hun productiekosten.

Eén van de belangrijkste aspecten van fotovoltaïsche energieconversie is de absorptie van licht. Door de hoeveelheid zonne-energie die wordt geabsorbeerd in zonnecellen te vergroten, kan de efficiëntie worden verhoogd. Dit geldt met name voor dunne-filmstructuren, die vanwege hun beperkte dikte moeite hebben om fotonen effectief te absorberen. Lichtmanagement omvat alle technieken die bedoeld zijn om de lichtabsorptie in fotovoltaïsche apparaten te maximaliseren en is het hoofdonderwerp van dit proefschrift. Het doel van dit werk is het onderzoeken en optimaliseren van lichtmanagementtechnieken op basis van periodieke structuren toegepast op verschillende dunne-filmzonneceltechnologieën, en door middel van deze analyse meer inzicht in te verkrijgen in hun optische prestaties en daarmee betere richtlijnen te bieden voor het ontwerp van zonnecellen.

Na een beschrijving van de theoretische achtergrond in **hoofdstuk 1** en de methodologie in **hoofdstuk 2**, onderzoekt **hoofdstuk 3** lichtmanagementtechnieken door middel van nanodraadroosters die zijn toegepast op dunne-film nano-kristallijn silicium zonnecellen. Er werd een prototype vervaardigd om



de haalbaarheid van het voorgestelde nieuwe ontwerp aan te tonen. Vervolgens werden simulaties gebruikt om de structuur van de nanodraadroosters te optimaliseren. Resultaten toonden de goede antireflectie- en verstrooiingseigenschappen van deze nanodraden aan, die de absorptie in de nano-kristallijne silicium laag aanzienlijk kunnen verhogen.

In **hoofdstuk 4** verschuift de focus naar periodieke meta-oppervlakken en het bereiken van perfecte absorptie in amorf silicium zonnecellen. Door het afstemmen van de grootte en rangschikking van de diëlektrische nano-structuren die het meta-oppervlak vormen, kan een absorptie van bijna 100% worden bereikt in het spectrale gebied waar amorf silicium moeite heeft om invallende fotonen efficiënt te absorberen. Met betrekking tot vlakke zonnecellen worden de prestaties aanzienlijk verbeterd, ondanks een vermindering van het materiaalverbruik van minstens 50%.

In **hoofdstuk 5** wordt een gedetailleerd onderzoek uitgevoerd naar periodieke roosters voor  $\text{Cu(In,Ga)Se}_2$  (CIGS) zonnecellen, inclusief de selectie van geschikte materialen die het mogelijk maken om de dikte van de zonnecel te verminderen met een minimaal verlies in zonnecelprestaties. De nauwkeurigheid van driedimensionale exacte modellen bij het voorspellen van de prestaties van echte CIGS zonnecellen werd voor het eerst aangetoond. Vervolgens werd een volledige studie van 1-D en 2-D roosters uitgevoerd, samen met een analyse van zonnecelarchitecturen die transparantere materialen aan de voorkant en sterk reflecterende metalen aan de achterkant gebruiken. De resultaten lieten een duidelijke toename zien van de lichtabsorptie, voornamelijk als gevolg van een lagere reflectie en een verminderde parasitaire absorptie. De hoge optische prestaties bleven behouden toen de dikte van de CIGS-laag met 60% werd verminderd, wat cruciaal is om het gebruik van indium in de zonnecel en de daarmee samenhangende kosten te verminderen.

In **hoofdstuk 6** wordt het concept van dubbele piramidale texturen aan de voor- en achterkant geïntroduceerd en uitgebreid onderzocht. De toepassing ervan op licht absorberende lagen van (nano-)kristallijn silicium heeft de voorkeur boven de toepassing op andere lagen in de zonnecel. Na zorgvuldige studie van de ontkoppelde textuurgeometrie, werden geoptimaliseerde optische prestaties bereikt die beter waren dan de traditionele Lambertiaanse verstrooiingslimiet.

In **hoofdstuk 7** wordt het concept van dubbele texturen verder geanalyseerd, door het toe te passen op het goedkope en niet schaarse materiaal bariumsilicide ( $\text{BaSi}_2$ ). Het optische potentieel van dit nieuwe PV-materiaal werd eerst gekarakteriseerd met spectroscopiemetingen en vervolgens met behulp van exacte simu-

laties beoordeeld in zonnecellen met zowel enkelvoudige als meervoudige juncties. De resultaten toonden aan dat  $\text{BaSi}_2$  dankzij de hogere absorptiecoëfficiënt beter presteert dan dunne-film silicium. Dit maakt dit nieuwe materiaal een veelbelovende kandidaat voor toepassing in zonnecellen, zowel met enkelvoudige als met meervoudige junctie.



*A mio papà, che mi ha insegnato  
tutto ciò che so*



---

# Contents

<b>Summary</b>	<b>v</b>
<b>Samenvatting</b>	<b>vii</b>
<b>1. Introduction</b>	<b>1</b>
1.1. Towards 2050 and beyond . . . . .	1
1.2. Photovoltaic energy conversion and technologies . . . . .	4
1.3. Light management in thin-film solar cells . . . . .	11
1.4. The optical performance of solar cells . . . . .	18
1.5. Aim and outline of this work . . . . .	22
1.6. Main contributions to the field . . . . .	23
<b>2. Characterisation methods and modelling approach</b>	<b>25</b>
2.1. Materials and devices characterisation . . . . .	25
2.2. Optical modelling of photovoltaic devices . . . . .	33
<b>3. Elongated nanostructures for thin-film silicon solar cells</b>	<b>39</b>
3.1. Introduction . . . . .	40
3.2. Crystalline silicon nanowire solar cell . . . . .	41
3.3. Nanowire array geometrical study . . . . .	45
3.4. Conclusions . . . . .	53
<b>4. Metasurfaces for amorphous silicon thin-film solar cells</b>	<b>55</b>
4.1. Introduction . . . . .	56
4.2. Results . . . . .	58
4.3. Discussion . . . . .	65
4.4. Conclusions . . . . .	68
<b>5. Copper indium gallium (di)selenide solar cells with periodic gratings</b>	<b>69</b>
5.1. Introduction . . . . .	70
5.2. Cell characterisation and simulator calibration . . . . .	70

---

5.3. CIGS solar cells on periodic gratings . . . . .	74
5.4. Conclusions . . . . .	83
<b>6. Thin-film silicon solar cells with different front and back textures</b>	<b>87</b>
6.1. Introduction . . . . .	88
6.2. Texturing: absorber vs supporting layers . . . . .	90
6.3. Optimisation of the front and back textures . . . . .	100
6.4. Conclusions . . . . .	117
<b>7. Barium silicide solar cells with 2-D periodic textures</b>	<b>119</b>
7.1. Introduction . . . . .	120
7.2. Optical characterisation of epitaxially-grown barium silicide . . .	120
7.3. Single-junction barium-silicide solar cells with periodic textures	122
7.4. Perovskite/barium silicide thin-film double junction solar cells .	125
7.5. Back-contacted barium-silicide architectures for 4-terminal devices	127
7.6. Conclusions . . . . .	131
<b>8. Conclusions and Outlook</b>	<b>133</b>
8.1. Conclusions . . . . .	133
8.2. Outlook . . . . .	135
<b>A. Refractive index data</b>	<b>137</b>
<b>B. Absorption limit for periodic gratings</b>	<b>145</b>
<b>C. Finite-difference time-domain simulations and multipole decomposition</b>	<b>153</b>
<b>D. Thin-film silicon solar cells based on 1-D asymmetric periodic gratings</b>	<b>155</b>
<b>Bibliography</b>	<b>180</b>
<b>Acknowledgements</b>	<b>181</b>
<b>List of publications</b>	<b>185</b>
<b>Curriculum vitae</b>	<b>189</b>

---

## CHAPTER 1

---

# Introduction

## 1.1 Towards 2050 and beyond

The coming years will see humanity facing significant challenges to ensure its continued survival.

In 2017, human-induced global warming had reached  $1^\circ \pm 0.2^\circ\text{C}$  above pre-industrial levels (years 1850-1900), with many regions experiencing even more intense temperature increases [1]. This has resulted in observable modifications of climate systems – including increase in land and ocean temperatures – and longer, more frequent and more intense heatwaves, heavy precipitations and droughts [2]. Significant evidence suggests that climate change has already had a significant impact on natural and human systems. In particular: risk of species loss and extinction, decrease of available (clean) water, reduction of crop, farm and fishery yields (and consequently food availability), and a decline in human health and well-being [2].

All these effects are likely to be exacerbated in coming decades, since global warming is expected to continue – based on both past emissions and predicted future trends. However, the extent of the impact of climate change will be significantly reduced if the increase in global temperature can be contained to  $1.5^\circ\text{C}$  (“well below  $2^\circ\text{C}$ ”), as recently reported by the Intergovernmental Panel on Climate Change [1, 2]. However, the accomplishment of this goal – explicitly included in the *Paris Agreement* signed in 2015 [3] – requires a significant reduction of emissions of carbon dioxide ( $\text{CO}_2$ ) and other greenhouse gasses, which have caused a sharp increase of atmospheric  $\text{CO}_2$  concentration (up to  $417.1\text{ ppm}^*$  in May 2020 [4]) and the related temperature increase, as shown in fig. 1.1. In particular, a recent report by the International Renewable Energy Agency (IRENA) highlighted that emission trends are not on track to meet the “ $2^\circ\text{C}$  goal” [5]. Even disruptive events like the COVID-19 crisis have only halted this course

---

\*Parts-per-million (ppm) indicates the number of atoms or molecules of a species contained in one million molecules of a solution. In this case, it counts the number of  $\text{CO}_2$  molecules in one million molecules of dry air.



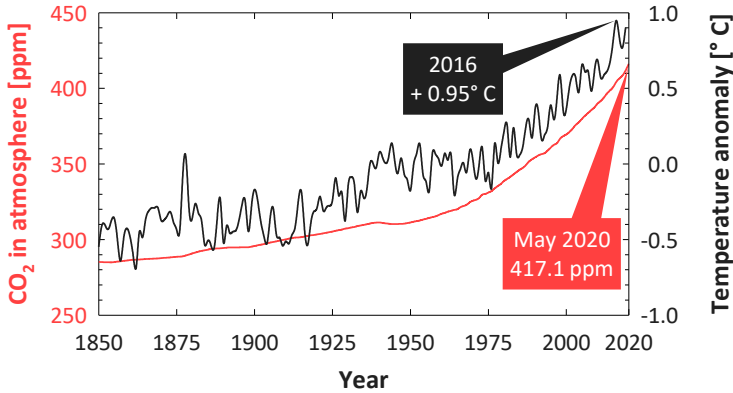


**Figure 1.1.** Concentration of CO<sub>2</sub> in the atmosphere (red) and temperature anomaly (black), in the period 1850-present. Temperature anomaly indicates the variation of the global mean temperature with respect to the average temperature between January 1951 and December 1980. The latest measured value of CO<sub>2</sub> concentration (March 2020) and the hottest year on record (2016) are both indicated. Data from [7, 8, 10].

temporarily. In fact, despite a global emission reduction of  $\sim 17\%$  in April 2020 (with respect to the previous year), CO<sub>2</sub> concentration has continued its steady increase [6] – achieving its higher recorded value in history during the following month [4, 7, 8]. Under current and planned policies, the cumulative emission budget for energy-related activities (760 Gt of CO<sub>2</sub>), to limit global temperature increase to 2°C, will already be exceeded in 2037. By 2050 emissions would reach a total of 1230 Gt of CO<sub>2</sub>, 470 Gt over the 2°C goal limit, corresponding to a predicted temperature increase of 2.6°–3.0°C. The issue is further complicated by the expected world population growth: from 7.55 billions in 2017, to 9.77 in 2050, to more than 11 billions before the end of the century [9]. This increase is mostly concentrated in Africa and Asia, where living standards are also expected to significantly increase – and energy demand with it.

Immediate action is thus crucial to meet the 2°C goal. The main pillars in the required transition are energy efficiency and utilisation of energy from renewable resources [5]. Both aspects need to expand in all sectors, from electrical power generation to industry, transport and buildings. The power sector will be at the core of the energy transition, given the progressive electrification of end-use sectors (transport and buildings in particular). In this sense, electricity generation has already made significant progress in recent years. In fact, the utilisation of renewable energy sources in this sector has increased at an average of 8% since

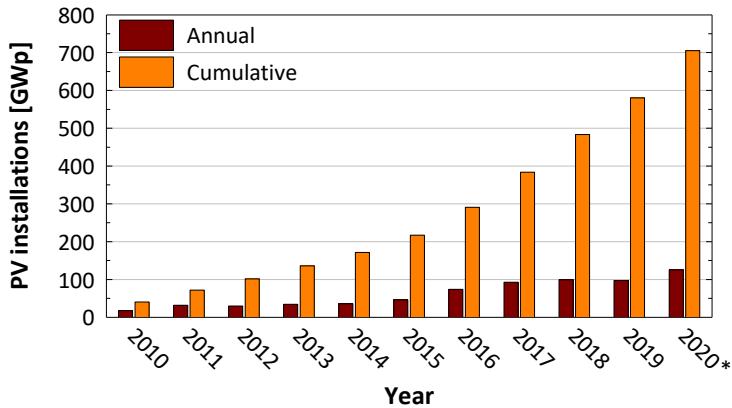


**Figure 1.2.** Annual (dark red) and cumulative (orange) PV installations between years 2010 and 2020. 2010-2019 data obtained from [11], \*2020 estimation from [12].

2010, resulting in the installation in 2017 of 174 GW of power capacity from renewable resources, of which  $92.6 \text{ GW}_p^\dagger$  were based on solar photovoltaic (PV) systems [11] – which convert sunlight directly into electricity.

In 2018 and 2019 PV installations have reached  $99.5 \text{ GW}_p$  and  $97.1 \text{ GW}_p$ , respectively, building up to a cumulative power capacity of  $580.2 \text{ GW}_p$  – according to data recorded by IRENA [11] (see fig. 1.2). The International Energy Agency (IEA) reports even higher values of annual and cumulative capacity for 2019:  $114.9 \text{ GW}_p$  and  $627 \text{ GW}_p$ , respectively [13]. Regardless of data uncertainty, the growing trend is expected to continue in 2020 – when annual installations are predicted to reach  $125 \text{ GW}_p$  [12]. Despite these great achievements and the continuous cost decrease of electrical power generation with PV system technologies [14], the deployment of photovoltaics (and renewable energy conversion more in general) needs to accelerate in order to minimise global warming and its impact on humans and the environment. However, the expansion of PV installations cannot rely solely on the growth of industrial production. In fact, the amount of installed power (and the corresponding generation of electricity) will increase if the efficiency of light-to-electricity conversion of PV devices is improved and if manufacturing costs are reduced. Photovoltaic research is thus fundamental to develop novel and more performing structures, and to replace or reduce the utilisation of expensive materials.

<sup>†</sup>Giga-watt peak, or  $\text{GW}_p$ , is a unit of power used in photovoltaics to indicate the power generated by a PV module in standard test conditions (temperature  $25^\circ\text{C}$ , irradiance of  $1000 \text{ Wm}^{-2}$  and air mass 1.5 spectrum).

## 1.2 Photovoltaic energy conversion and technologies

The sun is the main source of energy for our planet, both directly and indirectly – as the driver behind most renewable energy resources (e.g. wind energy, biomass, hydro-power). In fact, the surface of the Earth receives  $280.5 \times 10^6$  TWh<sup>‡</sup> of energy every year, in the form of electromagnetic radiation (i.e. light). This is more than 1000 times the annual primary energy demand of humankind ( $166.3 \times 10^3$  TWh) and significantly larger than all other energy sources, both finite and renewable [15, 16]. For these reasons, direct conversion of solar energy into electricity must be one of the pillars for the transition towards a sustainable future.

### 1.2.1 A brief history of photovoltaics

Solar cells are photovoltaic devices that convert solar energy directly into electricity – more specifically, the electromagnetic energy of sunlight into electrical energy. This process is based on the *photovoltaic effect*, which was discovered by Edmond Becquerel in 1839 and led to the development of the first solar cell by Charles Fritts in 1883 [17]. From that early device – which had an efficiency below 1% – development was slow until 1954, when Bell Laboratories demonstrated the first silicon-based solar cell [18]. Since then, the growth of photovoltaics has been fast. Propelled by the space race in the 1960s and the oil crisis in the 1970s, commercial module prices in 1977 reached a price of around 77 \$/W<sub>p</sub> [19, 20].

At that time, this price was considered to be too high. It was thus expected that new cell technologies for commercial photovoltaic applications would emerge, replacing silicon and leaving it to be used for space applications. However, while space solar cells have since moved to high-cost, high-efficiency multi-junction architectures based on so-called *III-V semiconductors* (see section 1.2.2), silicon has remained the prominent material employed in devices for terrestrial applications. In fact, in 2019 silicon-based PV devices accounted for more than 95% of the global PV industrial production [21]. Three main factors are responsible for this remarkable result. First, the device technology development: the learning curve of silicon solar cells, described by Swanson in 2006 [19], yielded a cost decrease of 20% for each doubling of the cumulative production. Second, incentive policies adopted in Europe, Japan and the U.S. facilitated the aforementioned development by creating a market for PV. Finally, in more recent years the emer-

---

<sup>‡</sup>One terawatt-hour, or TWh, is a unit of measure of energy corresponding to  $3.6 \times 10^{15}$  J.

gence of China and Asia as the main manufacturing hubs for photovoltaic resulted in a further and faster drop of production costs. Commercial modules in 2008 had already reached a price of  $4 \$/W_p$ . Since then, the decrease has been astonishing: after 10 years – at the end of 2018 – prices are 20 times lower at around  $0.22 \$/W_p$ . The corresponding negotiated levelised cost of electricity (LCOE) are now steadily below  $40 \$/MWh$  – and reached values below  $20 \$/MWh$  in 2017 [14]. Solar PV is now the cheapest technology to generate electricity, and is expected to become even cheaper in the coming years.

### 1.2.2 An overview of photovoltaic device technologies

The working principle of solar cells is based on the *photovoltaic effect*, which is “the generation of a potential difference at the junction of two different materials in response to electromagnetic radiation” [22]. The junction can be made of two semiconductors, or of one metal and one semiconductor. Photovoltaic devices are often categorised with respect to the semiconductor material used and their characteristic thickness. Commonly, 4 groups are defined [23]:

- Wafer-based crystalline silicon solar cells
- Thin-film solar cells
- III-V solar cells
- Organic and hybrid solar cells

Thin-film devices will be discussed more extensively in section 1.2.3. Here, the other 3 categories are briefly described. In fig. 1.3, a summary of the conversion efficiency records for different device technologies are reported.

#### Wafer-based crystalline silicon solar cells

Crystalline silicon (c-Si) is the dominant device technology in the PV market, representing more than 95% of the global annual production in 2019 [21]. Approximately 66% of the production of PV modules based on crystalline silicon solar cells is concentrated in China, where most of them are also installed (36% of global cumulative installations at the end of 2019). The vast majority of research and the entirety of industrial production is based on wafers of silicon, which can be mono- or multi-crystalline. These wafers have a thickness of a few hundreds of micrometres and are cut from larger ingots. Mono-crystalline

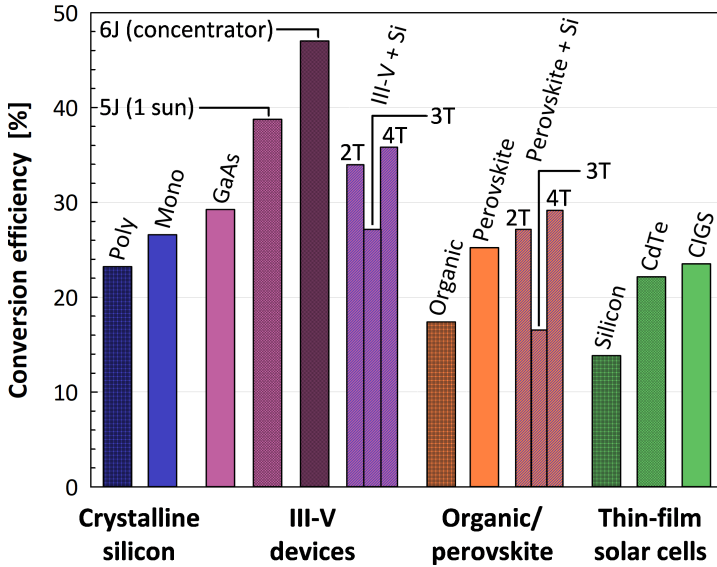


**Figure 1.3.** Power conversion efficiency records for different solar cell technologies: wafer-based crystalline silicon solar cells (mono- and multi-crystalline, in blue), III-V solar cells (single-junction GaAs, multi-junctions, and III-V + c-Si in 2-, 3- and 4-terminal configurations), organic and perovskite solar cells (in orange, including perovskite + c-Si 2-, 3- and 4-terminal architectures), and thin-film solar cells (silicon, CdTe and CIGS, in green). Data from [23, 24].

silicon wafers are in general more expensive, but perform better than their multi-crystalline counterparts. In fact, the current world record power conversion efficiency (PCE) values – for laboratory-scale devices – are 26.7% (mono) and 23.2% (multi) [25, 26]. Despite the higher manufacturing costs, the production of PV modules based on mono-crystalline silicon has rapidly increased in recent years and currently accounts for 66% of the global annual module production [21].

### III-V solar cells

The term *III-V solar cells* is commonly used to refer to PV devices that employ – as active layer – semiconductor alloys of group III and group V elements of the periodic table (indium, gallium, arsenic, and phosphor). Solar cells based on III-V materials can be categorised as thin-films, with typical thickness values of few micrometres. Despite being significantly thinner than typical crystalline silicon architectures, III-V solar cells are the most efficient devices currently manufactured. In particular, single-junction solar cells based on GaAs have achieved

conversion efficiencies up to 29.1% in standard test conditions [24], while multi-junction structures have reached values of PCE up to 38.8% under standard illumination and 47.1% under concentrated light [24, 27].

III-V solar cells are the preferred technology for space applications, due to their light weight and better resistance to radiation and harsh environments with respect to silicon solar cells. However, the high price of devices based on III-V semiconductors (currently  $> 150 \text{ \$/W}_p$ ) has so far prevented them to penetrate the (terrestrial-applications) PV market [28]. In an attempt to reduce costs, multi-junction devices that combine III-V materials and crystalline silicon have been recently developed and investigated. However, despite achieving high conversion efficiency values (35.9% for 4-terminal configurations, 26.4% for 3-terminal devices, and 34.1% for 2-terminal architectures), estimated costs are still too high ( $> 8 \text{ \$/W}_p$ ) to compete with crystalline-silicon modules [24, 29, 30]. To further decrease manufacturing costs (to  $< 1 \text{ \$/W}_p$ ), production needs to be up-scaled and growth of III-V semiconductor layers must switch from metal-organic vapour phase epitaxy (MOVPE) to hydride vapour phase epitaxy (HVPE) [28, 29].

### Organic and hybrid solar cells

Organic and hybrid organic-inorganic solar cells are PV devices that are either fully or partly based on organic materials. Organic solar cells employ organic polymers or molecules as absorber material, as opposed to the previously discussed device technologies in which inorganic elements (e.g. Si) or compounds (e.g. GaAs) are used. Organic solar cells have attracted a steady stream of attention, owing to their low manufacturing cost and ease of processing, the possibility of chemically tuning bandgap and absorption properties, and the capability of being integrated on flexible substrates [22]. Despite these advantages, the low efficiency (current lab-scale PCE record: 17.4%) and stability issues have so far prevented organic photovoltaics to compete with other technologies [31].

Conversely, a combination of organic and inorganic compounds can be used in what are sometimes called *hybrid organic-inorganic solar cells*. This category includes dye-sensitised solar cells (DSSCs) and perovskite solar cells. Both these device technologies have the advantage of low production costs and integration onto flexible substrate. However, they also suffer from instability (and in the case of DSSCs also low performance), which has so far prevented the commercial production of PV modules based on these technologies. Despite this drawback, a significant amount of research has been dedicated to this topic, particularly in last years to perovskite solar cells. As a result, relatively high PCE

values have been achieved: 25.2% for single-junction perovskite and 29.1% for a 2-terminal perovskite solar cell stacked on top of a crystalline silicon device [23, 24, 32]. 3- and 4-terminal devices, on the other hand, demonstrated slightly lower PCE values (17.1% and 26.7%, respectively). With the constant progress on stability demonstrated in recent years [33–35], perovskite solar cells (particularly silicon/perovskite multi-junctions) have the potential to become one of the main technologies in the PV market.

### 1.2.3 Thin-film solar cells

Thin-film solar cells are significantly thinner than wafer-based PV devices (e.g. c-Si). By this definition, the previously described III-V and organic/hybrid solar cells can also be considered part of the thin-film family. However, this section only focuses on those thin-film devices that are made of inorganic materials and are more commonly used in terrestrial applications. They include:

- Thin-film silicon solar cells (TFSSCs)
- Copper indium gallium diselenide solar cells (CIGS)
- Cadmium-telluride solar cells (CdTe)

All thin-film solar cells have several features in common. First, the typical thickness of these devices ranges from a few hundred nanometres up to several micrometres. This means that thin-film solar cells require a carrier for mechanical support [22]. This carrier can either be rigid (e.g. glass) or flexible (e.g. aluminium). Second, they rely on transparent conductive oxide (TCO) layers. While these materials are sometimes also employed in wafer-based architectures, all terrestrial thin-film technologies rely on TCOs as front contact (and sometimes as back contact as well).

When originally developed, thin-film solar cells were expected to become significantly more cost-effective than crystalline silicon devices. However, the sharp decrease in c-Si manufacturing costs now means that all thin-film device technologies are not economically more attractive than wafer-based silicon, while being at the same time less efficient (with the exception of III-V technologies, which are however significantly more expensive). Despite this, thin-film modules have managed to retain around 5% of the global PV market, and will probably remain viable for some specific application – e.g. those that require flexible or lightweight modules.

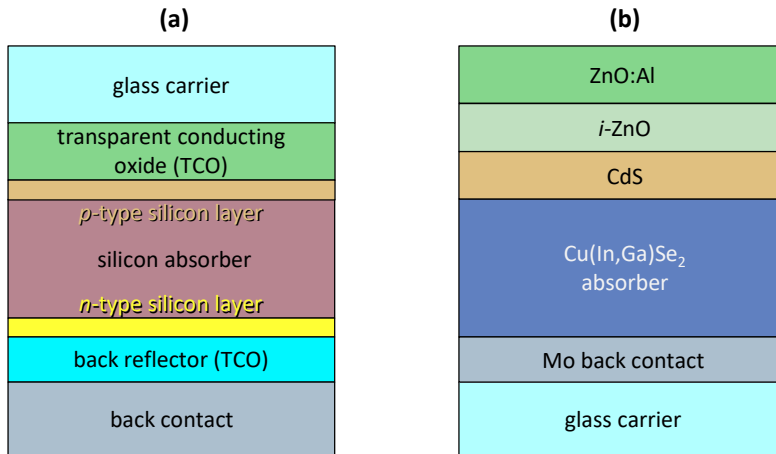


**Figure 1.4.** Typical structure of (a) single junction thin-film silicon and (b) copper-indium-gallium-selenide (CIGS) solar cells. Drawing not to scale.

### Thin-film silicon solar cells

Thin-film silicon solar cells are devices that use silicon alloys as absorber materials. These are mainly 2: hydrogenated amorphous silicon (a-Si:H) and hydrogenated nano-crystalline silicon (nc-Si:H) – sometimes called hydrogenated micro-crystalline silicon ( $\mu\text{c-Si:H}$ ). Films of these materials are usually deposited with plasma-enhanced chemical vapour deposition (PECVD), with the inclusion of hydrogen motivated by the need of passivating defects. Germanium is sometimes added as well, to form amorphous and nano-crystalline alloys (a-SiGe:H and nc-SiGe:H, respectively).

The typical structure of a single-junction thin-film silicon solar cell (see fig. 1.4a) can be described as follows:

- A glass carrier is normally used to sustain the structure (other materials can be employed as well).
- The first layer to be deposited is the front contact, made up of a TCO material. Some examples are: aluminium-doped zinc oxide (ZnO:Al or AZO), indium tin oxide ( $\text{In}_2\text{O}_3:\text{Sn}$  or ITO), fluorine-doped tin oxide ( $\text{SnO}_2:\text{F}$  or FTO), and hydrogenated indium oxide ( $\text{In}_2\text{O}_3:\text{H}$  or IOH).
- After the front TCO, the silicon junction is deposited. Normally, three different layers are included: a *p*-type doped film (i.e. where electrons are



the minority charge carriers), an intrinsic layer, and an  $n$ -type doped film (in which electrons are the majority charge carriers). The two doped layers create an electric field across the intrinsic layer, allowing for the separation of positive and negative charges photogenerated in the intrinsic absorber. Doped layers can be of the same material as the absorber (a-Si:H or nc-Si:H). However, alloys of silicon and oxygen are commonly used (a-SiO<sub>x</sub>:H and nc-SiO<sub>x</sub>:H), owing to their higher transparency and shunt-quenching properties [36].

- After the silicon junction, a back reflector is deposited. This layer needs to reflect as much light as possible back to the silicon layers, while at the same time allowing charges to pass through to the back contact. For this reason, TCOs are used once again.
- Finally, the back contact is deposited. Usually, metals such as aluminium and silver are employed.

The structure described above (and depicted in fig. 1.4a) is referred to as *superstrate* configuration, in which the physical carrier is positioned at the front. It is also possible (and indeed common) to manufacture devices where the supporting structure is located at the back; in this case, the layer deposition order is reversed. This *substrate* configuration offers the advantage of not requiring a transparent carrier, allowing for the use of other materials (e.g. metals).

Current lab-scale, single-junction stabilised conversion efficiency records are 10.2% for amorphous silicon and 11.9% for nano-crystalline silicon [37, 38]. To increase the performance, multiple junctions can be stacked on top to each other – thus improving utilisation of the solar spectrum. For double-junction devices (a-Si:H/nc-Si:H) the PCE records are 14.8% (initial) and 12.7% (stabilised) [37, 39], while for triple-junctions (and for TFSSCs in general) the records are 16.3% (initial) and 14.0% (stabilised) [40, 41]. Devices with more junctions have also been manufactured and are particularly useful for applications that require high operating voltages (e.g. photoelectrochemistry, internet of things). In fact, 4-junction devices with open-circuit voltage above 3 V have been reported (PCE of 14.6%) [42], while 5-junction solar cells with open-circuit voltage up to 3.5 V in low illumination conditions have been demonstrated [43]. Nevertheless, the low efficiency values have prevented thin-film silicon devices to gain a significant foothold in the PV market, despite their low manufacturing cost, the small cell-to-module losses [44], and the demonstrated industrial production of large flexible and rigid modules[45–49].

### Copper indium gallium diselenide solar cells

Chalcopyrite solar cells are made of chalcopyrites, alloys of elements of group I, III and VI. The most common of such material used in solar cells is *copper indium gallium diselenide*, or  $\text{Cu}(\text{In}_x\text{Ga}_{1-x})\text{Se}_2$  (CIGS) – where  $x = [0, 1]$ . This is a crystalline material, with a direct bandgap that can change between 1.7 eV ( $x = 0$ ,  $\text{CuGaSe}_2$ ) and 1.0 eV ( $x = 1$ ,  $\text{CuInSe}_2$ ). CIGS is a *p*-type semiconductor, hence it requires an *n*-type material to build a working junction. This is usually achieved by depositing cadmium-sulphide on top of the CIGS absorber. The *n*-type region is extended by the front TCO, which consists of two layers of intrinsic zinc oxide (*i*-ZnO) and aluminium-doped zinc oxide. This entire structure is deposited on a glass substrate, with molybdenum serving as back contact (see fig. 1.4).

Due to its good absorption and electronic properties, CIGS is able to achieve high conversion efficiency values. In fact, the current PCE world record for laboratory-scale solar cells stands at 23.35% [50]. However, issues with availability of indium and a general complexity of the manufacturing process has so far prevented the large-scale deployment of modules based on this technology.

### Cadmium telluride solar cells

Cadmium telluride (CdTe) is another direct bandgap (1.44 eV) crystalline semiconductor that can be used for solar cell applications. Naturally intrinsic, this alloy can be doped to obtain both *p*- and *n*-type layers. Usually, the junction is formed by a *p*-type CdTe layer and a CdS layer, similar to CIGS devices. At the front side a TCO is used, while the back contact consists of a metal layer (usually antimony telluride in combination with molybdenum). The current cell record efficiency has reached 22.1% [51] – and currently CdTe solar cells exhibit the lowest production costs per  $W_p$  of all thin-film device technologies and the lowest life-cycle impact [22, 52]. However, issues with the toxicity of cadmium have not allowed CdTe devices to become prominent in the PV market.

## 1.3 Light management in thin-film solar cells

The photovoltaic effect, i.e. the conversion of sunlight into electricity, can be divided into three steps [22]. In the first, the electromagnetic energy contained in photons is absorbed by the material – exciting bound valence electrons into an unbound state in which they become free to move. In ideal semiconductors, valence electrons can only occupy energy levels within the so-called *valence band*, while mobile electrons can exclusively populate levels in the *conduction*

*band*. Between these two bands, there are no energy states that can be occupied by electrons. This difference takes the name of energy gap or *bandgap* ( $E_{\text{gap}}$ ). Hence, only photons with energy larger than the semiconductor bandgap can be absorbed, where the photon energy ( $E_{\text{ph}}$ ) depends on the wavelength of light:

$$E_{\text{ph}} = \frac{h \cdot c}{\lambda} \quad (1.1)$$

where  $h = 6.626 \times 10^{-34} \text{ J} \cdot \text{s}$  is Planck's constant and  $c = 2.998 \times 10^8 \text{ m} \cdot \text{s}^{-1}$  is the speed of light *in vacuo*. When an electron is excited to energy levels into the conduction band, it leaves behind a void (a hole) which behaves like a positive particle. The second step is the separation of charge carriers (*electrons* and *holes*) at the junction. Semi-permeable materials are here required, allowing holes to travel in one direction (*p*-type layers) and electrons in the other (*n*-type layers). If the two carriers were not separated, they would recombine (i.e. the electron would return to an energy state in the valence band) and the absorbed energy would be released as a new photon (radiative recombination) or heat (non-radiative recombination). In the final step, the separated charge carriers are extracted at the solar cell contacts, where they can be used to perform work.

*Light management* deals with the first step of photovoltaic energy conversion. Its aim is to maximise the number of photons that excite electron-hole pairs, i.e. to increase as much as possible the generation of charge carriers inside the absorber of solar cells. The term light management is thus used to group all those techniques – used in the design and production of PV devices – that aim to increase the absorption of light inside the active layer(s)<sup>§</sup> of a solar cell. These approaches can be divided into two categories. First, those that maximise the amount of light that reaches the absorber layer (the *in-coupling* of light into the absorber). Second, those which aim at making photons travel inside the active layer for the longest possible distance (the *trapping* of light inside the absorber), to increase the chances that they are absorbed.

*Light management* is particularly important for thin-film solar cells, since their limited thickness makes it harder to absorb all incident light. This is particularly true for thin-film nano-crystalline silicon devices, because the indirect bandgap of silicon implies that its absorption coefficient (i.e. the ability to absorb light) is lower than that of other materials – particularly for photons with energy val-

---

<sup>§</sup>Active layers are those in which absorbed photons generate charge carriers that can be separated and collected. They are opposed to *supporting layers*, in which light absorption does not result in the excitation of useful charge carriers.

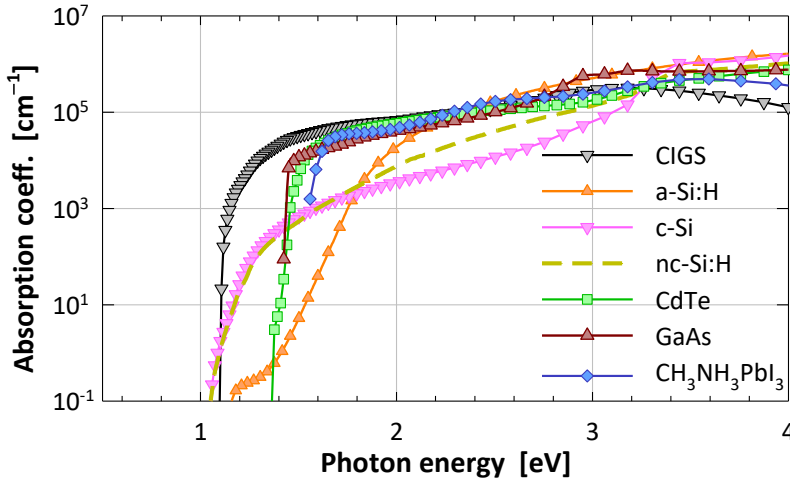


**Figure 1.5.** Absorption coefficient of several semiconductors used in PV: a-Si:H (internal measurements), nc-Si:H [53], c-Si [54],  $\text{CH}_3\text{NH}_3\text{PbI}_3$  (a perovskite material) [55], CdTe [56], GaAs [57], and CIGS (this work, chapter 5).

ues close to the bandgap (see fig. 1.5). Nevertheless, the light management approaches discussed in the following sections are also used in other PV device technologies.

### 1.3.1 In-coupling of light into the absorber

Of all the photons that reach the surface of a solar cell, only some are able to reach the absorber. Others are reflected before they can reach the active layer, while a few are absorbed elsewhere in the device. To maximise light in-coupling into the absorber, it is necessary to: (i) minimise the front reflectance of a solar cell, and (ii) employ supporting layers<sup>S</sup> that are as transparent as possible. To minimise the front reflectance of solar cells, two main techniques are used:

- Anti-reflection (AR) coatings
- Micro- and nano-textures

AR coatings are layers of materials that are deposited at the front side of a device, commonly above the uppermost layer of a solar cell (i.e. the front TCO, or even above the glass carrier). Two separate optical phenomena are used to correctly design these coatings: Rayleigh's film and interference.

When light impinges perpendicularly on the flat interface between two materials, the reflectance ( $R$ ) of that interface (i.e. the ratio of reflected over incident power) can be quantified with one of Fresnel's equations:

$$R = \left( \frac{n_1 - n_2}{n_1 + n_2} \right)^2 \quad (1.2)$$

where  $n_1$  and  $n_2$  are the (real) refractive indices of the the two materials (note that, in general,  $n$  is a wavelength-dependent quantity). When an anti-reflection coating is interposed between the two materials such that  $n_1 < n_{AR} < n_2$ , the total reflectance will be reduced. In particular, the optimum value that minimises reflectance is the geometrical mean between the refractive indices of the two materials:  $n_{AR} = \sqrt{n_1 \cdot n_2}$ .

The thickness of the AR coating is determined with the principle of interference. Light reflected at the two interfaces of an AR coating interfere with each other. Destructive interference, which quenches reflectance, is achieved when the thickness of the AR coating ( $d_{AR}$ ) is the following:

$$d_{AR} = \frac{\lambda}{4 \cdot n_{AR}} \quad (1.3)$$

where  $\lambda$  is the wavelength of light *in vacuo*. Pure destructive interference is only achieved at a particular wavelength. Hence, AR coatings are designed to promote destructive interference where the intensity of the solar spectrum is the highest ( $\lambda \approx 600$  nm). Single AR coatings are now commonly used in many PV devices, both at cell and module level. Multiple AR coatings – that promote a step-like grading of the refractive index – are also possible (see fig. 1.6a), but usually too expensive to be included in industrial processes.

Textures are another way to promote the in-coupling of light into the absorber layer. Light interacts with textures in different ways, depending on the characteristic size of the texture itself with respect to the wavelength of light. When the texture is much larger than  $\lambda$ , geometrical optics describes the interaction. Light beams that are reflected can get a second chance (and sometimes even a third) to hit the device surface (see fig. 1.6b) – as opposed to the flat case where it only gets one chance. In this way, more light can reach the absorber layer. On the other hand, a texture with features of the same or smaller size than  $\lambda$  promotes anti-reflection through a different process – that is better described with wave optics. In fact, the incident light beam will experience the texture as an effective medium, with a refractive index that transitions smoothly from that of the incident medium to that of the transmission medium (similarly to what happens

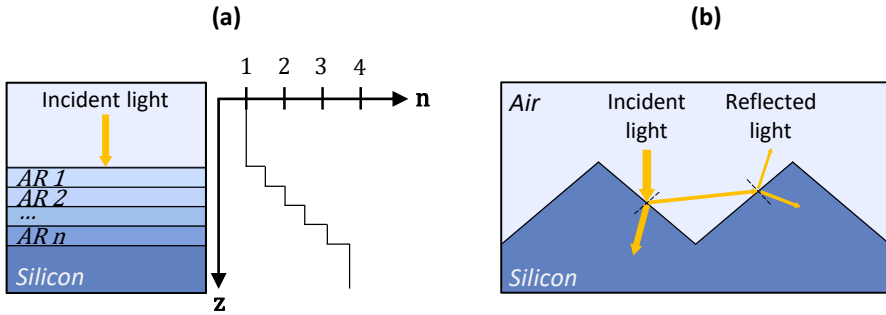


**Figure 1.6.** Illustrations of a) multiple anti-reflection coatings and b) surface texture – both applied to silicon to reduce its reflectance.

when multiple AR coatings are implemented). Textures with a combination of large and small features can be created to take advantage of both effects, reducing front reflectance to almost zero [39, 58, 59].

### 1.3.2 Trapping of light inside the absorber

Absorption of light is the process in which the electromagnetic energy carried by photons ( $E_{\text{ph}}$ ) is taken up by a material – transforming it into internal energy. In semiconductors, when  $E_{\text{ph}} > E_{\text{gap}}$  energy is transferred from photons to electrons – exciting them from a valence state to a conduction state. The *absorption coefficient* ( $\alpha$ ) is the property used to quantify the ability of a material to absorb photons. In semiconductors,  $\alpha$  is larger for high photon energy values and decreases as  $E_{\text{ph}} \rightarrow E_{\text{gap}}$ . In fig. 1.5, the absorption coefficient of several PV materials is plotted as function of  $E_{\text{ph}}$ . *Lambert-Beer's law* describes the attenuation of the intensity of the electromagnetic field ( $I$ ) as it travels through a material:

$$I(z) = I_0 \cdot e^{-\alpha z} \quad (1.4)$$

where  $z$  is the distance travelled by light inside the medium, and  $I_0$  the intensity of light that enters the medium (i.e. at  $z = 0$ ). Absorption ( $A$ ) quantifies the reduction of light intensity,  $I_0 - I(z)$ , with respect to its initial value:

$$A(z) = \frac{I_0 - I(z)}{I_0} = 1 - e^{-\alpha z} \quad (1.5)$$

It is apparent from eq. (1.5) that absorption increases when the *path length* ( $z$ ) of light inside the material is maximised. This is indeed the goal of light trapping: extending the path length of photons inside the absorber layer to increase the

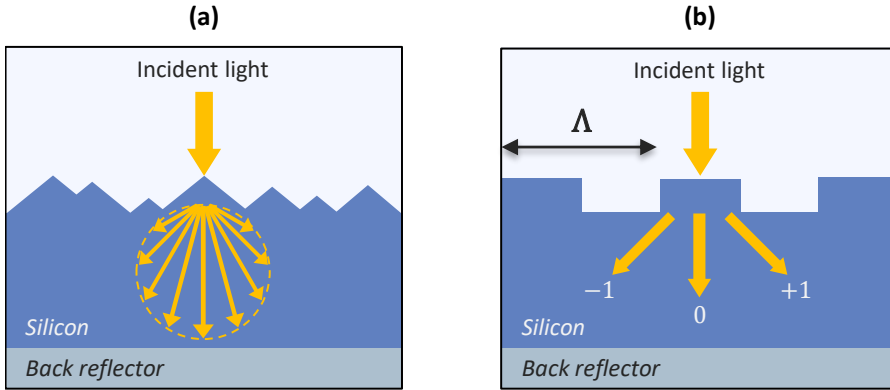


**Figure 1.7.** Scattering of light from a) a random texture and b) a periodic grating, where the numbers (0,  $\pm 1$ ) indicate diffraction modes and  $\Lambda$  is the grating period.

chance of their absorption. This becomes particularly critical for photons with  $E_{\text{ph}} \approx E_{\text{gap}}$  and for thin-film devices – in which the thickness of the active layer is reduced.

The first way to increase the path length is placing a reflector at the back side of the device. In this way, photons that would otherwise be transmitted out are instead reflected back to the absorber layer – getting a second chance to generate an electron-hole pair. Conveniently, back contacts made of metal have in general a high reflectivity and can thus fill the role of back reflectors as well. The second way to maximise the path length of light is to deflect it from its direction of propagation. Photons that impinge perpendicularly onto the textured surface of a solar cell can be deviated from their trajectory, thus prolonging the path travelled within the absorber. Moreover, if this deflection is sufficient total internal reflection (TIR) can be achieved – i.e. photons are continuously reflected back into the absorber, both at the top and bottom sides – effectively *trapping* them inside the active layer until they are absorbed. In thin-films, conditions of TIR give rise to so-called *guided modes*, which are the result of interference between the repeatedly reflected waves and effectively represent light *trapped* inside the thin absorber.

The trajectory of light propagating across the interface between two materials is normally governed by refraction, described by Snell's law:

$$n_1 \sin(\theta_{\text{inc}}) = n_2 \sin(\theta_{\text{trans}}) \quad (1.6)$$

where  $\theta_{\text{inc}}$  and  $\theta_{\text{trans}}$  are the angle of incidence and transmission of light, respec-

tively. However, eq. (1.6) only holds true when interfaces are flat or have textures that are much larger than the wavelength. In fact, when light encounters an object that is smaller or similar in size to  $\lambda$ , its propagation is deflected into multiple directions. This phenomenon, known as *scattering*, is very useful to increase the path length by deflecting perpendicularly incident light into oblique directions.

Depending on the type of texture, the scattering pattern will be different. A randomly textured interface scatters light into all directions, with an intensity distribution that has its maximum along the trajectory of the incident beam and gradually reduces as the deflection increases (see fig. 1.7a). On the other hand, when periodic textures (also called *gratings*) are used, the situation is radically different. The scattering profiles of each periodically arranged feature interfere with each other. As a result, light can only propagate along specific trajectories (see fig. 1.7b). These directions can be calculated with the following equation:

$$\theta_m = \arcsin \left[ \frac{m\lambda}{n_2\Lambda} + \frac{n_1}{n_2} \sin(\theta_{\text{inc}}) \right] \quad (1.7)$$

where  $\theta_m$  is the angle of scattered light,  $\Lambda$  the period of the texture, and  $m = 0, \pm 1, \pm 2, \dots$  is an integer. Equation (1.7) has real solutions only when the argument of arcsin is smaller or equal to 1 – i.e. only a finite number of discrete directions are allowed, commonly referred to as *diffraction orders*. The number of diffraction orders increases when the quantity  $[\lambda / (n_2\Lambda)]$  is minimised – thus at short wavelengths, for materials with a high refractive index, and for large values of the grating period.

Textures have long been applied to thin-film solar cells, particularly to TFSSCs. In fact, all record devices incorporate some type of scattering interfaces. Depending on the configuration (superstrate or substrate), these textures are applied to the front or back side. Front textures have the advantage to promote the in-coupling of light into the absorber. On the other hand, textures at the rear often result in a reduction of the reflectivity of the metallic back contact, owing to surface plasmonic effects at the metal/silicon interface and to the promotion of light in-coupling into the metal itself. However, the reflectivity of textured metal/silicon interfaces can be boosted by the interposition of a transparent layer [60, 61], that quenches these plasmonic losses. Of the current world-record efficiency devices, single-junction a-Si:H and double junction a-Si:H/nc-Si:H rely on a randomly textured superstrate [37], while single junction nc-Si:H and triple-junction a-Si:H/nc-Si:H/nc-Si:H on a periodic substrate texture [38, 41].



## 1.4 The optical performance of solar cells

The performance of a photovoltaic devices is quantified in terms of the power conversion efficiency ( $\eta$ ), which is the ratio of generated over incident power:

$$\eta = \frac{P_{\text{out}}}{P_{\text{in}}} = \frac{J_{\text{sc}} \cdot V_{\text{oc}} \cdot FF}{P_{\text{in}}} \quad (1.8)$$

where the generated power per unit area ( $P_{\text{out}}$ , in  $\text{Wm}^{-2}$ ) is the product of the current density in short-circuit conditions ( $J_{\text{sc}}$ ), the open-circuit voltage ( $V_{\text{oc}}$ ), and the fill-factor ( $FF = [0, 1]$ ) – which can be interpreted as an indication of the quality of a device.

Absorption of light is directly linked to  $J_{\text{sc}}$ , since every photon absorbed in the active layer of the solar cell can excite an electron:

$$J_{\text{sc}} = |q| \int_0^{\lambda_{\text{gap}}} \beta \cdot \gamma \cdot A(\lambda) \cdot \Phi(\lambda) d\lambda \quad (1.9)$$

where  $q = -1.602 \times 10^{-19} \text{ C}$  is the electron charge and the product of the wavelength-dependent absorption ( $A$ ) and spectral photon flux ( $\Phi$ , in  $\text{m}^{-2}\text{s}^{-1}\text{nm}^{-1}$ ) is integrated from a minimum value up to the bandgap of the absorber. The parameter  $\gamma$  indicates the number of electrons that are excited by one photon, and in most cases is equal to 1. On the other hand,  $\beta \leq 1$  represents the efficiency of charge collection – i.e. the proportion of excited charge carriers that are collected at the contacts of the solar cell. Absorption and short-circuit current can thus be used as a measure of the optical performance of a solar cell and to assess the quality of different light management approaches.

### 1.4.1 Benchmarks of absorption

The quality assessment of light management approaches relies on the accurate definition of absorption benchmarks. These are values of absorption determined in specific, well-defined conditions that become useful references to which the optical performance of solar cells can be compared. For all benchmarks commonly in use, which will be briefly described in this section, the assumptions are:

- No front reflectance, to focus on the ability of a layer to absorb all in-coupled light.
- Perpendicular incidence, which corresponds to standard test conditions.

The first fundamental concept to introduce is *single-pass* light absorption. In a flat slab with no back reflector, photons only pass through the layer once. The amount of absorbed light is thus described by eq. (1.5), in which the distance travelled by light is equal to the thickness of the slab ( $d$ ):

$$A_{\text{SP}}(\lambda) = 1 - e^{-\alpha(\lambda)d} \quad (1.10)$$

where the wavelength dependence of absorption and  $\alpha$  is made explicit. Single-pass absorption is used as reference (i.e. the lower limit) to calculate the absorption enhancement factor ( $EF$ ), which is defined as the ratio of measured, calculated or simulated absorption to  $A_{\text{SP}}$ :

$$EF_i(\lambda) = \frac{A_i(\lambda)}{A_{\text{SP}}(\lambda)} \quad (1.11)$$

When a lossless back reflector is implemented in such optical system, any light that could pass through the slab without being absorbed experiences a second pass. In this situation, the optical thickness of the layer doubles, and the amount of absorbed light is described by the *double-pass* absorption limit:

$$A_{2\text{P}}(\lambda) = 1 - e^{-2\alpha(\lambda)d} \quad (1.12)$$

As expected, in the weak absorbing region of the dielectric slab (i.e. where  $\alpha d \ll 1$ ),  $EF_{2\text{P}} = A_{2\text{P}}/A_{\text{SP}} = 2$ . That is, in the part of the spectrum in which either (or both)  $\alpha$  and  $d$  are very small, absorption is doubled with respect to the single-pass case, owing to the presence of a lossless back reflector.

Equation (1.12) implies that the introduction of a mirror at the back side of a device can enhance absorption by a maximum factor of 2. Any further gain must be achieved through a deflection of light from its perpendicular path, using scattering textures. But which textures should be considered, that maximise the path length of light inside the absorber? This question was first answered in 1982 and 1984 by Yablonoitch *et al.* [62, 63]. Considering a thick dielectric slab in air with no front reflection, a perfect back mirror, and ideal isotropic light scattering (also known as *Lambertian scattering*), absorption can be calculated as follows:

$$A_{\text{Lamb.}} = \frac{4n^2\alpha d}{1 + 4n^2\alpha d} \quad (1.13)$$

where the wavelength dependence of  $A_{\text{Lamb.}}$ ,  $n$ , and  $\alpha$  has been omitted for clarity. Equation (1.13) provides a very important benchmark for absorption, and has

been used since it was first presented as the reference for all light management approaches. However, its validity is limited to the weak-absorption regime, in which case  $EF_{\text{Lamb.}}$  assumes the well-known  $4n^2$  value. For this reason, in 2002 Martin Green generalised the results of Yablonoitch and developed an equation valid in all conditions [64]:

$$A_{\text{Lamb.}} = \frac{1 - e^{-4\alpha d}}{1 - \left(1 - \frac{1}{n^2}\right) e^{-4\alpha d}} \quad (1.14)$$

The results of Yablonoitch and Green are not in contrast with each other. In fact, one can observe that when  $\alpha d \ll 1$ , eq. (1.14) becomes eq. (1.13) and  $EF_{\text{Lamb.}}$  tends to the same value of  $4n^2$ . For silicon, this value represents a potential absorption enhancement of 50.

Periodic gratings can also be used to enhance absorption. However, the calculation of the enhancement is more complex than in the Lambertian scattering case, since results strongly depend on the period, dimension and shape of the grating. In general, values of  $EF$  larger than  $4n^2$  can be achieved, up to  $(8/\sqrt{3})\pi n^2$  for 2-dimensional hexagonal structures with  $\lambda \sim \Lambda$ . However, this high absorption enhancement is limited to a narrow spectral band, outside of which  $EF$  can be significantly lower than in the random-texture case. So, in most cases eq. (1.14) can be effectively considered as the *absorption limit* for solar cells. The derivation of the absorption limit for periodic structures is not reported here, but has been included in appendix B.

### 1.4.2 Optical efficiency limits

The direct correlation between absorption and short-circuit current (density) allows the use  $J_{\text{sc}}$  to assess the quality of light management. This is done by defining the optical efficiency of a solar cell as the ratio of  $J_{\text{sc}}$  to its maximum:

$$\eta_{\text{opt.}} = \frac{J_{\text{sc}}}{J_{\text{sc}}^{(\text{max})}} = \frac{\beta \cdot \gamma \int_0^{\lambda_{\text{gap}}} A(\lambda) \Phi(\lambda) d\lambda}{\beta \cdot \gamma \int_0^{\lambda_{\text{gap}}} \Phi(\lambda) d\lambda} \quad (1.15)$$

where  $J_{\text{sc}}$  is maximised when absorption is equal to 1 over the entire range of wavelengths. It is apparent that  $\eta_{\text{opt.}}$  is independent on charge collection ( $\beta$ ) or multiple excitation ( $\gamma$ ) and is only influenced by absorption of light. If eq. (1.14) and eq. (1.15) are combined, the limit of optical efficiency is obtained:

$$\eta_{\text{opt.}}^{(\text{max})} = \frac{\int_0^{\lambda_{\text{gap}}} A_{\text{Lamb.}}(\lambda) \Phi(\lambda) d\lambda}{\int_0^{\lambda_{\text{gap}}} \Phi(\lambda) d\lambda} \quad (1.16)$$

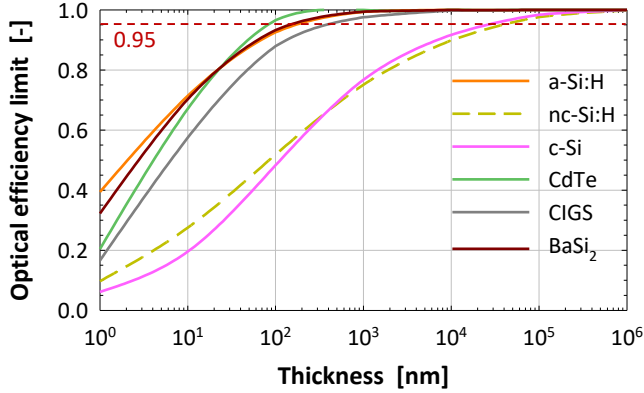


**Figure 1.8.** Values of  $\eta_{\text{opt.}}^{(\text{max})}$  for six different PV semiconductors, as function of the layer thickness (note the logarithmic scale).

This limit is an intrinsic property of a material (it depends on  $\alpha$  and  $n$ ) and is a function of its thickness – approaching 1 when  $d \rightarrow \infty$ . In fig. 1.8 the maximum optical efficiency of various materials is depicted. Here, it can be observed that for some materials very thin layers are sufficient to absorb most of the available photons (e.g. for CdTe, 80 nm are sufficient to absorb 95% of photons), while for semiconductors like c-Si and nc-Si:H tens of microns are necessary to achieve the same absorption levels.

The optical efficiency limit  $\eta_{\text{opt.}}^{(\text{max})}$  can be used to extend the analysis normally carried out with “traditional” efficiency limits. The two most commonly used are:

- The *ultimate efficiency* ( $\eta_{\text{ult.}}$ ), which calculates the theoretical efficiency of PV devices based solely on their absorber bandgap. Only losses due to non absorption of low-energy photons ( $E_{\text{ph}} < E_{\text{gap}}$ ) and due to thermalisation (i.e. loss of electron energy in excess of  $E_{\text{gap}}$ ) are considered. This corresponds to the assumption of  $FF = 1$  and  $V_{\text{oc}} = E_{\text{gap}}/|q|$ .
- The *Shockley-Queisser limit* ( $\eta_{\text{S-Q}}$ ) [65], which adds radiative recombination (which reduces  $V_{\text{oc}}$ ) and impedance losses (which reduce  $FF$ ) to the calculation of  $\eta_{\text{ult.}}$

Both aforementioned efficiency limits assume total absorption of photons with  $E_{\text{ph}} > E_{\text{gap}}$ . Hence, they do not depend on the real optical properties ( $\alpha$  and  $n$ ). When a more detailed analysis is required, one can multiply  $\eta_{\text{ult.}}$  or  $\eta_{\text{S-Q}}$  with

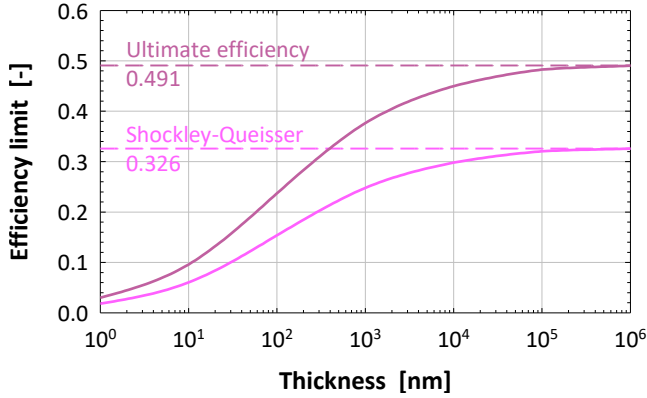


**Figure 1.9.** Values of ultimate and Shockley-Queisser efficiencies, both in their original definition (horizontal dashed lines) and “corrected” for optical losses (continuous lines).

eq. (1.16) to obtain ultimate and Shockley-Queisser efficiency curves “corrected” for optical losses due to finite thickness. An example of these calculations is provided in fig. 1.9 for crystalline silicon.

## 1.5 Aim and outline of this work

The target of this thesis is to investigate and optimise light management approaches – based on periodic structures – applied to different thin-film device technologies, and through this analysis provide guidelines for the design of photovoltaic devices and insight into their optical performance. A variety of periodic structures is studied, from nanowire arrays to metasurfaces, to 1- and 2-dimensional gratings. Depending on the selected application, the optimisation of light management can accomplish different goals. For inexpensive silicon devices, maximising absorption can increase the performance to a level similar to that of their thicker wafer-based counterparts. In high-efficiency CIGS solar cells, the large-scale deployment of which is hindered by scarcity of indium, it is paramount to reduce the device thickness without compromising the optical behaviour. In novel materials such as barium (di)silicide ( $\text{BaSi}_2$ ), the full analysis and optimisation of light management is fundamental to assess their potential for photovoltaic applications. In all cases, the comparison of results to theoretically calculated benchmarks is not only a useful tool, but also (and more importantly) a way to better understand how to approach and overcome those performance limits.

In this work, all of the aforementioned aspects are discussed extensively. After describing the theoretical background in **chapter 1** and the methodology in **chapter 2**, **chapter 3** begins the study of light management approaches by investigating nanowire arrays applied to thin-film nano-crystalline silicon solar cells. In **chapter 4**, the analysis shifts to periodic metasurfaces and the achievement of near-perfect absorption in amorphous silicon solar cells. In **chapter 5**, a thorough investigation of gratings for CIGS solar cells is carried out, complete with the selection of appropriate supporting materials to reduce the device thickness with a minimal sacrifice in performance. In **chapter 6**, the concept of different front and back pyramidal textures is introduced and fully explored. Its application to (nano-)crystalline silicon absorbers or to supporting layers is compared, achieving an optimised optical performance beyond the traditional Lambertian scattering limit. In **chapter 7** the concept of double textures is applied to novel barium silicide, the potential of which is first characterised and then assessed in both single- and multi-junction configurations. Finally, in **chapter 8** the work is summarised and concluded, and recommendations for future work are put forward.

## 1.6 Main contributions to the field

The work carried out in this thesis has played a small part in the advancement of the photovoltaic scientific community. The main contributions are summarised here:

- Evaluation of the optical performance of nanowire arrays applied to thin-film (nano-)crystalline silicon.
- Study of amorphous silicon metasurfaces to promote near-perfect absorption for photovoltaic applications.
- Demonstration of the accuracy of rigorous 3-dimensional modelling and investigation of scattering gratings applied to CIGS solar cells.
- Analysis and optimisation of decoupled front/back textures for thin-film silicon PV, achieving an optical performance in excess of the traditional Lambertian scattering absorption limit.
- Characterisation of the optical properties and assessment of the potential of barium silicide.



# Characterisation methods and modelling approach

*ABSTRACT* – In this chapter, an overview of the methods used for characterisation of PV materials and devices – and of the modelling approach employed for the simulations of solar cell structures – are described. In the first part, the equipment and procedures employed for characterising materials and devices investigated in this thesis are presented. Then, a description of the modelling approach employed is given, with most details focusing on the main software used to obtain the results presented in chapters 3 to 7.

## 2.1 Materials and devices characterisation

In this first part of the chapter, the characterisation of PV materials and manufactured devices of this thesis is presented. Most of the measurements were carried out with the goal of obtaining the wavelength-dependent complex refractive index –  $\tilde{n}(\lambda) = n(\lambda) + j\kappa(\lambda)$  – of all materials used in the modelling phase\*. In fact, the (real part of the) refractive index ( $n$ ) and the extinction coefficient ( $\kappa$ ) are – together with the device geometry – necessary simulation input parameters. In addition, measurements to determine surface and device morphology were carried out, to build models as similar to real devices as possible. This last aspect is of particular importance when the simulator needs to be calibrated (see Chapter 5), by comparing computed results with real measured behaviour – i.e. optical performance and external parameters of manufactured devices.

---

\*Note that  $j = \sqrt{-1}$  is the imaginary unit.



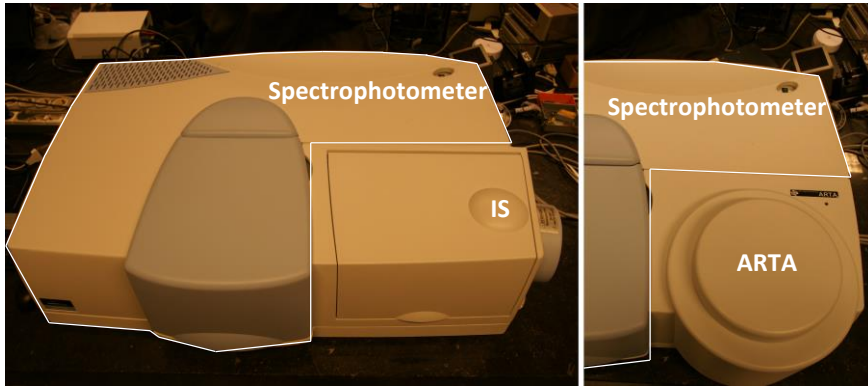


**Figure 2.1.** The LAMBDA 950 UV/Vis/NIR spectrophotometer by Perkin Elmer, with mounted IS (left) or ARTA (right) accessories. Picture adapted from [69].

### 2.1.1 Reflectance-Transmittance measurements

Reflectance-transmittance ( $R - T$ ) measurements were carried out by means of spectrophotometry. This technique allows the measurement of reflectance and transmittance of a layer or device, as function of the wavelength of incident light ( $\lambda$ ). In a typical spectrophotometer, a source of light impinges on diffraction gratings, which are able to select specific wavelengths of light. Through a series of mirrors, the light beam is re-directed towards the sample. Light transmitted or reflected by the sample is then captured by a detector. Information from the detector is then compared (wavelength by wavelength) to reference transmittance and reflectance spectra, thus obtaining results expressed in relative terms (i.e. as a percentage of the intensity of incident light).

The equipment used to carry out  $R - T$  measurements is the LAMBDA 950 UV/Vis/NIR Spectrophotometer [66], depicted in fig. 2.1. The machine is equipped with two light sources, a deuterium arc lamp for ultraviolet light ( $\lambda < 320$  nm) and a tungsten-halogen lamp, which can cover the spectrum 300 nm – 3300 nm. Two different accessories can be used with this spectrophotometer: the integrating sphere (IS) and the automated reflectance/transmittance analyser (ARTA) [67]. Both accessories contain two different detectors: a photomultiplier for the ultra-violet (UV) and visible (Vis) regions and a PbS detector that for the near-infrared (NIR) part. The switching between the two detectors takes place at  $\lambda = 860.60$  nm, which is the weakest operating region of both detectors [68].

The integrating sphere has a diameter of 150 mm and is internally coated with

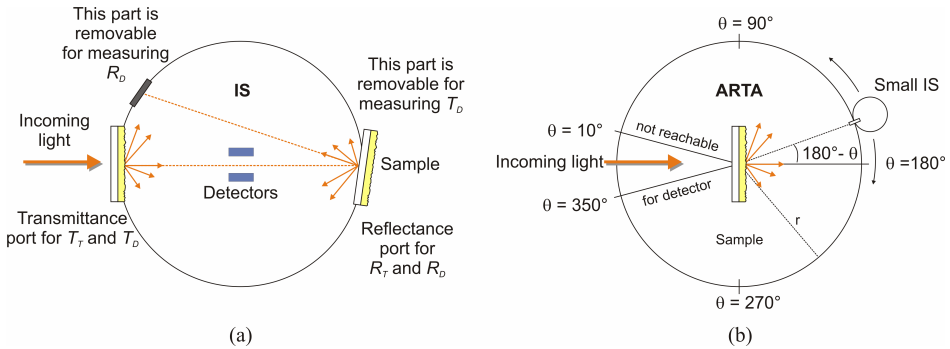


**Figure 2.2.** Sketch of the IS (a) and ARTA (b) accessories for the Perkin Elmer Lambda 950 spectrophotometer. Adapted from [69].

a highly reflective material with a Lambertian behaviour<sup>†</sup>. When light enters through the sample positioned at the transmittance port (see fig. 2.2a), due to multiple internal reflections total transmittance  $T_{\text{tot}}(\lambda)$  can be measured. In order to measure diffuse transmittance  $T_{\text{diff}}(\lambda)$ , it is possible to remove a cap located at the reflectance port, opening in this way a hole through which the perpendicular component of transmitted light can leave the sphere.

In a similar way to transmittance measurements, by positioning the sample at the reflectance port of the IS the total reflectance  $R_{\text{tot}}(\lambda)$  can be measured, as well as its diffuse part  $R_{\text{diff}}(\lambda)$  – once another cap is removed to allow the specular component of reflected light to escape the sphere. Knowing both total reflectance and transmittance, it is possible to calculate the absorbance of a film or device ( $A = 1 - R_{\text{tot}} - T_{\text{tot}}$ ), noting however that the substrate carrier on which the layer or device are deposited may also absorb some of the light in the inspected wavelength range [69].

The ARTA accessory (fig. 2.2b) has a diameter of 180 mm and is used to conduct reflectance (transmittance) measurements for different angles of incidence of light ( $\theta_{\text{inc}}$ ) and different angles of reflection  $\theta_r$  (transmission,  $\theta_t$ ) – once again as function of the wavelength of incident light. The sample can be rotated between  $-90^\circ$  and  $90^\circ$ , while a small integrating sphere revolves around the sample and measures either reflectance (if in front of the sample) or transmittance (if at the back). ARTA also includes a polariser, to allow for measurements with  $p$ - and  $s$ -polarised light. Results of such measurements give an indication of a

<sup>†</sup>A Lambertian surface scatters light uniformly in all directions; such surface obeys Lambert's cosine law:  $I = k \cdot \cos(\theta)$ , where  $I$  is the intensity of (scattered) light,  $k$  is a proportionality factor and  $\theta$  is the scattering angle.

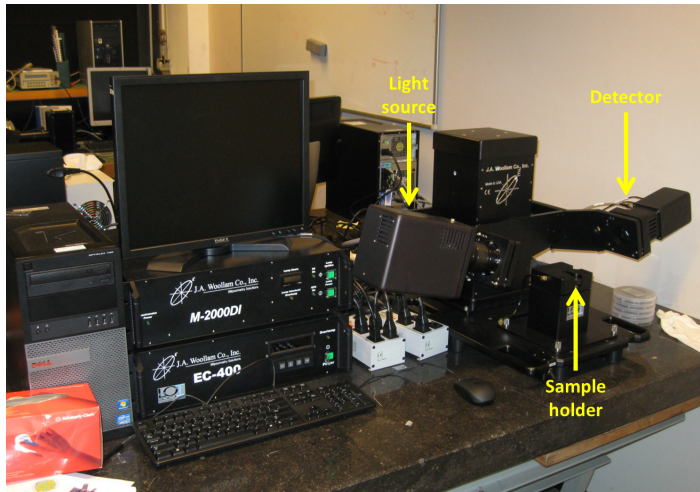


**Figure 2.3.** The J.A. Woolam Co. ESM-300 spectroscopic ellipsometer. Obtained from [69].

film / device optical performance (reflectivity and transmittivity) in different illumination conditions, as well as the scattering properties of a sample – by computing the angular intensity distribution  $AID(\lambda)$  of reflected (transmitted) light:  $AID_r(\lambda) = R(\lambda, \theta_r) / I_{inc}(\lambda)$ , where  $I_{inc}$  is the intensity of incident light.

The IS was used to measure the reflectance of nanowire (Chapter 3) and CIGS solar cells (Chapter 5). ARTA measurements were carried out to obtain the complex refractive index of intrinsic and aluminium-doped zinc oxide (Chapter 5).

### 2.1.2 Spectroscopic ellipsometry

Spectroscopic ellipsometry (SE) is an optical technique used to determine the wavelength-dependent dielectric properties (complex refractive index or dielectric function) of thin films. SE can be used to characterise composition, roughness, thickness (depth), and other material properties [70]. The term spectroscopic refers to the broad-band light source employed, as opposed to single-wavelength ellipsometry which uses monochromatic sources.

Ellipsometers measure the polarisation change as incident radiation interacts with the measured sample. In the most common configuration, light impinging with incident angles larger than 0 is reflected by the sample, and the specular component of reflected light is collected by a detector positioned symmetrically to the light source – with respect to the normal to the sample surface. The polari-

sation change can be quantified by an amplitude ratio,  $\Psi$ , and a phase difference,  $\Delta$ , between incident and reflected light.  $\Psi$  and  $\Delta$  are related by eq. (2.1):

$$\tan(\Psi) \cdot e^{j\Delta} = \rho = \frac{r_p}{r_s} \quad (2.1)$$

where  $\rho$  is the ratio of the reflectivity of  $p$ -polarised light ( $r_p$ ) to the one of  $s$ -polarised light ( $r_s$ ). Hence,  $\tan(\Psi)$  represents the magnitude of  $\rho$  and  $\Delta$  its phase [70]. Because the reflected signal depends on the thickness as well as on the material properties, ellipsometry can be a universal tool for contact free determination of thickness and optical constants of films of all kind [70].

The equipment used is the ESM-300 spectroscopic ellipsometer by J.A. Woolam Co. (see fig. 2.3). It consists of a light source, which emits a beam of broad-band light towards the sample holder – where the sample is positioned. The robotic arm holding the light source can rotate to change the angle of incidence of light on the material. On the other side of the machine, a symmetrically positioned arm holds the detectors. The two arms move together in order to allow the detectors to collect the specular component of light reflected by the sample. There are two detectors present, one for UV/Vis light and the other for NIR light.

The measured parameters ( $\Psi$  and  $\Delta$ ) are fitted with different functions, depending on the material under analysis. When the fitting is deemed sufficiently accurate, the optical properties of the material, the layer thickness and the roughness of the top surface can be obtained. In particular, the complex dielectric function  $\tilde{\epsilon}$  can be extracted. Knowing the relation between  $\tilde{\epsilon}$  and  $\tilde{n}$ :

$$\tilde{\epsilon} = \epsilon_1 + j\epsilon_2 = (n + j\kappa)^2 = \tilde{n}^2 \quad (2.2)$$

It is possible to determine the values of  $n$  and  $\kappa$ :

$$\begin{aligned} n &= \sqrt{\frac{\sqrt{\epsilon_1^2 + \epsilon_2^2} + \epsilon_1}{2}} \\ \kappa &= \sqrt{\frac{\sqrt{\epsilon_1^2 + \epsilon_2^2} - \epsilon_1}{2}} \end{aligned} \quad (2.3)$$

SE measurements were used to determine most of the complex refractive index data used in simulations in all chapters of this work, with the exception of the properties obtained from literature. SE was particularly important to determine

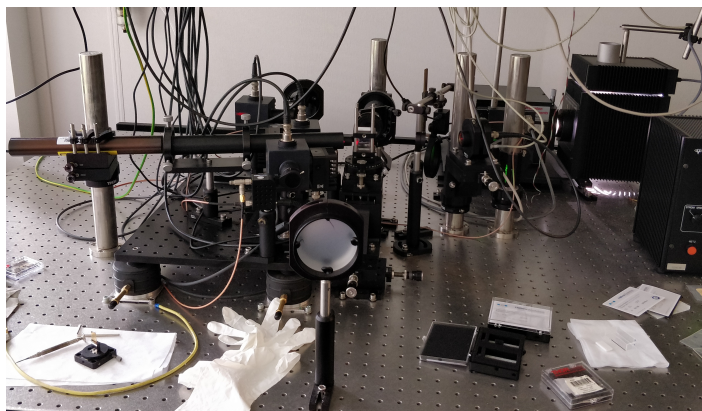


**Figure 2.4.** The photothermal deflection spectroscopy system of the PVMD group.

the input parameters for the calibration of the modeller for CIGS devices (Chapter 5) and – together with photothermal deflection spectroscopy (PDS, see next section) – for the determination of the absorption coefficient of  $\text{BaSi}_2$ .

### 2.1.3 Photothermal Deflection Spectroscopy

Photothermal deflection spectroscopy (PDS) is used to determine the optical properties of materials. In particular, a chopped light source impinges on a thin layer. Through a series of mirrors, reflected and transmitted light can be directed to two separate integrating spheres and thereby be measured. This procedure already offers an advantage with respect to spectrophotometry, since  $R$  and  $T$  are measured on the same place of the sample. In addition, PDS directly measures absorbance – by means of a (red) laser grazing the surface of the film. All light neither reflected nor transmitted is absorbed by the material, assuming a transparent substrate is used (quartz in the experiments of this work). Most of the absorbed energy becomes heat, increasing the film temperature. The heat is then released into the surrounding environment (quartz is a thermal insulator), which in the case of the setup here described (see fig. 2.4) is a thermally sensitive liquid: perfluorohexane (FC-72). The refractive index of FC-72 changes with temperature, hence absorption in the measured film will induce a deflection of the red laser path. This deflection is measured, with the help of a lock-in amplifier [71].

Due to the peculiar working principle, PDS is particularly indicated for measuring weak absorption and related properties. For example, it can be used to quantify sub-bandgap absorption, which can be then associated with defects or

other structural and/or composition properties of materials [72, 73]. In the work of this thesis, PDS is used in combination with SE to determine the absorption coefficient of epitaxially-grown BaSi<sub>2</sub> samples.

### 2.1.4 Scanning Electron Microscopy

Scanning electron microscopy (SEM) was used to visually study the surface of nanowire devices (Chapter 3) and the cross-section of the calibration CIGS solar cell (Chapter 5). The working principle of SEM is based on the detection of electrons emitted by a specimen under observation, being irradiated by a highly energetic electron beam (from 0.2 keV to 40 keV). Such beam, emitted by a LaB<sub>6</sub> crystal, is focussed through one or two lenses and is deflected along the  $x$ - and  $y$ - directions by means of scanning coils. In this way, a so-called *raster scan* of the sample surface or cross-section is enabled. Secondary electrons emitted by the specimen are detected and interpreted as brightness and contrast signals. A scanning electron microscope can inspect wide areas with many levels of zoom, and typical achievable resolutions are in the order of hundreds or tens of nanometres. In this work, a Philips XL-50 SEM system located in the clean room class 100 of the Else Kooi Laboratories (EKL) was employed.

### 2.1.5 Atomic Force Microscopy

Atomic force microscopy (AFM) was employed for the determination of the roughness of CIGS layers, in Chapter 5. This process was instrumental for the numerical study of statistical parameters of the texture geometry, which was a necessary step in the calibration of the modelling software for the simulation of CIGS devices.

In AFM, a laser beam – reflected by a metal-coated silicon-based cantilever and detected by photodiodes – provides an indirect image of the surface of a sample. On the non coated side, the cantilever has a tip with radius of curvature of few nanometres, which is used to scan the surface. The substrate to scan is mounted on a piezoelectric (PZT) stage, which can translate electrical inputs into small movements in the  $x$ -,  $y$ -, and  $z$ -directions. The stage is smoothly lifted up (in the  $z$ -direction) until the cantilever starts to deflect – due to the interaction between the cantilever tip and forces established at nanometric distances. The effect, initiated at the (non-coated) tip side, is sensed indirectly at the opposite (coated) side by two photodiodes. In fact, the difference of their optical response – i.e. the reflection of the laser beam on the metallic surface – is proportional to the cantilever deflection. The PZT stage moves the substrate in the  $x$ - and  $y$ -directions,

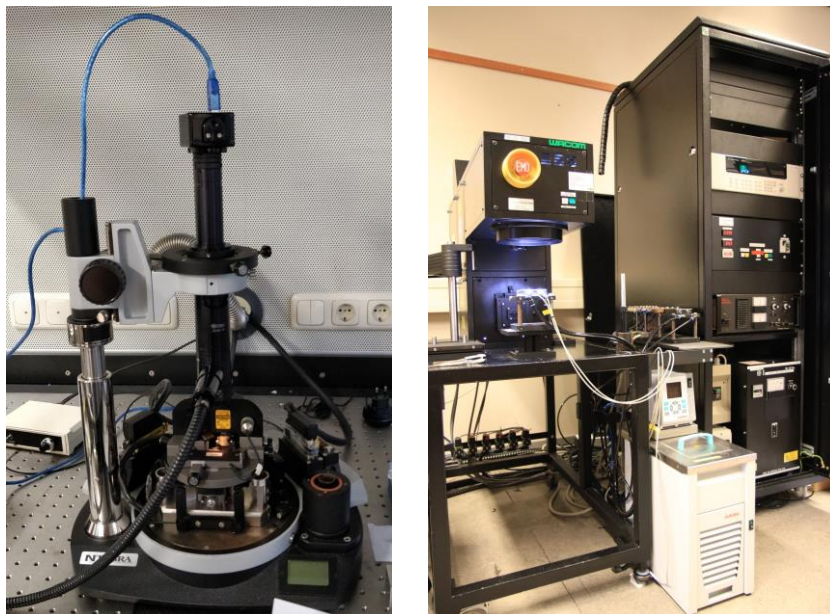


**Figure 2.5.** The nTegra NT-MDT atomic force microscope of the PVMD group (left), and the current-voltage measurement setup with a continuous solar simulator from WACOM (right).

allowing the scan of the surface. AFM systems present resolutions in the order of nanometres, thus higher than scanning electron microscopes. However the reachable area without physically displacing the specimen is in the order of  $100 \times 100 \mu\text{m}^2$  up to  $200 \times 200 \mu\text{m}^2$ , depending on the model and on the scan configuration.

### 2.1.6 Current-voltage response

Current-voltage properties of the nanowire solar cells (Chapter 3) were measured with a dedicated setup located in the PVMD group measurement rooms. A WACOM solar simulator (continuous type) was employed to mimic the standard AM1.5 spectrum [74]. A mask was used to ensure illumination of only the active area of the devices. Metallic probes were used for contacting with the positive and negative sides of the devices. The voltage difference applied at the probes was swept, and the generated current was measured. Once the complete curve was obtained (voltage from 0 to the open-circuit value), fill factor and efficiency are calculated – provided the device area is known. To ensure accurate

results, the value of the short-circuit current density – which is the parameter most sensitive to shape and intensity of the spectrum – is usually corrected with the value obtained via non-biased external quantum efficiency measurements.

### 2.1.7 Spectral response

The spectral response of nanowire (Chapter 3) and CIGS solar cells (Chapter 5) was characterised by external quantum efficiency (EQE) measurements. EQE quantifies the amount of collected charge carriers with respect to the total number of impinging photons – as function of the wavelength of incident light. The manufactured device is contacted on both front and back side with metallic probes. Monochromatic light (of known intensity, thanks to calibration with a photodiode) is then shone on the solar cell. A voltage can be applied to the device, and the response is measured and then converted into the ratio of collected carriers to incident photons, for every wavelength measured (commonly the range  $300 \text{ nm} < \lambda < 1200 \text{ nm}$  was employed).

Since the obtained results are calculated as the ratio to the intensity of the light source, the obtained EQE spectra are independent of the source itself (provided its intensity is known). As such, it is possible to convolute the obtained EQE with a known spectrum, such as the standard AM1.5, to obtain the photogenerated current density. If the voltage bias applied to the device is 0, this computed value corresponds to the short-circuit current density of the solar cell – and can be thus used to correct the value obtained directly by employing a wide-band spectrum such as the one of the WACOM solar simulator.

The setup used in this work was built in house, and comprises a Newport illuminator/monochromator, a chopper (to minimise the effect of peripheral light), a substrate holder with magnetic pads to hold the probes, and a lock-in amplifier. In addition – since the output light of the monochromator may exhibit a preferential polarisation due to the gratings used to select the individual wavelengths – a wedge depolariser made of quartz and fused silica lenses is mounted after the output port to ensure random polarisation of the light beam.

## 2.2 Optical modelling of photovoltaic devices

In the second part of this chapter, the modelling approach used throughout this work to assess the optical performance of various solar cell structures is explained. Provided that the material properties used were correctly characterised, and that the device geometry was precisely replicated, simulations yield accurate values of reflectance and absorptance in each layer of the modelled architectures.



These results can be used as a first indication of the performance that can be achieved in equivalent manufactured solar cells, while providing – at the same time – a great insight into the physical phenomena related to the interaction between light and matter. Modelling is thus a fundamental part of the design and optimisation of photovoltaic devices, provided that it is accurately carried out and that its results are interpreted as guidelines for manufacturing, rather than hard predictions of real structures performance.

Moreover, it is important to point out that the simulations of this thesis are all carried out with models of solar cells in air. Industrial devices, on the other hand, are characterised by a few more layers – necessary to encapsulate the solar cells within the structure of a module. Hence, the results of all simulations of this work (in terms of optimal geometry and performance) might not perfectly correspond to the optima for those same devices when part of a photovoltaic module. Nevertheless, the general analysis and trends observed are applicable for industrial architectures – but it is crucial to keep this mismatch in mind.

In this thesis, the high frequency structure simulator (HFSS) developed by ANSYS has been used [75]. After providing a brief description of the finite element method, on which HFSS is based, the operational procedure to get the result presented in Chapter 3 through 7 is detailed.

### 2.2.1 The finite element method for solving Maxwell equation

The finite element method (FEM) is a numerical technique used to find approximate solutions to mathematical problems, Maxwell equations in the case of this work. When using 3-dimensional FEM, the volume of the simulated structure (i.e. the solar cell) is divided into tetrahedra and the components of the electromagnetic field at their vertices are computed. In this method the Faraday and Ampere-Maxwell laws are combined to obtain the Helmholtz vector equation [76], in terms of the electric field  $\mathbf{E}$  (a similar equation can be derived for the magnetic field  $\mathbf{H}$ ):

$$\nabla \times \frac{1}{\mu_r} \nabla \times \mathbf{E} - k_0^2 \epsilon_r \mathbf{E} = jk_0 Z_0 \mathbf{J} \quad (2.4)$$

where  $\mathbf{J}$  is the electric current density (in  $\text{Am}^{-2}$ ),  $\epsilon_r$  ( $\mu_r$ ) the relative electric permittivity (magnetic permeability) of the medium under consideration,  $k_0 = 2\pi/\lambda$  the wavenumber *in vacuo*, and  $Z_0 = \sqrt{\mu_0/\epsilon_0} = 377 \Omega$  the impedance of free space<sup>‡</sup>. Applying different methods, it is possible to combine eq. (2.4) and its equivalent for the magnetic field into the matrix form  $\underline{\mathbf{A}} \cdot \mathbf{x} = \mathbf{b}$ . The vector  $\mathbf{x}$

<sup>‡</sup>The quantities  $\epsilon_0$  and  $\mu_0$  indicate the permittivity and permeability of free space, respectively.

represents the unknown (spacial) components of the electromagnetic field, while the vector  $\mathbf{b}$  is determined by boundary conditions and forced excitation (thus being known). The matrix  $\mathbf{A}$  is square, sparse and symmetric, with its elements indicating material (optical) properties at the nodes. Such systems of equations can be generally solved with iterative or direct techniques. Direct solving methods can be used only for small size problems, owing to their high computational demands. Hence, iterative method-based approaches are normally used, owing to their efficient handling of sparse linear systems.

FEM was chosen over other methods for three main reasons. First, the mesh calculated by FEM algorithms – that describes the volume of each (thin) layer – follows the actual geometry of the interfaces between different materials (i.e. there is no stair-case approximation) [77–79]. Second, FEM-based algorithms feature very fast calculations in a 3-D space – provided that an adequate amount of random access memory is available [80]. Third, the wavelength-dependent optical properties of the materials involved in the simulations can be used as-measured (i.e. no fitting is required) [69]. In this respect, Appendix A shows the optical properties of all the materials used in this thesis. These features make FEM the preferred choice to solve electromagnetic problems over complicated structures, such as the ones studied throughout this thesis.

### 2.2.2 The High Frequency Structure Simulator

The software used for the optical modelling is based on the rigorous solution of Maxwell equations via 3-D FEM, and it is the high-frequency structure simulator (HFSS) by ANSYS [75]. The procedure followed 4 steps:

1. Design of the model
2. Definition of boundaries, excitation and spectrum range
3. Solution of the electromagnetic problem
4. Exporting and processing of solutions

#### Design of the model

HFSS is equipped with a computer-aided design interface, allowing for the design complex 3-D geometries. For multi-layer structures, the user must create a geometry for each of the layers, and then combine them to obtain the full structure. After all the geometry of the model is defined, materials and their (optical) properties need to be assigned to each layer. Materials must be defined by the

real part of the dielectric function  $\varepsilon_1$  and by the loss tangent – i.e. the ratio of imaginary to real part of the relative permittivity  $\tau_{\text{loss}} = \varepsilon_2/\varepsilon_1$ . In this work, all materials used in simulation models were characterised in house – unless otherwise specified (see appendix A).

### Definition of boundaries, excitation and spectrum range

After all layers have a material assigned, boundary conditions must be defined. By setting them up appropriately, large solar cell models can be reduced to small structures, reducing in this way the simulated volume of the so-called *unit cell* [81]. A *unit cell* is defined as the smallest possible structure than can be repeated an infinite amount of times to obtain a full solar cell model.

Several boundary conditions can be implemented in HFSS. For this work, *primary-secondary* (P-S) boundary conditions [82], were employed. P-S boundaries are surfaces that mimic the periodicity of a structure in their normal direction. In the case of the example structure of fig. 2.6, they are applied to surfaces parallel to the  $x$ - $z$  and  $y$ - $z$  planes – replicating the *unit cell* in the  $y$  and  $x$  directions, respectively. The components of the electromagnetic field calculated at the *primary* surface are equalised to those at the *secondary* one, and in this way continuity is achieved. A phase shift  $\Phi_{\text{P-S}}$  can be introduced between *primary* and *secondary*:

$$\Phi_{\text{P-S}} = \frac{d_{\text{P-S}}}{\lambda} \sin(\theta_{\text{inc}}) \cos(\phi_{\text{inc}}) \quad (2.5)$$

where  $d_{\text{P-S}}$  is the distance between linked P-S surfaces, and  $\theta_{\text{inc}}$  and  $\phi_{\text{inc}}$  are the polar coordinates indicating the direction of the incident field.  $\Phi_{\text{P-S}} = 0$  indicates perpendicular incidence ( $\theta_{\text{inc}} = 0^\circ$ ), while values greater than 0 can be chosen to model oblique incidence (see chapter 3 and chapter 6).

Next, Floquet ports (FPs) are adopted at the top and bottom horizontal surfaces of the *unit cell* ( $x$ - $y$  plane) to create absorbing boundary conditions. FPs simulate an infinite media in which light can propagate unaffected. They have been preferred to alternatives – such as perfectly matched layers – because of faster meshing time required and easier computation of front reflectance [81]. FPs at the top of the unit cell are used to measure reflected light, while a FP positioned at the bottom can be used to compute (eventual) transmittance.

Finally, the frequency range and resolution has to be defined. For the simulations of this work, a constant wavelength step size was preferred to a fixed frequency step size. For all simulations, the starting frequency corresponds to a wavelength of 300 nm. The end frequency depends on the absorber material un-

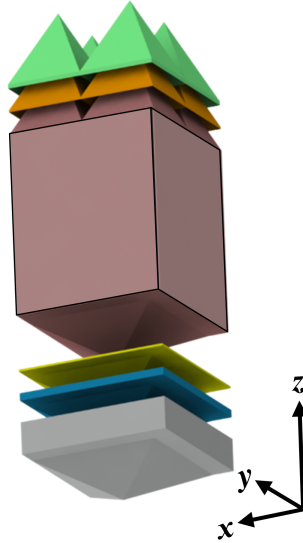


**Figure 2.6.** Example of a device *unit cell*, with different layers identified by different colours.

der investigation and needs to be larger than its bandgap wavelength, to ensure that all useful absorption is considered.

### Solution of the electromagnetic problem

Once all the previously described steps have been completed, FEM-based algorithms in HFSS operate through three phases: meshing, solving, and sweeping. First, the volume of the designed structure is discretised in finite elements (tetrahedra). Then, the linear system of equations  $\underline{\mathbf{A}} \cdot \mathbf{x} = \mathbf{b}$  is iteratively solved; at each iterative step the number of elements increases – to better approximate the structure (mesh adaptation) – until convergence is achieved<sup>§</sup>.

Finally, the electromagnetic field is calculated for each wavelength previously set up [69]. Parameters such as minimum and maximum number of elements, convergence threshold, etc. are defined by the user.

### Results

Calculated solutions are processed to evaluate the optical performance of simulated structures. Reflectance ( $R$ ), transmittance ( $T$ ) and absorptance in each

<sup>§</sup>Convergence is defined, for the purpose of this work, as a sufficiently small result difference achieved by two consecutive iterative steps.

layer  $i$  of the model ( $A_i$ ) are calculated as function of  $\lambda$ . Total reflectance and transmittance were calculated in terms of wavelength-dependent S-parameters as  $R = |S_{11}|^2$  and  $T = |S_{21}|^2$ . Absorptance of the  $i^{\text{th}}$  layer was calculated as the integral, over the layer volume  $v_i$ , of the square of the magnitude of the electric field  $\mathbf{E}$ :

$$A_i = \frac{1}{2} \varepsilon_0 \operatorname{Im}(\varepsilon_i) \omega \int_{v_i} |\mathbf{E}(x, y, z)|^2 dv, \quad (2.6)$$

where  $\varepsilon_i$  is the relative permittivity of the  $i^{\text{th}}$  layer,  $\omega$  is the angular frequency of light and  $(x, y, z)$  denote the coordinates inside the  $i^{\text{th}}$  layer. Note that the wavelength dependence of  $A_i$ ,  $\varepsilon_i$ ,  $\omega$  and  $\mathbf{E}$  is not explicitly indicated. The convolution of each simulated spectrum with the photon flux of the standard AM1.5g irradiance –  $\Phi_{\text{AM1.5}}(\lambda)$  [74] – results in the implied photocurrent density  $J_{\text{ph},i}$  generated (in the active layer) or lost (in supporting layers or due to reflection or transmission):

$$J_{\text{ph},i}(\lambda) = |q| \int_{\lambda_1}^{\lambda_2} X_i(\lambda) \Phi_{\text{AM1.5}}(\lambda) d\lambda \quad (2.7)$$

where  $X_i(\lambda)$  is either  $A_i(\lambda)$ ,  $R(\lambda)$  or  $T(\lambda)$ ,  $|q| = 1.602 \times 10^{-19}$  C is the elementary charge, and  $\lambda_1 < \lambda < \lambda_2$  is the wavelength range considered.

## Elongated nanostructures for thin-film silicon solar cells

This chapter is based on the following publication:

**R. Vismara**, O. Isabella, A. Ingenito, F. T. Si, and M. Zeman, "Geometrical optimisation of core-shell nanowire array for enhanced absorption in thin crystalline silicon heterojunction solar cells," *Beilstein Journal of Nanotechnology* **10**(1), 322-331 (2019).

*ABSTRACT* – In this chapter, elongated nanostructures applied to crystalline silicon heterojunction solar cells are studied. First, a proof-of-concept, wafer-based device was manufactured and characterised. Improved light in-coupling and trapping were observed with respect to a flat reference – only partially hindered by reduced carrier collection resulting in a (best-device) conversion efficiency of 11.8%. Then, a study on the effect of the geometrical parameters of the nanostructure array was carried out, by means of rigorous 3-D optical modelling. Results showed weak dependence of absorption on the height of the nanowires, while their cross-section had a much stronger effect on the optical performance. An implied photocurrent density close to  $27 \text{ mAcm}^{-2}$  was achieved in a  $2 \mu\text{m}$  crystalline silicon layer – for angles of incidence of light between  $0^\circ$  and  $60^\circ$ .

### 3.1 Introduction

Elongated nanostructures, such as nanowire arrays, are an attractive approach to improve absorption in photovoltaic devices. While their nano-scale dimensions can excite various types of resonances of the electromagnetic field within the absorber – such as wave-guiding [83–86], cavity modes [83, 86–89], Fabry-Perót and whispering gallery modes [90] – their characteristic high aspect ratio promotes anti-reflection, allowing for more light to be coupled into the active layer of the solar cell [91–93]. In addition, radial-junction nanowires have the advantage of decoupling absorption and collection by orthogonalising the path of light with respect to the direction of charge carrier collection [92, 94, 95]. This aspect allows for the use of lower quality materials, characterised by short minority carrier diffusion length and/or low absorptivity.

Multiple studies of nanowire solar cells can be found in literature, using different materials: indium-phosphide [96, 97], gallium-arsenide [98, 99], zinc-oxide [93, 100], crystalline silicon [84, 86, 89–91, 94, 95, 101–112], amorphous silicon alloys [113–115], and recently perovskite [116–119]. In this chapter, the performance of crystalline silicon (c-Si) nanowire arrays is investigated. The study is divided in two parts. First, a proof-of-concept device was fabricated, consisting of a heterojunction of amorphous silicon on a *p*-type c-Si nanowire array. The standard manufacturing process of c-Si heterojunction solar cells was followed, with the only addition of a cost-effective mask-less reactive ion etching step to create nanowires on the surface of the *p*-type Si wafer. The resulting  $5 \times 5 \text{ mm}^2$  cell exhibits a best-device efficiency of 11.8%, with an open-circuit voltage of 500 mV and fill factor of 0.67. This ensures the feasibility of the proposed device architecture – in particular of the deposition of conformal passivation and contact layers on the high aspect ratio nanowire geometry.

In the second part, a geometrical study of the nanowire array is carried out, using rigorous optical modelling. An ultra-thin c-Si absorber is employed, to focus the analysis on the effect of nanowires on the propagation of light inside the solar cell. Implied photocurrent densities close to  $27 \text{ mAcm}^{-2}$  are achieved, for a  $2\text{-}\mu\text{m}$  thick c-Si absorber coated with nanowires. The enhanced optical performance – with respect to a flat device – is explained by excitation of resonances both inside the nanowires and in the bulk c-Si absorber. In addition, good angular resilience is displayed, with high implied photocurrent density values (i.e. strong absorption) observed for angles of incidence of light up to  $60^\circ$ , making the proposed solar cell architecture attractive in a wide range of illumination conditions.

## 3.2 Crystalline silicon nanowire solar cell

### 3.2.1 Device manufacturing and characterisation

The nanowire array was manufactured on a *p*-type mono-crystalline silicon (c-Si) wafer by reactive ion etching (RIE) using a gaseous mixture of SF<sub>6</sub> and O<sub>2</sub>, followed by standard cleaning, rinsing in de-ionised water and drying of the substrate. In particular, the SF<sub>6</sub>/O<sub>2</sub> plasma provides a continuous flow of fluorine radicals (F<sup>\*</sup>) and oxygen radicals (O<sup>\*</sup>), which feeds two competing chemical reactions: F<sup>\*</sup> and Si react to form SF<sub>4</sub><sup>+</sup> ions, while from the reaction of O<sup>\*</sup> and Si a silicon oxyfluorine (SiO<sub>x</sub>F<sub>y</sub>) layer is formed. Such layer acts as mask against F<sup>\*</sup> etching, but is physically broken by sputtered ions bombarding the surface of the sample. Such effect occurs with higher speed on the horizontal rather than the vertical plane, due to the larger angle of incidence of ions hitting the vertical side walls. Such phenomenon leads to a strong anisotropy of the Si etching rate. The process is made mask-less by the precipitation of SiO<sub>x</sub>F<sub>y</sub> particles, which start the formation of randomly distributed etch pits [120]. Such regions become deeper during the process, thanks to the strong anisotropic nature of this RIE.

A back side emitter was formed by phosphorous ion implantation, with energy of  $2 \times 10^{15} \text{ cm}^{-2}$  and dose of 20 keV. Oxidation and annealing were carried out in a dry ambient at 850 °C for 90 min, resulting in a sheet resistance ( $R_{\text{SH}}$ ) of 60 Ω/□. Before depositing the coating layers, the silicon wafer with nanowires on top was treated with diluted hydrofluoric acid, to remove the thin native oxide layer from the surface. Plasma-enhanced chemical vapour deposition (PECVD) was used for growing thin-film silicon and silicon alloys layers, to implement surface passivation and front surface field. Intrinsic hydrogenated amorphous silicon a-Si:H – with a thickness equivalent to 30 nm on a flat substrate – was first coated onto the front surface of the wafer, on which the nanowires were distributed. Following a hydrogen-plasma treatment, highly-transparent boron-doped hydrogenated nano-crystalline silicon oxide (*p*-type nc-SiO<sub>x</sub>:H) with a 30 nm equivalent thickness was deposited on a-Si:H. For the front electrode, a 100-nm thick tin-doped indium oxide layer (In<sub>2</sub>O<sub>3</sub>:Sn, ITO) was deposited at low power and low temperature, using radio-frequency (RF) magnetron sputtering. The cell area was defined as 5 mm × 5 mm, using a mask during ITO deposition. The reported equivalent thickness values of thin films on flat c-Si substrate were characterised via spectroscopic ellipsometry. Finally, using physical vapour deposition, metal electrodes consisting of Ag/Cr/Al were



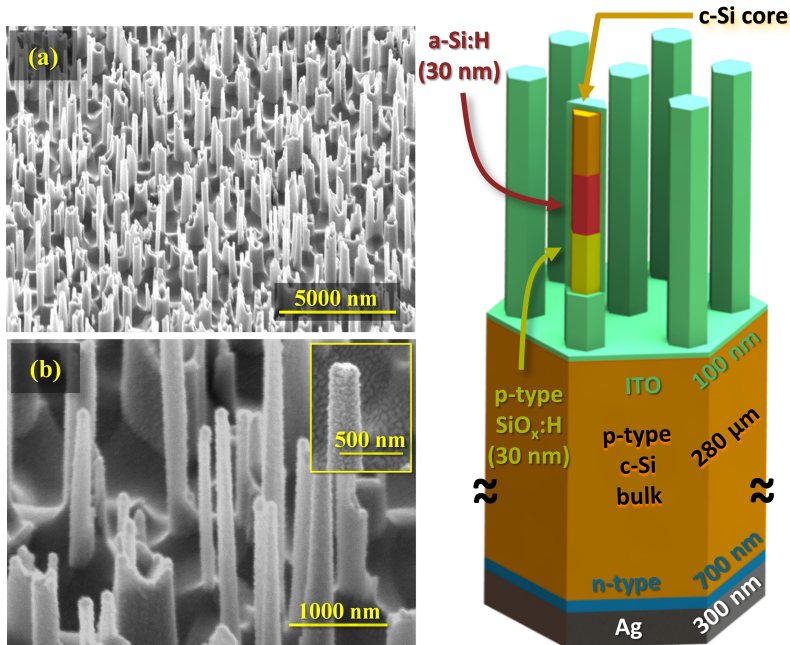


**Figure 3.1.** On the left: scanning electron microscope picture of bare (a) and coated (b) nanowires on the c-Si substrate. In the inset of (b), the enlargement of a single c-Si nanowire wrapped with supporting layers is depicted, showing excellent coating uniformity. On the right: 3-D rendering of the nanowire solar cell (note: thickness not to scale).

deposited at the front (as patterned grids) and at the rear surfaces of the wafer (full-area), with thickness of 300 / 30 / 300 nm and 300 / 30 / 2000 nm, respectively. In fig. 3.1, pictures of the bare (a) and coated (b) nanowire arrays are presented, obtained with a Philips XL-50 scanning electron microscope, as well as a 3-D sketch of the entire device (on the right).

### 3.2.2 Device performance

Two series of devices were manufactured: nanowire heterojunction solar cells, with the procedure described in the previous section, and flat references, characterised by the same process except for the RIE step. The nanowire array has the following (average) dimensions: height  $\bar{h} \approx 2 \mu\text{m}$ , diameter  $\bar{d} \approx 200 \text{ nm}$  and distance  $\bar{\Lambda} \approx 800 \text{ nm}$ . For both architectures, 48  $5 \text{ mm} \times 5 \text{ mm}$  solar cells were

made, on 4-inch c-Si wafers with an initial thickness of 280  $\mu\text{m}$ .

In fig. 3.2 (a), the (non-biased) EQE of both nanowire (NW) and flat (FLAT) devices are depicted. The nanowire solar cell performs better at short and long wavelengths, while its performance suffers in the range between 450 nm and 950 nm. The higher EQE of the nanowire solar cell at short wavelengths (up to  $\lambda = 450$  nm) can be mainly explained by better in-coupling of light, promoted by the nano-structure array at the front side (see reflection depicted in the inset of fig. 3.2b). Lower parasitic absorption at the front side can also explain the improvement, since for  $\lambda < 450$  nm the IQE of the NW cell is higher than in the FLAT case. This results in a net gain in photocurrent density of  $0.30 \text{ mAcm}^{-2}$ . At longer wavelengths, scattering of photons adds to the anti-reflective effect, resulting in a significant performance increase ( $+1.66 \text{ mAcm}^{-2}$ ) with respect to the FLAT device. An additional explanation for the higher performance in these two spectral regions (i.e. short and long wavelengths) is an increased injection level achieved there, due to the same or larger amount of absorption taking place in less material. These higher carrier concentration results in a performance closer to the radiative limit, which is evidenced by the higher IQE observed at both short and long wavelengths (see fig. 3.2b).

On the other hand, the lower EQE in the 450 – 950 nm spectral region can be ascribed to higher charge carrier recombination (i.e. lower collection efficiency), as highlighted by the IQE curves presented in fig. 3.2 (b). While recombination affects the performance across the entire spectrum, at short and long wavelengths this effect is not apparent in fig. 3.2 since the absorption increase promoted by the nanowires compensates the decreased collection efficiency. Across the 48 individual cells, the low average open circuit voltage ( $V_{\text{oc}} = 500$  mV) and fill factor ( $FF = 0.67$ ) are evidence of high recombination, likely caused by the larger interface area with respect to the flat device. The short-circuit current density ( $J_{\text{EQE}}^{\text{(NW)}} = 35.1 \text{ mAcm}^{-2}$ ), calculated from EQE measurements, is only slightly higher than the value obtained for the flat reference ( $J_{\text{EQE}}^{\text{(FLAT)}} = 34.8 \text{ mAcm}^{-2}$ ), since the absorption gains observed at short and long wavelengths are almost entirely offset by higher charge carrier recombination. The resulting conversion efficiency is  $\eta = 11.8\%$ , nevertheless one of the highest reported values for this type of device [107, 110, 111]. More importantly, it was demonstrated that working nanowire-array devices can be manufactured with relatively cheap manufacturing technologies, such as reactive ion etching (nanowires), plasma-enhanced chemical vapour deposition (silicon alloys) and RF sputtering (front TCO). In table 3.1, the measured best-cell external parameters are summarised.

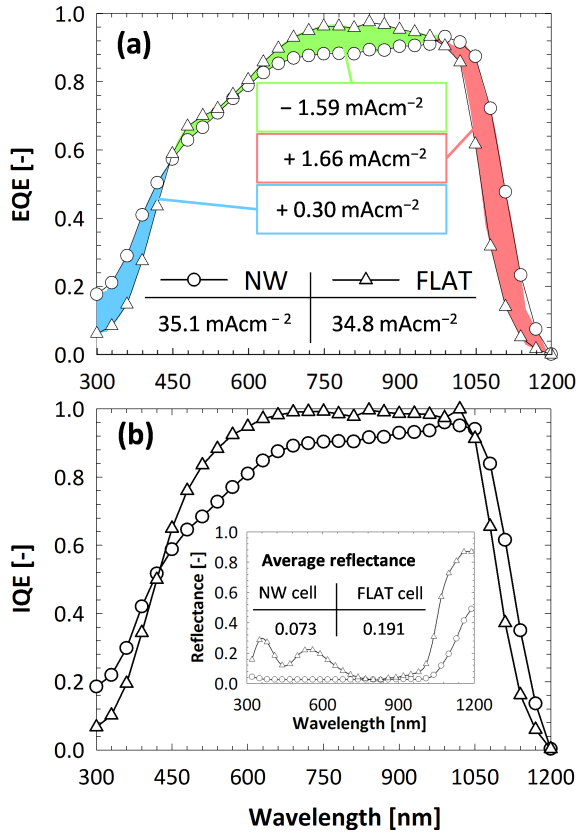


**Figure 3.2.** Measured EQE (a) and calculated IQE (b) of the best nanowire heterojunction solar cell (NW) and of the flat reference (FLAT). The coloured areas in (a) indicate the net current gain (blue and red) or loss (green) of NW with respect FLAT. In the inset of (b), the measured reflectance of the two architectures is reported.

The extremely low fill-factor of the flat device is caused by problems that arose during the ITO deposition, which resulted in a layer significantly thinner than the expected 100 nm. No such issue was observed in the nanowire device.

It can be concluded that the presence of the nanowire array improves the optical performance of the solar cell, namely by promoting good light in-coupling at the front side and by scattering of photons in the near infra-red region of the spectrum – where absorption in c-Si is weak. However, charge-collection efficiency suffers resulting in low  $V_{oc}$  and  $FF$  and a reduced quantum efficiency, particularly in the visible part of the spectrum. This setback could be (partly) avoided

**Table 3.1.** Measured external parameters of the best flat and nanowire solar cells.

Parameter	Flat	Nanowire
$V_{oc}$	600 mV	500 mV
$J_{EQE}$	34.8 mAcm <sup>-2</sup>	35.1 mAcm <sup>-2</sup>
$FF$	0.39	0.67
$\eta$	7.9%	11.8%

by deploying a defect removal etching to improve surface passivation [59], but is expected to remain an intrinsic characteristic of all nanowire devices – due to their large interface area.

### 3.3 Nanowire array geometrical study

In the previous section, the feasibility of the proposed nanowire array structure was verified – particularly the nanowire passivation and the conformal deposition of a transparent front contact. In this section the focus shifts to ultra-thin crystalline silicon solar cells, and how their performance is affected by the presence of a nanowire array. Simulations are thus not carried out on a model of the real solar cell, but rather on

#### 3.3.1 The model

To further understand the interaction of light with nanowires, and how the presence of the NW array affects the absorption in the active silicon layer, optical simulations were used. First, a comparison of the absorption is carried out between a flat reference and a device model endowed with nanowires. The array is assumed periodic (due to modelling constraints) and arranged in a hexagonal lattice. The hexagonal distribution was chosen after a short preliminary study (not reported here for brevity) showed that the hexagonal lattice resulted in slightly higher absorption with respect to square or rectangular ones. This effect was attributed to the larger number of diffraction modes excited by the hexagonal array. Nevertheless, differences between the different arrangements were small. It is thus assumed that a perfectly random arrangement – such as the one of the manufactured device (fig. 3.1) – would yield similar results in terms of absorption and photogenerated current density, despite larger number of excited modes (with respect to periodic structures).

The nanowire geometrical properties mirror the dimensions of the manufactured nanostructures: the distance (or period of the array) is  $\Lambda = 800$  nm, the

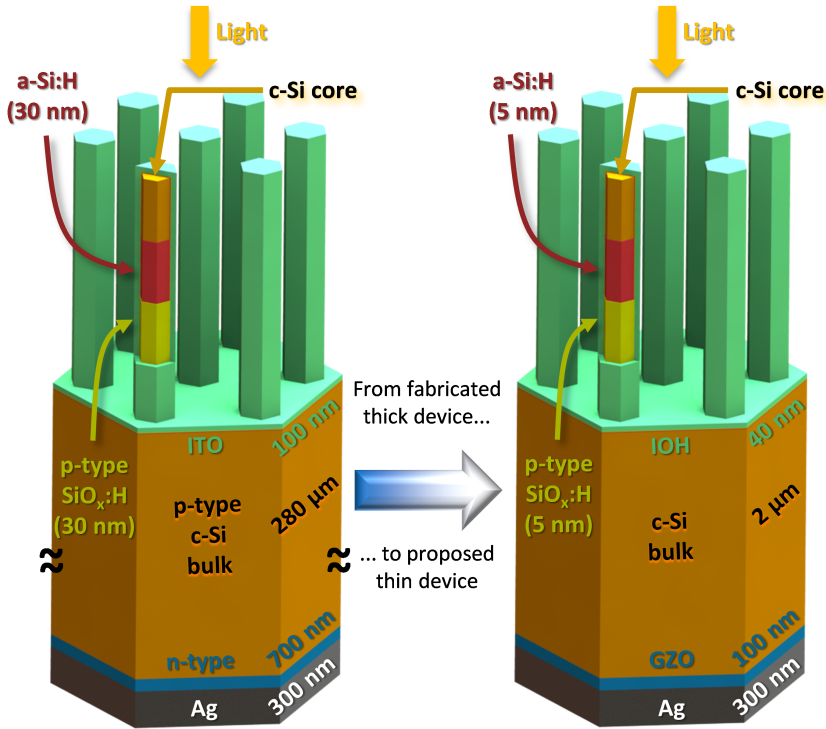


**Figure 3.3.** 3-D rendering of the real device (left) and of the simulation model (right). The differences are: thinner absorber (device: 280 μm, model: 2 μm), thinner and more transparent supporting layers at the front, introduction of a TCO between silicon and metal at the back in place of the implanted *n*-type doped silicon layer. The core of the nanowire (c-Si, orange) is peeled off in both figures, to show the layers that are coating it radially.

height is  $h = 2 \mu\text{m}$  and the cross-section is  $d = 200 \text{ nm}$ . A depiction of the simulation model is presented in fig. 3.3 on the right. Appropriately defined periodic boundary conditions ensure the creation of a complete solar cell endowed with an hexagonal nanowire array. The crystalline silicon bulk has a thickness of only 2 μm, to better highlight the effect of the presence of nanowires. At the front side, a stack of a-Si:H (thickness of 5 nm) and *p*-type nc-SiO<sub>x</sub>:H (5 nm) forms the hole-selective contact, followed by In<sub>2</sub>O<sub>3</sub>:H (IOH, 40 nm) in the role of front transparent conductive oxide (TCO). The three layers uniformly coat both the nanowires and the exposed portion of the bulk. At the back side, the negative

contact consists of another TCO – ZnO:Ga (GZO, 100 nm) [53, 121] – and silver (300 nm). With respect to the manufactured solar cells, the model employed has a few differences (in addition to the thinner bulk and the periodicity of the nanowire array): (i) to reduce parasitic absorption at the front, the a-Si:H and  $p$ -type nc-SiO<sub>x</sub>:H layers are significantly thinner, and IOH is preferred to ITO due to its higher transparency and conductivity [122, 123]; (ii) at the back, GZO is introduced to improve the reflectivity of the contact. The flat reference employs the same layers (material and thickness) as the nanowire model, the only difference being the absence of the nano-structure array.

### 3.3.2 Nanowire vs flat

In fig. 3.4, the calculated absorption in the c-Si layer ( $A_{c-Si}$ ) is depicted, for both nanowire device (NW) and flat reference (FLAT). For  $400 \text{ nm} < \lambda < 550 \text{ nm}$ , the optical performance of the NW model is inferior to the FLAT reference. This result can be explained by higher absorption in front layers, particularly a-Si:H, which in the model endowed with nanowires have to cover a larger surface area. In addition, the geometry of the nanowires can result in light being trapped in the front layers and thereby being parasitically absorbed. On the other hand,  $A_{c-Si}^{(NW)}$  is larger than  $A_{c-Si}^{(FLAT)}$  for  $\lambda > 600 \text{ nm}$ . In this region of the spectrum, the absorptivity of supporting layers is weaker, thus the optical performance of the active layer is not strongly affected by their presence.

The difference between NW and FLAT architectures is to be ascribed to two factors: (i) the NW solar cell model exhibits lower reflectivity than the FLAT reference, due to the presence of nanowires at the front side; (ii) light propagates differently inside the absorber layer – in particular the absorption spectrum of the NW device displays more (resonance) peaks, as highlighted in fig. 3.4 (b) for wavelengths between 800 nm and 1000 nm. In this spectrum range,  $A_{c-Si}^{(FLAT)}$  follows the typical profile of a Fabry-Perót interference (F-P), due to the total model thickness being in the same order of magnitude of the wavelength of light. In fact, the position (i.e. the wavelength) of peaks and valleys – black vertical lines in fig. 3.4 (b) – can be accurately predicted by imposing the condition that the phase difference between primary reflection (air-IOH interface) and secondary reflection (GZO-silver interface) is an integer multiple of  $\pi$ :

$$\lambda_{F-P} = \frac{4\pi \sum_i d_i n_i(\lambda)}{m\pi - [\varphi_b^{(r)}(\lambda) - \varphi_f^{(r)}(\lambda) + \sum_j \varphi_j^{(t)}(\lambda)]} \quad (3.1)$$

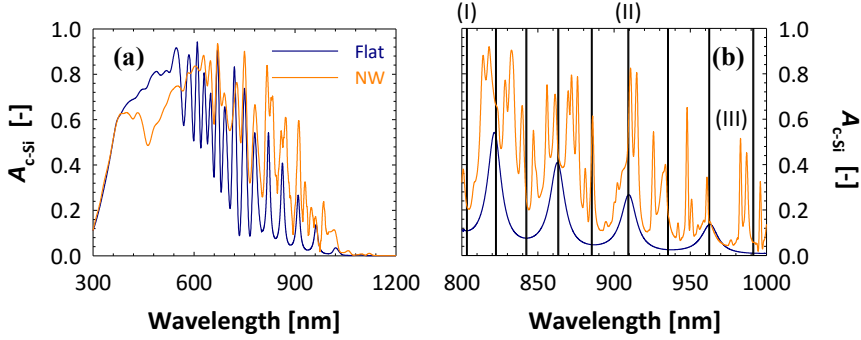


**Figure 3.4.** Calculated absorption in c-Si – as function of wavelength – of the flat reference (FLAT, blue) and nanowire (NW, orange) device models in the range 300 nm – 1200 nm (a) and between 800 nm and 1000 nm (b). Black vertical lines in indicate the position of interference resonances.

where  $\lambda_{F-P}$  is the wavelength (*in vacuo*) at which there is constructive or destructive interference between front and back reflected beams.  $d_i$  and  $n_i$  are the thickness and (wavelength-dependent) refractive index of the  $i^{\text{th}}$  layer,  $m = 0, 1, 2, \dots$ ,  $\varphi_f^{(r)}$  and  $\varphi_b^{(r)}$  are the (wavelength-dependent) phase shifts taking place when light is reflected at the front and back interfaces, respectively, and  $\varphi_j^{(t)}(\lambda)$  is the (wavelength-dependent) phase shift happening during transmission at the  $j^{\text{th}}$  interface (between layer  $i$  and  $i + 1$ ). The absorption profile of the NW model, on the other hand, presents a significantly larger number of peaks, suggesting the excitation of significantly more resonant modes.

The electric field ( $\mathbf{E}$ ) distribution inside the device is useful to understand how the propagation of light is affected by the presence of the array. To this purpose,  $|\mathbf{E}|$  inside the c-Si absorber layer is presented in fig. 3.5, for three different wavelengths. At  $\lambda^{(I)} = 803$  nm, Fabry-Perót interference results in a valley in the absorption profile (see (I) in fig. 3.4). As expected  $|\mathbf{E}|$  is small, with some higher intensity spots located within the nanowires. This weak guided resonance – combined with the presence of more absorber material – explains  $A_{c-Si}^{(NW)} > A_{c-Si}^{(FLAT)}$  for  $\lambda = 803$  nm. On the other hand, at  $\lambda^{(II)} = 909$  nm several high-intensity regions are observed, particularly in the c-Si bulk. In particular, resonances are excited in both the vertical direction (i.e. the direction of incident light,  $\perp$ ), due to F-P interference, and in the horizontal one ( $\parallel$ ), due to diffraction modes inside the silicon layer. The two effects combine to increase the total intensity of the electric field within the absorber layer. This in turn results in a value of absorp-

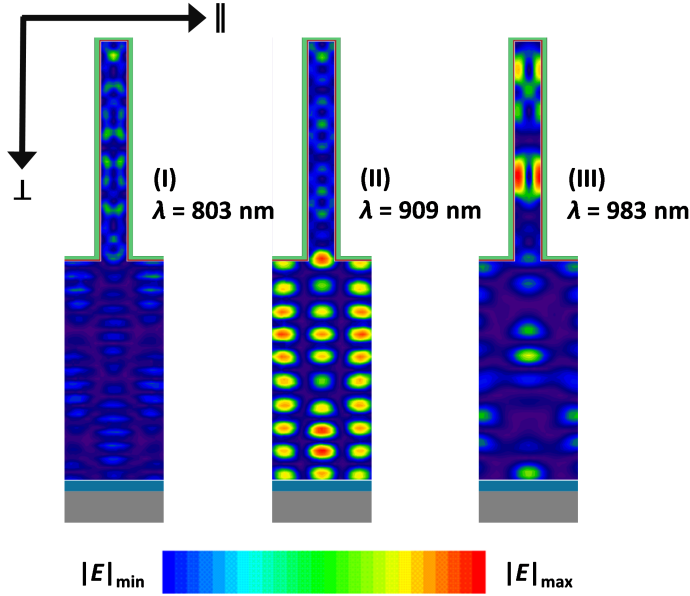


**Figure 3.5.** Distribution of  $|E|$  inside the absorber layer of the NW device for three different wavelengths: (I) 803 nm, (II) 909 nm and (III) 983 nm.

tion – for the NW model – significantly enhanced with respect to the FLAT case, as evidenced in fig. 3.4 at (II). Finally, at  $\lambda^{(III)} = 983$  nm a peak in  $A_{c-Si}^{(NW)}$  can be seen, while  $A_{c-Si}^{(FLAT)}$  is very low due to being close to a Fabry-Perôt minimum. At this wavelength  $|E|$  is strongly enhanced within the nanowires, which appear to act as cavities for the electromagnetic field. The distribution of  $|E|$  does not follow the typical F-P interference or diffraction patterns, but can still explain the boost in absorption observed at (III) in fig. 3.4.

The convolution of  $A_{c-Si}$  with the photon flux of the solar spectrum allows for the quantification of the optical performance improvement introduced by the presence of nanowires. The implied photocurrent density generated in the absorber of the NW device ( $21.8 \text{ mAcm}^{-2}$ ) is significantly higher than the value computed for the FLAT reference ( $17.6 \text{ mAcm}^{-2}$ ), but can be further increased by careful optimisation of the nanowire geometry. To this purpose, the height ( $h$ ) and cross-section ( $d$ ) of nanowires were varied in the ranges  $0 - 5 \mu\text{m}$  and  $0 - 700$  nm, respectively. The distance between individual nanowires was kept constant at  $\Lambda = 800$  nm.  $h$ ,  $d$  and  $\Lambda$  were varied or kept constant within such values as they are expected to be achievable with the developed RIE process.



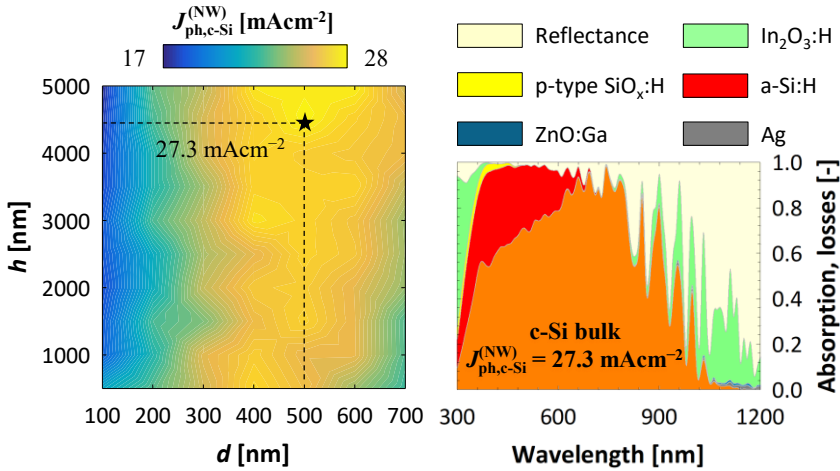


**Figure 3.6.** On the left: implied photocurrent density generated in the c-Si absorber, as function of the nanowire cross-section ( $d$ ) and height ( $h$ ). The maximum ( $J_{\text{ph,c-Si}}^{(\text{NW})} = 27.3 \text{ mAcm}^{-2}$ ) is achieved for  $(d, h) = (500 \text{ nm}, 4500 \text{ nm})$ . on the right, the calculated reflection and absorption in each layer of the model are plotted, for the “best” structure.

### 3.3.3 Geometrical optimisation

In fig. 3.6 (left), the value of  $J_{\text{ph,c-Si}}^{(\text{NW})}$  as function of  $d$  and  $h$  is plotted, while fig. 3.7 depicts reflectance and parasitic absorption losses as function of the same parameters. It can be observed that an increase in NW height reduces reflectance, as expected since (in general) taller nanostructures exhibit better anti-reflection properties. Conversely, losses in supporting layers increase, since more material needs to cover the taller nanowires. The net results of the two opposite trends is a  $J_{\text{ph,c-Si}}^{(\text{NW})}$  that does not display a strong dependence on  $h$ . In fact, for all values of  $d$  the difference in implied photocurrent density between best and worst performing architecture is smaller than  $3 \text{ mAcm}^{-2}$ .

A stronger performance dependence is observed on the nanowire cross section. On one hand, parasitic absorption losses are (almost) independent on the value of  $d$ , for the amount of material used in supporting layers does not depend on the NW lateral size. On the other hand, reflectance losses are significant for narrow nanowires ( $d < 200 \text{ nm}$ ), decreasing sharply until reaching a minimum between  $400 \text{ nm}$  and  $500 \text{ nm}$ . For larger values of the cross-section ( $d > 500 \text{ nm}$ ), reflection losses become larger once again. This behaviour can be explained as fol-

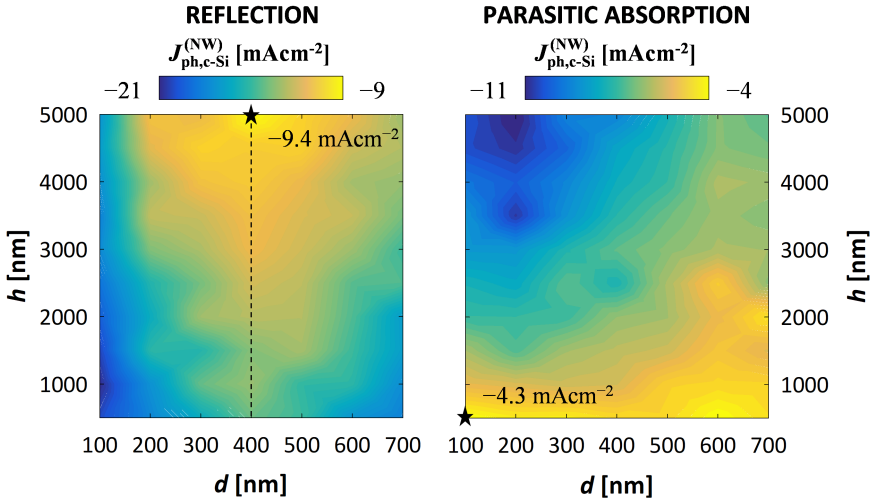


**Figure 3.7.** Reflectance (a) and parasitic absorption losses (b), quantified as implied photocurrent density reduction, as function of nanowire diameter ( $d$ ) and height ( $h$ ). Reflectance is lowest for  $(d, h) = (400 \text{ nm}, 5000 \text{ nm})$ , while parasitic losses reach their minimum when both  $d$  and  $h$  are minimised.

lows. When  $d$  is too small the space between individual wires is wide, reducing the amount of light that hits the NWs and can there be absorbed. By increasing the cross-section, a larger portion of the incident radiation will hit the nanostructures and thereby be absorbed. If  $d$  becomes too large, however, more and more light is reflected by the top surface of the nanowire, thus increasing total reflection. Anttu *et al.* suggest another possible explanation for the optimal cross-section value [97]. In their work on III-V semiconductor nanowire array study, they observed the presence of optimum, bandgap-dependent nanowire diameter values. They associate the calculated optima with specific, diameter-tunable nanophotonic resonances, implying that for a specific semiconductor material an optimal value of the diameter can be found, that maximises absorption owing to the excitation of resonant modes at specific wavelengths.

The final result is that the  $J_{\text{ph,c-Si}}^{(\text{NW})}$  achieves its maximum where reflection is at a minimum (i.e. for  $d = 400 - 500 \text{ nm}$ ). The highest performance is achieved for a solar cell model with  $d = 500 \text{ nm}$  and  $h = 4500 \text{ nm}$ , reaching an implied photocurrent density value of  $27.3 \text{ mAcm}^{-2}$ . Further analysis of the optical losses of the "best" structure (fig. 3.6, right) reveal that a significant amount of light is parasitically absorbed in the intrinsic a-Si:H layer. On the other hand, it is well

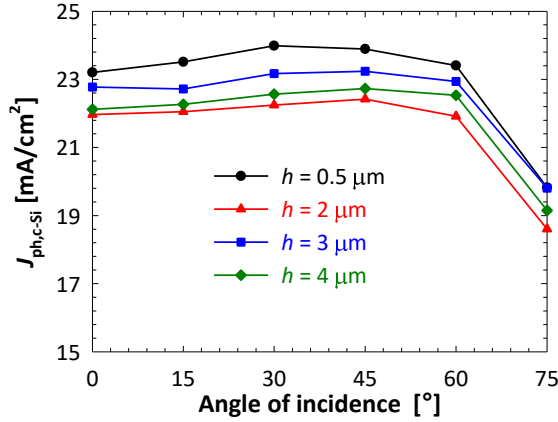


**Figure 3.8.** Calculated implied photocurrent density inside the c-Si layer as function of the angle of incidence of light, for different values of the nanowire height and fixed period ( $\Lambda = 800$  nm) and cross-section ( $d = 200$  nm). For clarity of the picture, only selected results are included ( $h = 0.5, 2, 3, 4 \mu\text{m}$ ).

known that a-Si:H layers in heterojunction devices do contribute to the charge generation, thus adding to the short circuit current density [124]. This effect can be noted in fig. 3.2 (a), where the EQE is higher than the absorption depicted in fig. 3.6, and could be quantified with a rigorous electrical simulation, which is however beyond the scope of this chapter. Nevertheless, the choice of a more transparent passivating layer could result in significant increase of absorption, particularly at short wavelengths ( $\lambda < 600$  nm), and an increase of  $J_{\text{ph,c-Si}}^{(\text{NW})}$  up to  $4 \text{ mAcm}^{-2}$ . It must be noted that the best implied photocurrent density value achieved ( $27.3 \text{ mAcm}^{-2}$ ) is significantly smaller than what was measured for the manufactured NW device ( $35.1 \text{ mAcm}^{-2}$ ). This can be only ascribed to the significant difference in thickness, which in the case of the modelled structures is more than 100 times smaller ( $2 \mu\text{m}$ ) than the nanowire solar cell ( $280 \mu\text{m}$ ).

Finally, the effect of light's angle of incidence ( $\theta_{\text{inc}}$ ) was studied. For different heights and constant values of the period ( $\Lambda = 800$  nm) and cross-section ( $d = 200$  nm),  $\theta_{\text{inc}}$  was varied between 0 and  $75^\circ$ . Results (expressed in terms of  $J_{\text{ph,c-Si}}^{(\text{NW})}$ ) are presented in fig. 3.8 and that optical performance remains fairly constant for a wide range of angles of incidence. Only for very large angles ( $\theta_{\text{inc}} > 60^\circ$ ) a decrease in  $J_{\text{ph,c-Si}}$  is observed. Device models with different nanowire height all follow this same trend, showing that nanowire solar cells can efficiently absorb light in a wide range of illumination conditions, independent on

the size of the NWs. In addition, the performance for different values of  $h$  is similar within the entire range of angles of incidence ( $0^\circ < \theta_{\text{inc}} < 60^\circ$ ). These results are consistent with the findings of the height sweep in the perpendicular incidence case – fig. 3.6(a) – for which it was shown that  $h$  has little-to-no effect of the calculated implied photocurrent density of the absorber.

### 3.4 Conclusions

Nanowires have the potential to improve the optical performance of ultra-thin ( $\sim 2\ \mu\text{m}$ ) c-Si solar cells. The fabricated heterojunction c-Si NW-based device displayed enhanced absorption of light. However, the electrical performance suffered – limiting the final conversion efficiency to 11.8%. The optical simulation of NW-based solar cells demonstrated that NWs excite a significantly larger number of resonant modes, with respect to Fabry-Perót interference typical of flat architectures. The study of the effect of the nanowire geometrical parameters on light absorption was then carried out. For a given periodicity ( $\Lambda = 800\ \text{nm}$ ) of the NW array and thickness of supporting layers, the optimal NW dimensions were determined resulting in  $J_{\text{ph,c-Si}}^{(\text{NW})} = 27.3\ \text{mAcm}^{-2}$ . It should be noted that an optimisation of the array periodicity could further improve the optical performance, particularly by choosing a value of  $\Lambda$  closer to the band-gap wavelength of c-Si ( $\lambda_{\text{gap}} = 1107\ \text{nm}$ ) [125, 126]. However, the manufacturing of such device would require abandoning the proposed mask-less approach in favour of a (potentially) more expensive lithography process and was thus not investigated in this chapter. Finally, it was observed that NW-based solar cells maintain high performance for a wide range of angle of incidence of light, up to  $60^\circ$ .



---

## CHAPTER 4

---

# Metasurfaces for amorphous silicon thin-film solar cells

This chapter is based on the following publication:

**R. Vismara**, N. Odebo Länk, R. Verre, M. Käll, O. Isabella, and M. Zeman, "Solar harvesting based on all-dielectric perfect absorbing metasurfaces," *Optics Express* **27**(16), A967-A980 (2019).

*ABSTRACT* – In this chapter, an investigation is carried out on metasurfaces composed of an array of hydrogenated amorphous Si (a-Si:H) nanoparticles on a mirror, that can achieve nearly complete light absorption close to the bandgap. The concept is applied to realistic device structures and predict a boost in the optical performance of thin-film solar cells made of such a-Si:H nanoparticles. By optimisation of the exact geometrical parameters, a system which could achieve initial conversion efficiency values well beyond 9% is predicted – using only the equivalent of a 75-nm thick active material. The device absorption enhancement is 30% compared to an unstructured device in the 400 nm – 550 nm spectral region and more than 250% in the 650 nm – 708 nm range. Such large values are related to the metasurface anti-reflection properties and to the perfect absorption mechanism.

## 4.1 Introduction

Nanoparticles made of high-permittivity materials have attracted extreme interest in the context of nanophotonics. These systems support multipolar geometrical Mie-like resonances and act as nanoantennas, with electric and magnetic field enhancement within their volume. These characteristics make all-dielectric nanoparticles a perfect platform for multiple applications, such as lasing, metamaterials, flat lenses and photon up-conversion to name a few [87, 127–132]. At the same time, all-dielectric nanoantennas are often associated with low Ohmic losses and a clear connection with light harvesting and solar cells has not yet been drawn: these research fields have not yet strongly interacted.

Nanostructures made of all-dielectric nanoantennas have been proposed and used to boost and improve the efficiency of different types of solar cell [133, 134], but they have been mostly used as scatterers to increase the optical path length inside the absorbing material, or as anti-reflection coatings. An alternative approach is to boost absorption inside the nanoantennas themselves and harvest the generated electron-hole pairs. Despite all-dielectric nanoantennas generally showing small absorption cross-sections in the red region of the visible spectrum, far-field interference effects could be used to increase their absorption. This effect could in theory be used for photon harvesting. In particular, if particles are arranged in a metasurface fashion, it is possible to reach complete absorption in specific wavelength ranges [135]. In the past few years, several studies on perfect absorbers have been reported, both for plasmonic and all-dielectric nanoantennas, and the phenomenon has been used for phase-based sensing [136, 137], terahertz absorption [138], strong coupling [139], light harvesting [127, 140], and photocatalysis [141].

In this chapter, a novel type of solar cell is proposed, where the concept of perfect absorption in a particle-on-a-mirror geometry is employed to boost the efficiency of a-Si:H thin film solar cells. The system under study consists of all-dielectric nanoparticle (nanodisk) arrays arranged in a metasurface-like fashion and placed atop a thick mirror. In this configuration, sketched in fig. 4.1a, the mirror clearly prevents transmission. At the same time, the relative reflection phase difference between the mirror and the metasurface can be controlled by varying the distance between the two. If the spacing and the particle geometry are chosen such that (i) the relative phase shift between metasurface and mirror reflections is  $180^\circ$  and (ii) the respective amplitude is the same, reflection is suppressed and 100% absorption inside the dielectric particles can be achieved

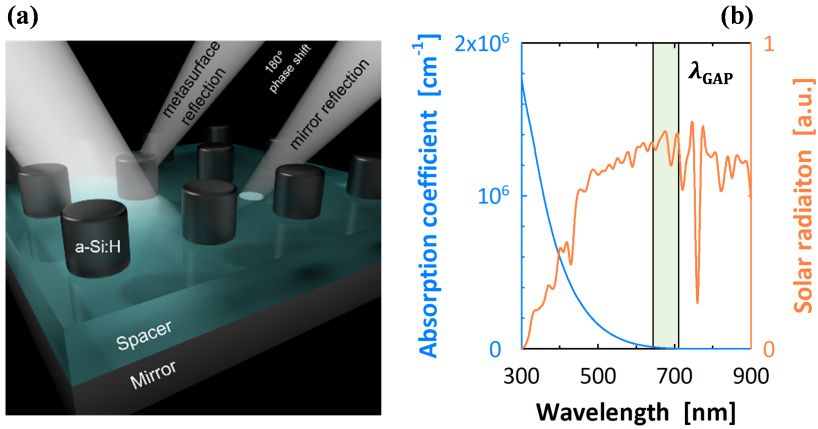


**Figure 4.1.** (a) Sketch of the perfectly absorbing metasurface-on-a-mirror geometry. When the phase difference between metasurface and mirror reflections is  $180^\circ$ , perfect absorption can be achieved. (b) Absorption coefficient of hydrogenated amorphous silicon (blue line) together with the standard AM1.5 solar spectrum radiation (orange line). By engineering the size of the nanoparticles, absorption between 650 nm and 708 nm (green area in b) can be boosted.

– albeit at specific wavelengths. By careful design of the metasurface properties, resonant absorption enhancement can thus be tuned to the spectral region where the intrinsic a-Si:H absorption is low (green region in fig. 4.1b) but the solar spectrum still contains significant energy. By contacting the a-Si:H nanodisks at top and bottom, electron-hole pairs that are generated inside the nanoparticles can be harvested. This concept is new in the sense that the particles that compose the metasurface not only act as light concentrators, but also constitute the active medium of the solar cell. The proposed structure should not pose challenges when it comes to contacting, while surface recombination could represent an issue, despite the particles being embedded in a silicon-oxide layer – a material commonly and effectively used to passivate silicon photovoltaic devices [44, 142–144]. In this way, issues of high recombination and contacting commonly found in nano-structured solar cells can be avoided.

The chapter is organised as follows: after analysing the simple case of a nano-structured metasurface on a mirror, a realistic device is proposed and its geometrical properties are optimised *via* a rigorous 3D Maxwell equation solver – using experimentally-determined permittivity data (see Appendix A). A photocurrent density  $J_{\text{ph}} > 14 \text{ mAcm}^{-2}$  is predicted, using 300-nm tall disks. This



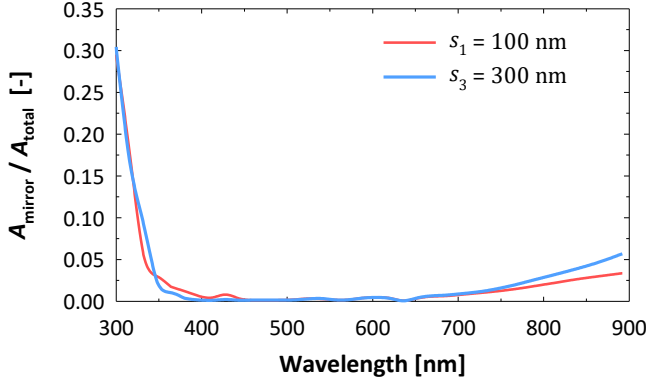


**Figure 4.2.** Absorption in the silver mirror. The plot shows  $A_{\text{mirror}} = 1 - A_{\text{NP}} - R$  as ratio to the total absorption in the system  $A_{\text{total}} = 1 - R$ . Two different spacer thicknesses are shown:  $d_{s_1} = 100$  nm and  $d_{s_3} = 300$  nm.

corresponds to a theoretical initial efficiency beyond 9.5% for an equivalent active material thickness  $< 75$  nm. The predicted photocurrent value represents an enhancement of  $> 2.5$  times with respect to absorption in thick flat layer with the same total 300nm thickness in the 650 nm – 708 nm part of the spectrum (where  $\lambda_{\text{GAP}} = 708$  nm is the bandgap wavelength of amorphous silicon), i.e. in the region where the perfect absorption mechanism was optimised.

## 4.2 Results

### 4.2.1 Perfect absorption in a particle-on-a-mirror geometry

To illustrate the concept of perfect absorption in a particle-on-a-mirror geometry the simplest case possible was chosen, i.e. a periodic array of a-Si:H nanodisks on top of an infinite Ag mirror, separated by a glass spacer with thickness  $d_s$  and refractive index  $n_s = 1.46$  (c.f. sketch in fig. 4.1a). First, the particle-on-a-mirror metasurface was modelled using FDTD methods [145]). The nanodisks have a fixed height ( $h = 300$  nm) and diameter ( $D = 140$  nm), and are arranged in a square lattice configuration with period of  $\Lambda = 250$  nm. For this value of the periodicity the a-Si:H array essentially acts as a metasurface, since the distances and dimensions considered are much smaller than the incident wavelength (no diffuse scattering is present). Optical absorption in the nanodisk was calculated by integrating the Poynting vector on a surface enclosing the particle, but excluding the mirror (see Appendix B for more details). Light absorption in the

active material was thus decoupled from all other loss channels, such as any surface plasmons excited on the mirror interface or other absorption in the silver. It was also verified that most (98%) of the total absorption took place inside the metasurface, rather than in the silver mirror (see fig. 4.2).

In fig. 4.3a, the absorption amplitude for this system at  $\lambda_1 = 630$  nm and  $\lambda_2 = 700$  nm is shown, as function of the mirror distance  $d_s$ . The amplitudes oscillate with a period  $\Lambda_i = \lambda_i/(2n_s) = 210$  nm and 233 nm, respectively (where  $i = 1, 2$ ). The differences in the period of oscillations can be simply understood as a Fabry-Perot like resonance, as the system setup is analogous to a Salisbury screen perfect absorber [146] for specific wavelengths. Absorption in such a screen is maximised when  $d_s = \lambda/(4n_s)$ , i.e. when the reflections present  $180^\circ$  phase difference. Indeed, for  $\lambda_1 = 630$  nm a maximum in absorption can be observed at  $d_s = 105$  nm (fig. 4.3a).

Interestingly, reflection and absorption at specific wavelengths (630 nm with the present nanodisk dimensions) can be modulated from 40% to 100%, by simply modifying the spacer thickness. Fabry-Perot oscillations can also be seen in the absorption spectra *versus* wavelength, for fixed spacing of the mirror (fig. 4.3b). In this case, however, they are modulating the resonant behaviour of the Si nanodisk array. The full absorption spectral dependence on the mirror distance is shown in fig. 4.3c. The system response for varying array periods was also studied – keeping the spacer distance constant at  $d_{s1} = 100$  nm. Absorption as function of the period  $\Lambda$  (fig. 4.3d) shows a rich dispersion and coupling of various modes. The data confirms that the overall absorption is decreased at larger periodicities – as less active material is present – and that the diffractive modes appear in the region of high absorption, i.e. 300 nm – 500 nm, i.e. where  $\lambda \approx n_s P$ .

### 4.2.2 Design of an a-Si:H solar cell based on perfect absorption

So far, the possibility to achieve enhanced absorption in the very simple case of a-Si:H nanodisks on top of a mirror was demonstrated, owing to Fabry-Perot like interference effects between the a-Si:H layer and mirror reflections. Shifting the attention to calculations of a realistic device, a nanophotonic metasurface consisting of a-Si:H nanodisks embedded in a transparent lossless dielectric medium ( $\text{SiO}_2$ ) is proposed. The nanostructures have a fixed height of 300 nm. The particle diameter ( $D$ ) and the period of the array ( $\Lambda$ ) were varied in the ranges  $D = 80 - 240$  nm and  $\Lambda = 100 - 500$  nm, respectively. A commercially available 3D Maxwell equation solver based on the finite element method (FEM)[75] was employed to model the entire device structure.

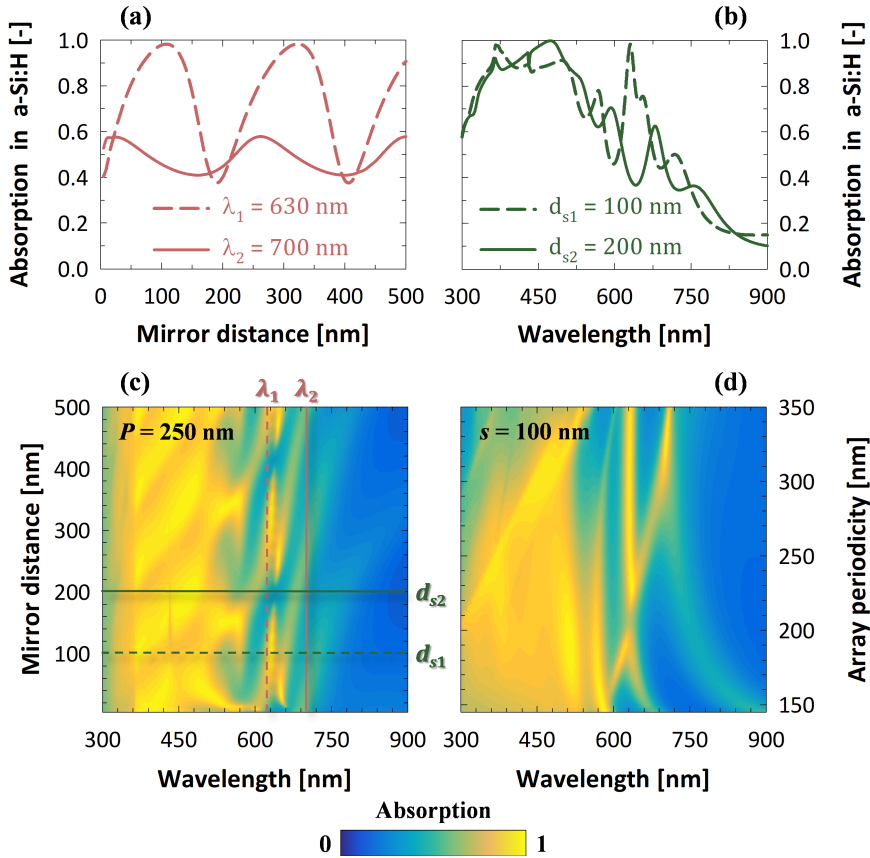


**Figure 4.3.** (a) Absorption in a-Si:H as function of the distance from the mirror, at  $\lambda_1 = 630$  nm and  $\lambda_2 = 700$  nm. (b) Absorption spectra for two specific mirror distances,  $d_{s1} = 100$  nm and  $d_{s2} = 200$  nm. (c) Absorption spectra as a function of mirror distance, for  $\Lambda = 250$  nm. The vertical (red) and horizontal (green) coloured lines are related to the data shown in (a) and (b), respectively. (d) Absorption spectra as a function of the array periodicity, for  $d_s = 100$  nm.

A 20 nm thick (boron-) phosphorous-doped nano-crystalline silicon oxide (nc-SiO<sub>x</sub>:H) layer is added at the (top) bottom of the absorber, to separate photo-generated charge carriers (electrons, e<sup>-</sup> and holes, h<sup>+</sup>). They are then collected on opposite sides: e<sup>-</sup> at the negative, *n*-contact and h<sup>+</sup> at the positive, *p*-contact. At the front side (*p*-contact, top), a highly transparent conductive oxide (TCO) is selected, In<sub>2</sub>O<sub>3</sub>:H (IOH, thickness: 100 nm), thanks to its favourable optoelectri-

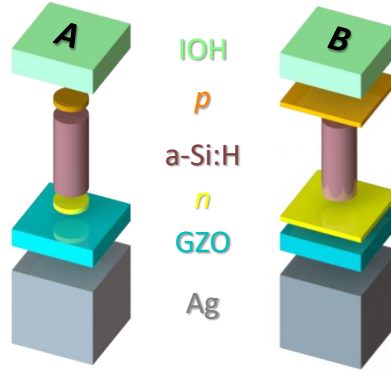


**Figure 4.4.** 3-D sketches of the simulation models, with textured (A, left) and full-area (B, right) doped layers. Note that the  $\text{SiO}_2$  filler is not depicted for clarity.

cal properties [122, 123]. At the back ( $n$ -contact, bottom), a TCO-metal combination of ZnO:Ga (GZO [121]) and silver (Ag) is selected, with thickness of 70 nm and 300 nm, respectively. Both values are typically used in thin-film silicon photovoltaics [60, 147, 148]. The presence of GZO between semiconductor and metal improves the reflectivity of the back side [60] – and the thickness was chosen to allow efficient electron collection at the metal contact. At the same time, the GZO layer serves as the spacer for achieving destructive interference between the two reflections, thus maximising absorption in the  $\text{SiO}_2$ -filled metasurface. Regarding the  $p$ - and  $n$ -type layers, two possible configurations can be devised. First, they can be included in the metasurface structure (structure type A), i.e. being a part of the a-Si:H nanodisks on each side. Alternatively, they can be deposited on the entire device area (type B). Both possibilities were considered, and the respective device models are depicted in the insets of fig. 4.4.

The nanodisks are ordered in a 2D square lattice. However, similar results can be expected using randomly dispersed particles [135]. In fig. 4.5a,b, the implied photocurrent density in the absorber ( $J_{\text{ph,a-Si:H}}$ ) is shown – as a function of diameter  $D$  and periodicity  $\Lambda$  – for device types A and B. For both configurations, two general trends are observed. First,  $J_{\text{ph,a-Si:H}}$  increases when the distance between disks is reduced. Second, a better performance is observed for structures with larger diameter. Both effects correlate to the total amount of absorbing material, which increases with both a decrease in  $\Lambda$  and an increase in  $D$ . However, the optimum response is observed at  $(\Lambda, d) = (250 \text{ nm}, 140 \text{ nm})$ , which does not correspond to the maximum amount of absorbing material within the solar

cell. It is also interesting to note that, for both configurations, the best performance ( $13.80 \text{ mAcm}^{-2}$  and  $14.14 \text{ mAcm}^{-2}$  for structures A and B, respectively) is achieved for the same  $(\Lambda, d)$  pair. In the following, it will be demonstrated that it is the interference between metasurface and mirror reflection that maximises the solar cell performance. Considering state-of-the-art  $V_{oc}$  and  $FF$  values of *substrate* [149] and *superstrate* [150] a-Si:H single-junction devices – deploying  $\sim 250\text{-nm}$  thick absorbers – the calculated best photocurrent densities would imply an initial conversion efficiencies between 8.1% and 9.6 % (for both configurations), albeit for an active material with equivalent thickness  $< 75 \text{ nm}$ . To better outline the different performance between configurations A and B, the respective absorption spectra as function of the wavelength  $\lambda$  are analysed (fig. 4.5c,d). In both cases, distinct absorption peaks are observed for  $\lambda > 600 \text{ nm}$ . Device model B suffers from higher parasitic absorption losses in the p-type nc-SiO<sub>x</sub>:H layer, due to the fact that it covers the entire area rather than only the a-Si:H nanodisks. However, reflection is smaller in the blue range, providing similar overall absorption and efficiency.

It is also instructive to compare the device absorption with a simple unstructured 300 nm thick a-Si:H layer, which is a typical thickness in standard a-Si:H solar cells. The film is sandwiched in the same environment as the metasurface (IOH/p/a-Si:H/n/GZO/Ag). Only the thickness of the GZO layer is changed to 40 nm, which was found to be the optimum in the flat reference configuration. The spectrum, overlaid as a black dashed line in fig. 4.5c,d helps clarifying the absorption of the metasurface itself. Fabry-Perot modes – which depend on the layer thickness – appears at around  $\lambda = 560 \text{ nm}$  and  $\lambda = 620 \text{ nm}$  for both metasurface and unstructured layer. However, additional absorption appears both at shorter and at longer wavelengths for the metasurface. Close to the band gap, the system presents resonances that concentrate the light within the active medium and increase absorption. The significant enhancement in the 350 nm – 550 nm is instead related to diminished reflection. In fact, the metasurface contains roughly four times less a-Si:H than the unstructured layer, so its effective refractive index is lower ( $n_{\text{SiO}_2} < n_{\text{meta}} < n_{\text{a-Si:H}}$ ). This improved impedance matching between layers reduces reflection and enhances absorption. The metasurface thus acts as its own effective anti-reflection coating in this spectral range.

Switching to the wavelength interval  $650 \text{ nm} < \lambda < \lambda_{\text{GAP}} = 708 \text{ nm}$ , it can be seen that absorption in the metasurface is clearly enhanced compared to a homogeneous a-Si:H film. In order to quantify the resonant absorption enhancement

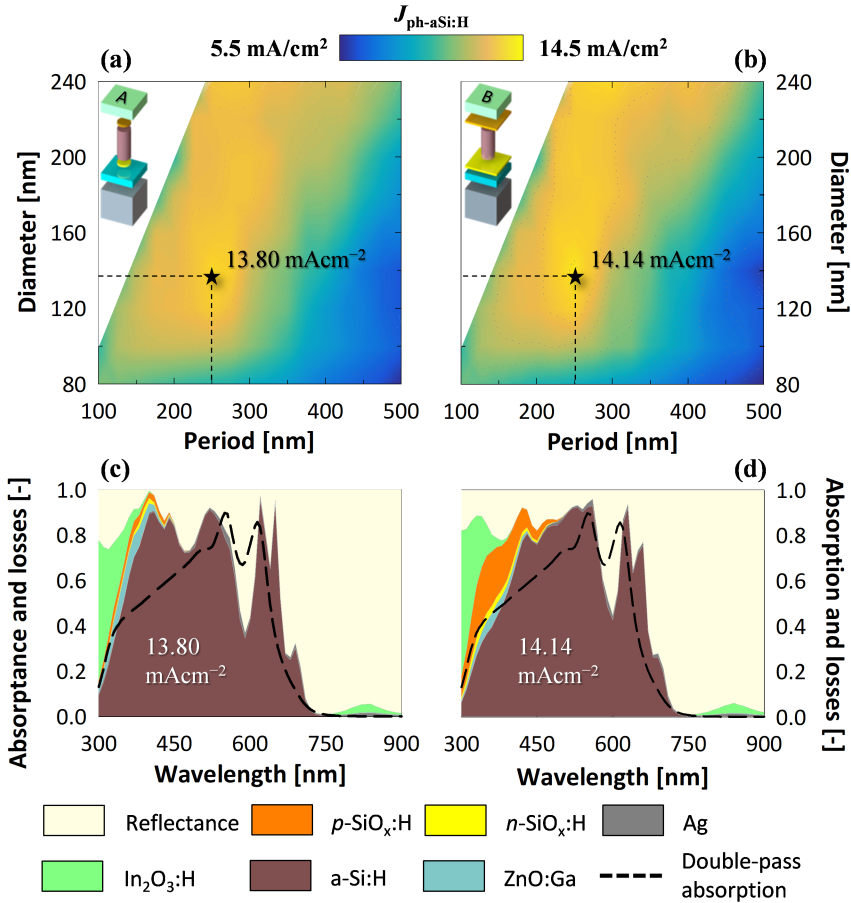


**Figure 4.5.** Implied photocurrent density in the absorber ( $J_{\text{ph,a-Si:H}}$ ), as function of nanodisk diameter and distance, for device configurations A (a) and B (b). The star indicates the parameters that maximise  $J_{\text{ph,a-Si:H}}$ . The corresponding absorption spectra of the optimised structures are depicted in (c) and (d). The dashed black line indicates absorption in an unstructured layer with the same thickness placed in the same environment.

close to the bandgap, a multipolar analysis of the EM field inside the amorphous silicon nanodisks was carried out – for the most efficient type A configuration. This allows for the identification of resonant modes excited in the nanodisks. The multipolar response for different electric and magnetic multipoles is plotted in fig. 4.6, for a system without (a) and with (b) mirror at the back side. The

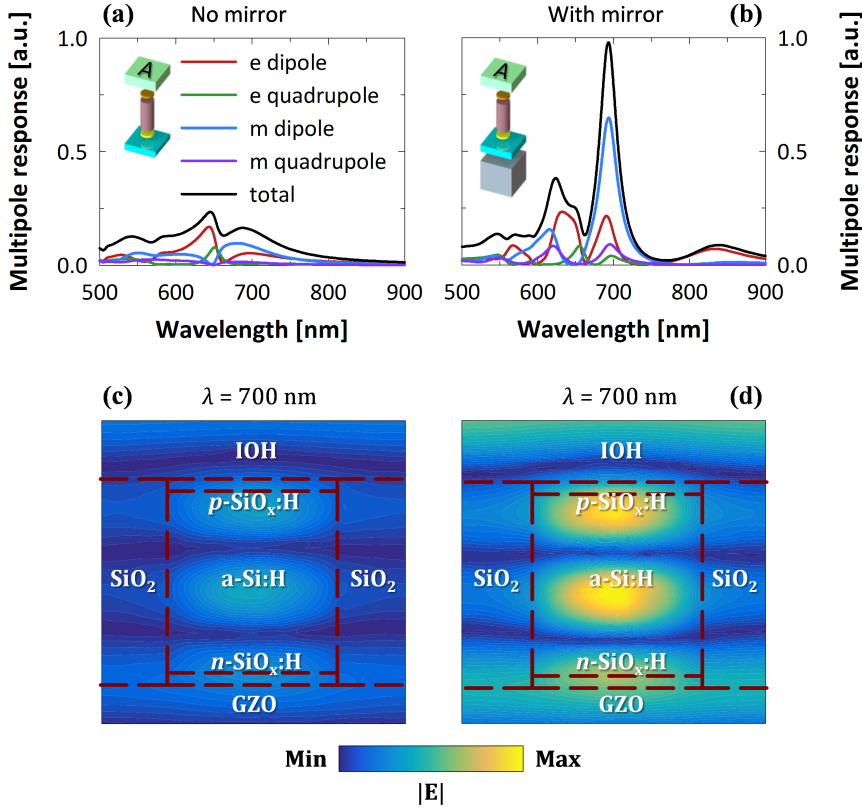


**Figure 4.6.** Multipolar analysis for the solar cell (structure A), for parameters corresponding to the maximum implied photocurrent density without (a) and with (b) back-mirror reflector. A large increase in the modes amplitudes in the 550 – 700 nm wavelength range is observed, due to interference effects with the mirror. The amplitude increase is accompanied by an enhanced near field distribution inside the nanoparticles, shown in (c) and (d) for the two cases (without and with mirror, respectively) at  $\lambda = 700$  nm.

internal fields were projected on a spherical multipole basis, [151] and the mode amplitudes of individual particles – for electric ( $a_\ell$ ) and magnetic ( $b_\ell$ ) multipoles – were calculated (see appendix C for details). Note that this decomposition assumes a homogeneous dielectric environment, which is not fulfilled here. A precise decomposition requires knowledge of the Green’s function outside the particle. However, the analysis carried out in this work is adequate for the purpose of showing the nature of the modes and the related absorption enhancement.

The decomposition of the internal fields shows a rich resonance structure in the spectral region of interest. In particular, various multipolar responses (electric and magnetic dipoles and quadrupoles) are overlapped. Nevertheless, the response of the nanodisk array is dominated by electric and magnetic dipolar resonances, whose amplitudes are enhanced more than 4 times close to the bandgap – once the system is placed on top of the mirror. This behaviour is clearly related to scattering suppression due to destructive interference, which increases the lifetime of the modes and thus absorption. A different, but equivalent, way to see this is by looking at the field enhancement inside the dielectric nanodisks (fig. 4.6c,d). Absorption takes place within these a-Si:H nanoparticles and is proportional to  $A \propto \text{Im}(\epsilon_{\text{aSi:H}}) \int |\mathbf{E}(\mathbf{r})|^2 dV$ , where  $\mathbf{r}$  is the position within the volume  $V$ . Simulations show that fields are significantly larger inside the nanodisks when a mirror is employed, explaining the enhancement observed in fig. 4.6a,b.

In fig. 4.6, all multipolar modes that are excited within each nanodisk are depicted. The presence of high order spherical harmonic modes overlapped with the dipolar response is due to the complex nature of the structure and the presence in it of highly dispersive layers. Nevertheless, it is possible to study the real modes' pseudo-dispersion by simply plotting absorption spectra as a function of the particle diameters (fig. 4.7). For  $\lambda < 500$  nm, where the absorptivity of a-Si:H is very high, absorption is clearly almost independent of the diameter  $D$ . For  $500 \text{ nm} < \lambda < \lambda_{\text{GAP}} = 708$  nm, several clear resonances are observed, which disperse almost linearly with the diameter. These peaks in the absorption spectra red-shift when nanodisks with larger diameter are used, at a different rate, providing an additional route to fine tune the absorption and the response of the system. In particular, the geometrical optimum  $D = 140$  nm was found to coincide with a balance between the separation between these modes and convoluted with the absorption in a-Si:H.

### 4.3 Discussion

From a practical point of view, the particle-on-a-mirror system presented here is possible to fabricate. The most likely route would rely on patterning of the nanodisks using self-assembled large scale nanoimprint methods [152], followed by a planarization step and the deposition of the top contact. Due to the departure from full planar deposition, and therefore not dealing with bulk absorbers, it is also expected that such nano-structuring would help quenching light-induced degradation in thin-film a-Si:H solar cells [153]. The design proposed here is also general in the sense that it can be adapted to other types of



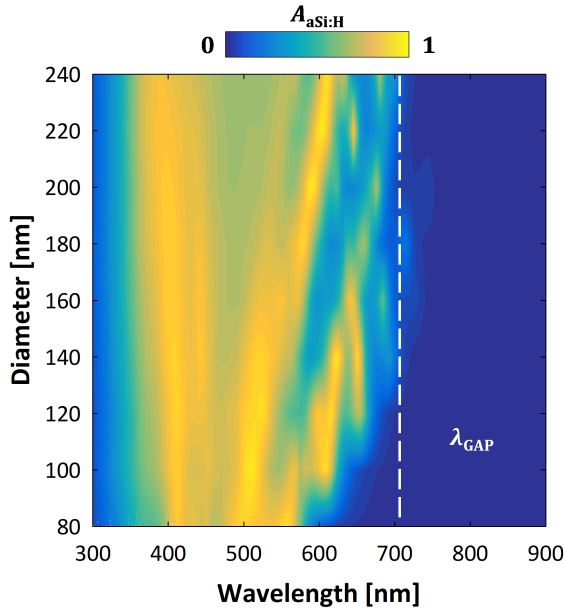


**Figure 4.7.** Absorption spectra in the a-Si:H metasurface, as a function of the particle diameter, for device structure A and  $\Lambda = 250$  nm ( $\lambda_{\text{gap}} = 708$  nm).

solar cell architectures, provided the active material possesses large permittivity values. For example, Mie modes were already shown to be supported by both GaAs [99, 154, 155] and perovskite nanoparticles [156, 157]. This means that the particle-on-a-film geometry could be adapted to standard crystalline thin film solar cells as well as thin-film devices based on direct bandgap materials. In fact, the approach detailed in this work might suit such materials even better, owing to their high absorptivity values for larger wavelengths range due to the narrower bandgap [55, 57]. The metasurface geometry and spacer thickness would then need to be optimised accordingly and in different wavelength regions.

Clearly, one of the main limitations of the perfect absorption concept is that it relies on far-field interference and only works at a single wavelength. While the focus of this work is placed on the lowest energy modes – as they provide a clearer picture for a proof of principle application – current research in all-dielectric nanophotonics aims at realising, through nanostructuring, new eigenmodes [158, 159]. For example, once particles of several hundreds of nm are used, several multipolar resonances appear and can be engineered to overlap. This can broaden the effective optical response of the system, or give rise to

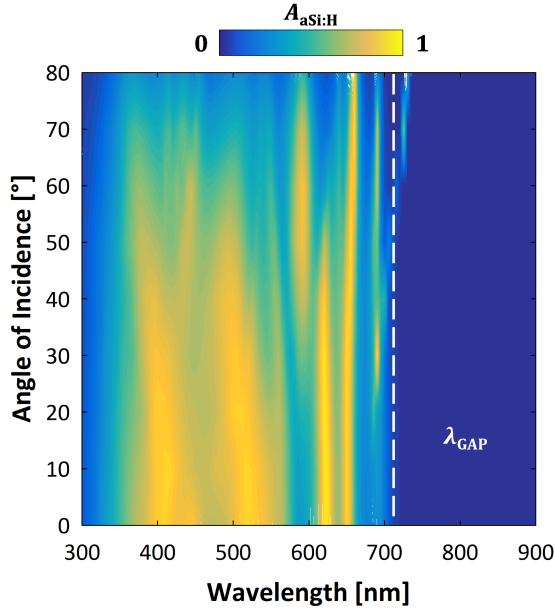


**Figure 4.8.** Absorption spectra of a-Si:H, as function of the angle of incidence of light.

unusual response that can boost light-matter interaction even further. Another problem of the particle-on-a-mirror system proposed in this contribution is that the geometry has been optimised for normal incidence (i.e. perpendicular illumination). However, the phase between the different reflections does not strongly depend on the illumination angle; an incident angle of  $30^\circ$  gives a change in phase of around 10%\*. This means that the optimised wavelength of operation of the perfect absorption concept is quite robust to changes in illumination conditions. In fact, this is shown in fig. 4.8, where the device absorption spectrum as function of the angle of incidence (AoI) of light is plotted. For  $\lambda < 550$  nm, it can be observed that absorption is almost constant for values of AoI up to  $40^\circ$ . Only for AoI  $> 40^\circ$  a decrease of  $A_{\text{aSi:H}}$  is observed. Of particular interest is the behaviour that can be observed in the spectral region between 550 nm and  $\lambda_{\text{gap}}$ . As already depicted in fig. 4.5(c), three absorption peaks can be observed: at  $\lambda \approx 620$  nm, at  $\lambda \approx 650$  nm and at  $\lambda \approx 690$  nm. These three peaks are also clearly visible in fig. 4.8. While their intensity varies with AoI (except for  $\lambda \approx 650$  nm), their position is not affected by the angle

\*Based on the difference in optical path length,  $2d / \cos \theta_2$ , where  $\theta_2$  is the angle of refraction

of incidence. This indicates that the wavelengths at which confinement of the electromagnetic field within the nanodisks takes place – which results in resonances in the absorption spectra – are only dependent on the disk diameter and distance, as previously shown in fig. 4.5 and fig. 4.7. The global performance, expressed in terms of  $J_{\text{ph-aSi:H}}$ , remains almost constant for values of AoI up to  $40^\circ$  –  $J_{\text{ph-aSi:H}}(\text{AoI} = 40^\circ) = 13.2 \text{ mAcm}^{-2}$ . For  $\text{AoI} > 40^\circ$  the implied photocurrent drops significantly, mainly due to increased reflection at the front side of the solar cell. Finally, using the same concept presented here, one could imagine adapting the design to a photo-detector and, owing to the flexibility in the design of all-dielectric nanoantennas, directional, chiral or other types of exotic efficient light harvesters could be envisioned.

## 4.4 Conclusions

In this chapter, the discussion of how all-dielectric nanoantennas can be adapted as solar harvesters was carried out. The basic idea is the following: by exploiting far-field interference effects it is possible to increase the absorption in regions where material generally presents low absorptivity. A novel and potentially attractive solar cell structure was presented, employing an all-dielectric silicon metasurface as active layer in a traditional thin-film silicon solar cell architecture. The nanodisks composing the metasurface can realise perfect (near 100%) absorption at specific wavelengths, due to interference between light reflected by the nanostructures and by the underlying mirror. The operational wavelength can be tuned by changing the system parameters and can boost absorption near the bandgap of the material, i.e. where the absorption coefficient is generally low. The configuration displaying the best optical performance yields an implied photocurrent density of  $14.14 \text{ mAcm}^{-2}$ , with the potential to achieve initial conversion efficiencies above 9.5%, in line with current state-of-the-art amorphous silicon solar cells which employ significantly thicker absorber layers. An in-depth analysis showed that the optical nanodisks have the multiple function of acting as (i) cavities, trapping the electromagnetic field within, (ii) as the solar cell active medium and (iii) as anti-reflection agents, strongly decreasing parasitic reflection in the blue-green region of the visible spectrum. These results can thus be considered as a proof-of-principle study where the advantages of all-dielectric nanoantennas have been adapted to develop a solar harvester based on a new concept.

---

## CHAPTER 5

---

# Copper indium gallium (di)selenide solar cells with periodic gratings

This chapter is based on the following publication:

C. Onwudinanti, **R. Vismara**, O. Isabella, L. Grenet, F. Emieux, and M. Zeman, "Advanced light management based in periodic textures for Cu(In,Ga)Se<sub>2</sub> thin-film solar cells," *Optics Express* **24**(6), A693-A707 (2016).

*ABSTRACT* – In this chapter, 3-D optical modelling is used to investigate light management concepts based on periodic textures and material selection for photovoltaic devices based on Cu(In,Ga)Se<sub>2</sub> as absorber material. After calibration of the software, the effects of 1-D and 2-D symmetric gratings on the cell performance were studied, showing significant reflection quenching and absorptance enhancement in the active layer. The use of In<sub>2</sub>O<sub>3</sub>:H as front and back contacts, combined with an optimised 2-D grating structure, led to a > 25% increase of the implied photo-generated current density with respect to an equally-thick flat device. Most of the performance increase was kept when the absorber thickness was reduced from 1500 nm to 600 nm.

## 5.1 Introduction

Cu(In,Ga)Se<sub>2</sub> (CIGS) is a prominent absorber material in thin-film solar cells technology, having demonstrated efficiencies up to 23.35% [50]. High-performing devices usually employ absorbers with thickness of 2.5 to 3 μm [160–163]. Due to indium scarcity, however, reduction of CIGS thickness is of great importance. In fact, cell-manufacturing costs could be decreased, further promoting the diffusion of this technology into the photovoltaic (PV) market. On the other hand, absorber thickness reduction has significant drawbacks, in particular increased impact of recombination at the back contact and significant decrease of light absorption [164, 165]. As explained in the chapter 1, absorptivity of the thin active layer can be increased by using textures – either random or periodic – to achieve light trapping. Extensive research has been carried out on light trapping for thin-film silicon solar cells, while only in recent years several studies on light management for CIGS devices have been published [164–191].

In this chapter, the study of CIGS solar cells endowed with 1-D and 2-D periodic gratings is carried out. First, the careful characterisation of a reference flat device was carried out, as well as the determination of the optical constants of all materials used for the modelling of CIGS solar cells. Then, the simulation software was calibrated with respect to the reference, to ensure the accuracy of the modelling. After calibration, CIGS devices endowed with 1-D gratings were studied and optimised. Then, 2-D gratings were investigated, as well as the possibility of substituting traditionally used materials with ones that can reduce parasitic losses – thus increasing absorption in CIGS. Finally, the optical performance of devices with a thinner active layer was evaluated. Despite a reduction of the CIGS consumption of 60%, an implied photocurrent density increase of > 18% was achieved.

## 5.2 Cell characterisation and simulator calibration

To ensure that simulation results are a good approximation of the behaviour of real CIGS solar cells, calibration of the modelling software is necessary. To this purpose, the morphology and performance of a device provided by CEA-LITEN were characterised (from now on indicated with 'CAL'). Then, the same architecture was modelled, using the High Frequency Structure Simulator (HFSS) software [75]. Atomic force microscopy (AFM) and a scanning electron microscope (SEM) were used to characterise the surface morphology of the CIGS surface and of the whole device (fig. 5.1). From the AFM measurement, a series of statisti-

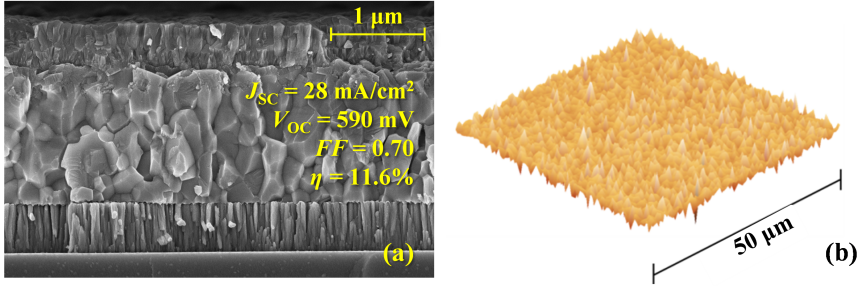


**Figure 5.1.** (a) Cross-sectional scanning electron microscope (SEM) image of the calibration device, with measured external parameters indicated. (b) Surface morphology of the CIGS layer, obtained via atomic force microscopy (AFM).

cal parameters were extracted. Most important are the average dimensions of the surface morphological features: height ( $H_f = 215$  nm) and generalised correlation length ( $L_{CG} = 185$  nm, [192]), which gives an indication on the feature horizontal dimensions. These parameters are important to correctly model the surface morphology of the absorber layer. On the other hand, the thickness of each layer of the device was estimated from the cross-sectioned SEM image, depicted in fig. 5.1(a). A summary is presented in table 5.1. These values are fairly typical for CIGS devices, with the exception of the absorber (1500 nm) and the front contact (400 nm). In fact, typical (record) CIGS solar cells employ absorbers with thickness between 2.5  $\mu$ m and 3  $\mu$ m, and thinner aluminium-doped zinc oxide layers (ZnO:Al/AZO, 200 – 300 nm) [160–163]. While the choice of a thinner CIGS layer was arbitrary, a thicker front transparent oxide (TCO) was necessary due to the low conductivity of the deposited ZnO:Al material.

Along with the geometry of the individual layers, the optical properties of all materials involved play the most important role in obtaining accurate results. Hence, high-resolution and wavelength-dependent complex refractive index data ( $\tilde{n} = n + i\kappa$ ) is required as input of the simulations, where  $\tilde{n}$  is the complex refractive index, and  $n$  and  $\kappa$  are its real and imaginary parts, respectively\*. For cadmium sulphide (CdS), data was obtained from the work of Hara *et al.* [193]. All other characteristics of materials used in the CAL device were measured internally, using a combination of spectroscopic ellipsometry (SE) and spectrophotometry transmittance and reflectance measurements. In Appendix A,  $n$  and  $\kappa$  of all materials used in the simulations are presented.

\*Please note that  $\kappa$ , i.e. the imaginary part of the refractive index, is also known as the *extinction coefficient*

**Table 5.1.** Material and thickness of each layer of the reference device.

Layer	Material	Thickness
Back reflector	Molybdenum	500 nm
Absorber	CIGS	1500 nm
Buffer	Cadmium sulphide	55 nm
Window	Intrinsic zinc oxide	40 nm
Front TCO	Al-doped zinc oxide	400 nm

Following the AFM characterisation results, a model with an irregular, pseudo random texture on the CIGS surface was prepared. The pseudo-random texture was devised as follows: using a (pseudo-)random number generator, a series of random numbers whose average was equal to the correlation length ( $L_{CG}$ ) of the features on the CIGS surface was generated. A similar set was created for the average feature height ( $H_f$ ). These sets were then combined to yield a pseudo-random set of truncated square pyramids [53], whose average dimensions were equal to the average dimensions ( $H_f$  and  $L_{CG}$ ) yielded by the AFM scan of the reference cell. Alternative elementary feature shapes such as tetrahedra, hemispheres, and triangular pyramids were tested, as well as craters. However, these other shapes provided no clear discernible benefit and are less simply implemented in the 3-D design. The CdS and intrinsic ZnO layers were constructed to be conformal to this texture on the CIGS, given their small thickness ( $\sim 50$  nm). On the other hand, the ZnO:Al layer was built to have features smoothed compared to the ones on the CIGS surface, given the relatively large thickness of the layer ( $\sim 400$  nm). Observations of the SEM cross-section – fig. 5.1(a) – confirm that the roughness of the cell front surface is significantly lower than the one of CIGS. The molybdenum layer, meanwhile, was modelled with regular nano-features ( $\sim 30$  nm), determined from both observation of the SEM cross section and from reports of similar analysis in literature [193]. The eventual presence of an oxide layer ( $\text{MoO}_3$ ) on top of the metal was also investigated, but its inclusion in the modelled structures did not significantly influence the simulation results.

The pseudo-random approach was preferred to modelling the texture with regular (periodic) features, in order to correctly simulate the scattering effects of the CIGS random texture (opposed to the diffraction of light in discrete modes, which takes place when periodic structures are employed). A perfectly random structure can be defined as a grating with an infinite period  $\Lambda$  (i.e. the same pattern is never repeated). On the other hand, simulations can be significantly

quicker and less computationally demanding if the simulated domain (i.e. the width of the so-called *unit cell*) is as small as possible, and then repeated an infinite amount of times by means of (periodic) boundary conditions. A study by Jäger *et al.* showed that, for random textures with relatively small features sizes (similar to those deployed in this chapter), a unit cell width of  $3 \times L_{CG}$  is sufficient to closely approximate the randomness of larger areas [194]. A similar preliminary analysis conducted for this work (and not presented here) showed that the minimal unit cell size required to obtain sufficient randomness was  $4 \times L_{CG}$ . Larger unit cells were modelled and simulated, but did not show significant improvements in accuracy.

A 3-D rendering of the unit cell model is depicted in fig. 5.2, together with the results of the calibration – i.e. the comparison between the simulation results with external quantum efficiency (EQE) and reflectance ( $R$ ) measurements. Each coloured area in the plot of fig. 5.2 indicates either reflectance or absorptance in each layer of the cell. Calculated absorption in CIGS (blue area) and measured EQE (dashed line) are well matched<sup>†</sup>, except in 2 parts of the spectrum:

- $\lambda_1 = 350 \text{ nm} - 450 \text{ nm}$ . In this region, calculated absorptance spectrum in CIGS –  $A_{CIGS}(\lambda)$  – is higher than the measured EQE( $\lambda$ ). Since simulations do not include recombination mechanisms, it is generally expected that  $A_{CIGS}(\lambda) > EQE(\lambda)$ .
- $\lambda_2 = 950 \text{ nm} - 1150 \text{ nm}$ . In this portion of the spectrum, results display  $A_{CIGS}(\lambda) < EQE(\lambda)$ . Most likely, this underestimation of CIGS absorption is caused by the difference in mode excitation and light-trapping performance between the real random texture and the simulated pseudo-random arrangement.

Over the analysed spectrum, the average difference between calculations and measurements is 0.038, in line with similar studies carried out by other groups (0.028 [168], 0.027 [193]). It must be noted, however, that the two aforementioned works both employ 1-D simulators, while this contribution employs a rigorous 3-D Maxwell equation solver. The convolution of both  $A_{CIGS}(\lambda)$  and EQE( $\lambda$ ) with the photon flux of the standard AM1.5 spectrum (in the wavelength range 300 nm – 1300 nm) yields very similar values of the photocurrent density:  $J_{ph} = 30.7 \text{ mAcm}^{-2}$  (simulation) and  $J_{EQE} = 30.8 \text{ mAcm}^{-2}$  (measurement).

<sup>†</sup>The good agreement between modelling and measurements was verified by repeating simulations with different combinations of pseudo-random pyramids.



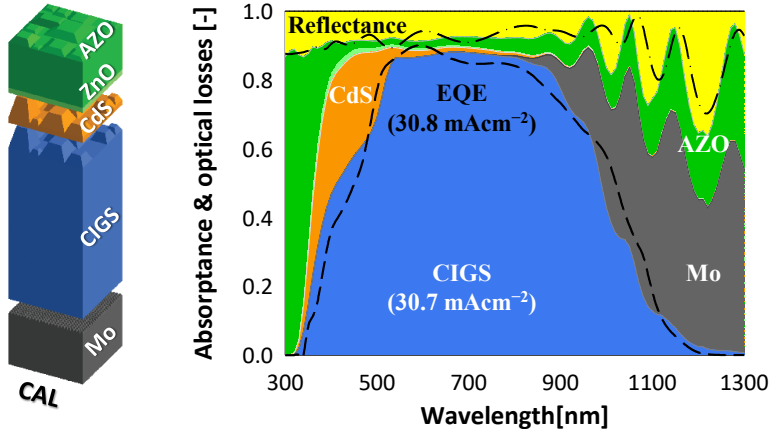


**Figure 5.2.** Unit cell model of the CIGS calibration solar cell (left), and results of the comparison between simulation results with reflectance and EQE measurements of the (real) calibration device.

## 5.3 CIGS solar cells on periodic gratings

### 5.3.1 1-D gratings

1-D gratings are here defined as structures which are uniform in one direction and periodic in the other<sup>‡</sup>. The one-dimensional gratings modelled in this work take the shape of an isosceles triangle, defined by the base and height, i.e. the period  $\Lambda$  and the height  $h$  of the grating (see fig. 5.3, on the left).  $\Lambda$  and  $h$  are set to starting values of 2000 nm and 500 nm, respectively. The value of the period is chosen to be larger than the 1500 nm thickness of the CIGS absorber layer. In fact, Tan *et al.* showed that this condition minimises the growth of defective areas – in the case of micro-crystalline silicon layers [195]. In turn, this has a favourable impact on the device electrical performance. Additionally, Sai *et al.* demonstrated that grating periods should exceed the micro-crystalline silicon absorber thickness for optimum  $J_{sc}$  [196]. It is expected that these considerations hold true also for CIGS layers. The simulation model of the 1-D grating structure included once again the pseudo-random textures representing the roughness of deposited CIGS.

Results of this first simulation with 1-D periodic gratings ( $\Lambda = 2000$  nm,  $h = 500$  nm) are depicted in fig. 5.3 on the right, where each calculated spectrum is

<sup>‡</sup>Both directions are in the plane perpendicular to the propagation direction of incident light

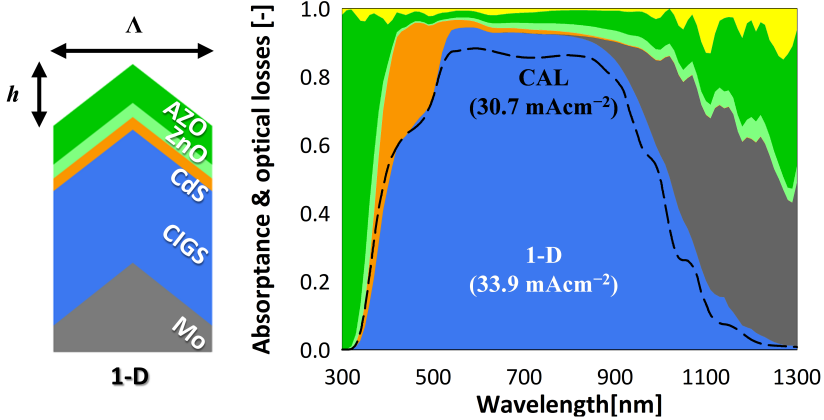


**Figure 5.3.** 1-period sketch of the device endowed with a 1-D grating (left, pseudo-random roughness not included in the sketch for clarity) and simulation results with  $\Lambda = 2000$  nm and  $h = 500$  nm. The dashed line indicates the calculated absorption spectrum of the calibration (CAL) model.

the average between those computed for S- and P-polarisation. An increase of  $A_{\text{CIGS}}$  over the whole spectrum range is observed, with respect to the *flat* reference case (CAL). The improvement can be mainly ascribed to good anti-reflection properties of the grating, which allow for a smooth transition of the refractive-index from air (the incident medium) to the device. In fact, it can be observed that the total cell reflectance is greatly reduced. In addition, scattering of near infrared photons explain the enhanced response at long wavelengths. Overall, the (implied) photocurrent density generated in the absorber is increased from  $30.7 \text{ mAcm}^{-2}$  (CAL device) to  $33.7 \text{ mAcm}^{-2}$  (1-D).

The analysis continued with the optimisation of the grating dimensions. With  $\Lambda$  fixed to 2000 nm, a sweep of  $h$  between 100 nm and 900 nm was carried out. Results are summarised in fig. 5.4(a), where the implied photocurrent density generated or lost in each cell layer is plotted as function of  $h$ :

- Reflectance losses decrease for larger values of  $h$ , because taller gratings have better light in-coupling properties. However, having height values larger than 500 nm does not provide additional benefits in this respect.
- Losses in the Mo back contact increase with larger values of  $h$ , because taller structures couple more light onto the surface of the metal.
- Losses in other layers remain approximately constant, and no clear depen-

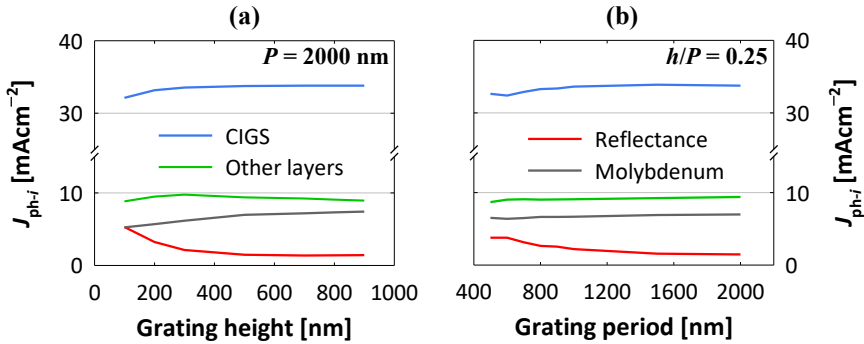


**Figure 5.4.** Implied photocurrent density generated in the active layer (CIGS) or lost (in supporting layers or due to reflectance) as function: (a) of the grating height – for constant period, and (b) of the grating period, for constant aspect ratio ( $h/P$ ).

dency on  $h$  is observed.

The best performance ( $J_{ph,CIGS} = 33.8 \text{ mAcm}^{-2}$ ), achieved when  $h = 900 \text{ nm}$ , is only slightly higher than the result obtained when  $h = 500 \text{ nm}$  ( $33.7 \text{ mAcm}^{-2}$ ).

A similar analysis was carried out to evaluate the effect of the grating period. In this case, the grating height-to-period ratio ( $h/P$ ) was kept constant and equal to 0.25, so that all gratings have the same aspect ratio. Values of  $\Lambda$  between 500 nm and 2000 nm were considered. Results are depicted in fig. 5.4(b):

- Losses in Mo and other non-active layers remain constant, for all values of  $\Lambda$ . This suggests that light coupling into the metallic layer does not solely depend on the grating height, but rather on the height-to-period ratio.
- Reflectance reduces when  $\Lambda$  is increased. Since the aspect ratio was kept constant, larger values of the period correspond to taller gratings – which were already shown to reduce reflectance more effectively than shorter gratings.

To conclude, for 1-D grating with  $\Lambda = 2000 \text{ nm}$  and  $h = 500 \text{ nm}$  an implied photocurrent density of  $33.7 \text{ mAcm}^{-2}$  was achieved. It must be noted that a slightly higher performance was achieved for a smaller grating period of 1500 nm and when taller gratings were employed. However, it was decided to prefer larger, shallower gratings ( $\Lambda = 2000 \text{ nm}$ ,  $h = 500 \text{ nm}$ ) – which will allow for the growth of a higher quality material in manufactured devices.

### 5.3.2 2-D gratings

The study continues with the analysis of 2-D gratings. Pyramidal features were employed, with the same dimensions of the previously optimised 1-D gratings: period of 2000 nm and height of 500 nm (see sketch depicted in fig. 5.5, on the left). It must be noted that tiny regular truncated pyramids were used to model the natural roughness of the front CIGS surface, rather than pseudo-randomly generated ones. An initial study, not reported here for brevity, showed no difference in the simulated spectra when using pseudo-random or regular truncated pyramids – in models in which periodic gratings were also endowed. For ease of design, the regular arrangement was thus selected.

While 2-D gratings could be more complicated to manufacture, they offer some advantages over 1-D structures. In particular, they can diffract more light away from the incident direction, exciting a higher number of guided modes in the absorber. Results of this work (fig. 5.5, on the right) show that the pyramidal 2-D grating can further suppress reflectance when compared to the 1-D structure. In this way almost all incident light is coupled into the device. However, since reflectance was already very low in the case of triangular 1-D gratings, the benefits in term of  $J_{\text{ph,CIGS}}$  are relatively small (1-D case:  $33.9 \text{ mAcm}^{-2}$ , 2-D case:  $34.2 \text{ mAcm}^{-2}$ ). Nevertheless, a careful observation of  $A_{\text{CIGS}}$  of both textured solar cell models shows the presence of a small peak in the 1100 nm – 1150 nm region of the spectrum. This peak is more pronounced for the model endowed with 2-D grating, suggesting that light diffraction and wave-guiding phenomena are taking place more strongly than in 1-D grating case.

### 5.3.3 Alternative cell configurations

Despite improvements in the device anti-reflection properties, owing to the presence of gratings, further performance enhancements are prevented by high parasitic absorption in supporting layers, particularly in the Mo back contact and in the ZnO:Al front TCO (see fig. 5.3). For this reason, alternative cell configurations which mitigate or eliminate these losses are of great interest. The use of (i) a dielectric spacer layer between absorber and metal, (ii) Mo-free back reflectors [185, 189], and (iii) highly-transparent front TCOs are thus investigated.

Molybdenum is the conventional metallic back reflector/contact used in CIGS solar cells: it allows for the growth of large CIGS grains, it remains inert during deposition [197], and forms an ohmic contact for the majority charge carriers (holes) through the formation of an intermediate MoSe<sub>2</sub> layer [198, 199]. On the other hand, it exhibits lower reflectance with respect to other metals (e.g. silver).

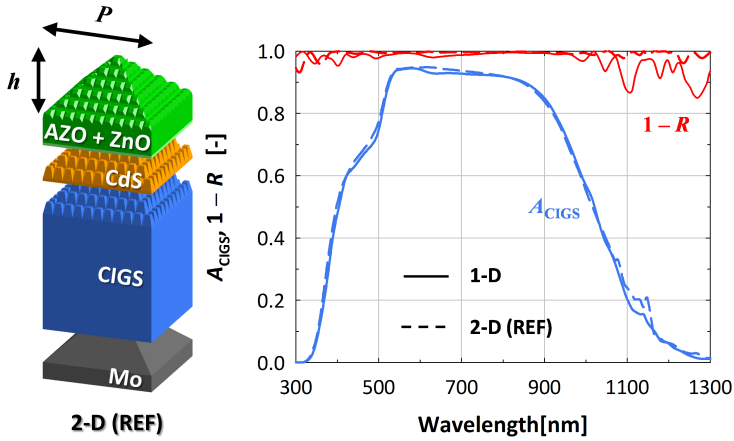


**Figure 5.5.** Calculated absorption spectra and  $1 - R$  of devices endowed with 1-D and 2-D gratings.

This results in relatively high parasitic absorption losses [197], as shown in the simulations presented in the previous sections. In real devices the replacement of Mo with alternative materials remains a challenge, but several possibilities have been investigated. Metals like W, Ta and Nb are promising, since they remain inert during CIGS deposition. However, they do not appear to offer clear advantages with respect to Mo [197]. Other metals are less stable at the high temperatures typical of CIGS deposition, and their diffusion into the absorber layer would cause a significant degradation of the cell performance.

Absorption in metallic (textured) back contacts may be reduced by using a dielectric spacer layer between absorber and reflector, as is common practice in wafer-based and thin-film silicon solar cells [61, 147, 200]. Requisites of this spacer are high vertical conductivity and transparency. Investigations of ZnO/Mo back contacts have been conducted, as well as ZnO/Ag [168]. Approaches in which non-conductive spacers and local point contacts between metal and absorber have also been extensively researched [188, 201–207]. However, such approaches are not treated in this chapter. In this work, the potential of molybdenum trioxide ( $\text{MoO}_3$ ) as spacer layer between CIGS and Mo was first tested.  $\text{MoO}_3$  is a transparent material with relatively high temperature stability and low absorption, particularly at long wavelengths (see appendix A); it also has sufficiently high vertical conductivity [208], making it potentially suitable as

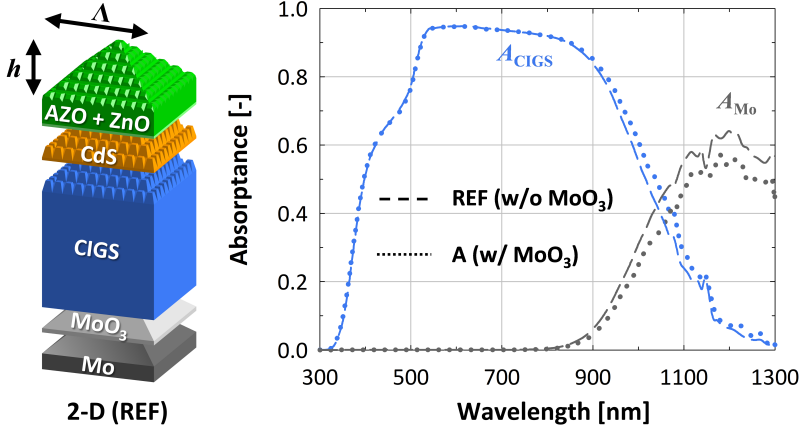


**Figure 5.6.** On the left, sketch of structure A (2-D gratings with MoO<sub>3</sub> spacer). On the right, absorption in CIGS ( $A_{\text{CIGS}}$ , in blue) and in molybdenum ( $A_{\text{Mo}}$ , in grey) – as function wavelength – for structure A (dotted lines) and the 2-D grating reference model (REF, dashed lines).

back transparent conductive oxide. An 80-nm thick MoO<sub>3</sub> buffer layer is tested in a 2-D grating cell model (see fig. 5.6); grating dimensions are  $\Lambda = 2000$  nm and  $h = 500$  nm. Two models, one with spacer layer (REF) and one without (A), were compared. A preliminary study determined that 80 nm was the optimal thickness, guaranteeing sufficient hole conductivity and, at the same time, ensuring the quenching of parasitic absorption in molybdenum ( $A_{\text{Mo}}$ ). Simulation results of the aforementioned 2-D gratings based models (fig. 5.6) indicate that the presence of the MoO<sub>3</sub> spacer effectively reduces  $A_{\text{Mo}}$ . As a consequence, absorbance in the CIGS layer is slightly augmented, and  $J_{\text{ph,CIGS}}$  increased from  $34.2 \text{ mAcm}^{-2}$  (REF) to  $34.8 \text{ mAcm}^{-2}$  (device configuration A).

A complete removal of molybdenum from the back reflector could further improve the device optical performance. To this purpose, configurations using a TCO deposited directly on the glass substrate were studied. To prevent transmittance losses at the back side, a thin layer ( $\sim 300$  nm) of silver (Ag) is added on the opposite side of the glass carrier. In this way, diffusion of the metal into the cell layers can be prevented [165, 168]. At the same time, the high reflectivity of Ag guarantees that no light is transmitted from the back side of the device. Two different TCO materials were tested: tin-doped indium oxide (In<sub>2</sub>O<sub>3</sub>:Sn, ITO) and hydrogenated indium oxide (In<sub>2</sub>O<sub>3</sub>:H, IOH). Both materials have high conductivity and transparency [121, 122], however IOH exhibits lower free-carrier

**Table 5.2.** Summary of alternative cell structures investigated in this chapter.

Layer	A	B	C	D
Reflector	-	Silver (300 nm)		
Substrate	Glass			
Back contact	Mo (300 nm)	ITO (80 nm)	IOH (80 nm)	
Absorber	CIGS (1500 nm)			
Buffer	CdS (55 nm)			
Window	ZnO (40 nm)			
Front TCO	AZO (450 nm)			IOH (80 nm)

absorption in the near infrared region of the spectrum. On the other hand, ITO has higher stability at elevated temperatures, and has already been successfully tested as back contact in thin-film CIGS solar cells [209].

Various alternative configurations were analysed and compared. As already previously mentioned, REF indicates the device with optimised pyramidal gratings and a traditional molybdenum back contact, while A denotes the model with the same 2-D texture and an 80-nm MoO<sub>3</sub> spacer. B is a solar cell model where the Mo back reflector is replaced by ITO, with a layer of silver on the other side of the substrate to prevent transmission of light. Model C is identical to B, but where the ITO layer is replaced by IOH. These configurations are depicted in fig. 5.7, while layer thicknesses are summarised in table 5.2.

Building a realistic model in HFSS with a glass/Ag back reflector configuration would result in an unwieldy large structure, straining computational resources due to the necessarily large thickness of the glass layer (hundreds of micrometres, as opposed to the nanometre-scale of all other layers). To overcome this obstacle, models employ a 300-nm thick glass. Due to the presence of 2-D gratings on this necessarily thin substrate, interference phenomena are suppressed – thus modelling the incoherent propagation of light as in an equivalent bulk glass substrate. In addition, the silver layer is treated as a perfectly conductive layer (i.e. an ideal mirror). As a result, absorption in the Ag reflector and transmission at the back side of the device are exactly zero. While these are necessary approximations, results can be considered reliable since: (i) Ag has a very high reflectivity, particularly in the near infrared (NIR) part of the spectrum and when is deposited on a flat surface (as in this case), and (ii) a millimetre-thick glass carrier would only absorb a very small amount of NIR light.

Results of the simulations (fig. 5.8) showed that the Mo-free back reflector con-

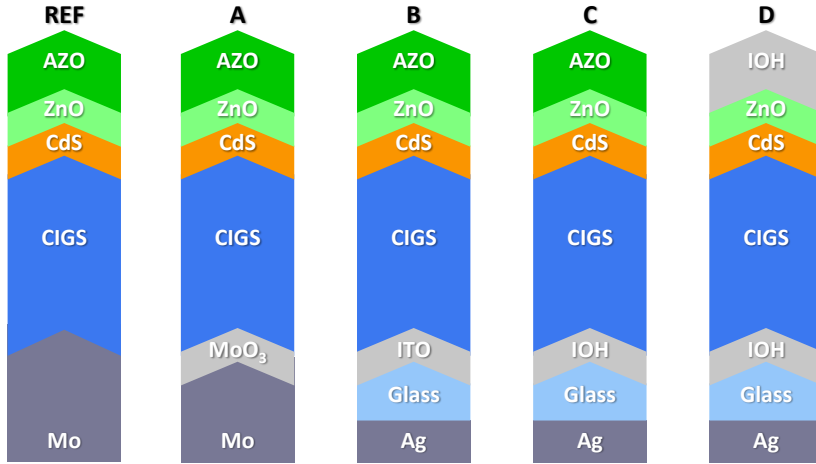


**Figure 5.7.** Cross-section of alternative cell structure configurations studied in this work. The pseudo-random roughness was included in all models, but is not depicted here for clarity.

figurations (B and C) perform better than structure where Mo is included (REF and A). At short wavelengths, all devices display similar values of  $A_{\text{CIGS}}$ . However, the advantage of Mo-free architectures becomes apparent in the long-wavelength region ( $\lambda > 850 \text{ nm}$ ), where molybdenum would be parasitically absorbing. In fact, absorptance in the CIGS layer is increased in this region of the spectrum for the Mo-free models. This translates into an increase of the implied photo-generated current density in the absorber: from  $34.8 \text{ mAcm}^{-2}$  (model A) to  $35.6 \text{ mAcm}^{-2}$  (B) and  $35.7 \text{ mAcm}^{-2}$  (C). The performance of devices with ITO and IOH as back TCO layers is very similar, with the latter showing a slightly higher  $J_{\text{ph,CIGS}}$  due to the higher infrared transparency of  $\text{In}_2\text{O}_3\text{:H}$ .

In addition to Mo absorption, losses in the AZO front TCO contribute to reducing the photocurrent density generated in the CIGS layer. The ZnO:Al layer used in this work needs to be relatively thick ( $> 300 \text{ nm}$ ), to guarantee sufficient electron conductivity (i.e. low resistivity). An IOH TCO, thanks to its high carrier mobility, can be made much thinner (80-100 nm) [123]. Combined with its high transparency (i.e. low extinction coefficient  $\kappa$ , see Appendix A),  $\text{In}_2\text{O}_3\text{:H}$  is an ideal candidate as front TCO in thin-film solar cells. In the work here presented, the 400 nm thick ZnO:Al layer was substituted with an 80-nm thick IOH front TCO, while at the back side the IOH/glass/Ag configuration of model C was employed. This results in the device indicated with D in fig. 1.4. Simulations



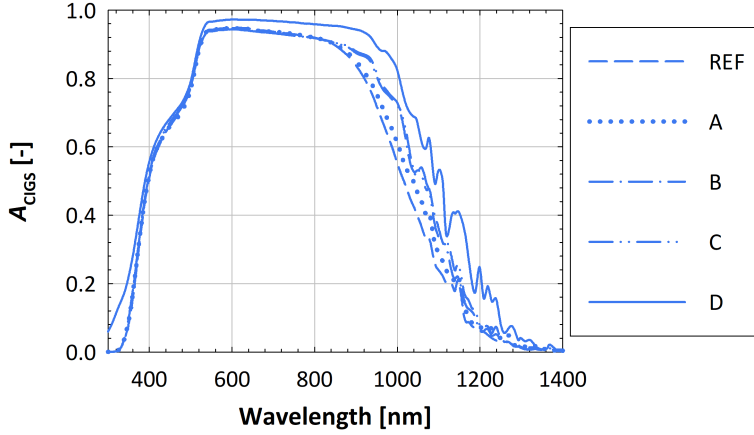


**Figure 5.8.** Absorption in the CIGS active layer, for different device configurations.

showed that this optimised structure (D) yields an increase of  $A_{\text{CIGS}}$  over the whole spectral range (continuous line in fig. 5.8), since the highly-transparent front layer allows more light of all wavelengths to enter the absorber. Integration with the AM1.5 photon flux results in a  $J_{\text{ph,CIGS}}$  of  $38.6 \text{ mAcm}^{-2}$ . This value represents a  $7.9 \text{ mAcm}^{-2}$  increase (+26%) over the results obtained for the *flat* calibration device (CAL).

### 5.3.4 Reduction of CIGS thickness

Scarcity of indium could prevent the widespread diffusion of  $\text{Cu(In,Ga)Se}_2$  technology into the PV market. Reduction of the absorber thickness – while maintaining high absorption levels– can help decreasing production costs and promoting diffusion of CIGS solar cells. To verify the effectiveness of the light management approach presented, the performance of devices with sub-micron thick absorbers was investigated. Thickness of CIGS down to 600 nm were tested, in a cell configuration with IOH used both as front and back TCO (model D). As can be observed in fig. 5.9, the thinner architecture (600 nm) maintained the high performance of the thicker device (1500 nm) up to  $\lambda \approx 800 \text{ nm}$ . At longer wavelengths, a decrease of  $A_{\text{CIGS}}$  can however be noticed. This is expected, since the thinner layer struggles to efficiently absorb light in this region of the spectrum – where the absorption coefficient of CIGS is lower. Nevertheless, the solar cell model with a 600-nm thick CIGS still outperformed the much thicker, flat device (CAL), reaching a  $J_{\text{ph,CIGS}}$  value of  $36.4 \text{ mAcm}^{-2}$ .

This shows how, by geometrical optimisation of gratings and careful choice of

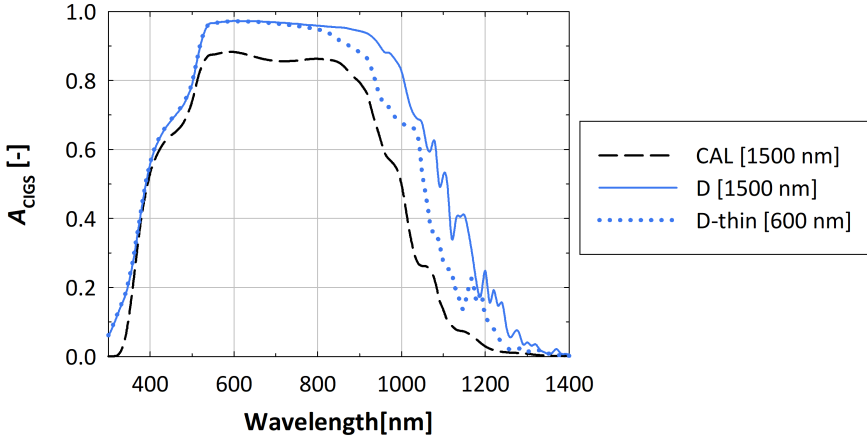


**Figure 5.9.** CIGS absorption in the calibration cell (CAL) and in device configuration D with thickness of the absorber of 1500 nm (D) and 600 nm (D-thin).

supporting layer materials, it is possible to obtain a substantial improvement of the optical performance ( $\Delta J_{\text{ph,CIGS}} = +5.7 \text{ mAcm}^{-2}$ ) and, at the same time, reduce material utilisation in the device (-60% CIGS thickness). At this point it should be noted, however, that the effective implementation of IOH in CIGS devices requires careful investigation. This study shows the benefits of including this material in the solar cell architecture, namely the reduction of parasitic absorption in the front TCO and at the back side. However, only an experimental analysis of devices with IOH front and back TCO can determine if this solutions can be applied to real devices. Also, the inclusion of indium-based transparent contacts partially offsets the reduction of rare-earth material utilisation. However, the small thickness of the IOH would still result in lower indium consumption when the thinner CIGS layer is employed.

## 5.4 Conclusions

In this chapter, a satisfactory optical model of a real thin-film CIGS solar cell was presented. A good match between simulations and measurements was obtained. These results were only achieved when a pseudo-random texture was included, necessary to correctly model the effects of the random self-occurring roughness of CIGS and other layers on the propagation of light. The results of the application of gratings to the solar cell models led to the following conclusions:

- The application of periodic gratings results in strong reflection quenching

**Table 5.3.** Summary of all results presented in this chapter.

Cell	CIGS thickness	$J_{ph,CIGS}$	Gain
Calibration [CAL]	1500 nm	30.7 mAcm <sup>-2</sup>	-
1-D	1500 nm	33.7 mAcm <sup>-2</sup>	+9.9%
2-D [REF]	1500 nm	34.2 mAcm <sup>-2</sup>	+11.4%
2-D + MoO <sub>3</sub> [A]	1500 nm	34.8 mAcm <sup>-2</sup>	+13.4%
2-D + ITO back [B]	1500 nm	35.6 mAcm <sup>-2</sup>	+16.0%
2-D + IOH back [C]	1500 nm	35.7 mAcm <sup>-2</sup>	+16.3%
2-D + IOH front & back [D]	1500 nm	38.6 mAcm <sup>-2</sup>	+25.7%
2-D + IOH front & back [D-thin]	600 nm	36.4 mAcm <sup>-2</sup>	+18.6%

and CIGS absorption enhancement. 2-D structures only showed little performance improvement over their 1-D counterparts.

- The implied photocurrent density in the absorber increases with the height and period of the grating. These trends level out for values of the period greater than the absorber thickness (1500 nm) and of the grating height-to-period ratio values above 0.25.
- Improvements in CIGS absorption and anti-reflection are always accompanied by increased (parasitic) absorption in the molybdenum back contact.

The poor optical performance of Mo as back reflector remains an obstacle to efficiency improvements in typical CIGS devices. However, the use of a MoO<sub>3</sub> dielectric spacer between absorber and back contact can reduce parasitic losses in the back contact. Nevertheless, absorption in Mo remains high, and only its replacement with alternative configurations (TCO/glass/metal) can further increase the device optical performance. The front ZnO:Al TCO is also a major source of parasitic absorption in CIGS solar cells. Significant improvements can be achieved if a more transparent and conductive material like IOH is employed. Benefits are evident in a wide spectral range, since more light is allowed to couple into the absorber and contribute to the photocurrent density generation.

Last, simulations of cells with reduced CIGS absorber thickness of 600 nm indicate that the cumulative impact of the modelled light management techniques can result in devices that exceed the photocurrent density generation of the 1500-nm thick reference flat solar cell. These results, as illustrated in Table 3, indicate that the optical performance, and subsequently the photocurrent density and

efficiency of state-of-the-art CIGS solar cells, can be further improved by the application of optimised periodic textures and by the inclusion of more performing materials in the cell stack. Integration of this materials in the device architecture, however, needs to be further investigated by experimental analysis.



---

## CHAPTER 6

---

# Thin-film silicon solar cells with different front and back textures

This chapter is based on the following publications:

O. Isabella, **R. Vismara**, A. Ingenito, N. Rezaei, and M. Zeman, "Decoupled front/back dielectric textures for flat ultra-thin c-Si solar cells," *Optics Express* **24**(6), A708-A719 (2016).

and

O. Isabella, **R. Vismara**, D. N. P. Linssen, K. X. Wang, S. Fan, and M. Zeman, "Advanced light trapping scheme in decoupled front and rear textured thin-film silicon solar cells," *Solar Energy* **162**, 344-356 (2018).

*ABSTRACT* – In this chapter, the impact of different front and back periodic textures on the absorption of crystalline silicon slabs and hydrogenated nano-crystalline silicon solar cells is assessed. First, a comparison between textured absorber and supporting layers is conducted. Then, the periodic structures are optimised to maximise the photocurrent density of thin-film single-junction silicon solar cell. The obtained optical performance, beyond the Lambertian scattering limit, is explained by near-perfect light in-coupling and by the excitation of resonant wave-guided modes inside the absorber layer.

## 6.1 Introduction

Solar cells based on silicon as light absorber currently dominate the photovoltaic (PV) market [21]. Next to record solar cells fabricated on (thick) wafers of crystalline silicon (c-Si) [25, 210–216], multi-junction thin-film silicon solar cells (TFSSC) based on alloys of hydrogenated amorphous silicon (a-Si:H) have been recently reported to have initial conversion efficiencies up to 16.3% [40, 217–219] and record stabilised conversion efficiency up to 14% [41]. Even though this PV technology currently realises lower conversion efficiency than other thin-film alternatives, such as CIGS [50], CdTe [51], perovskite [220], and GaAs [24], it displays the smallest cell-to-module losses [44], with demonstrated industrial-scale flexible [45, 46] and rigid modules [47–49] up to 6.5-m<sup>2</sup> wide area. That is, this technology is industrially mature in terms of nanometric-scale thickness uniformity, hundreds of Megawatt-scale throughput, and resilience against moisture [44]. For these reasons, thin films developed for a-Si:H-based solar cells constitute instrumental building blocks in current record c-Si solar cells [211, 213, 215] achieved industrially at wafer (i.e. large area) level. Extensive research efforts have also focus on investigating the potential of ultra-thin c-Si devices, prepared with either solid phase [221–225] or liquid phase crystallisation of silicon layers [226–229]. The latter in particular has recently demonstrated efficiency values up to 14.2% [230]. Due to the lower absorption coefficient of c-Si and a-Si:H alloys – with respect to other PV absorber materials – and to their reduced thickness, ultra-thin c-Si and TFSSC technologies are the best platform for testing (at both lab- and industrial-scale) a variety of photonic approaches aimed to enhance the absorption of light in thin dielectric slabs (random/periodic texturing, dielectric spacers and reflectors, metallic nano-particles, etc.) [44, 140, 148, 231–236].

Today's and next-generation TFSSCs are and will be entirely dependent on three factors. The first is the fabrication of a-Si:H alloys with band gap ( $E_{\text{gap}}$ ) between 0.75 eV and 2 eV, to ensure high open-circuit voltage as well as wide utilisation of the solar spectrum in multi-junction architectures [237]. The second is the quality of non-crystalline materials and interfaces, to efficiently collect photo-generated charge carriers. The third is the enforcement of an efficient light trapping scheme to maximise light absorption, thus generating substantial short-circuit current densities (also necessary for the development of high-efficiency ultra-thin c-Si devices). The expression light trapping means the concurrent application of several light management techniques for (i) broadband light in-coupling at the front side of the (multi-junction) solar cell, (ii) light scattering

inside the absorber layer(s) and (iii) high internal rear reflectance [234, 238]. Next to bandgap and optical properties of silicon-based absorbers, other material characteristics need to be considered. For amorphous absorbers with  $E_{\text{gap}} > 1.2 \text{ eV} - 1.4 \text{ eV}$ , it is crucial to enhance the resilience against light-induced degradation [153, 239–241], using for example triode-based plasma-enhanced chemical vapour deposition [37] and/or varying deposition temperature and plasma compositions [242, 243]. For nano-crystalline absorbers with  $E_{\text{gap}} < 1.2 \text{ eV}$ , properly designed light management is instead helpful to ensure high photocurrent density while keeping the thickness in the range of  $2 \mu\text{m} - 3 \mu\text{m}$ . This is to cope with the reduced electrical performance of nc-Si:H with respect to higher quality c-Si – when textured substrates are deployed [244].

The maximisation of the photocurrent density delivered by ultra-thin c-Si absorbers and a fully functional single junction nano-crystalline silicon (nc-Si:H) solar cell is the primary aim of this chapter. The perspective is that a solar cell based on low band gap c-Si or nc-Si:H endowed with a light trapping scheme delivers a certain photocurrent density. This value can be interpreted as the sum of the photocurrent densities of a monolithically integrated multi-junction device. In this respect, the cells based on c-Si or nc-Si:H are the bottom junction, and the thickness of the (amorphous) top cell need only to be tuned to meet current-matching conditions [53]. It follows that the maximisation of light absorption in the bottom cell alone results in a maximised total photocurrent density available for a multi-junction device in which such bottom cell is deployed.

In a previous contribution by Wang *et al.* [245], decoupled front and rear surface textures were considered to structure an ultra-thin c-Si absorber. Using the rigorous coupled wave analysis, the front and back surfaces were separately optimised for light trapping and anti-reflection, respectively, leading to broadband light absorption close to the classical Lambertian scattering limit. In this chapter, starting from the concept of decoupled textures, the effect of texturing supporting layers is first assessed against the more common approach of endowing the texture on the c-Si absorber – in terms of optical performance (i.e. absorption and implied photocurrent density). Differences are explained in terms of in-coupling of light at the front surface and scattering of near-infrared photons, mostly at the back side of the device. In the second part of the chapter, the same front/back double texture is optimised within a fully-functional TFSSC structure, based on a nc-Si:H absorber layer. The effect of the texture geometrical dimensions, of the supporting layers' material and thickness, and of the back reflector configuration are all studied. The obtained wide-band absorption beyond the traditional



Lambertian scattering limit is explained, by analysing the electric field propagation and the excitation of wave-guided modes within the thin absorber layer, resulting in the highest light-trapping efficiency value so far reported [246].

## 6.2 Texturing: absorber vs supporting layers

In the first part of the chapter, a comparison between texturing supporting layers or the solar cell absorber is carried out. Record devices typically rely on textured interfaces between active and supporting layers – realised either by endowing the texture on a wafer (in case of thick c-Si architectures) or by depositing the entire solar cell structure on a rough substrate (as for thin-film silicon solar cells). In both instances, the absorber / supporting layer interfaces are both *optically* and *electrically flat*. While the first property is desirable, promoting efficient light in-coupling and trapping in the active layer of the solar cell, non-flat junctions usually result in higher surface recombination of photogenerated charge carriers and consequent reduction of the open-circuit voltage ( $V_{oc}$ ) and fill-factor ( $FF$ ) of solar cells [22]. While high efficiencies can still be achieved when high-quality surface passivation is deployed [59], alternative approaches in which optical and electrical roughness can be decoupled are of interest. To this purpose, Spinelli *et al.* proposed a flat c-Si solar cell architecture endowed with a front passivating textured dielectric layer [133], whose features are known as *Mie resonators*. In this section, a similar approach will be applied to 2- $\mu\text{m}$  thick c-Si slabs, endowed with pyramidal periodic textures at both front and back side. In this way, the two gratings are tailored to achieve different light management purposes – namely near-perfect light in-coupling at the front and scattering on long-wavelength photons at the rear. The comparison of the optical performance between textured absorber and supporting layers is done, by evaluating absorption spectra and corresponding implied photocurrent density in the c-Si layer.

### 6.2.1 Proposed device structures

3-D sketches of the simulated models are depicted in fig. 6.1. In particular, the structures in fig. 6.1 a-d (textured supporting layers) exhibit:

- Front side texturing consisting of  $\text{TiO}_2$  pyramids with a base  $b_f = 600$  nm and a height  $h_f = 750$  nm (fig. 6.1 b,d);
- A 2- $\mu\text{m}$  thick flat c-Si slab (absorber);
- back side texturing formed by larger and shallower pyramids of  $\text{SiO}_2$  with base  $b_b = 1200$  nm and height  $h_b = 300$  nm (fig. 6.1 c,d).

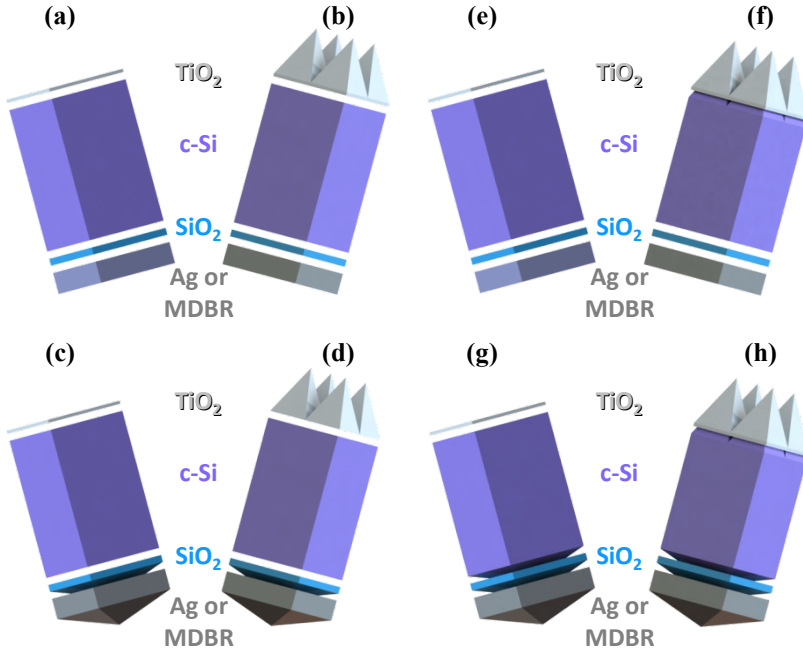


**Figure 6.1.** 3-D sketches of all models used for simulations. (a)-(d) are structures where the supporting (oxide) layers are textured, while in (e)-(h) architectures in which pyramids are directly endowed on the crystalline silicon absorber.

Regarding the flat front surface architectures (fig. 6.1 a,c),  $\text{TiO}_2$  has a thickness of 47 nm such that destructive interference is achieved at  $\lambda_{\text{ar}} = 500 \text{ nm}$  – where  $\lambda_{\text{ar}}$  indicates the wavelength at which the anti-reflective effect is achieved\*. On the other hand, the  $\text{SiO}_2$  layer in fig. 6.1 a,b is 100-nm thick, the typical value for which plasmonic resonances are completely blue shifted to the UV region and absorption in the crystalline silicon slab is not hindered [61].

Similar models for cells with textured c-Si absorber were also created, and are sketched in fig. 6.1 e-h. In this case, front / back texturing consisted of pyramids made of c-Si with the same dimensions as the ones realised in previous cases on  $\text{TiO}_2$  and  $\text{SiO}_2$ . All textured c-Si slabs have an equivalent thickness  $d_{\text{eq,c-Si}} = 2 \mu\text{m}$  (i.e. the absorber volume is the same as that of a flat c-Si slab with thickness  $d_{\text{c-Si}} = 2 \mu\text{m}$ ). The front  $\text{TiO}_2$  and the back  $\text{SiO}_2$  are merely 47-nm and 100-nm

\*The desired anti-reflective coating thickness ( $d_{\text{arc}}$ ) is calculated as:  $d_{\text{arc}} = \frac{\lambda_{\text{ar}}}{4n}$ , where  $n$  is the (real part of the) refractive index of the anti-reflection coating material.

thick, respectively, and serve either as flat coatings (fig. 6.1 e-g) or as conformal coatings for the pyramids (fig. 6.1 f-h).

As for the absorber thickness, while the ultimate efficiency in c-Si PV technology can be achieved with  $\sim 40$ - $\mu\text{m}$  thick c-Si [247], it was chosen to focus on  $2$ - $\mu\text{m}$  thick architectures for four main reasons. First, with  $1$ -to- $5$ - $\mu\text{m}$  thick absorbers wave-guided modes can be excited, possibly resulting in absorption and implied photo-generated current density values beyond those predicted by the Lambertian scattering ( $4n^2$ ) limit. In particular, it is interesting to observe whether front- and back-side textured supporting layers could trigger resonances in the flat absorber. Second, a thickness of  $2$   $\mu\text{m}$  is thin enough to support wave-guided modes, but still thick enough to distinguish the optical effects of the front texture from those of the rear one. Third,  $2$   $\mu\text{m}$  is a typical thickness of ultra-thin silicon absorbers in modelling studies concerning nc-Si:H, poly-Si, mc-Si and c-Si [246]. Fourth,  $50$ - $\mu\text{m}$  thick c-Si slabs with front dielectric textures and rear DBR were previously simulated in a separate work [248]. Good light in-coupling was achieved, but virtually no scattering could be observed – as absorption in silicon was practically equal to the double-pass case. Knowing especially this last result, the goal of this section is to examine a thickness for which the front dielectric textures could become more effective. Therefore, the objective is not to demonstrate the ultimate possible photo-current density in relation to the highest possible conversion efficiency for c-Si solar cells, but rather elaborate on the optical effect that textured supporting layers have on a flat absorbing slab – with respect to a textured absorbing slab merely coated with the same materials.

About the gratings shape, it was found [249, 250] that pyramidal structures are – at least – not second from the optical point of view to alternatives with similar geometrical dimensions and for comparable thickness of the absorber material (e.g. rectangular gratings [251], convex gratings [252], concave gratings [253]). For the front side of an absorbing dielectric slab, tapered / pyramidal textures, such as those reported in this chapter, exhibit an optical behaviour very close to an ideal multiple-anti-reflection coating (ARC) – for which a very large number of layers would be needed to achieve broad-band light in-coupling. This is due to the smooth matching of the refractive index from the incident medium (in this case air) to the absorber material (in this case silicon). For the rear side, the employment of pyramidal-like textures has been reported – in both experimental and modelling studies – to have a strong impact on the absorption of light in the active layer of solar cells [53, 217, 234, 245, 249, 254]. While there is no absolute evidence that pyramidal texturing is the absolute best for the purpose of this

work, it is safe to assume that the results here achieved are not second in performance to those carried out with the same models, but endowed with different grating shapes (rectangular, concave, convex). Therefore, since this section focuses on the comparison between flat absorbers and their textured counterparts, the generality of the scientific message here relayed is not lost.

In terms of optical performance, the outcome of the proposed pyramidal texturing (reported in the following subsections) could be further improved – either by re-arranging the current rectangular 2-D lattice into an hexagonal one [255], or by choosing non-commensurate periodicities (see second part of this chapter). Finally, previous studies on purely optical systems [234] or complete solar cell devices [59] endowed with different front and rear textures or modulated surface textures indicate that the combination of tapered front nano-texture and micro-scale pyramids results in excellent light in-coupling and scattering of long-wavelength photons, in 20-to-280- $\mu\text{m}$  thick wafers. That is, the simulated models with different front/back textures are expected to work well not only in 2- $\mu\text{m}$  thick c-Si layers, but also in thicker slabs. Finally, for the geometrical parameters of the front texture, as long as the dimensions are in sub-micron scale (100 nm – 1000 nm) and the aspect ratio larger than one (i.e. features are taller than they are wide), excellent broad-band light in-coupling can be achieved.

The choice of dielectric materials such as  $\text{TiO}_2$  at the front and  $\text{SiO}_2$  at the rear side was mainly motivated by optical considerations. In fact,  $\text{TiO}_2$  is a wide band gap material with relatively high refractive index ( $n_{\text{TiO}_2} \approx 2.5$  for  $500 \text{ nm} < \lambda < 1200 \text{ nm}$ ), thus achieving a smooth matching of  $n$  between air and silicon. On the other hand,  $\text{SiO}_2$  with its low refractive index determines ( $n_{\text{SiO}_2} \approx 1.45$ ) a high mismatch of  $n$  between silicon and back reflectors. Such mismatch could be in principle surpassed by using very-low refractive index materials such as  $\text{MgF}_2$  ( $n \approx 1.38$ ); however,  $\text{SiO}_2$  still holds an edge with respect to in-fabrication process compatibility with c-Si solar cells, especially in case of high-thermal budget ( $> 850^\circ\text{C}$ ) architectures. Moreover, pyramidally-textured  $\text{SiO}_2$  in the role of periodic grating at the rear side also acts as an effective spacer layer, shifting plasmonic losses – arising at the textured interface with metal – towards shorter wavelengths [61, 200].

For all simulated structures, either a 300-nm thick Ag back reflector (AgBR) or a modulated distributed Bragg reflector (MDBR) was applied at the rear side. The latter is the result of two different distributed Bragg reflectors (DBRs) placed on top of each other as shown in fig. 6.2a. The first DBR (DBR1) consists of 6 pairs of hydrogenated amorphous silicon nitride ( $\text{a-SiN}_x\text{:H}$ , thickness  $d_{\text{SiN}_x,1} =$

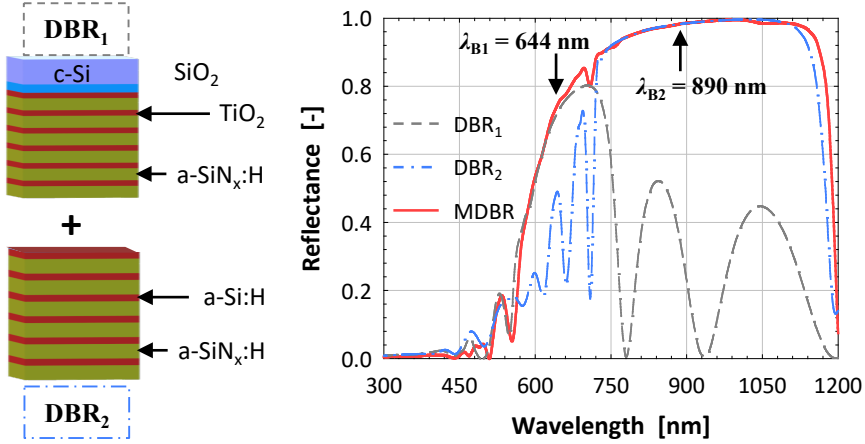


**Figure 6.2.** On the left, structure of the two distributed Bragg reflectors (DBR<sub>1</sub> and DBR<sub>2</sub>) that make up the modulated distributed Bragg reflector (MDBR), located at the back of the c-Si absorber coated with a 100-nm thick SiO<sub>2</sub> spacer. On the right, calculated reflectance at interface between SiO<sub>2</sub> and DBR<sub>1</sub>, DBR<sub>2</sub> and MDBR.

90 nm) and TiO<sub>2</sub> ( $d_{\text{TiO}_2} = 64$  nm) layers. Such reflector is designed to (ideally) deliver a reflectance  $R = 100\%$  in the wavelength range  $580 \text{ nm} < \lambda < 723 \text{ nm}$  (Bragg wavelength:  $\lambda_{\text{B1}} = 644$  nm). The second DBR (DBR<sub>2</sub>) is made of 6 pairs of a-SiN<sub>x</sub>:H ( $d_{\text{SiN}_{x,2}} = 125$  nm) and hydrogenated amorphous silicon (a-Si:H,  $d_{\text{a-Si:H}} = 60$  nm) layers. DBR<sub>2</sub> is also designed to deliver  $R = 100\%$ , but in the wavelength range  $722 \text{ nm} < \lambda < 1159 \text{ nm}$  ( $\lambda_{\text{B2}} = 890$  nm). Therefore, as reported in fig. 6.2b, when stacking DBR<sub>1</sub> and DBR<sub>2</sub> a reflectance very close to 100% can be delivered in a broad wavelength range ( $580 \text{ nm} < \lambda < 1159 \text{ nm}$ ). At such wavelengths, light penetration depth in c-Si becomes larger than the thickness of the absorber layer ( $2 \mu\text{m}$ ). Therefore, high internal rear reflectance is necessary to enhance the length of light's path inside the absorber. DBR<sub>2</sub> is located below DBR<sub>1</sub> to reduce parasitic absorbance in a-Si:H layers.

## 6.2.2 Results and discussion

### Flat device: assessment of back reflector

As a start, simulations of perfectly flat models with either AgBR or MDBR were carried out. This test was done to verify the quality of the proposed dielectric MDBR in comparison to a state-of-the-art metallic reflector. Results show that there is no major difference between the performance of the two back reflectors

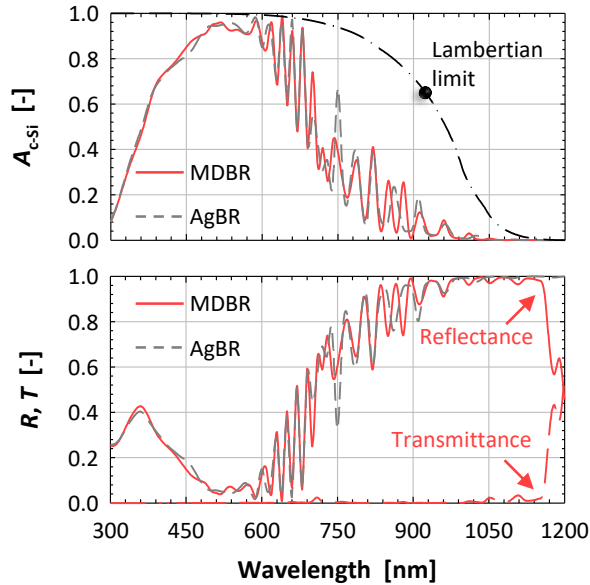


**Figure 6.3.** Absorption (top) and  $1 - \text{reflectance}$  and transmittance (bottom) of the flat reference model endowed with a silver back reflector (AgBR) and a modulated distributed Bragg reflector (MDBR). The Lambertian limit absorption curve (dash-dotted black line in the top graph) is calculated for a  $2\text{-}\mu\text{m}$  thick c-Si slab.

(see fig. 6.3). Both of them give similar values of: (i) absorption in silicon and (ii) total cell reflectance. It can thus be concluded that the MDBR on a flat interface not only ensures sufficient reflectivity in the desired wavelength range, but also does not let the electromagnetic field propagate through it, resulting in limited transmission ( $T$ ) losses – at least for  $\lambda < 1150\text{ nm}$ . Consequently, no big difference in the implied photo-generated current density of the absorber is observed (fig. 6.4). For these flat optical systems, reflectance is rather high due to: (i) poor in-coupling of photons at the air / optical system interface and (ii) no trapping of light in the absorber. As it can be seen in following sections, these loss mechanisms can be reduced by texturing only front or back side or both sides, resulting in broad-band quenching of total device reflectivity.

### Textured front side

Introduction of a nano-texture at the front side of a dielectric slab or of a solar cell allows for better light in-coupling into the device. This contributes to a reduction of total cell reflection, by reducing the reflectivity of the top layer. Previous work

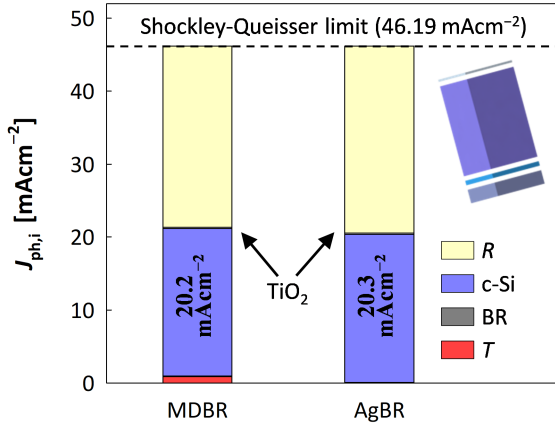


**Figure 6.4.** Implied photocurrent density generated (in c-Si) or lost in the flat reference devices, embedded with a modulated distributed Bragg reflector (MDBR) and a silver back reflector (AgBR).

showed that high aspect ratio features characterised by sub-micron geometrical dimensions can accomplish very low values of  $R$  [59, 234]. Hence, in this work it was also decided to employ high aspect-ratio pyramids at the front side of the models ( $b_f = 600$  nm,  $h_f = 750$  nm).

Looking at the implied photocurrent density generated in the c-Si absorber ( $J_{ph,c-Si}$ ), results show that the MDBR performs slightly better than the AgBR in both textured supporting layers and textured c-Si models (see fig. 6.5). For both back reflector configurations, the structure with textured c-Si can deliver a higher absorption enhancement with respect to the equivalent architecture made of textured  $TiO_2$ . The reason for that is related to the decrease of the optical losses at the front side due to a better light in-coupling for textured c-Si structure compared to the flat one. The Si texturing, in fact, provides a smoother grading of the refractive index from air ( $n_{air} = 1$ ) to bulk c-Si ( $n_{c-Si} \approx 3.5$ ), hence the reflectivity of the top layer is lower. Nevertheless,  $TiO_2$  pyramids have good anti-reflective properties, as can be seen in fig. 6.6. Here, a comparison is drawn between simulated absorptance and reflectance of models with  $TiO_2$  pyramids (fig. 6.1b), a flat reference (fig. 6.1a), and an architecture with cylindrical  $TiO_2$ -based Mie resonators [133], with  $b_{Mie} = 600$  nm and  $h_{Mie} = 300$  nm (see fig. 6.6). The three models were endowed with the same MDBR<sup>†</sup>. The pyramidal texture shows better light in-coupling, especially in the range  $300$  nm  $< \lambda < 600$  nm .

<sup>†</sup>An equivalent study was conducted with a silver back reflector, and similar results were obtained.

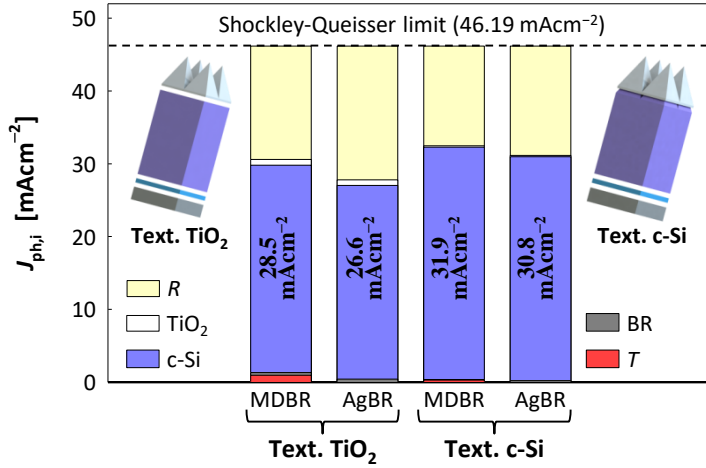


**Figure 6.5.** Implied photocurrent density generated (in c-Si) or lost in the front-textured devices, embedded with a modulated distributed Bragg reflector (MDBR) and a silver back reflector (AgBR), in the case of textured supporting layers (TiO<sub>2</sub>, left) and textured absorber (c-Si, right).

Consequently, absorptance for these architectures is higher than in devices with Mie resonators (6.4% higher  $J_{ph,c-Si}$ ). However, high cell reflectivity at longer wavelengths ( $900 \text{ nm} < \lambda < 1100 \text{ nm}$ ) suggests that no significant trapping of light is promoted by either texture. In fact, light reflected at the device back side is not scattered into large angles, and can thus easily out-couple at the front side and escape the solar cell. To prevent this and increase the absorption in c-Si, the introduction of a micrometre-scale back texture is required.

### Textured back side

Micrometre-scale textures at the back side of a solar cell promote scattering of long wavelengths photons ( $\lambda > 900 \text{ nm}$ ) [234, 245]. In this spectral region absorption of light by c-Si is weak, hence the enhancement of the length of light's path in the absorber can significantly increase the optical performance. Pyramidal structures with relatively large periods can effectively diffract near-infrared light into large angles, thus ensuring a substantial lengthening of light's path in c-Si. On the other hand, texturing with low aspect-ratio features is desirable for low charge recombination and high electrical performance. For this reason, shallow pyramids were used ( $b_b = 1200 \text{ nm}$ ,  $h_b = 300 \text{ nm}$ ). Results show that the AgBR performs better than the MDBR in both flat c-Si and textured c-Si models



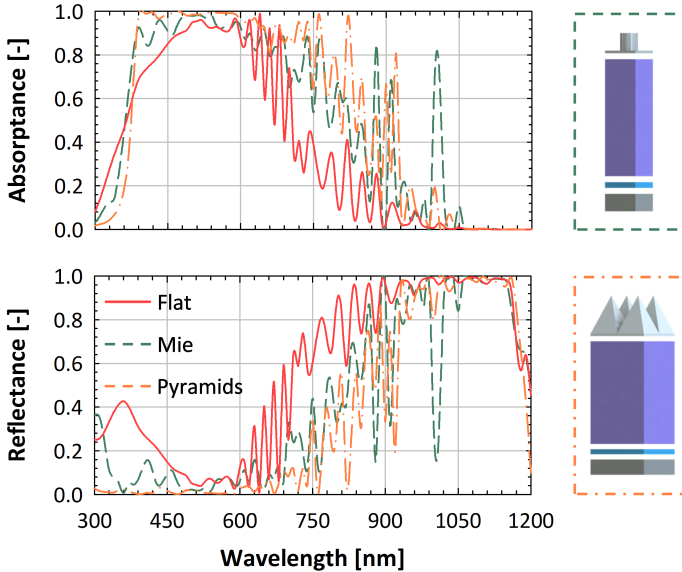


**Figure 6.6.** Calculated absorbance in c-Si (top) and device reflectance (bottom) of a flat reference model, a device endowed with Mie resonators (see sketch at the top, on the right), and a device with  $\text{TiO}_2$  pyramids at the front, (sketch at the bottom, on the right).

(see fig. 6.7). Since the thickness of layers used in DBR1 and DBR2 are optimised for the deposition on flat substrates, when the MDBR is applied to a textured surface it allows more light to go through ( $T$  losses become more significant) [256]. As seen previously, pyramids of c-Si result in a higher absorbance than features based on a dielectric material ( $\text{SiO}_2$  in this case). This result was expected, since c-Si has a higher refractive index than  $\text{SiO}_2$  ( $n_{\text{c-Si}} \approx 3.5$ ,  $n_{\text{SiO}_2} \approx 1.45$ ). Thus, more diffraction modes can be excited at the c-Si/ $\text{SiO}_2$ /BR interface (c-Si pyramids) than at the  $\text{SiO}_2$ /BR interface ( $\text{SiO}_2$  pyramids).

### Front and back textures with different geometries

Finally, nanometre-scale high-aspect ratio features at the front side for broadband light in-coupling and micrometre-scale shallower pyramids at the back side for light scattering are combined. Results show that the MDBR performs better than AgBR when dielectrics ( $\text{TiO}_2$  and  $\text{SiO}_2$ ) are textured, while MDBR performs worse than AgBR in the optical system with textured silicon (see fig. 6.8). In terms of optical performance, dielectric-coated pyramids based on c-Si are better than textured supporting layers on flat c-Si, as was already shown indepen-

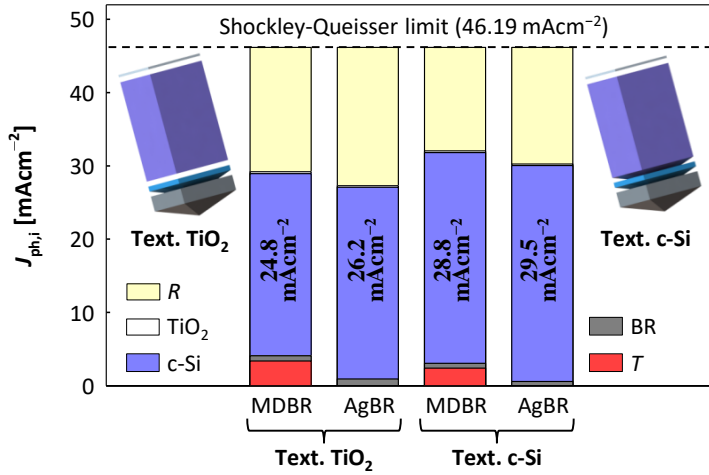


**Figure 6.7.** Implied photocurrent density generated (in c-Si) or lost in the back-textured devices, coated with a modulated distributed Bragg reflector (MDBR) or a silver back reflector (AgBR), in the case of textured supporting layers ( $\text{TiO}_2$ , left) and textured absorber (c-Si, right).

dently for both front- and back-texturing. Considering the same BR, in case of AgBR (MDBR) the textured supporting layers model exhibits a  $J_{ph,c-Si}$  which is  $7.2 \text{ mAcm}^{-2}$  ( $4.3 \text{ mAcm}^{-2}$ ) lower with respect to their textured c-Si counterpart – corresponding to a -20.6% (-13%) decrease of the optical performance. This difference can be mainly attributed to the textured  $\text{TiO}_2$  at the front side, which: (i) absorbs more than the the simple  $\text{TiO}_2$  coating due to its bigger volume and (ii) offers less effective anti-reflection with respect to the textured c-Si. In addition, the textured  $\text{SiO}_2$  at the rear can excite a lower number of diffraction modes with respect to c-Si pyramids, due to its lower refractive index.

Finally, the best textured dielectric model – which is fully dielectric – results in  $J_{ph,c-Si} = 28.8 \text{ mAcm}^{-2}$ , while the best structure with textured c-Si (with AgBR) achieved a  $J_{ph,c-Si} = 35.0 \text{ mAcm}^{-2}$ . As can be seen in fig. 6.9, this difference in performance is due to: (i) greater absorption losses in the textured front  $\text{TiO}_2$  with respect to a 47-nm thick  $\text{TiO}_2$  coating of the front side c-Si texture; (ii) higher transmittance and absorption losses in the MDBR due to its deposition on textured  $\text{SiO}_2$  with respect to the AgBR deposited on 100-nm thick  $\text{SiO}_2$  coating the back side of the textured c-Si; (iii) narrower good light in-coupling and poorer light scattering of the textured supporting layers model with respect to the textured c-Si one.

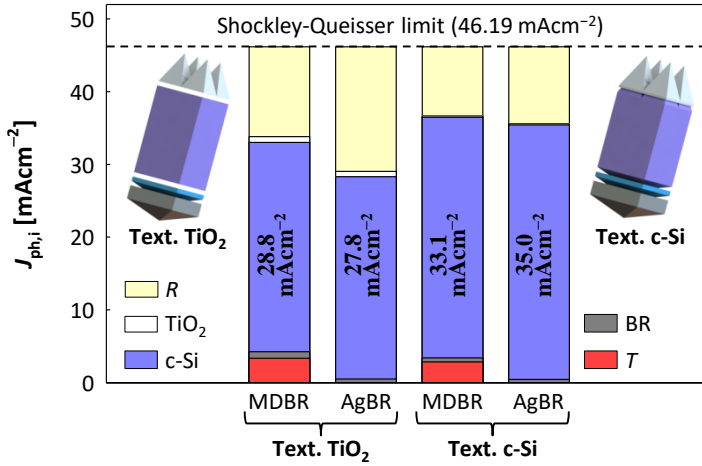


**Figure 6.8.** Implied photocurrent density generated (in c-Si) or lost in the front/back textured devices, embedded at the back side with a modulated distributed Bragg reflector (MDBR) or a silver back reflector (AgBR), in the case of textured supporting layers (TiO<sub>2</sub>, left) or textured absorber (c-Si, right).

### 6.3 Optimisation of the front and back textures

The second part of this chapter deals with the optimisation and optical performance analysis of both front and back pyramidal textures endowed in a fully-functioning thin-film solar cell architecture – based on hydrogenated nano crystalline silicon absorbers. The (equivalent) thickness of the active layer was maintained constant at 2- $\mu\text{m}$ , as in the previous section. The choice of nc-Si:H in favour of c-Si is motivated by the desire to analyse the optical performance in a realistic thin-film solar cell configuration. While ultra-thin c-Si architectures are attracting more and more interest in recent years, devices with thickness around or below 2  $\mu\text{m}$  have not yet been investigated. On the other hand, such values are typical for TFSSCs. Hence, the findings of this section (and of the next chapter) can be readily compared with the state-of-the-art<sup>‡</sup>.

This section is structured as follows: after presenting the typical structure and some useful definitions, a thorough optimisation of the device architecture is carried out, divided in 4 phases. In phase 0, the advantages of using an asymmetric grating are portrayed. Phase 1 deals with the geometrical optimisation of the

<sup>‡</sup>It must be always kept in mind that the results of this thesis are the product of modelling, and not of experimentally manufactured devices.

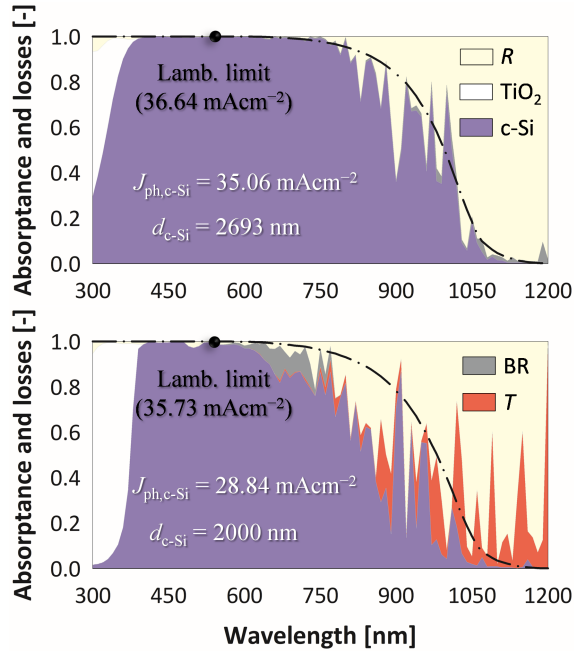


**Figure 6.9.** Absorption in c-Si and losses for the best textured-absorber structure (top, with AgBR) and for the best textured-supporting layers architecture (bottom, with MDBR).

front and back periodically-arranged pyramids. In phase 2, the use of different materials for supporting layers is investigated. Finally, in phase 3 parasitic absorption in the front transparent conductive oxide is tackled. The second part of this section delves deeper into the reasons behind the achieved performance, by first looking at how the electromagnetic field propagates within the structure, and then at how the excitation of wave-guided mode can explain the peaks observed in the modelled absorption spectra. Finally, the overall performance of the best simulated structure is assessed in terms of light trapping efficiency (*LTE*) [246] and for different illumination angles.

### 6.3.1 Device structure

A schematic view of the typical solar cell deployed in the simulations of this section is presented in fig. 6.10. This figure shows what is defined as a unit cell: the smallest indivisible piece of a solar cell that is still recognisable as such. The

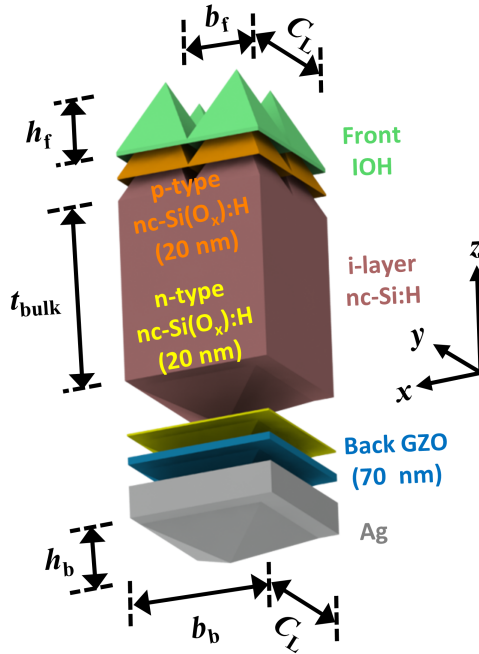


**Figure 6.10.** 3-D rendering of the typical solar cell modelled in this section.

squared common lattice,  $C_L^2$ , is the  $xy$ -area of the unit cell; that is the area within which both front and rear nano-pyramids can be accommodated. When repeated in a 2-D square pattern, the unit cell forms a full solar device at macroscopic scale and the nano-pyramids form the surface textures.

The geometry of the nano-pyramids is given by their height  $h_m$  and base width or period  $b_m$ , where  $m = f$  is used for the front surface and  $m = b$  for the back surface. The thickness of the intrinsic nc-Si:H that does not include the nano-pyramids is called bulk thickness ( $t_{\text{bulk}}$ ). A 3-D model was prepared for every structure within the investigated parameter space. On the front surface, high aspect ratio nano-pyramids were explored (as in the previous section), as the height was varied between 500 nm and 900 nm, while the base width was changed between 300 nm and 700 nm [245]. On the rear surface, shallower nano-pyramids were once again deployed, as the height was varied between 100 nm and 500 nm and the base width was varied between 800 nm and 1200 nm [249, 250]. As will be discussed in the next subsection, each combination of dimensions of front and rear nano-pyramids determined the associated  $t_{\text{bulk}}$ , since the total amount

of absorber material used in every model is the same (and corresponding to an equivalent thickness of  $2 \mu\text{m}$ ).

Certain combinations in the chosen parameter space resulted in non commensurate base widths between front and rear side of the unit cell. To ensure reasonable simulation times (i.e. to limit the size of the simulated unit cell), the common lattice  $C_L$  was used, along with the duty cycle. The latter is defined as  $D_m = N_m \cdot b_m / C_L$ , where  $N_m$  is the number of nano-pyramids, either at the front ( $m = f$ ) and or at the rear side ( $m = b$ ) of the model, along the  $x$ - or  $y$ -direction in the unit cell. The quantity  $1 - D_m$  is a measure of the space left non-textured around the nano-pyramids – either at the front or at the rear side. In the 3-D model shown in fig. 6.10,  $C_L = 2 \cdot b_f > b_b$ , resulting in perfectly packed front texture ( $D_f = 1$ ) and in a non-textured area around the rear nano-pyramid ( $D_b = b_b / C_L < 1$ ). In other 3-D models evaluated in this section, the case  $C_L = b_b > 2 \cdot b_f$  was also handled, that on the contrary left a non-textured area around the front nano-pyramids.

To conclude this section, at the front side of the unit cell, a 20-nm thick  $p$ -type layer and a 100-nm thick front  $\text{In}_2\text{O}_3\text{:H}$  (IOH) transparent conductive oxide (TCO) were considered (in phase three of the optimisation, the latter is thinned down to 40 nm). At the rear side of the unit cell, a 20-nm thick  $n$ -type layer, a 70-nm thick back  $\text{ZnO:Ga}$  (GZO) TCO and a 300-nm thick silver reflector were deployed. For all these thin supporting layers, a geometry conformal to the nc-Si:H  $i$ -layer endowed with front and rear nano-pyramids was assumed.

### 6.3.2 Volumetric and optical equivalent thickness

The reference thickness ( $t_{\text{ref}}$ ) of high efficiency single junction nc-Si:H solar cells is 2000 nm ([244, 257]). As the number of photons absorbed in the  $i$ -layer is directly proportional to its volume ([245]), the amount of absorber material in any simulated unit cell must stay the same for fair comparison. To fulfil such requirement in each simulated unit cell, an equivalent volume  $V_{\text{eq}} = t_{\text{veq}} \cdot C_L^2$  was defined, where the volumetric equivalent thickness ( $t_{\text{veq}}$ ) was kept constant at 2000 nm. Obviously, to account for the volume of the absorber material inside the front and rear nano-pyramids,  $t_{\text{bulk}}$  was varied to keep the volume  $V$  constant and equal to  $V_{\text{eq}}$ :

$$V = t_{\text{bulk}} \cdot C_L^2 + N_f^2 \cdot \frac{b_f^2 \cdot h_f}{3} + N_b^2 \cdot \frac{b_b^2 \cdot h_b}{3} \quad (6.1)$$

Hence,  $t_{\text{bulk}}$  can be determined by equating  $V$  and  $V_{\text{eq}}$ :

$$t_{\text{bulk}} = t_{\text{Veq}} - \frac{1}{3}(D_{\text{f}}^2 \cdot h_{\text{f}} + D_{\text{b}}^2 \cdot h_{\text{b}}) \quad (6.2)$$

Next, it should be noted that front and rear textured  $i$ -layers are optically active from the uppermost to the bottom-most morphological features [246]. This means that not only  $t_{\text{bulk}}$ , but also the peak-to-valley height of front and of the rear features must be considered. In this respect, the optical thickness ( $t_{\text{opt}}$ ) was defined as follows:

$$t_{\text{opt}} = h_{\text{f}} + t_{\text{bulk}} + h_{\text{b}} \quad (6.3)$$

In summary, for each simulated unit cell, eq. (6.2) is used to determine the bulk thickness of the  $i$ -layer, while eq. (6.3) is employed to assess its optical performance with respect to light absorption limits (i.e. single-, double-pass and Lambertian scattering limits).

### 6.3.3 Structure optimisation

#### Phase zero: Non-commensurate geometries

Referring to the left panel of fig. 6.11, the 3D-models presented in this section are in the first quadrant of the coordinate system ( $x > 0$  and  $y > 0$ ). For unit cells with either top or bottom duty cycle  $< 1$ , the leftover space between pyramids allows to displace these textures away from each other. This causes a level of asymmetry that is dependent on the duty cycle (i.e. a smaller duty cycle allows for greater asymmetry). The right panel of fig. 6.11 shows the spectral difference in absorptance of the  $i$ -layer ( $A_i$ ) between a symmetric and an asymmetric structure – obtained by diagonally displacing top and bottom textures. Results show that displacing such non-commensurate geometries increases  $A_i$  across the whole wavelength range of interest.

It would also be possible to create a non-diagonal asymmetry by displacing the top and the bottom textures only in the  $x$ - or  $y$ -directions. These cases are not reported here, since a diagonal displacement always creates the largest deviation with respect to the symmetric case. Further, asymmetric structures could be also created for commensurate geometries, for example by enforcing a duty cycle smaller than 1. Finally, pyramids could also be displaced and sliced in an arbitrary plane while still forming a perfect unit cell in an infinitely repeating pattern of pyramids. These approaches were not considered since the goal is to minimise the size of unit cells and their modelling complexity.

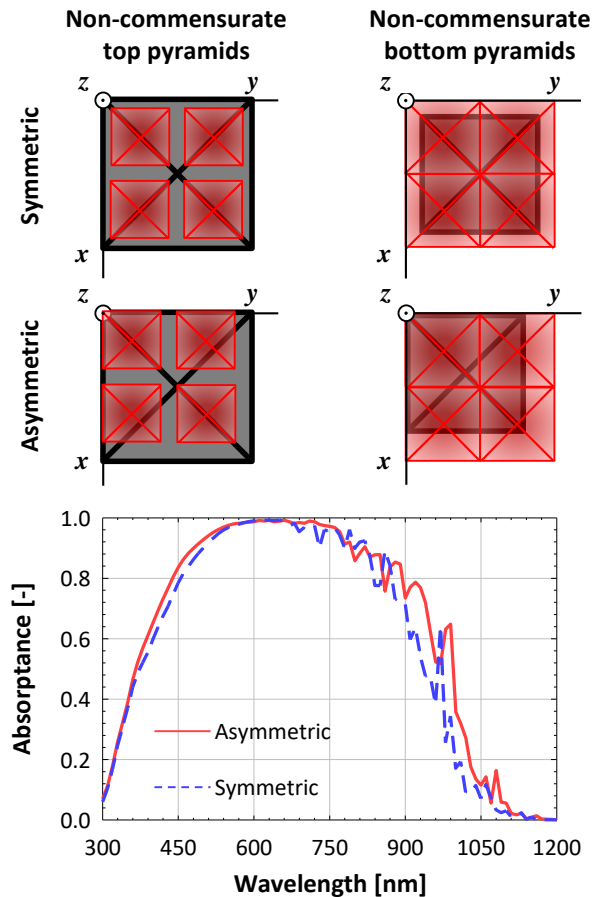


**Figure 6.11.** At the top, schematic view of unit cells with non-commensurate top or bottom pyramids, in symmetric and asymmetric simulation domains. At the bottom, simulated absorption in the  $i$ -layer in symmetric and an asymmetric domains.

### Phase one: Sweeping geometrical parameters

A geometric optimisation was first performed. The dimensions of the surface texture, described by the geometric attributes of the nano-pyramids, determine the diffraction of light and consequently its absorption. In the simulations, the morphology of pyramids on the top and bottom surfaces were separately varied in an ample parameter space, and optimised for maximum anti-reflection at the front and maximum near-infrared light diffraction at the back. By always assess-



**Table 6.1.** Input parameters and results of the three best structures in the geometrical parameter sweep.  $J_{\text{Lamb}}$  indicates the calculated photocurrent density in the Lambertian scattering limit case, using for each structure its corresponding optical thickness ( $t$ )<sub>opt</sub>.

Parameter	Structure #1	Structure #2	Structure #3
$b_f$ [nm]	700	700	700
$h_f$ [nm]	700	700	900
$b_b$ [nm]	1200	1200	1200
$h_b$ [nm]	500	300	500
$t_{\text{bulk}}$ [nm]	1644	1693	1577
$J_{\text{ph-}i}$ [mAcm <sup>-2</sup> ]	33.81	33.62	33.68
$J_{\text{Lamb}}$ [mAcm <sup>-2</sup> ]	36.05	35.89	36.18

ing a combination of front and back textures, light absorption in the  $i$ -layer was maximised. The best performing structures from this first optimisation phase have similar properties. Tall nano-scale pyramids at the front side of the device promote excellent in-coupling of light, by allowing for a smooth transition of the refractive index from air (incident medium) to the  $i$ -layer. At the rear side of the device, larger pyramids are necessary to diffract long-wavelength light, effectively extending its path length in the absorber. These features also need to be (relatively) shallow, to avoid significant parasitic absorption in the back reflector. The results of the three best performing structures can be reviewed in table 6.1. The structure that achieves the highest absorption (structure #1) is asymmetric and it has top surface pyramids with dimensions  $(b_f, h_f) = (700 \text{ nm}, 700 \text{ nm})$  and bottom surface pyramids  $(b_b, h_b) = (1200 \text{ nm}, 500 \text{ nm})$ , with 200 nm of flat surface in both  $x$ - and  $y$ -directions to fill a common lattice ( $C_L$ ) of 1400 nm. The simulated absorption was then integrated with the AM1.5 spectrum [74], to obtain an implied photocurrent density  $J_{\text{ph-}i}$  of 33.81 mAcm<sup>-2</sup>. After the material optimisation described in phase two and three, however, it was found that structure #2 could achieve a higher optical performance than structure #1. Hence, from now on all results presented will concern structure #2 (asymmetric,  $(b_f, h_f) = (700 \text{ nm}, 700 \text{ nm})$ ,  $(b_b, h_b) = (1200 \text{ nm}, 300 \text{ nm})$ ).

### Phase two: Doped layers and metal-oxide rear interface

To further enhance the optical performance, it is useful to analyse and optimise the structure of supporting layers that – in combination with the absorber – form a complete solar cell device. These supporting layers are crucial for the optimal functioning of solar cells, but can also be an obstacle to achieve high optical per-

**Table 6.2.** Results of the investigation of different doped layers and back TCOs, for structure #2.  $\Delta_{\text{Lamb.}}$  indicates the relative deviation of  $J_{\text{ph-}i}$  from  $J_{\text{Lamb.}}$ .

Structure #2				
Layer/parameter	Design I	Design II	Design III	Design IV
Back TCO	–	GZO	–	GZO
Doped layers	nc-Si:H	nc-Si:H	nc-SiO <sub>x</sub> :H	nc-SiO <sub>x</sub> :H
$J_{\text{ph-}i}$ [mAcm <sup>-2</sup> ]	31.84	33.62	34.37	35.18
$\Delta_{\text{Lamb.}}$ [%]	–11.28%	–6.33%	–4.24%	–1.99%

formance. In particular, small amounts of light are absorbed in these layers, thus not contributing to the total photocurrent density generated in the solar cell. By reducing these parasitic losses, a significant gain in absorption in the *i*-layer can be obtained. To this purpose, four solar cell designs were investigated, each with a different combination of *p*-type layer, *n*-type layer and back TCO. Note that here the thickness of the supporting layers was not changed (front IOH: 100 nm, *p*-/*n*-type layers: 20 nm, back GZO: 70 nm), but rather the use of different materials was investigated. The geometries of these devices are based on those of the three best performing structures from phase one (see table 6.1). As mentioned above, the largest  $J_{\text{ph-}i}$  value achieved in this phase for structure #2.

Materials and results are summarised in table 6.2. Designs I and II employ *p*- and *n*-type nc-Si:H, while designs III and IV use more transparent nc-SiO<sub>x</sub>:H as doped layers. In addition, designs II and IV include a TCO between the *n*-type layer and the back silver reflector, while designs I and III do not. The function of this spacer is to improve reflectivity at the back side, mainly by reducing parasitic absorption in the metallic contact [200, 258]. GZO was chosen as back TCO, owing to its high transparency and conductivity [121]. In addition, its presence shifts plasmonic resonance from the near infrared part of spectrum to shorter wavelengths, effectively quenching (eventual) plasmonic losses in the silver layer – since higher-energy photons are absorbed by silicon before they reach the semiconductor-metal interface. For design I, Without a back-TCO and using doped nc-Si:H significant losses in the silver back reflector can be observed, resulting in the lowest performance of all designs with  $J_{\text{ph-}i} = 31.84 \text{ mAcm}^{-2}$ . This corresponds to a deviation from the Lambertian scattering limit<sup>§</sup> of –11.28%.

In this regard, a significant improvement in the absorption spectrum of the

<sup>§</sup>The deviation from the Lambertian scattering limit ( $\Delta_{\text{Lamb.}}$ ) is calculated as follows:  $\Delta_{\text{Lamb.}} = (J_{\text{ph-}i} - J_{\text{Lamb.}}) / J_{\text{Lamb.}}$ .

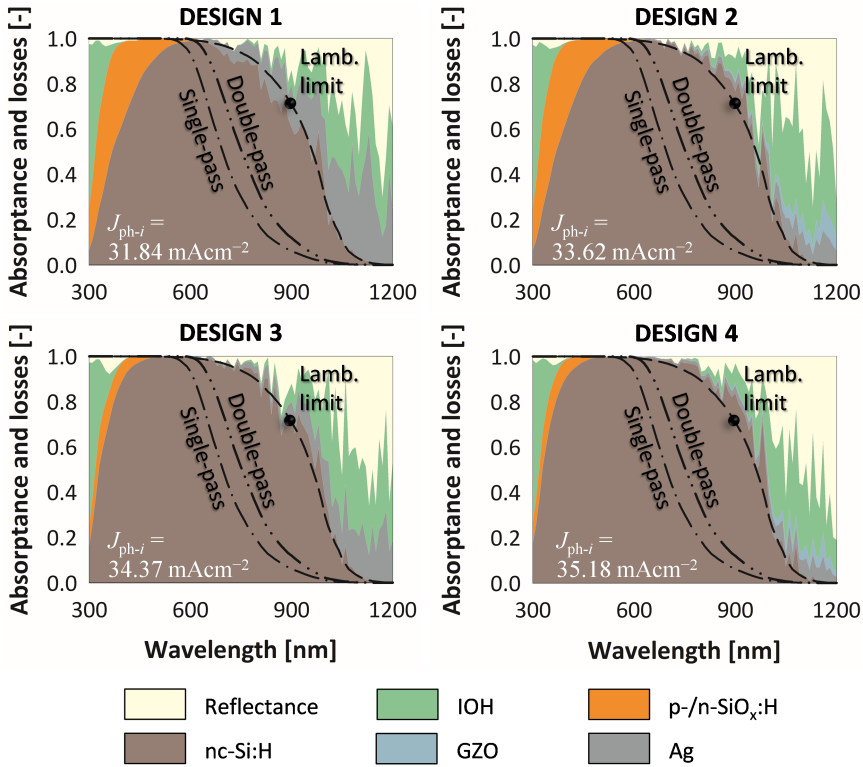


**Figure 6.12.** Absorption and optical losses in models with different supporting layers configurations (design I-IV), based on structure #2. The single-, double-pass and Lambertian limit photocurrent density values are  $21.16 \text{ mAcm}^{-2}$ ,  $24.72 \text{ mAcm}^{-2}$  and  $35.89 \text{ mAcm}^{-2}$ , respectively.

*i*-layer is achieved by design II, where a back-TCO is included. Absorption losses related to the silver layer have been quenched – as plasmonic resonances have been blue-shifted. The resulting performance was recovered to  $\Delta_{\text{Lamb.}} = -6.33\%$ . In design III, the inclusion of doped nc-SiO<sub>x</sub>:H layers, instead of regular nc-Si:H, is assessed. Without a back-TCO, parasitic losses in the silver layer are still apparent. They are however considerably smaller than in the case of doped nc-Si:H layers (without a back-TCO, design I), owing to the lower refractive index of nc-SiO<sub>x</sub>:H (i.e. *n*-type nc-SiO<sub>x</sub>:H acts both as doped layer and spacer to quench absorption in the metallic back contact). In the short wavelength region, parasitic losses in the *p*-type layer have decreased (with respect

to designs I and II), due to the much larger band gap of nc-SiO<sub>x</sub>:H, resulting in  $\Delta_{\text{Lamb.}} = -4.24\%$ . Finally, in design IV both doped nc-SiO<sub>x</sub>:H supporting layers and GZO as back-TCO are included. Reintroduction of the GZO-layer further suppresses parasitic absorption in the back reflector, due to the larger spacing between the *i*-layer and the metal. This result in an additional increase of the absorption ( $J_{\text{ph-}i} = 35.18 \text{ mAcm}^{-2}$ ,  $\Delta_{\text{Lamb.}} = -1.99\%$ ).

### Phase three: Front TCO thickness sweep

Studying the spectral responses depicted in fig. 6.12, some parasitic absorption losses in the front TCO can still be observed (green-coloured areas). For this layer, IOH is employed, a highly-transparent and conductive TCO commonly used in state-of-the-art thin-film silicon solar cells [39, 41, 259, 260]. In previous phases, the thickness of this layer was fixed to 100 nm. In this phase, the impact of having a thinner front TCO is analysed. Reducing the thickness of this layer to improve the optical properties of the cell has a major drawback. A thinner front TCO will increase the series resistance of the cell, effectively reducing its fill factor. In the perspective of deploying the findings of this chapter in current-matched multi-junction devices, it is expected that the short-circuit current density of the overall device is smaller than the one of the single junction here modelled, relaxing the requirement on the front TCO thickness [261]. Therefore, a thickness sweep from 100 nm to 40 nm was conducted. The device model with the thinnest IOH layer (40 nm) managed to achieve a  $J_{\text{ph-}i} = 36.0 \text{ mAcm}^{-2}$  (see fig. 6.13) This value surpasses the Lambertian-limit photocurrent ( $J_{\text{Lamb.}} = 35.89 \text{ mAcm}^{-2}$ ), demonstrating the excellent light-trapping capabilities of the proposed front and rear double texture.

At this point in this study, the results are compared to those obtained by Wang *et al.* [245], on whose findings the work of this chapter is based. Wang *et al.* also conducted a separate optimisation of the top and bottom surfaces of his device, but only considered a textured c-Si slab with a volumetric equivalent thickness  $t_{\text{veq}} = 2000 \text{ nm}$ . This means that parasitic losses in the surrounding layers, as they would occur in a real solar cell, were not considered. In this chapter, instead, the layers included in a state-of-the-art fully-functional solar cell were taken into account, therefore including all possible optical losses that can occur within a real device. Consequently, parasitic absorption in the short wavelength range of the spectrum ( $300 \text{ nm} < \lambda < 450 \text{ nm}$ ) can be still observed, owing to the presence of the front TCO and of the *p*-type layer. Nonetheless, the absorption enhancement in the near infrared region is so pronounced that a significant

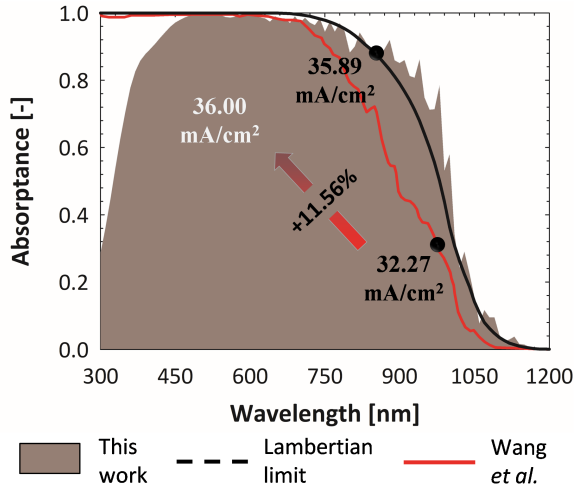


**Figure 6.13.** Comparison between the best results of this chapter and those obtained by using the structure proposed by Wang *et al.* [245].

improvement over previous results was achieved. Due to a minimisation of parasitic losses and to the occurrence of guided modes, the simulated absorption in the *i*-layer is enhanced beyond the Lambertian limit ( $\Delta_{\text{Lamb.}} = +0.31\%$ ) and realises an 11.56% improvement with respect to the results of the previous study by Wang *et al.* This significant increase of absorption can be mainly ascribed to a better trapping of infrared photons inside the absorber, promoted by the asymmetry of the structure and by the presence of lower refractive index supporting layers on both sides of the absorber. In particular, the *p*- and *n*-type nc-SiO<sub>x</sub>:H films act similar to the cladding in optical fibres, confining light inside the central high-refractive index material. While these layers are a significant source of parasitic absorption losses, particularly in the blue and UV regions, their presence appear to be quite beneficial – from an optical performance standpoint – in the remaining part of the spectrum, where they only absorb a small portion of incident light.

### 6.3.4 Electric field distribution and enhancement factor

To understand the reasons behind the excellent optical performance achieved by the optimised double-textured model, it is worthwhile to look at the electric field distribution inside the structure. This distribution is an indication on how light is propagating inside the device, thus providing an insight on which optical phe-

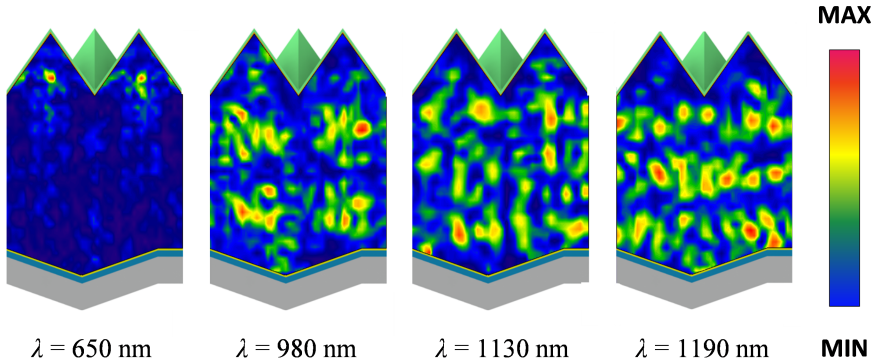


**Figure 6.14.** Distribution of the electric field inside the solar cell model, as several wavelengths of interest.

phenomena are taking place owing to the presence of the both textures. Consider a diagonal slice (i.e. the cross-section in the direction  $x = y$ ) of the unit cell, showing the electric field distribution at a wavelength of 650 nm (fig. 6.14, on the left). Since silicon is highly absorptive at this wavelength, light is absorbed closer to the front of the device. There, resulting from light interacting with the front texture, it is possible to distinguish strong localised absorption enhancements inside the top pyramids. At the same time, low intensity of the electric field is observed at the rear side. At longer wavelengths, it is noticeable that the electric field propagates through the entire absorber thickness and interacts with the bottom part of the device. Several high-intensity regions with a periodic character can be observed at specific wavelengths (e.g. 980 nm, 1130 nm and 1190 nm, see fig. 6.14). Their presence suggests that the front and rear textures induce resonances in the nc-Si:H layer, thus enhancing absorption. Also, it evidences that the absorber layer is acting as a wave-guide, supporting in the longitudinal direction approximately two periods of the electric field at 980 nm, three periods at 1130 nm and possibly more at 1190 nm.

Currently, it is challenging to determine whether the electric field distribution inside the absorber layer is more influenced by the front or the back texture. However, it is nonetheless possible to show that both textures actively contribute to the absorption enhancement. In this respect, it is useful to compare the wavelength-dependent enhancement factor of the best modelled structure not only with the theoretical enhancement in the Lambertian limit, but also with the theoretical maximum values calculated with the temporal coupled-mode (TCM)

theory [125, 126]. As a reminder, the enhancement factor  $EF$  is the ratio of calculated absorption (e.g.  $A_i$ , the absorption of the  $i$ -layer, or  $A_{\text{Lamb.}}$ , the Lambertian limit absorption) to single-pass absorption ( $A_{\text{sp}}$ ), i.e. the theoretically determined absorption of a non-reflective slab of material with the same thickness. For this purpose, to get higher spectral resolution in the wavelength range of interest, next to the 10-nm stepped absorption spectra so far reported, simulation at every 1 nm intervals were carried out for the best structure. The TCM theory predicts  $EF$  values beyond the conventional  $4n^2$  (Lambertian) limit, for 2-D periodically-textured dielectric slabs with feature sizes in the same order of magnitude as the wavelength of incident light *in vacuo*. The formula, derived by Yu *et al.* for a 2-D periodic square lattice [125, 126], was used to calculate the theoretical  $EF(\lambda)$  depicted in fig. 6.15. It is worth noting that such closed formula is valid in the over-coupling regime, that is when the rate of light absorption in the dielectric is significantly lower than the rate at which light is out-coupled (i.e. can escape from the absorber). In fig. 6.15, the upward-pointing triangles indicate the  $EF$  calculated using the period of the front grating ( $b_f = 700$  nm), while the downward-pointing triangles were computed using the period of the back grating ( $b_b = 1400$  nm). For comparison only, the circles represent the sum of the two previously calculated  $EF$  curves.

As previously seen in fig. 6.13 and as expected from the TCM theory, the modelled absorption spectrum of the best structure results in  $EF_i$  beyond that of the Lambertian limit – at specific wavelengths. The  $EF_i$  simulated every 10 nm reaches its highest values at the wavelengths where the electric field distribution shows a resonant behaviour. For example,  $EF_i = 10.48n^2 \approx 130$  at 1130 nm, that is almost three times higher than  $EF_{\text{Lamb.}}$ . Comparing the results here presented to the TCM theory, up to 1050 nm – 1070 nm the computed  $EF_i$  are mostly within the theoretical curve carried out for  $b_b$ . In addition, they follow the discontinuity foreseen by the TCM theory. In fact, passing from 990 nm to 1000 nm, the number of leakage channels suddenly decreases, leading to a higher theoretical  $EF$  for  $\lambda > 1000$  nm. On the other hand, beyond 1050 nm – 1070 nm the  $EF_i$  of both modelled spectra is consistently well above both TCM-determined  $EF$ , indicating a superposition of effects due to both front and rear gratings. The latter finding should not surprise, since (i) the TCM theory was developed for one-sided textured dielectric slabs with perfect electrical conductor as ideal rear mirror, and (ii) the structure of the nc-Si:H thin-film solar cell might not operate in the over-coupling regime, due to the presence of front supporting layers acting as (weak) cladding against optical leakage. This highlights the need to

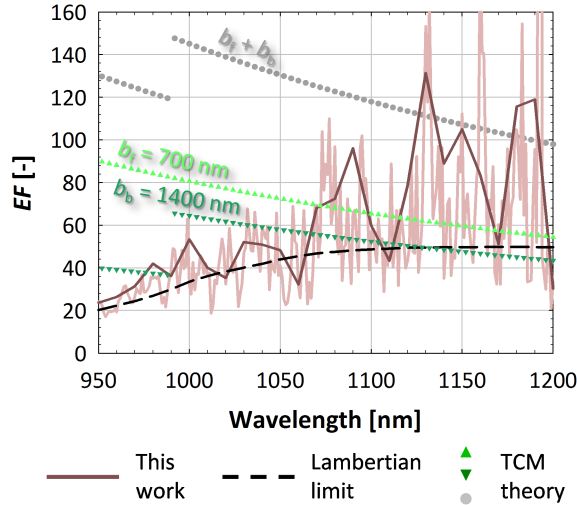


**Figure 6.15.** Enhancement factor ( $EF$ ) of the best model (structure #2, design IV, 40-nm thick front IOH), computed every 10 nm (dark brown) and every 1 nm (light brown). The dashed black line indicates the theoretical  $EF$  in the Lambertian limit case, while dark and light green curves depict the theoretical  $EF$  calculated with the temporal coupled mode theory for back and front periods, respectively. The grey curve is simply the sum of the values of the two green lines.

modify the TCM theory, extending its validity to the case of double front and back texturing and finding out whether the threshold range 1050 nm – 1070 nm only conveniently points at the (weighted) average effect of the front and rear grating, or if different physical phenomena are at play.

### 6.3.5 Wave-guiding in the absorber

Supported by wave-guide mode theory, the nature and the energy position of absorption peaks observed in both 10-nm and 1-nm stepped  $A_i$  spectra of the best modelled structure are here discussed, for  $\lambda > 950$  nm. Following reflection pole method (RPM) calculations [262, 263], all wave-guided modes supported by the absorber are plotted in the dispersion diagram depicted in fig. 6.16. Red lines represent modes for s-polarised light, while blue lines refer to those for p-polarised light. Vertical lines, representing the centre of Brillouin zones of the front (light green) and back textures (dark green), are also reported. Continuous green lines indicate Brillouin zone centres distanced by  $2\pi/b_m$  (i.e. in the  $x$  and  $y$  directions), while dashed green lines represent zone centre with distance



$2\sqrt{2}\pi/b_m$ , where  $b_m$  is the texture period at the front ( $m = f$ ) or at the back side ( $m = b$ ) of the absorber layer. Black lines indicate the maximum allowed value of the parallel component of the wave vector ( $k_{\parallel}$ ) at a specific photon energy  $E$ , for a given material with refractive index  $n$  ( $k_{\parallel} = E \cdot 2\pi n/hc$ , where  $h = 6.63 \times 10^{-34}$  Js is Planck's constant, and  $c = 2.998 \times 10^8 \text{ms}^{-1}$  is the speed of light *in vacuo*). Between the light lines of  $p$ -type nc-SiO<sub>x</sub>:H and nc-Si:H, intersections of the centre of Brillouin zones and the available modes in nc-Si:H indicate the excitation of a guided mode in the absorber. In turn, this is expected to cause a significant increase of absorption at the corresponding wavelength/photon energy. In the plot, grey bands indicate these intersections and the corresponding peak(s) in the absorption plot (on the right panel of fig. 6.16). Due to several approximations, mainly the resolution of simulations and calculations and the fact that the RPM assumes flat interfaces, it was preferred to provide energy bands where those resonances are likely to happen, instead of individuating the exact photon energy at which a resonance is taking place,. Moreover, modes that are excited closer to the light line of  $p$ -type nc-SiO<sub>x</sub>:H layer, are coupled more strongly to the absorber [255, 264], hence only those were considered. It is important to note that Brillouin zones from both the front- and the back-surface textures are of influence. This means that a concurrent excitation of wave-guided modes takes place in the front and rear textured device. In other words, both the front and the rear gratings work together – mutually reinforcing the excitation.

### 6.3.6 Light-trapping efficiency

Having established the best structure from phase three of this study, it is useful to proceed with calculations of the light trapping efficiency (*LTE*). *LTE* is a figure of merit for the comparison of the optical performance of solar cells [246]. Usually, the classical  $4n^2$  limit is employed to assess the performance of light trapping schemes. However, this is of limited use when comparing results across studies, because the deviation from such limit strongly depends on the absorber thickness and on the materials chosen for the eventual supporting layers. *LTE* as a comparison tool circumvents device specifics, and allows to compare results here presented to previously obtained results, whether numerical or experimental. Concretely, *LTE* is defined as:

$$LTE = \frac{J_{\text{ph-i}} - J_{\text{fe}}}{J_{\text{Lamb.}} - J_{\text{dp}}} \quad (6.4)$$

For the numerator of eq. (6.4), two rigorous simulations are needed, to carry

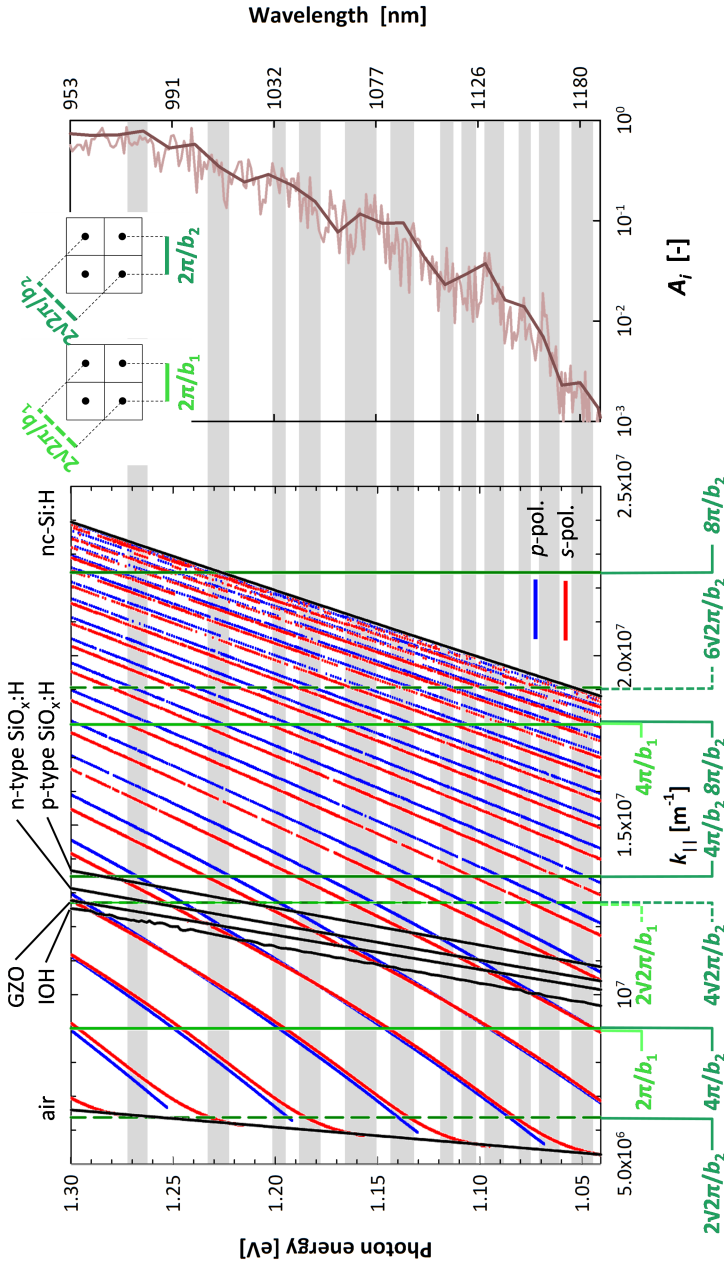


**Figure 6.16.** On the left, dispersion diagram of the best modelled device (structure #2, design IV,  $4\text{ext}$ -nm thick IOH layer). Intersections between centres of Brillouin zones (in green, and depicted in the inset) and available wave-guided modes in the absorber (blue and red lines) are correlated to peaks in the absorption spectra, presented on the right. Dark and light brown curves indicate calculated absorption in the  $i$ -layer every 10 nm and 1 nm, respectively.

out the implied photocurrent density of the  $i$ -layer in a textured solar cell and in a corresponding flat equivalent (FE) structure –  $J_{\text{ph-}i}$  and  $J_{\text{fe}}$ , respectively. As for the denominator, the implied photocurrent densities in the Lambertian scattering case ( $J_{\text{Lamb.}}$ ) and in the double-pass case ( $J_{\text{dp}}$ ) need to be calculated. Notice that  $LTE = 1$  is extremely difficult to achieve or overcome, because the reference structures (flat equivalent, Lambertian and double-pass) are computed for  $t_{\text{opt}}$ , which is always equal or larger than  $t_{\text{bulk}}$ . This results in a numerator generally smaller than the denominator, unless an advanced light trapping scheme is enforced in the textured cell.

The optical thickness of the absorber for the geometry in structure #2 is 2693.2 nm. The implied photocurrent density of the FE structure was computed to  $J_{\text{fe}} = 23.05 \text{ mAcm}^{-2}$ , while that of the double pass was calculated at  $J_{\text{dp}} = 24.72 \text{ mAcm}^{-2}$ .  $J_{\text{dp}}$  is slightly higher than  $J_{\text{fe}}$  due to the assumptions (in the double-pass case) of ideal front light in-coupling and back reflection – as well as the absence of supporting layers. The Lambertian limit evaluated at perpendicular incidence yields  $J_{\text{Green}} = 35.89 \text{ mAcm}^{-2}$ , while the performance of the best design is  $J_{\text{ph-}i} = 36.0 \text{ mAcm}^{-2}$ . Finally, an  $LTE = 1.16$  is obtained. It is worth mentioning that the outcome of an  $LTE$  greater than unity is not an anomaly. It means that the surface structure exhibits better light trapping properties than an ideal Lambertian scatterer. Further, no other work has yet been able to achieve an  $LTE > 1$ , especially for an optical system modelling a fully-functional solar cell architecture.

### 6.3.7 Angle of incidence

Solar cells are generally optimised to perform best under perpendicularly incident sunlight. However, for textured cells this may no longer be the case. In fact, incident light may be trapped inside the cell more efficiently when light impinges on a device with an angle of incidence ( $\theta_{\text{inc}}$ ) larger than  $0^\circ$ . This is mainly because lower order diffraction modes (i.e. the more energetic ones) may be trapped – instead of being reflected – at large  $\theta_{\text{inc}}$ . In fig. 6.17, the performance of the best textured solar cell is reported as function of  $\theta_{\text{inc}}$  and in terms of deviation from the Lambertian limit. The best optical result was achieved for  $\theta_{\text{inc}} = -30^\circ$ , yielding  $\Delta_{\text{Lamb.}} = 2.64\%$  and  $J_{\text{ph-}i} = 36.84 \text{ mAcm}^{-2}$ . This result indicates that it may be possible to find an optimal morphology for operation at  $\theta_{\text{inc}} > 0^\circ$ , with an absorption enhancement far greater than that obtained here. Also, it is evident that the modelled solar cell performs differently for positive and negative angles, due to the misalignment (asymmetry) between top and bottom textures.

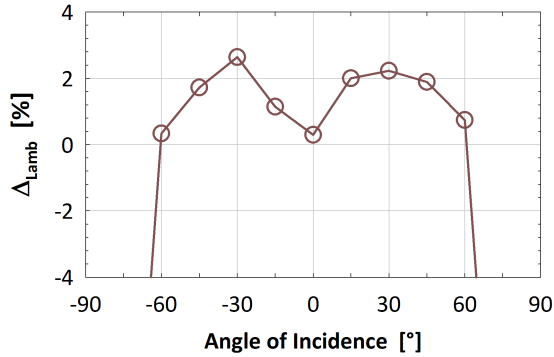


**Figure 6.17.** Relative deviation of the implied photocurrent density from the Lambertian limit case, as function of the angle of incidence of light.

Finally, it can be noted that absorption is enhanced beyond the perpendicular incidence performance for a very wide range of  $\theta_{\text{inc}}$ , up to  $\pm 60^\circ$ , consistent with the findings of Yu *et al.* [125]. This result is especially promising for PV systems that do not employ auxiliary tracking mounting and yet exhibit tracking-like high performance.

## 6.4 Conclusions

In this chapter, the potential of front and back textures with different geometries was assessed – applied to c-Si and nc-Si:H absorbers. In the first part, it was shown that texturing (low refractive index) supporting layers decreases absorption in the ultra-thin c-Si structures, with respect to the case of textures endowed directly on the active layer. This effect is mainly ascribed to the poor ability of low refractive index gratings to trap light in the absorber, since they were still able to show a very good light in-coupling behaviour (comparable to that of c-Si textures). The second part dealt with the optimisation of the front and back textures for thin-film silicon solar cells based on a nc-Si:H absorber. The careful sweep of geometrical parameters and employed materials resulted in broadband absorption beyond the Lambertian scattering limit. Such exceptional performance, maintained in a wide range of illumination angles ( $\pm 60^\circ$ ), is attributed to the excitation of wave-guided modes in the nc-Si:H layer, and the resulting light trapping efficiency  $LTE = 1.16$  is the highest reported value so far.



---

## CHAPTER 7

---

# Barium silicide solar cells with 2-D periodic textures

This chapter is based on the following publications:

**R. Vismara**, O. Isabella, and M. Zeman, "Organometallic halide perovskite / barium di-silicide thin-film double-junction solar cells," in *Proceedings of SPIE* **9898**, 9898J (2016).

and

**R. Vismara**, O. Isabella, and M. Zeman, "Back-contacted BaSi<sub>2</sub> solar cells: an optical study," *Optics Express* **25**(8), A402-A408 (2017).

*ABSTRACT* – In this chapter, the optical performance of barium (di)silicide as potential thin-film PV absorber is investigated. Results showed that this novel, but earth-abundant material could significantly outperform state-of-the-art thin-film silicon devices, with potential efficiency values up to 27% and a significant improvement of the implied photocurrent density with respect to equally-thick nano-crystalline silicon solar cells.

## 7.1 Introduction

Recent years have seen the emergence of crystalline silicon (c-Si) as the dominant technology in the photovoltaic (PV) market [21]. Thin-film approaches for terrestrial applications – e.g. CdTe, Cu(In<sub>x</sub>Ga<sub>1-x</sub>)Se<sub>2</sub> (CIGS) and thin-film silicon – have so far not been able to outperform c-Si devices [24]. For this reason, materials that are high-performing, abundant and low cost attract great attention. One of such materials is barium (di)silicide (BaSi<sub>2</sub>), which exhibits attractive optoelectrical properties, such as high absorptivity [265–271], large carrier mobility values [272–274], a quasi-direct bandgap between 1.1 eV and 1.3 eV [265–270], abundance and inexpensiveness [275]. Given its (relatively) narrow energy bandgap, barium silicide could be a good candidate as bottom absorber in multi-junction devices, eventually replacing crystalline silicon solar cells currently employed in this role – in combination with III-V semiconductors [29, 276, 277] or perovskite materials [32, 278].

In this chapter, the optical potential of BaSi<sub>2</sub> is thus assessed. After measuring and characterising the material properties, single-junction PV devices based on a  $\sim 2\text{-}\mu\text{m}$  absorber are shown to be able to achieve photocurrent density values above  $41\text{ mAcm}^{-2}$ . Then, the combination of BaSi<sub>2</sub> with an organometallic halide perovskite in a 2-terminal double junction architecture yields potential conversion efficiencies up to 28%. Both results are obtained by applying advanced light management schemes aimed at promoting: (I) broadband in-coupling of incoming radiation and (II) diffraction of red and near infrared (NIR) photons to enhance their chances of being absorbed. Finally, an alternative BaSi<sub>2</sub> solar cell structure is introduced and investigated: a back-contacted architecture, in which hole- and electron-selective contacts are alternated at the back side of the device. The optical performance of the proposed layout was studied and optimized, with the goal of maximizing absorption in the barium silicide layer. An implied photocurrent density of  $40.3\text{ mAcm}^{-2}$  is achieved for an absorber thickness of only  $1\text{ }\mu\text{m}$ , highlighting the great potential of BaSi<sub>2</sub> as novel material for photovoltaic applications.

## 7.2 Optical characterisation of epitaxially-grown barium silicide

A sample of barium silicide ( $\sim 150\text{ nm}$ -thick), epitaxially grown on a high-resistivity c-Si(111) substrate (thickness of  $500\text{ }\mu\text{m}$ , resistivity  $\rho > 1000\text{ }\Omega\text{cm}$ ) and

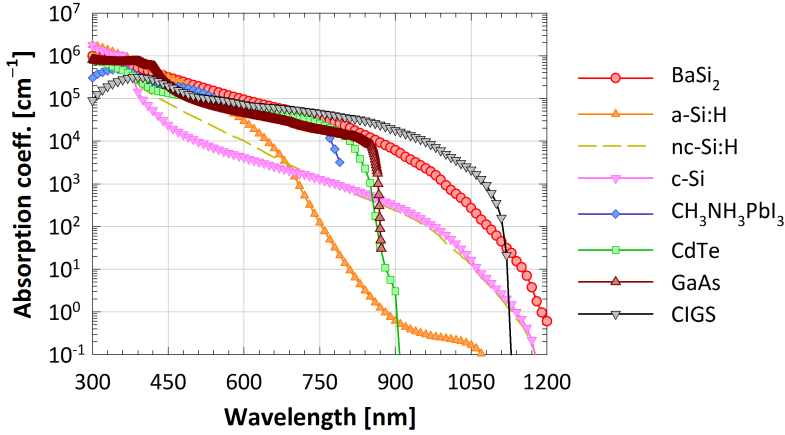


**Figure 7.1.** Absorption coefficient of  $\text{BaSi}_2$ , compared to several semiconductors used in PV: a-Si:H (internal measurements), nc-Si:H [53], c-Si [54],  $\text{CH}_3\text{NH}_3\text{PbI}_3$  [55], CdTe [56], GaAs [57], and CIGS (this work, chapter 5).

coated with an ultra-thin ( $\sim 3$  nm) amorphous silicon layer (to prevent oxidation), was characterised. SE measurements were fitted with a Cody-Lorentz oscillator, yielding a material band-gap  $E_g = 1.25$  eV. This result is well in accordance with findings previously reported [270].

By comparing SE and SP measurements with the ones previously published by Latiff et al. [269], the value of the (complex) refractive index  $\tilde{n} = n + i\kappa$  and the absorption coefficient  $\alpha$  was obtained – in the spectral range  $300 \text{ nm} < \lambda < 1200 \text{ nm}$ . Results are depicted in fig. 7.1. In particular, the absorption coefficient is compared with that of other materials used as absorbers in PV devices. It can be clearly observed that  $\text{BaSi}_2$  performs better than c-Si and hydrogenated nano-crystalline silicon (nc-Si:H) at all wavelengths (e.g. at  $E - E_g = 0.5$  eV,  $\alpha_{\text{BaSi}_2} = 4.6 \times 10^4 \text{ cm}^{-1}$ , while  $\alpha_{\text{nc-Si:H}} = 0.1 \times 10^4 \text{ cm}^{-1}$  – for  $\text{BaSi}_2$  and nc-Si:H, respectively). Absorptance in the UV and visible parts of the spectrum is similar to the one of best-performing materials employed in thin-film solar cells, such as cadmium-telluride (CdTe), CIGS and perovskite ( $\text{CH}_3\text{NH}_3\text{PbI}_3$ ). In the near-infrared region, only CIGS appears to have a slightly higher value of the absorption coefficient. This comparison shows that  $\text{BaSi}_2$  has absorption properties equal or better than the ones of other absorber materials commonly employed in solar cells. In the remaining part of this chapter, the optical performance of  $\text{BaSi}_2$  as absorber in thin-film solar cells will be investigated and compared to state-of-the-art photovoltaic technologies.



### 7.3 Single-junction barium-silicide solar cells with periodic textures

In first approximation, due to its (multi)crystalline structure, it was assumed that  $\text{BaSi}_2$  could simply replace nc-Si:H inside the structure of single- and multi-junction thin-film solar cells, without the necessity of further modifying the device configuration (i.e. supporting layers). It was hence decided to use the double front/back texture proposed in chapter 5 to compare the optical performance of  $\text{BaSi}_2$  and nc-Si:H solar cell models. The two structures are depicted in fig. 7.2 (nc-Si:H) and fig. 7.3 ( $\text{BaSi}_2$ ). At the front side, high aspect-ratio pyramidal structures with height  $h_f = 700$  nm and base  $b_f = 700$  nm were employed, while at the back shallower features were used ( $h_b = 300$  nm,  $b_b = 1200$  nm). As for the device configuration, the structure is the following (from top to bottom): a 40-nm thick highly transparent and conductive  $\text{In}_2\text{O}_3\text{:H}$  (IOH) layer [122, 123], 20-nm thick  $p$ -type nc- $\text{SiO}_x\text{:H}$ , a 2  $\mu\text{m}$ -thick absorber (either nc-Si:H or  $\text{BaSi}_2$ ), 20-nm thick  $n$ -type nc- $\text{SiO}_x\text{:H}$ , an 80-nm thick back transparent conductive oxide layer made of ZnO:Ga [121], and a 300-nm thick silver back reflector, which also acts as rear contact. The layers and thickness values used correspond or are compatible to the ones employed in state-of-the-art thin-film silicon devices with nc-Si:H absorbers [38, 39, 279].

Results of the simulations of the nc-Si:H device are presented in fig. 7.2 and were already extensively discussed in Chapter 6. In summary:

1.  $300 \text{ nm} < \lambda < 450 \text{ nm}$ : in this part of the spectrum, absorption in  $\text{In}_2\text{O}_3\text{:H}$  (green area) and  $p$ -type nc- $\text{SiO}_x\text{:H}$  (orange area) reduces the amount of light that is absorbed in the active layer (brown area).
2.  $450 \text{ nm} < \lambda < 750 \text{ nm}$ : in this region, parasitic absorption losses and total reflectance (light-yellow area) are very low, hence absorption in the nc-Si:H layer is close to unity. This effect can be ascribed to the excellent light in-coupling provided by the high aspect-ratio front texture.
3.  $750 \text{ nm} < \lambda < 1200 \text{ nm}$ : this is the portion of the spectrum in which the absorption coefficient of nc-Si:H is low. For this reason, light-trapping schemes need to be implemented to lengthen the path of light inside the solar cell. The shallow pyramids at the back side can efficiently scatter light into discrete angles, exciting a series of resonant modes available in the thin slab of nc-Si:H and enhancing absorption beyond the Lambertian scattering limit.

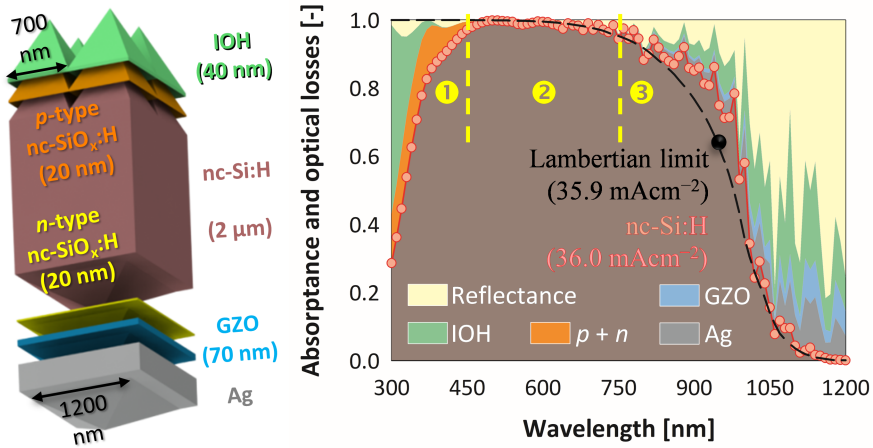


**Figure 7.2.** Model of the nc-Si:H single-junction solar cell (left) and absorption in each layer of the structure (right). Zones (1), (2) and (3) indicate areas where absorption in the active layer is mainly determined by: (1) parasitic absorption in top layers, (2) anti-reflection properties of the front texture, and (3) light-trapping properties of the entire structure.

For barium silicide, results of simulations can be found in fig. 7.3. As in the case of nc-Si:H, results can be better analysed by dividing the spectrum in three separate regions:

1.  $300\text{ nm} < \lambda < 450\text{ nm}$ : once again the presence of IOH and p-doped SiOX:H limits the device optical performance in this part of the spectrum. Architectures with nc-Si:H and BaSi<sub>2</sub> thus show similar values of absorption.
2.  $450\text{ nm} < \lambda < 950\text{ nm}$ : this is the spectral region where there are hardly any losses, hence absorption in BaSi<sub>2</sub> is close to 1. When compared to the result of the nc-Si:H model, it is possible to observe that this very high optical performance is achieved in a wider portion of the spectrum: up to  $\lambda = 950\text{ nm}$  for BaSi<sub>2</sub>, while only until  $\lambda = 750\text{ nm}$  for nc-Si:H. This effect can be ascribed to the higher absorption coefficient of barium silicide with respect to that of nc-Si:H in the region  $750\text{ nm} < \lambda < 950\text{ nm}$ , hence the good in-coupling provided by the front pyramids is sufficient to ensure that photons with wavelength up to 950 nm are effectively absorbed.
3.  $950\text{ nm} < \lambda < 1200\text{ nm}$ : in this region, the absorption coefficient of BaSi<sub>2</sub> is

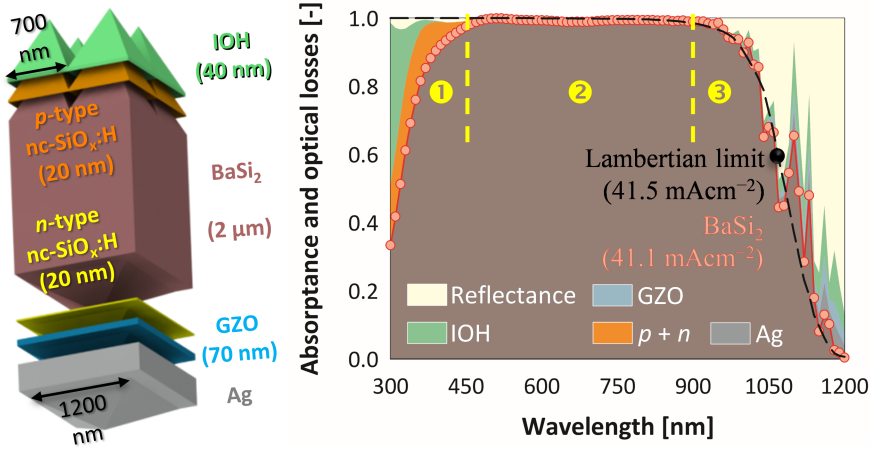


**Figure 7.3.** Barium silicide single-junction solar cell model (left) and absorption in each layer of the structure (right). As in fig. 7.2, zones (1), (2) and (3) indicate regions in which the active layer absorption is mainly determined by: (1) parasitic absorption in supporting layers, (2) anti-reflection properties of the front texture, and (3) light-trapping properties of the entire structure.

becomes low. Hence, photons can escape the device and light-trapping becomes of paramount importance. As observed for nc-Si:H, at some wavelengths absorption in the BaSi<sub>2</sub> layer can exceed the Lambertian scattering limit, owing to diffraction and coupling into (guided) modes – promoted by the periodic grating at the back side of the device. However, the enhancement is less pronounced than in the nc-Si:H case, as shown by the calculated implied photocurrent densities of the simulated model (41.1 mAcm<sup>-2</sup>) and of the Lambertian limit (41.5 mAcm<sup>-2</sup>). The reasons for this behaviour lay in the properties of nc-Si:H and BaSi<sub>2</sub>. Barium (di)silicide exhibits an absorption coefficient which is significantly higher than the one of silicon (at  $\lambda = 1100$  nm,  $\alpha_{\text{BaSi}_2} = 0.6 \times 10^2 \text{ cm}^{-1}$  while  $\alpha_{\text{nc-Si:H}} = 0.3 \times 10^1 \text{ cm}^{-1}$ ). Since the  $4n^2$  absorption enhancement limit is valid for weakly absorptive materials, it is relatively easier to improve the performance of material with low absorption coefficient (e.g. nc-Si:H) than the performance of better absorbers (like BaSi<sub>2</sub>).

These two comparative simulations showed that the architecture with a 2-μm thick BaSi<sub>2</sub> absorber performs significantly better than an equally-thick device based on nc-Si:H ( $\Delta J_{\text{ph}} = +5.1 \text{ mAcm}^{-2}$ , +14%). In fig. 7.4, the simulated opti-

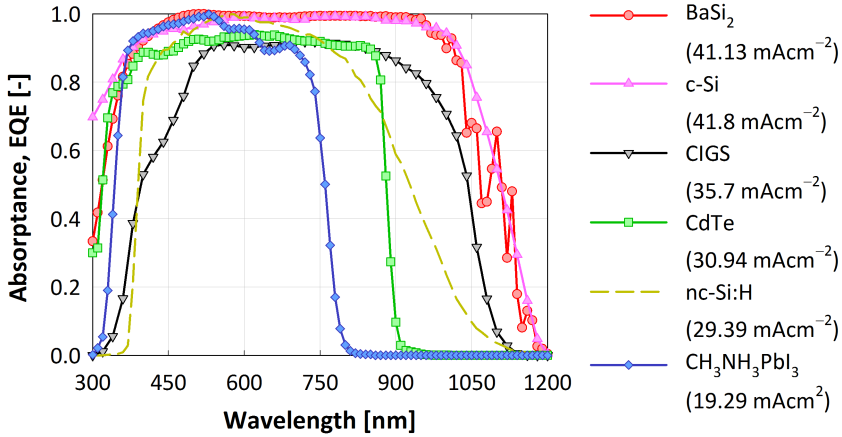


**Figure 7.4.** Calculated absorption in 2- $\mu\text{m}$  thick single-junction BaSi<sub>2</sub> solar cell (red line), compared to external quantum efficiency measurements of state-of-the-art devices: c-Si [280], CIGS [281], CdTe [282], nc-Si:H [281], and CH<sub>3</sub>NH<sub>3</sub>PbI<sub>3</sub> [283].

cal performance of the BaSi<sub>2</sub>-based solar cell is compared with the external quantum efficiencies (EQEs) of state-of-the-art (world record) PV technologies. It can be observed that only c-Si, which employs a much thicker absorber layer, can achieve similar values of photocurrent. All other (thin-film) technologies could potentially be outperformed, provided that charge-collection issues in manufactured BaSi<sub>2</sub> devices will not significantly hinder its efficiency.

## 7.4 Perovskite/barium silicide thin-film double junction solar cells

To test the ultimate potential of barium silicide, a  $< 2\text{-}\mu\text{m}$  thick monolithic double junction solar cell was simulated. The bottom device is based on the single junction BaSi<sub>2</sub> structure depicted in fig. 7.3. The top cell thin layers are then assumed to conformally coat the bottom device. The structure of the thin-film tandem architecture was thus conceived as follows (from illuminated side, see fig. 7.5): IOH (80 nm) / Spiro-OMeTAD (100 nm, hole-transport layer) / CH<sub>3</sub>NH<sub>3</sub>PbI<sub>3</sub> (methylammonium lead iodine or MAPI, 350 nm, top absorber) / TiO<sub>2</sub> (10 nm, electron-transport layer) / ZnO:Ga (60 nm, intermediate reflector/contact) / p-type poly-Si (20 nm) / BaSi<sub>2</sub> (1000 nm) / n-type poly-Si (20 nm) / ZnO:Ga (70 nm) / Ag (300 nm). This model is realistic in structure, deployed materials, thickness of the layers, and thermal budget – provided that the bottom cell is

**Table 7.1.** One-diode parameters of single-junction top and bottom component cells.  $J_0$  is the dark current,  $R_s$  the series resistance and  $R_p$  the shunt (parallel) resistance.

Cell	$\text{CH}_3\text{NH}_3\text{PbI}_3$	$\text{BaSi}_2$
$J_{\text{ph}}$ [ $\text{mAcm}^{-2}$ ]	19.84	18.81
$J_0$ [ $\text{mAcm}^{-2}$ ]	$3 \times 10^{-10}$	$1.4 - 24 \times 10^{-14}$
<b>Ideality factor</b>	2.2	1.2
$R_s$ [ $\Omega\text{cm}^2$ ]	0.48	0.05
$R_p$ [ $\Omega\text{cm}^2$ ]	8900	884000

deposited first. In fact, the structure of the top perovskite junction is similar to the one of a monolithic tandem  $\text{CH}_3\text{NH}_3\text{PbI}_3/\text{c-Si}$  solar cell architecture devised by Werner et al. [284], but without the implementation of a  $\text{MoO}_x$  buffer layer.

Regarding the bottom cell, two modifications with respect to the single junction  $\text{BaSi}_2$  architecture were introduced:

1. The thickness of the  $\text{BaSi}_2$  absorber was reduced from 2000 nm to 1000 nm. Preliminary simulations (not included here) showed that the thinner device could deliver  $J_{\text{ph,BaSi}_2} = 40.5 \text{ mAcm}^{-2}$  in single-junction configuration. This represents a reduction of photocurrent density of only  $\Delta J_{\text{ph,BaSi}_2} = 0.6 \text{ mAcm}^{-2}$  ( $-1.5\%$ ) with respect to the thicker architecture (2000 nm), despite a 50% decrease of active material utilization.
2. The p- and n-type  $\text{nc-SiO}_x\text{:H}$  layers in the bottom cell were substituted with equally-thick doped poly-Si layers. Having decided for a substrate configuration (i.e. the bottom cell manufactured first, then the top junction is deposited), such substitution is necessary due to the high temperature step that  $\text{TiO}_2$  layers typically undergo to achieve a good electrical behaviour. In this respect, doped poly-Si layers are stable at temperatures  $> 400^\circ\text{C}$ .

Simulation results (fig. 7.5) show a slightly bottom-limited implied photo-current density ( $J_{\text{ph,MAPI}} = 19.84 \text{ mA/cm}^{-2}$ ,  $J_{\text{ph,BaSi}_2} = 18.81 \text{ mA/cm}^{-2}$ ), which is not necessarily detrimental given the possible degradation of the top cell in real conditions. The summed implied photocurrent density ( $J_{\text{ph,SUM}} = 38.65 \text{ mA/cm}^{-2}$ ) is lower than the aforementioned  $J_{\text{ph,BaSi}_2}$  of the 1- $\mu\text{m}$  thick  $\text{BaSi}_2$  single-junction. This result can be ascribed to the presence of more supporting layers which exhibit parasitic absorptance, particularly Spiro-OMeTAD.

Considering state-of-the-art electrical properties for the perovskite top junction [285], and assuming for the  $\text{BaSi}_2$  bottom cell properties close to those of c-Si

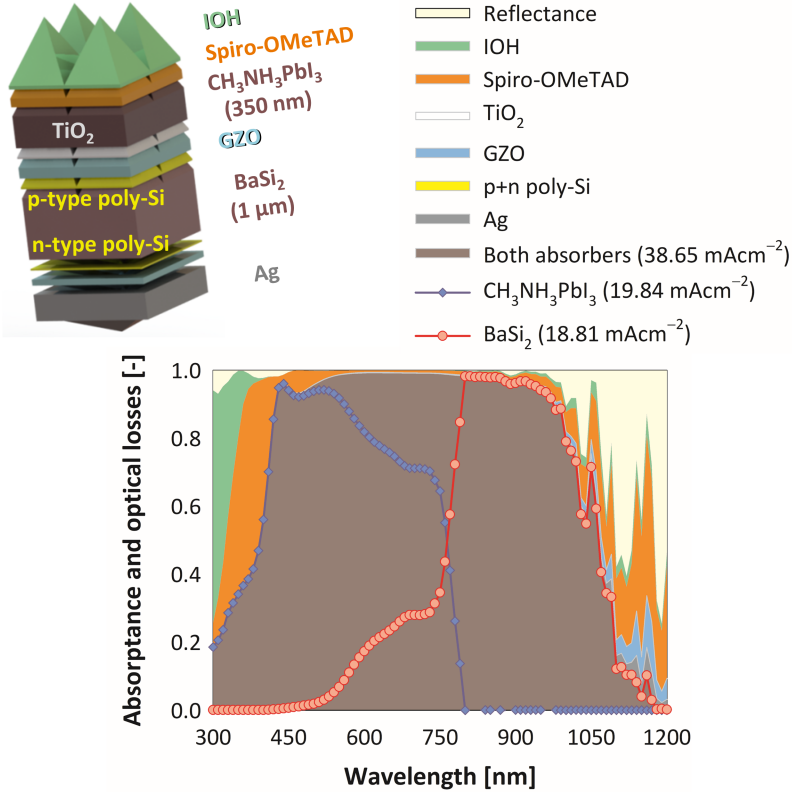


**Figure 7.5.** Model of the MAPI/ $\text{BaSi}_2$  tandem device (top) and calculated absorption in each layer of the structure (bottom).

solar cells (see table 7.1), it is possible to predict – using a simple 1-diode model – conversion efficiencies between of 25.9% and 27.2%. Such high conversion would represent a marked improvement over thin-film silicon devices and is close to current record efficiencies of perovskite on c-Si tandem solar cells, which consist of significantly thicker ( $\times 100$ ) architectures [32, 278].

## 7.5 Back-contacted barium-silicide architectures for 4-terminal devices

In the previous section, a  $\text{BaSi}_2$  solar cell architecture suitable for single-junction and 2T tandem devices was proposed and characterised. Such structure, how-

ever, relies on the concept of double-side texturing, posing severe manufacturing challenges in real devices – due to the presence of very tall and steep features. In addition, texturing of BaSi<sub>2</sub> layers has not yet been reported in literature. A back-contacted BaSi<sub>2</sub> solar cell represents an alternative to the architecture previously proposed. The presence of both hole- and electron-selective contacts at the back side of the device makes this configuration suitable for 4 terminal (4T) devices and allows for complex texturing of the front side (where no contacts are located). In this contribution, only the BaSi<sub>2</sub> bottom junction is investigated. Possible top-junction solar cells include – among others – amorphous Si and perovskite materials, which thanks to their higher bandgap energy could reduce thermalisation losses (with respect to the single-absorber BaSi<sub>2</sub> solar cell).

A 3D model of the proposed back-contacted BaSi<sub>2</sub> solar cell is depicted in fig. 7.6 (top). At the front side, a series of pyramids with base and height  $b = h = 750$  nm is included. This periodic texture reduces, front reflectance, while at the same time scattering light into discrete angles, promoting the excitation of guided modes in the BaSi<sub>2</sub> layer, thus increasing its absorption. Pyramids are coated with two thin (5 nm each) layers of a-Si:H and AlO<sub>x</sub>, to guarantee passivation of the top surface [286–288]. At the back side, fingers of *p*- and *n*-doped SiO<sub>x</sub> are alternated and contacted with silver, to create hole- and electron-selective contacts, respectively. Such doped materials are chosen for their relatively large bandgap ( $E_g \sim 2$  eV), ensuring transparency at long wavelengths [258, 289], and for their good thermal stability. The gaps between metallic strips are covered with a distributed Bragg reflector (DBR), significantly reducing transmittance losses which would otherwise take place. The DBR consists of 6 alternating pairs of a-Si:H (69 nm) and silicon nitride (SiN<sub>x</sub>, 146 nm), making the structure highly reflective around a wavelength  $\lambda_{\text{Bragg}} = 1000$  nm. A 100-nm thick SiO<sub>2</sub> spacer was positioned between absorber and DBR, to improve the reflectance of the back side [234, 256]. The thickness of the BaSi<sub>2</sub> layer was fixed to 1  $\mu\text{m}$ , which has demonstrated sufficient to achieve  $J_{\text{ph,BaSi}_2}$  values above 40  $\text{mAcm}^{-2}$ , when endowed with a double front/back periodic texture.

### 7.5.1 Design and optimisation of the back contact

The structure was optimised to achieve the best optical performance (i.e. maximise  $J_{\text{ph,BaSi}_2}$ ). The position (i), size (ii) and distance (iii) between hole- and electron-selective contacts were investigated. (i) Two positions of the doped SiO<sub>x</sub> layers are possible: one where the fingers are within the absorber (IN), the other where they are simply deposited on top of BaSi<sub>2</sub> layer (OUT). Results (see

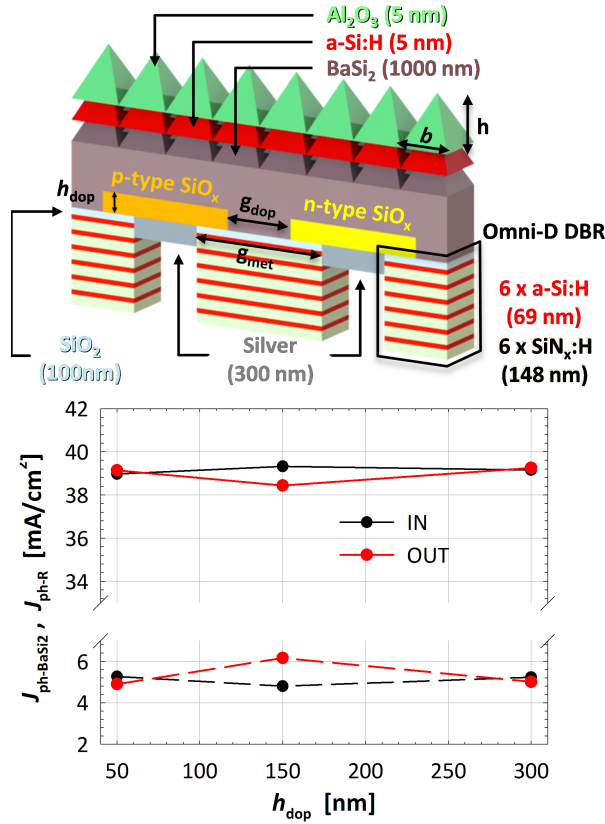
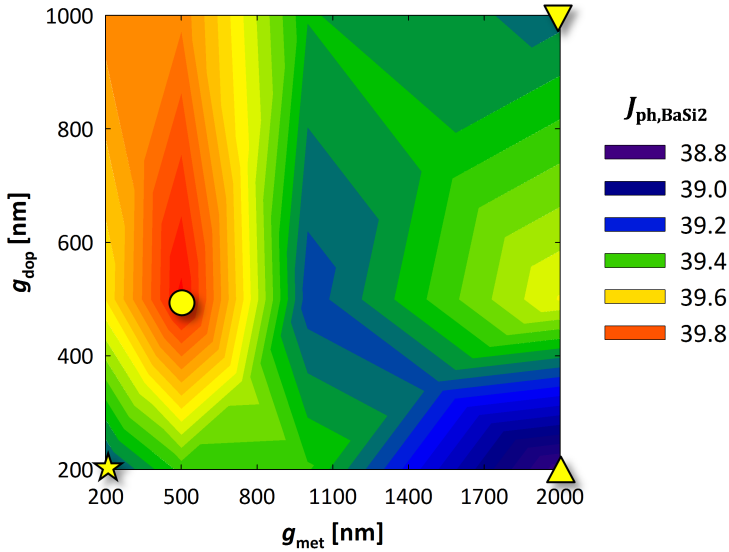


**Figure 7.6.** (Top) 3-D sketch of the back-contacted  $\text{BaSi}_2$  solar cell model. (Bottom) Implied photocurrent density generated in the absorber ( $J_{\text{ph,BaSi}_2}$ ) and lost due to reflection ( $J_{\text{ph,R}}$ ), for different values of doping layers height ( $h_{\text{dop}}$ ).

fig. 7.6b) show that there is almost no difference between IN and OUT architectures. (ii) The thickness of the doped layers ( $h_{\text{dop}}$ ) was varied between 50 nm and 300 nm, for both IN and OUT configurations.  $h_{\text{dop}}$  also appears to have little effect on the device optical performance, with all models yielding similar values of  $J_{\text{ph,BaSi}_2}$ . IN configuration with  $h_{\text{dop}} = 150$  nm could achieve a slightly higher performance than the alternatives ( $J_{\text{ph,BaSi}_2} = 39.2 \text{ mAcm}^{-2}$ ) and was thus selected. (iii) The distance between doping layers ( $g_{\text{dop}}$ ) and silver fingers ( $g_{\text{met}}$ ) can also have an impact of the model performance. In this respect,  $g_{\text{dop}}$  was changed between 200 nm and 1000 nm, while  $g_{\text{met}}$  between 200 nm and 2000 nm. Results, presented in fig. 7.7, show that smaller values of  $g_{\text{met}}$  (larger metal area)





Marker	★	▲	●	▼
BaSi <sub>2</sub> [mA/cm <sup>2</sup> ]	39.27	38.8	<b>39.89</b>	39.27
Ag [mA/cm <sup>2</sup> ]	0.62	0.28	0.59	0.31
R [mA/cm <sup>2</sup> ]	5.04	5.61	4.23	5.16
T [mA/cm <sup>2</sup> ]	0.30	0.44	0.48	0.49
Total losses [mA/cm <sup>2</sup> ]	5.96	6.29	<b>5.30</b>	5.96

**Figure 7.7.** (Top)  $J_{ph,BaSi2}$  for different values of distance between doped fingers ( $g_{dop}$ ) and between metal contacts  $g_{met}$ . (Bottom) Breakdown of the implied photocurrent density absorbed (BaSi<sub>2</sub>) and lost in silver (Ag), due to reflectance ( $R$ ) or transmittance ( $T$ ), for values of  $g_{met}$  and  $g_{dop}$ .

result in larger parasitic losses in the silver contacts. On the other hand, larger gaps between metallic fingers increase transmittance losses. Ultimately, an optimum is found for  $g_{dop} = g_{met} = 500$  nm, for which the sum of parasitic losses in the metallic back contact and transmittance losses through the DBR is minimised. An implied photocurrent density value of  $39.9 \text{ mAcm}^{-2}$  is achieved.

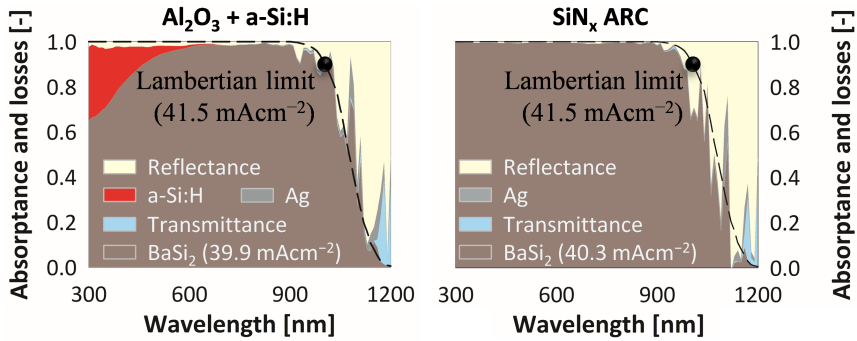


**Figure 7.8.** Absorbance in  $\text{BaSi}_2$  and optical losses for an architecture with  $\text{Al}_2\text{O}_3$  + a-Si:H passivation (left) and with a 40 nm-thick  $\text{SiN}_x$  antri-reflection coating (ARC, right).

### 7.5.2 Optimisation of the anti-reflection front texture

In fig. 7.8 on the left, reflection and absorption in each layer of the structure optimised in the previous subsection are shown. It can be observed that: (i) light in-coupling is not ideal, since reflectance is significant even in the region where  $\text{BaSi}_2$  is a strong absorber ( $300 \text{ nm} < \lambda < 900 \text{ nm}$ ); (ii) The passivating a-Si:H layer parasitically absorbs a substantial amount of light in the short wavelength part of the spectrum ( $300 \text{ nm} < \lambda < 600 \text{ nm}$ ). Light in-coupling can be improved by using taller and steeper pyramids at the front side, while parasitic absorption of passivating layers can be reduced by employing more transparent materials. Thus, a new pyramidal structure was modelled, keeping the same base ( $b = 750 \text{ nm}$ ) while increasing the height ( $h$  from  $750 \text{ nm}$  to  $875 \text{ nm}$ ). The grating was coated with a 40-nm thick  $\text{SiN}_x$  layer, in place of a-Si:H. Result, depicted in fig. 7.8 on the right, show that reflectance and parasitic absorption at the front side are significantly reduced. The  $J_{\text{ph},\text{BaSi}_2}$  of the new structure increases by  $0.4 \text{ mAcm}^{-2}$  to  $40.3 \text{ mAcm}^{-2}$ , a value very close to the best front/back contacted  $1\text{-}\mu\text{m}$  thick structure modelled in section 6.2.

## 7.6 Conclusions

In this chapter, a study of the (optical) potential of barium silicide as absorber for thin-film solar cell applications was carried out. First, the characterisation of the material optical properties showed that  $\text{BaSi}_2$  has an absorption coefficient comparable or higher than commonly used PV absorbers. Simulations of single-junction devices embedded with an optimised double front/back tex-

ture resulted in implied photocurrent values significantly higher than equivalent structures based on a nc-Si:H active layer – owing to the higher absorptivity of BaSi<sub>2</sub>. Finally, possible double-junction architectures based on barium silicide bottom solar cells were investigated. While a < 2μm monolithically-integrated MAPI/BaSi<sub>2</sub> architecture has the potential to achieve efficiencies up to 28%, a back-contacted BaSi<sub>2</sub> device for 4-terminal tandem solar cells could be a better option to manufacture a high-performing working device. Further investigation of the material is necessary, though, to assess its true potential in real (manufactured) solar cells.

## Conclusions and Outlook

The target of this thesis was to investigate and optimise light management approaches applied to different thin-film technologies, and through this analysis provide guidelines for the design of photovoltaic devices and insight into their optical performance. In this chapter, all achieved results are summarised and an outlook on future developments based on those achievements is presented.

### 8.1 Conclusions

In this work, a wide variety of light management approaches was studied, applied to a range of thin-film photovoltaic materials. Across the different cases, some clearly observable trends were found:

- The maximisation of absorption relies on high-quality light in-coupling and trapping. To achieve both, the most effective approach requires a separate optimisation of the front and back sides of the device – making double front/back textures with different geometries an optimal solution.
- The superposition of two or more periodic structures is very effective at achieving broadband light trapping, while single-period gratings can only provide a significant absorption enhancement in narrow regions of the spectrum.
- When materials with higher absorption coefficients are employed, light in-coupling and reduction of parasitic absorption become more critical than light trapping. This is the case of semiconductors such as CIGS and – to a lesser extent – barium silicide, owing to their direct (or quasi-direct) bandgap.

Starting with **chapter 3**, nanowire arrays were shown to have the potential to improve the optical performance of thin-film nano-crystalline silicon solar cells. The feasibility of their cost-effective manufacturing was first demonstrated by

realising a working, wafer-based device. Then, the investigation of the light-nanowire interaction showed the arise of several resonances within the thin absorber layer. These are responsible for a significant enhancement of absorption, which is upheld in a wide range of angles of incidence.

In **chapter 4**, the discussion of how amorphous silicon nanoantennas can be adapted as solar harvesters was carried out. A novel solar cell structure was presented, employing an all-dielectric silicon metasurface as active layer. The nanodisks composing the metasurface achieve near-perfect absorption at specific wavelengths, which can be tuned by changing the system parameters. Good broadband enhancement of the optical performance was demonstrated, in what is one of the first attempts in adapting sensor technology for solar harvesting applications.

In **chapter 5**, modelling of CIGS solar cells was carried out. First, a satisfactory optical model of a real device was presented, ensuring the accuracy of the selected modelling approach. Then, gratings were applied to the solar cell models and optimised, leading to a significant improvement of the optical performance – owing mostly to anti-reflection effects. The observation of high parasitic absorption losses in the front TCO and in the back contact layers prompted the study of alternative layers configurations. The removal of molybdenum at the rear and substitution of zinc-oxide with indium-oxide at the front resulted in a substantial enhancement of absorption, which was mostly maintained even when the thickness of CIGS was reduced by more than 50%.

In **chapter 6**, the potential of double front and back textures with different geometries was assessed – applied to c-Si and nc-Si:H absorbers. First, it was shown that endowing textures directly on the active layer is preferable to manufacturing gratings on supporting layers, due to the lower refractive index of the latter. Then, a study of the double front/back texture for thin-film nanocrystalline silicon solar cells was carried out. The careful optimisation of geometrical parameters and materials resulted in broadband absorption enhancement beyond the Lambertian scattering limit – for a wide range of illumination angles.

Finally, in **chapter 7** a study of the optical potential of barium silicide for solar cell applications was carried out. The material optical properties were first characterised, showing that  $\text{BaSi}_2$  has an absorption coefficient comparable or higher than commonly used PV absorbers. Simulations of textured single-junction devices resulted in absorption values significantly higher than equivalent structures based on silicon. Finally, possible double-junction architectures based on

barium silicide bottom solar cells were investigated – showing great potential for the integration of this novel material in thin-film devices.

## 8.2 Outlook

The largest part of the work carried out in this thesis relies on optical modelling of lab-scale solar cells. Hence, the optimised geometry and performance found are specific to those devices. Therefore, the integration of any of the proposed light management approaches in industrial architectures (i.e. PV modules) needs to take into account the differences between solar cell and module structures (e.g. encapsulation). Moreover, the feasibility of some of the proposed approaches needs to be verified with experimental studies. In particular:

- The applicability of nanowire manufacturing through a mask-less reactive ion etching process to thin nano-crystalline absorbers needs to be checked. Alternatively, a different process can be devised to promote the growth of such elongated nanostructures. Moreover, nanowire passivation must improve to make such devices competitive against more traditional textures.
- While the performance of silicon metasurfaces was experimentally verified, their inclusion into fully-fledged devices needs to be tested, with a particular attention to carrier collection and passivation.
- For CIGS devices, the success of substituting currently-employed materials with more transparent (at the front) or reflective ones (at the back) is subject to their compatibility with the deposition process of the absorber.
- The feasibility of applying double front and back textures to thin-film silicon absorbers could prove to be challenging and will need to be investigated. Nevertheless, this concept could find application in wafer-based technology – where it could be implemented more easily be.
- With respect to barium silicide, the analysis provided in this work is mostly concerned on the optical performance. Before the material can become a successful alternative to silicon and other thin-film materials, more research needs to be carried out. Two particularly critical aspects will be the stability of material during and after processing, and the development of a cheap, high-quality deposition method to replace slow and expensive epitaxial growth of layers.



---

## APPENDIX A

---

# Refractive index data

In this appendix, all (complex) refractive index data used in every result chapter is presented. These properties constituted – together with the device geometry – the input of all simulations carried out in the work of this thesis. Data was taken from internal measurements, except for the following materials:

- Cadmium sulfide (CdS), data from [193].
- Gallium-doped zinc oxide (ZnO:Ga, GZO), data from [121].
- Hydrogenated indium oxide ( $\text{In}_2\text{O}_3\text{:H}$ , IOH), data from [122].
- Indium tin oxide ( $\text{In}_2\text{O}_3\text{:H}$ , ITO), data from [121].



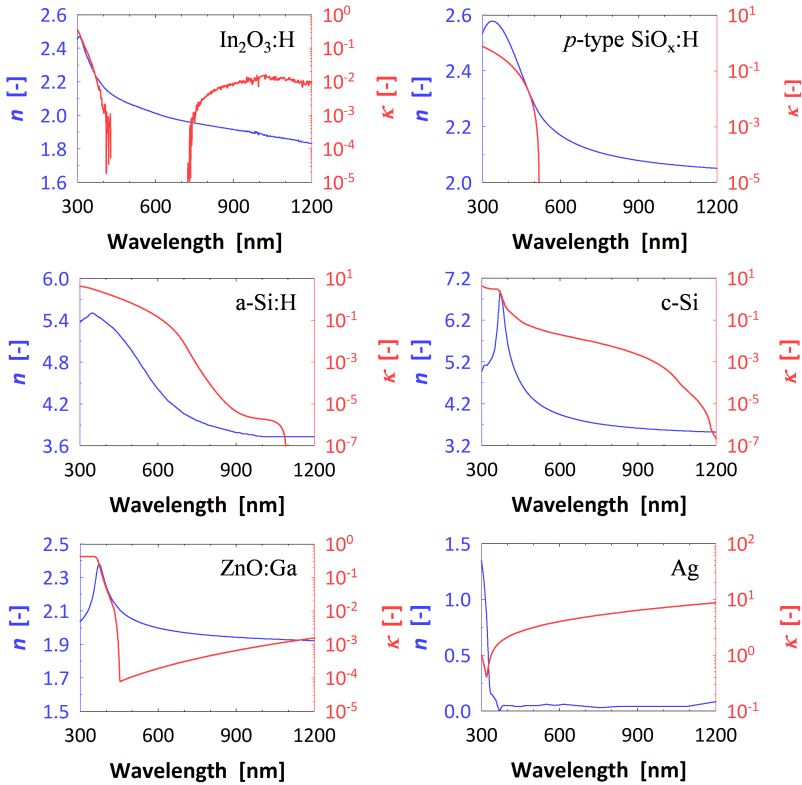


**Figure A.1.** Complex refractive index of all materials used in the simulations of chapter 3 (c-Si HT) nanowire solar cells), as function of the wavelength of light *in vacuo*.

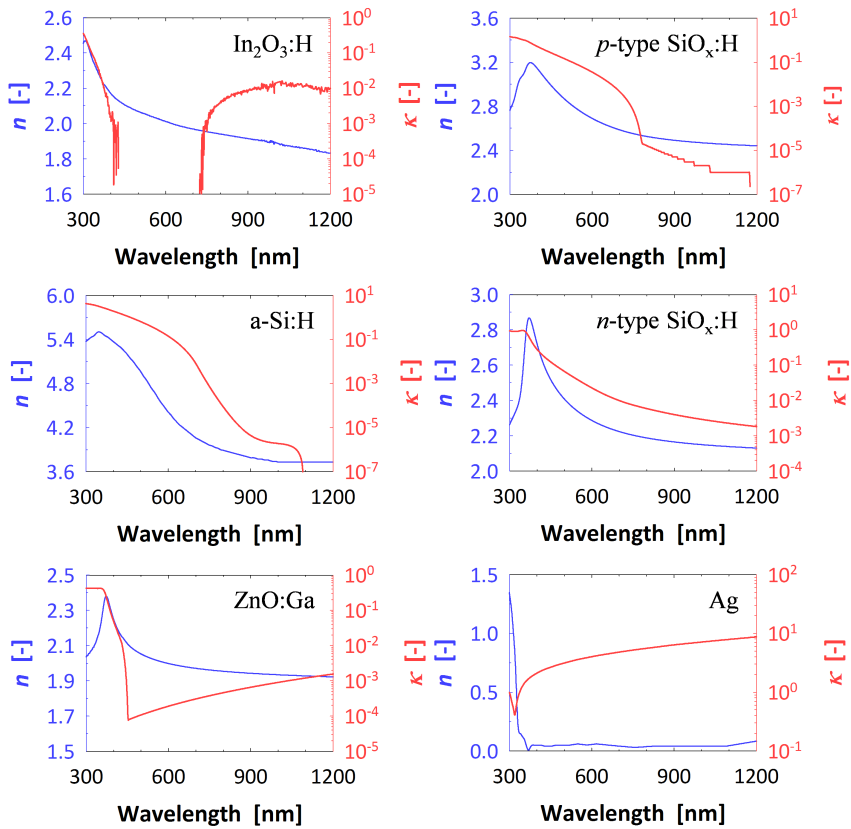


**Figure A.2.** Complex refractive index of all materials used in the simulations of chapter 4 (a-Si:H metasurfaces), as function of the wavelength of light *in vacuo*.

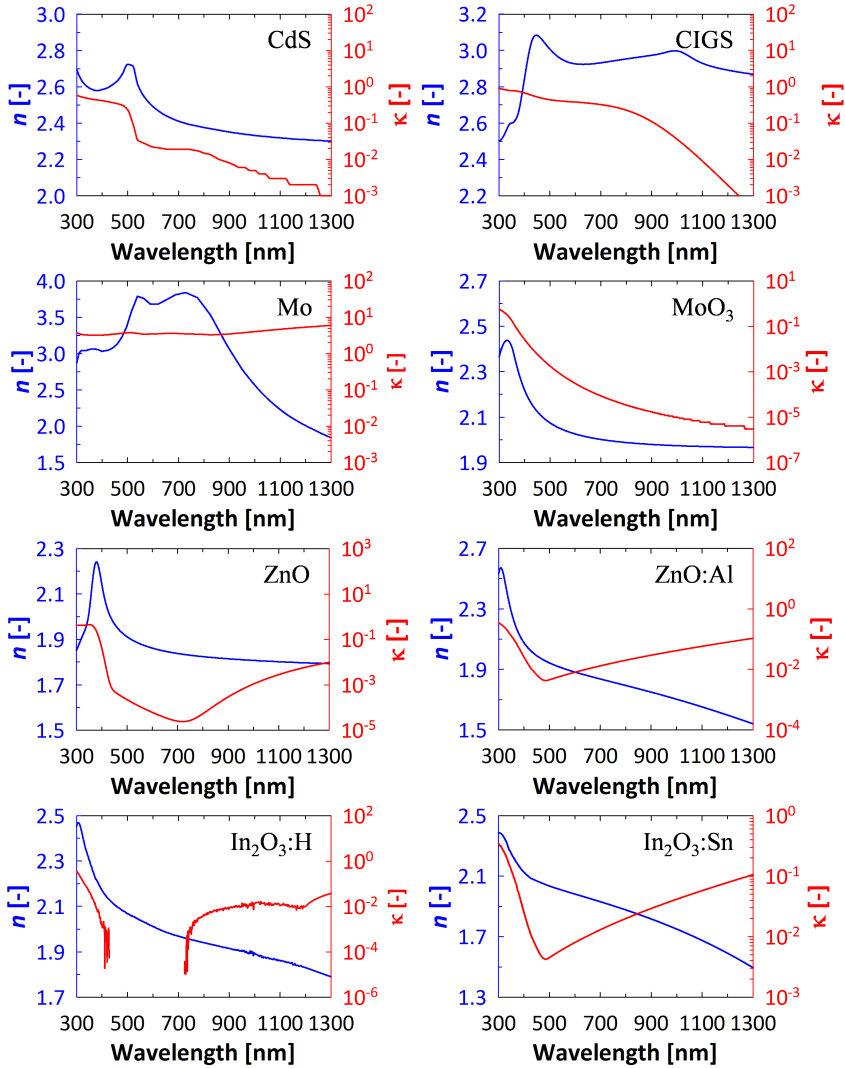


**Figure A.3.** Complex refractive index of all materials used in the simulations of chapter 5 (CIGS), as function of the wavelength of light *in vacuo*.

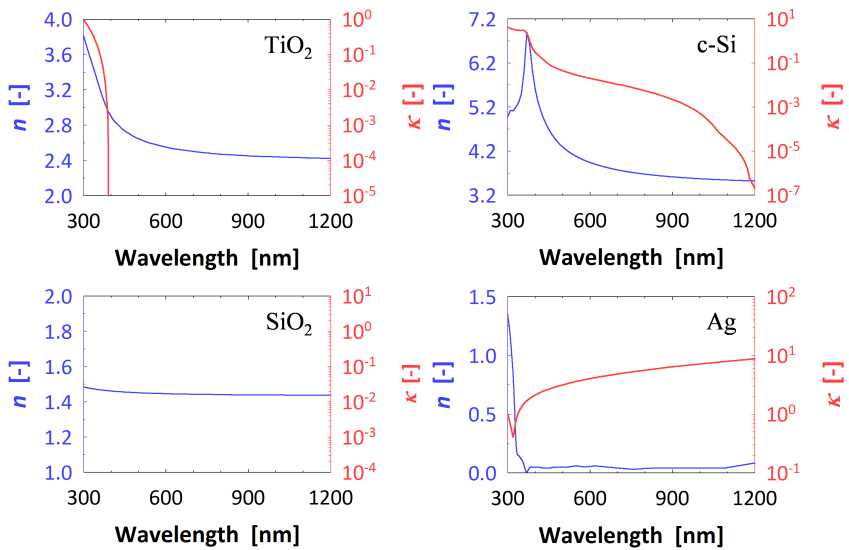


**Figure A.4.** Complex refractive index of all materials used in the simulations of chapter 6 (c-Si decouple-textured slabs), as function of the wavelength of light *in vacuo*.

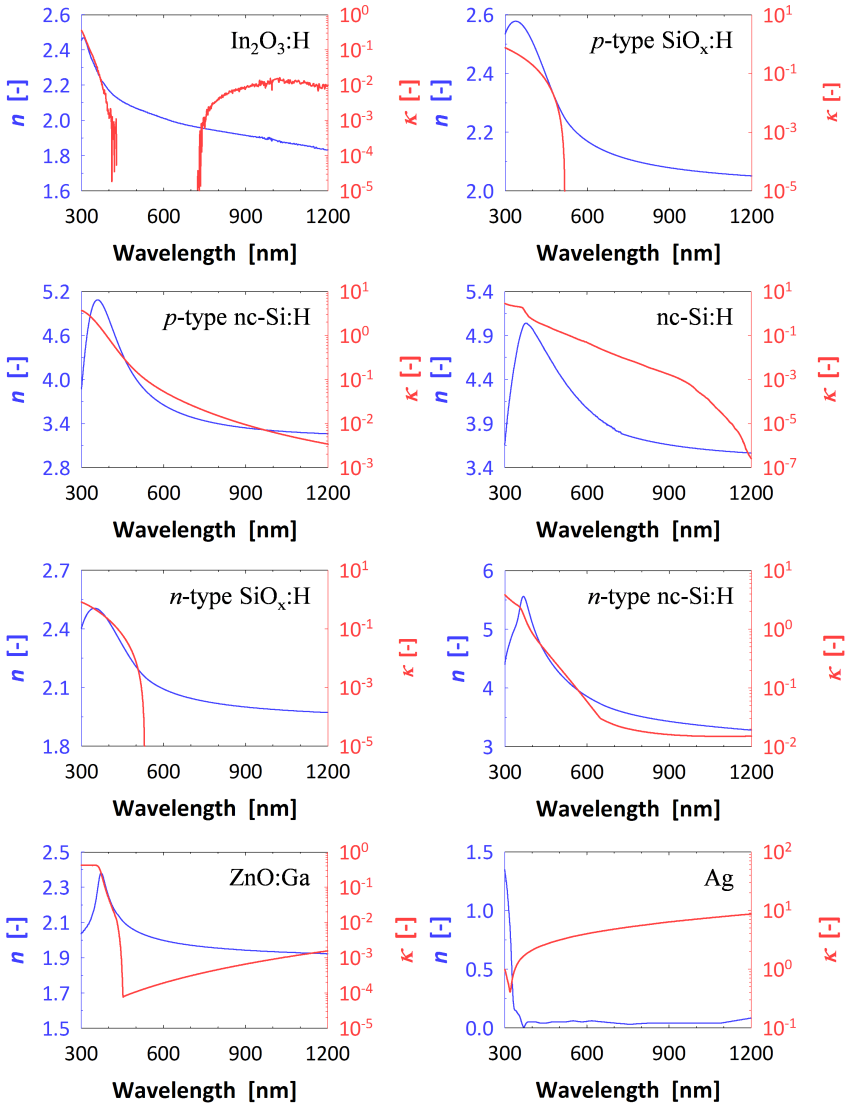


**Figure A.5.** Complex refractive index of all materials used in the simulations of chapter 6 (nc-Si:H decouple-textured solar cells), as function of the wavelength of light *in vacuo*.

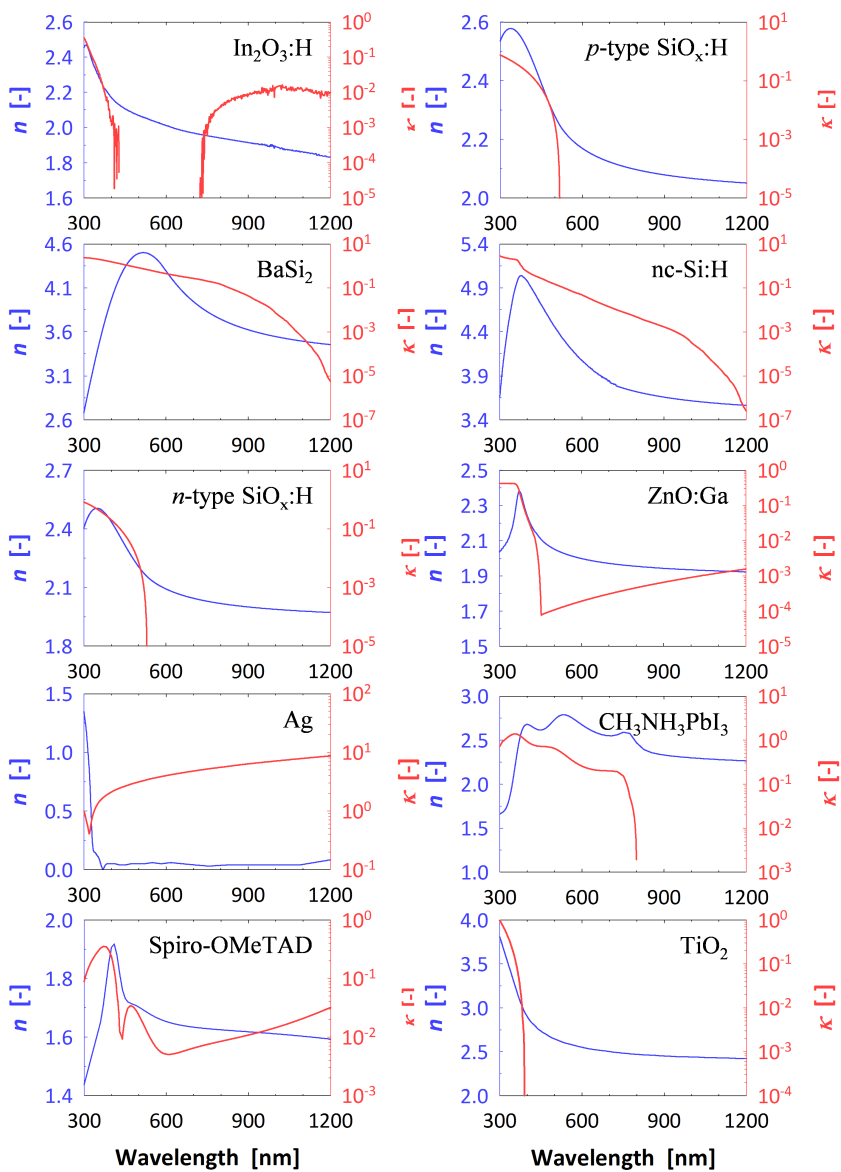


**Figure A.6.** Complex refractive index of all materials used in the simulations of chapter 7 (nc-Si:H and BaSi<sub>2</sub> devices), as function of the wavelength of light *in vacuo*.



## Absorption limit for periodic gratings

This chapter discusses the definition of absorption limits for dielectric slabs endowed with periodic gratings. Due to the discrete nature of light-matter interaction in the case of periodic structures, the calculate maximum absorption will depend on the dimension and size of the gratings, thus losing the generality intrinsic to the Lambertian scattering limit discussed in chapter 1. Nevertheless, the calculation presented here are useful in both analysis and design of light management approaches for photovoltaic applications, giving useful indications on how to select and manufacture the best possible structure for different applications. The content on this chapter is largely based on and expands upon the work of Yu *et al.* [125, 126].

### The temporal coupled mode theory

The calculation of the absorption limit for dielectric layers endowed with periodic gratings starts from the temporal coupled theory [290], which states that the amplitude ( $a$ ) of a resonance\* – normalised to the amplitude of the incident wave  $S$  – is described by this equation:

$$\frac{d}{dt}a = \left( j\omega_0 - \frac{N\gamma_e + \gamma_i}{2} \right) a + j\sqrt{\gamma_e}S \quad (\text{B.1})$$

where  $j = \sqrt{-1}$ ,  $\omega_0$  the resonant frequency,  $N$  the number of *leakage* channels,  $\gamma_e$  is the leakage rate, and  $\gamma_i$  the intrinsic loss rate of the resonance (i.e. the decay rate due to absorption).  $\gamma_i$  is an intrinsic material property, which can be calculated as follows:  $\gamma_i = \alpha \cdot c/n$  where  $\alpha$  and  $n$  are the absorption coefficient and refractive index of the material, respectively, and  $c$  is the speed of light *in vacuo*. The number of leakage channels  $N$  can be understood as the number of allowed directions of propagation for light that escapes the dielectric slab, which depends on the size and dimension of a grating. Assuming that the leakage

---

\*For the purpose of this work, the term resonance is used as a synonym of guided mode.



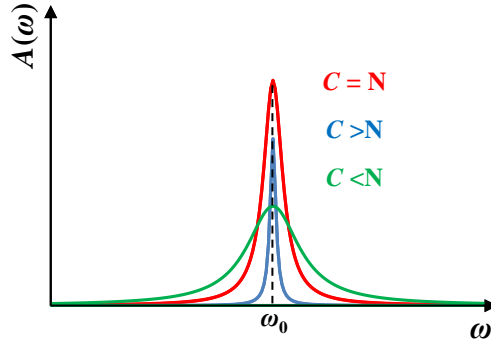


**Figure B.1.** Absorption profile of a resonance in different coupling conditions.

rate  $\gamma_e$  is equal for each of the  $N$  channels, absorption of the resonance can be calculated with this equation:

$$A(\omega) = \frac{4\gamma_i\gamma_e}{4(\omega - \omega_0)^2 + (\gamma_i + N\gamma_e)^2} \quad (\text{B.2})$$

The typical profile of absorption as function of the frequency  $\omega$  is depicted in fig. B.1.

The integral of eq. (B.2) represents the *spectral cross-section* of the resonance, indicated with  $\sigma$ . Under the assumption that the bandwidth of incident light ( $\Delta\omega$ ) is much larger than  $\sigma$ ,  $\sigma/\Delta\omega$  represents the contribution of one resonance to total absorption. The integral of eq. (B.2) yields the following equation:

$$\sigma = \int_{-\infty}^{+\infty} A(\omega) = 2\pi \frac{\gamma_i}{N + C} \quad (\text{B.3})$$

where  $C = \gamma_i/\gamma_e$  is a parameters that indicates the coupling regime. Equation (B.2) can be re-written as function of  $C$ , allowing to define the height of the absorption peak as follows:

$$\max(A) = A(\omega = \omega_0) = \frac{4C}{(N + C)^2} \quad (\text{B.4})$$

Equation (B.4) is maximised when  $C = N$ , which is defined as the *critical coupling condition*, where  $\max(A) = 1/N$ . An important consequence of this condition is that the maximum absorption peak of a resonance cannot exceed  $1/N$ . Perfect absorption with a single resonance can thus be achieved only when  $N = 1$ , while

in all other cases  $\max(A) \leq 1/2$ . Looking into the other cases, when  $C > N$  the height of the peak decreases, while at the same time the resonance becomes narrower. On the other hand, when  $C < N$  the peak still reduces, but the resonance becomes broader.

For solar cells, the analysis becomes interesting in the *over-coupling regime* ( $\gamma_i \ll \gamma_e$ ), corresponding to *weak absorption* conditions – since  $\gamma_e$  and  $\alpha$  are directly proportional. In this regime  $C \rightarrow 0$ , and eq. (B.3) assumes its maximum value:

$$\sigma_{\max} = 2\pi \frac{\gamma_i}{N} \quad (\text{B.5})$$

The maximum absorption that a solar cell endowed with periodic gratings can achieve is the sum of the contribution of all resonances:

$$A_{\text{periodic}} = \frac{\sum \sigma_{\max}}{\Delta\omega} = \frac{2\pi\gamma_i}{\Delta\omega} \frac{M}{N} = \frac{2\pi\alpha}{\Delta k} \frac{M}{N} \quad (\text{B.6})$$

where  $k = \omega \cdot n/c$  is the wavenumber, and  $M$  indicates the number of excited resonances ( $\sum \sigma_{\max} = M \cdot \sigma_{\max}$ ). If eq. (B.6) is divided by single pass absorption, under the assumption  $ad \ll 1$ , the enhancement factor can be calculated:

$$EF_{\text{periodic}} = \frac{2\pi}{d\Delta k} \frac{M}{N} \quad (\text{B.7})$$

where  $d$  is the thickness of the dielectric slab. It is now possible to determine the absorption limit and enhancement factor for different periodic structures, by determining the values of  $M$  and  $N$ .

### Absorption enhancement in 1-D grating structures

Consider the 1-dimensional grating structure depicted in fig. B.2. The wave-number of light in air is:

$$k_0 = \frac{2\pi}{\lambda} = \sqrt{k_{0,\parallel}^2 + k_{0,\perp}^2} \quad (\text{B.8})$$

Assuming perpendicular incidence, the values of the parallel component of  $k_0$  can be determined with this equation:

$$k_0^{(i)} = i_1 \frac{2\pi}{\Lambda} < k_0 \quad (\text{B.9})$$

where  $i_1 = 0, \pm 1, \pm 2, \dots$  is an integer that counts the diffraction orders. The conditions of eq. (B.9) imposes that only a finite number of diffraction orders are

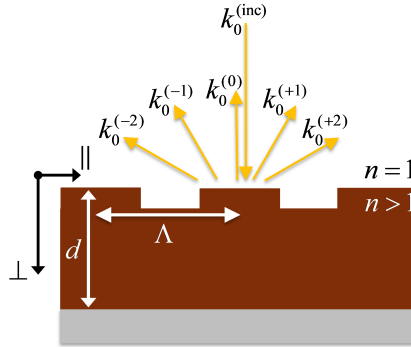


**Figure B.2.** Leakage channels for a 1-D grating structure.

allowed. Note that this equation is equivalent to eq. (1.7) presented in chapter 1. Defining  $s = \Lambda/\lambda$ , the number of leakage channels is calculated as follows:

$$N^{(1D)} = 2 \left\lfloor \frac{k_0}{2\pi/\Lambda} \right\rfloor + 1 = 2 \lfloor s \rfloor + 1 \quad (\text{B.10})$$

The situation inside the absorber is quite similar (see fig. B.3 on the right). The grating scatters light in discrete diffraction orders, with the parallel component once again described by this equation:

$$k^{(i)} = i_1 \frac{2\pi}{\Lambda} \quad (\text{B.11})$$

To achieve a resonance, the perpendicular component of the wavenumber needs to satisfy the following condition:

$$k_{\perp}^{(i)} = i_2 \frac{2\pi}{d} \quad (\text{B.12})$$

where  $i_2 = \pm 1, \pm 2, \dots$  is another integer that counts the order of thickness-induced interference. Considering the frequency range  $\Delta k$  of the incident spectrum, all frequencies that satisfy this equation can be considered resonances:

$$\mathbf{k} = \begin{pmatrix} k_{\parallel}^{(i)} \\ k_{\perp}^{(i)} \end{pmatrix}, k = k_0 \cdot n \in \left[ k - \frac{\Delta k}{2}, k + \frac{\Delta k}{2} \right] \quad (\text{B.13})$$

The first part of eq. (B.13) states the following: all scattered light (where  $k_{\parallel}$  satisfies eq. (B.11)) that interferes in the vertical direction (i.e.  $k_{\perp}$  is described by

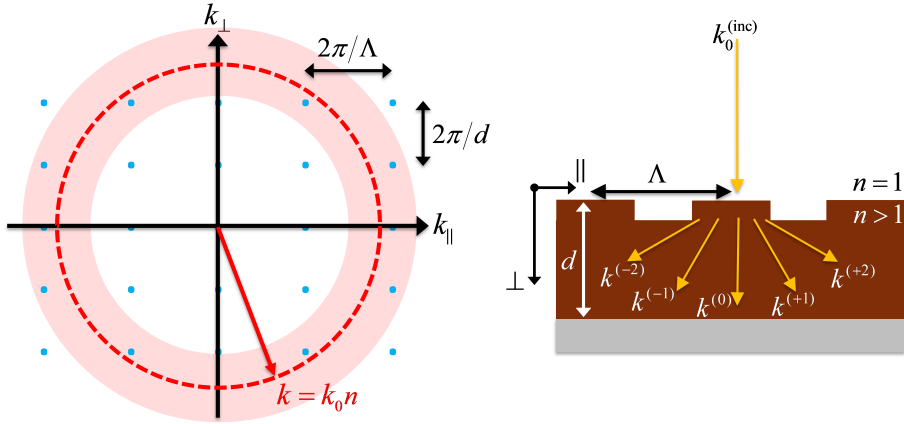


**Figure B.3.** Resonances for a 1-D grating structure.

eq. (B.12)) will excite a resonance. All resonances that are “available” are depicted by blue points in fig. B.3. These include points located on the  $\mathbf{k}_{\perp}$  axis ( $\mathbf{k}_{\parallel} = 0$ ), which are pure interference modes (also called *Fabry-Perot modes*), and all other points which are wave-guided modes proper. These two different types of resonances contribute differently to the absorption enhancement, as shown in the work of Ahmadpanahi *et al.* [291, 292]. The second part of eq. (B.13) simply enforces the condition that the wavenumber can only assume values within the frequency range of incident light (i.e. only the resonances corresponding to blue points that fall within the ring in fig. B.3 can actually be excited).

The number of excited resonances can be calculated with this equation:

$$M^{(1D)} = 2\pi \frac{k\Delta k}{(2\pi/d)(2\pi/\Lambda)} = n \cdot s \cdot d \cdot \Delta k \quad (\text{B.14})$$

The enhancement factor thus assumes the following form:

$$EF^{(1D)} = \frac{2\pi}{d\Delta k} \frac{M}{N} = \frac{2\pi n}{N} s \quad (\text{B.15})$$

It is interesting to look into two specific cases:

- When the grating period is similar to (but smaller than) the wavelength of light (i.e.  $s \rightarrow 1^-$ ), the enhancement factor assumes its maximum value of  $2\pi n$ .
- On the other hand, for periods that become very large ( $s \rightarrow \infty$ ), the enhancement factor tends to  $\pi n$ , which is exactly half of its maximum.

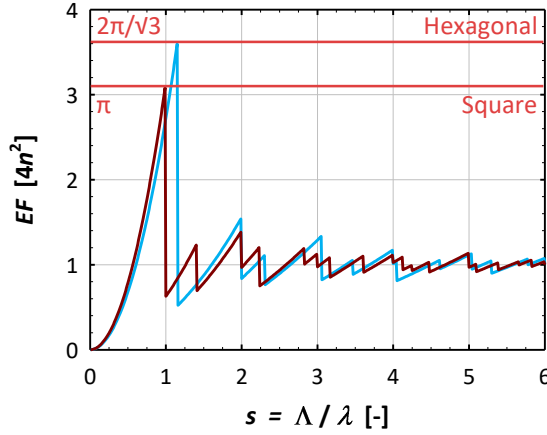


**Figure B.4.** Enhancement factor for 2-D square and hexagonal gratings.

It must be noted, however, that these values of the enhancement factor are well below the value that can be achieved with ideal random textures ( $4n^2$ ) and are highly dependent on the angle of incidence [292].

### Absorption enhancement in 2-D grating structures

The procedure just outlined for 1-D gratings can also be applied to 2-dimensional periodic structures. However, a distinction must be made between square gratings and hexagonal gratings. This time, no closed formula can be derived to count the number of leakage channels. Nevertheless, some considerations can be made. First,  $s < 1 \Rightarrow N = 2$ , because only one direction is allowed (the incident one) for both light polarisations. Second, when  $s \rightarrow \infty$  the following relationships are valid:

$$N^{(2D,sq)} = 2\pi s^2 \quad (\text{B.16a})$$

$$N^{(2D,hex)} = \sqrt{3}\pi s^2 \quad (\text{B.16b})$$

The number of excited resonances, on the other hand, is described by these equations:

$$M^{(2D,sq)} = 4n^2 s^2 d \Delta k \quad (\text{B.17a})$$

$$M^{(2D,hex)} = 2\sqrt{3}n^2 s^2 d \Delta k \quad (\text{B.17b})$$

In both cases, for  $s \rightarrow \infty$  the enhancement factor tends to  $4n^2$ . This is in accordance with the theory developed by Yablonovitch et al. [62, 63], since random

---

textures can be interpreted as 2-D grating with an infinitely large period. However, to determine the position and value of the maximum enhancement factor:

- For the square lattice,  $EF^{(2D,sq)} = 4\pi n^2$  for  $s \rightarrow 1^-$ .
- For the hexagonal grating,  $EF^{(2D,hex)} = 8\pi n^2 / \sqrt{3}$  for  $s \rightarrow 2/\sqrt{3}$ .

In both cases, an enhancement factor values well beyond the Lambertian scattering limit ( $4n^2$ ) can be achieved. More interestingly, hexagonal gratings can perform better than square lattices and achieve a maximum enhancement for slightly larger values of the period. The calculated  $EF$  for 2-D gratings is depicted in fig. B.4. Once again, these considerations are limited to the case of perpendicular incidence of light. In fact, Yu *et al.* showed that the enhancement shows a strong angular dependence – achieving a maximum when the angle of incidence is equal to  $0^\circ$  and decreasing to values well below the Lambertian scattering limit ( $4n^2$ ) for larger angles [126].



# Finite-difference time-domain simulations and multipole decomposition

The work on nanodisk-based hydrogenated amorphous silicon (a-Si:H) metasurfaces presented in chapter 4 was carried out not only relying on finite element method (FEM) simulations – employed in all other chapters. In fact, the modelling of the nanoparticle-on-mirror geometry was conducted via finite-difference time-domain (FDTD) modelling, using the FDTD Solutions software developed by Lumerical Inc., Canada [145]. The results of FDTD and FEM simulations – of both metasurface and full-device models – were then processed in MATLAB [293], to decompose the computed electric field in its multi-polar components.

## **FDTD particle-on-mirror simulations**

The nanoparticles were modelled as a cylindrical a-Si:H structure with diameter  $D = 140\text{ nm}$  and height  $h = 300\text{ nm}$ , while the metasurface arrangement was accomplished using periodic boundary conditions with a periodicity of  $P = 250\text{ nm}$  for the  $\text{SiO}_2$  spacer thickness sweep analysis, and  $145\text{ nm} < P < 350\text{ nm}$  for the periodicity study. The nanodisks were embedded in a dielectric medium with the refractive index of  $\text{SiO}_2$  ( $n_s \approx 1.46$ ). A semi-infinite silver substrate was placed at varying distances ( $d_s$ ) below the nanoparticles:  $5\text{ nm} < d_s < 500\text{ nm}$  for the investigation of the effect of the spacer thickness, and fixed at  $d_s = 100\text{ nm}$  for the analysis of the particle periodicity. Thus, in this model, the spacer between the metasurface and the mirror has the same refractive index as the embedding medium ( $n_s \approx 1.46$ ). The meshing employed on the nanostructure was  $dx = dy = dz = 2\text{ nm}$ , which was deemed sufficient to capture the spatial variation of the electromagnetic modes considered in this work. The (complex) dielectric functions used were fitted to experimental data for both a-Si:H (internally



measured) and the silver mirror [294]. Absorption in a-Si:H was calculated by integrating the total Poynting vector flow through a closed boundary enclosing the particle and normalised by the injected plane wave power. The surface was placed such that it did not intersect the mirror surface. Thus, the total integrated power flux through that surface corresponds exactly to the power absorbed by the nanostructure.

## Multipole decomposition

The multipole decomposition of the modes was performed by monitoring the internal electromagnetic fields in the nanostructure, as function of the wavelength of light. The fields were then projected on a basis of spherical multipoles as outlined in [151]. The electric fields were converted into polarisation current ( $\mathbf{J}$ ) according to

$$\mathbf{J} = -i\omega\epsilon_0[\epsilon_{\text{a-Si:H}}(\omega) - n_s^2]\mathbf{E} \quad (\text{C.1})$$

where  $\mathbf{E}$  is the total electric field inside the structure,  $\omega$  the frequency of light,  $\epsilon_0$  is the dielectric constant of vacuum, and  $\epsilon_{\text{a-Si:H}}$  is the (relative) dielectric function of amorphous silicon. Since the fields in the simulations (both the FDTD simulations and the FEM simulations) were defined on a Cartesian grid, the conversion to spherical coordinates was made through:

$$\begin{aligned} J_r &= \sin(\vartheta) \cos(\phi) J_x + \sin(\vartheta) \sin(\phi) J_y + \cos(\vartheta) J_z \\ J_\vartheta &= \cos(\vartheta) \cos(\phi) J_x + \cos(\vartheta) \sin(\phi) J_y - \sin(\vartheta) J_z \\ J_\phi &= -\sin(\phi) J_x + \cos(\phi) J_y \end{aligned} \quad (\text{C.2})$$

The multipole decomposition was subsequently calculated through integration on the Cartesian grid, and the coefficients here relate to those in Equations (15) and (16) of ref. [151] as:

$$\begin{aligned} |a_l|^2 &= (2l+1) \sum_{m=-l}^l |a_E(l, m)|^2 \\ |b_l|^2 &= (2l+1) \sum_{m=-l}^l |a_M(l, m)|^2 \end{aligned} \quad (\text{C.3})$$

# Thin-film silicon solar cells based on 1-D asymmetric periodic gratings

This chapter is based on the following publication:

**R. Vismara**, O. Isabella, and M. Zeman, "Optimization of thin-film silicon solar cells based on 1-D asymmetric periodic gratings," in *Proceedings of the 31<sup>st</sup> European Photovoltaic Solar Energy Conference and Exhibition (31<sup>th</sup> EU PVSEC)*, September 14<sup>th</sup>-18<sup>th</sup> 2015, Hamburg (Germany).

## Introduction

In order for thin-film silicon to compete in the global PV market, light management techniques must be implemented to increase the performance while keeping thin both top hydrogenated amorphous silicon (a-Si:H) and bottom hydrogenated nano-crystalline silicon (nc-Si:H) junctions. Periodic gratings are an attractive alternative to commonly-employed randomly textured substrates, due to the easy manipulation of scattering properties by means of controlling their geometrical features [295]. Recent studies have shown that thin-film silicon solar cells on periodically textured substrates can match the performance of devices deposited on random textures [296] and that, at specific wavelengths, exceed the  $4n^2$  absorption enhancement limit [125, 126], the well-known *Lambertian-scattering* or *Yablonovitch* limit [62]. Current world-record efficiency for single-junction nc-Si:H [38] and tandem a-Si:H/nc-Si:H (micromorph) devices [41] consist of cells on periodically-textured substrates. Asymmetric gratings have also attracted interest in the past, because they offer – at least in theory – an additional advantage with respect to symmetric structures: the possibility to achieve better light trapping (at specific wavelengths) by reducing the amount of in-coupled

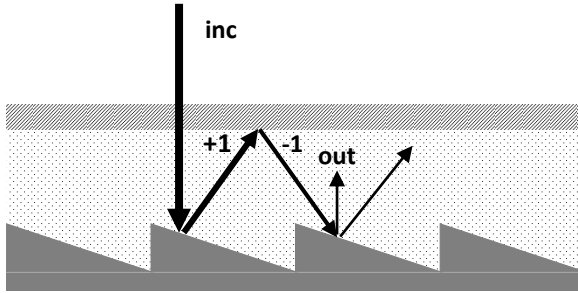


**Figure D.1.** Example of an asymmetric grating, which can suppress zero-order and left-travelling reflected orders, allowing only diffraction modes travelling to the right. In this way, out-coupling of light is reduced and light trapping improved. Picture adapted from [297].

light that can be out-coupled after the first pass inside the absorber [297]. In this chapter, a study of the optical performance of 1-D asymmetric triangular periodic gratings is presented, applied to single- and double-junction thin-film devices. 1-D triangular gratings were chosen, as they are relatively easy to manufacture and because, for similar aspect ratio textured substrates, they can offer better conditions for the growth of thin-films with respect to 2-D gratings or random features. The analysis was carried out by means of optical simulations, using a 3-D Maxwell equation solver based on the finite element method (FEM) [75].

### Diffraction at 1-D asymmetric gratings

Periodic gratings diffract light into specific directions (or modes), which can be calculated according to the grating equation [69]:

$$\sin(\theta_m) = \frac{m\lambda}{n_d P} \quad (\text{D.1})$$

where  $m$  is the order of diffraction,  $\theta_m$  the angle of the  $m$ -th diffracted order,  $\lambda$  is the wavelength of light *in vacuo*,  $n_d$  the refractive index of the diffractive medium, and  $\Lambda$  is the period of the grating. The main advantage that gratings offer over random textures is the possibility to tune the diffraction of light by modifying the geometrical parameters of the grating itself. In particular, the period ( $\Lambda$ ) determines the direction of diffracted light (according to the grating equation), while the intensity is regulated by the groove depth ( $h$ ) [69]. Symmetric gratings, however, cannot achieve perfect light trapping. In fact, according

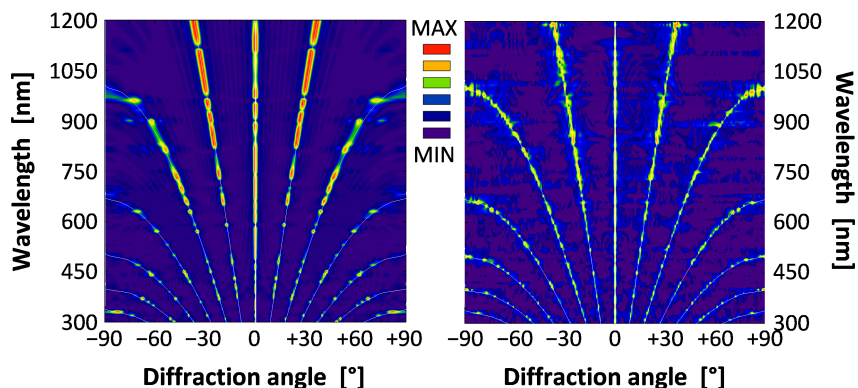


**Figure D.2.** Intensity of reflectance – normalised to the maximum value – of symmetric (left) and asymmetric triangular gratings (right), as function of  $\lambda$  and  $\theta$ . The superimposed white lines represent the value of  $\theta(\lambda)$  calculated with the diffraction equation.

the reciprocity theorem diffracted waves generated by an incoming (zero-order) wave will necessarily couple to an out-going zero-order wave. This behaviour can be (partly) avoided by the use of asymmetric geometries, as the blazed grating depicted in fig. D.1. This structure can suppress both zero-order as well as left-moving reflection orders; in this way, only right-moving diffraction orders are allowed to propagate [297]. When the right-travelling wave impinges on the grating (after being reflected at the front surface), it does not necessarily couple into the zero-order outgoing wave. Hence, at least in principle, (almost) perfect light trapping for selected wavelengths could be achieved.

In this experiment, the effect of asymmetric gratings on the diffraction of light was investigated. First, a set of simulations with symmetric and asymmetric triangular structures made of glass ( $n_{\text{glass}} = 1.5$ ) was done. The range  $300 \text{ nm} < \lambda < 1200 \text{ nm}$  was considered – and perpendicular illumination was assumed. Then, for each value of  $\lambda$  the reflectance ( $R$ ) as function of the angle of diffraction ( $\theta$ ) was calculated. Results shown in fig. D.2 indicate that symmetric (left) and asymmetric gratings (right) diffract light into the same directions, confirming the fact that  $\theta$  only depends the wavelength of light and on the grating and material properties, as indicated by the diffraction equation, and that asymmetry does not influence the direction of diffraction modes.

A second series of simulations to investigate the diffraction properties of asymmetric triangular gratings was carried out. This time models consisted of single-

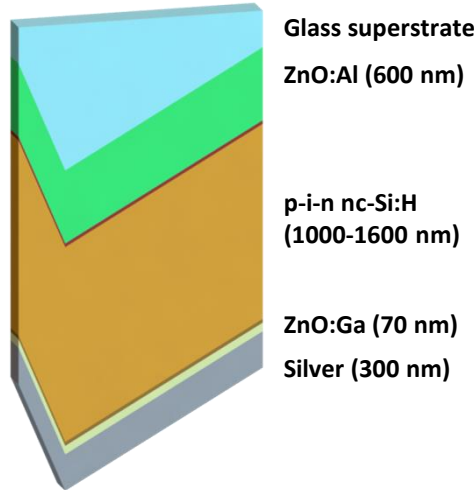


**Figure D.3.** 3-D rendering of the single-junction solar cell model used for simulations. Materials and thickness of each layer are indicated.

junction nc-Si:H solar cells on triangular glass gratings (see model depicted in fig. D.3), symmetric and asymmetric. Once again,  $R(\lambda, \theta)$  was computed in the simulations (with the method described in Chapter 2). Results (fig. D.4) show that the intensity of same-order positive and negative diffraction modes have equal intensity in the case of symmetric gratings. For asymmetric structures, however, this is not the case. In fact, high-order left-propagating ( $\theta < 0$ ) waves (indicated in fig. D.4 by arrows) have a higher intensity with respect to same-order modes travelling in the right direction ( $\theta > 0$ ). The geometry of the grating allows more light to travel to the left, thus reducing the intensity of right-moving waves.

### Optimisation of top and bottom junctions

Achieving the highest optical performance of tandem solar cells requires the optimisation of the single junctions that make up the device.

In the first step, the periodic asymmetric gratings were optimised to achieve the highest photocurrent density ( $J_{ph}$ ) in the bottom cell (nc-Si:H absorber). The value of  $\Lambda$  and height ( $h$ ) of the grating were fixed to 2000 nm and 900 nm respectively, since in previous studies features with these dimensions applied to nc-Si:H-based solar cells have shown good performance [195, 249]. Only the an-

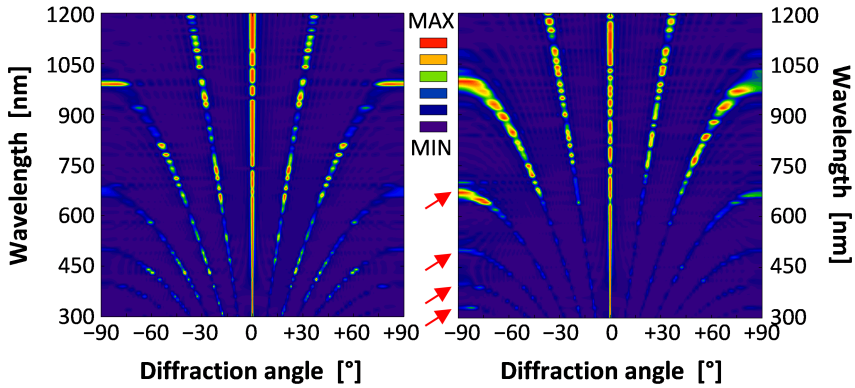


**Figure D.4.** Intensity of reflectance – normalised to the maximum value – of single-junction devices with nc-Si:H absorbers based on periodic symmetric (left) and asymmetric triangular gratings (right), as function of  $\lambda$  and  $\theta$ .

gle of the grating was changed, from zero (saw-tooth shape) to  $48^\circ$  (symmetric structure, see top axis in fig. D.5). The performance of the solar cell (see model in fig. D.3) was evaluated in terms on implied photocurrent density generated in the absorber layer, calculated following the procedure outlined in Chapter 2. Two set of simulations with different absorber thickness ( $d_{\text{nc-Si:H}} = 1600$  nm and  $d_{\text{nc-Si:H}} = 1000$  nm) were carried out. Simulation results, depicted in fig. D.5, show that asymmetric gratings perform better than their symmetric counterparts. The implied photocurrent density generated by all asymmetric architectures with angles between  $10^\circ$  and  $40^\circ$  was similar and above  $25 \text{ mAcm}^{-2}$  for the thicker absorber ( $d_{\text{nc-Si:H}} = 1600$  nm) and above  $22.5 \text{ mAcm}^{-2}$  for the thinner ( $d_{\text{nc-Si:H}} = 1000$  nm).

After the optimisation of triangular gratings, an investigation on how to improve the optical performance by using – in both top and bottom junctions – materials that are more transparent. was carried out For the front TCO,  $\text{In}_2\text{O}_3\text{:H}$  (IOH) was compared to  $\text{ZnO:Al}$  (AZO). IOH is more transparent and conductive than AZO [122, 123], and can thus be thinner to absorb less light. Additionally, the performance of *p*- and *n*-doped nc-SiOx layers was compared to the one of less transparent a-Si:H (top cell) and nc-Si:H (bottom cell) doped layers. Results are summarised in table D.1 and show how the implied photocurrent density in both junctions significantly increase ( $+ \sim 5 \text{ mAcm}^{-2}$ ) when more transparent layers are employed.

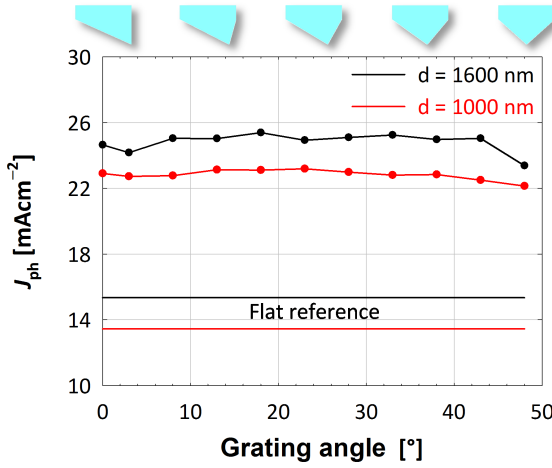


**Figure D.5.** Implied photocurrent density ( $J_{ph}$ ) generated inside the nc-Si:H layer, for different values of the grating angle and layer thickness  $d$ . 'Flat reference' indicates the  $J_{ph}$  generated by architectures with flat (non-textured) interfaces.

### Current matching of double-junction solar cell

After both grating and materials were optimised, it is important to adjust the thickness of top and bottom cells to achieve current matching. In fact, a significant mismatch of the implied photocurrent densities of the two junctions would result in lowered efficiency of the tandem device.

In the first series of simulations, the thickness of the bottom junction absorber (nc-Si:H) was kept constant and equal to 1600 nm. As shown in the previous section, this cell in single-junction configuration can deliver up to  $30.2 \text{ mAcm}^{-2}$  of implied photogenerated current. Hence, the goal for the tandem device is to achieve a matched photocurrent density of  $\sim 15 \text{ mAcm}^{-2}$ . The thickness of the

**Table D.1.** Result of material optimisation for top (a-Si:H) and bottom junctions (nc-Si:H). The thickness of both absorber layers ( $d$ ) is indicated.

Structure	a-Si:H ( $d = 150 \text{ nm}$ )	nc-Si:H ( $d = 1600 \text{ nm}$ )
Flat cell	$7.1 \text{ mAcm}^{-2}$	$15.3 \text{ mAcm}^{-2}$
Symmetric ( $\alpha = 48^\circ$ )	$10.9 \text{ mAcm}^{-2}$	$23.6 \text{ mAcm}^{-2}$
Asymmetric ( $\alpha = 48^\circ$ )	$12.0 \text{ mAcm}^{-2}$	$25.4 \text{ mAcm}^{-2}$
Optimised ( $\alpha = 48^\circ$ )	$16.7 \text{ mAcm}^{-2}$	$30.2 \text{ mAcm}^{-2}$

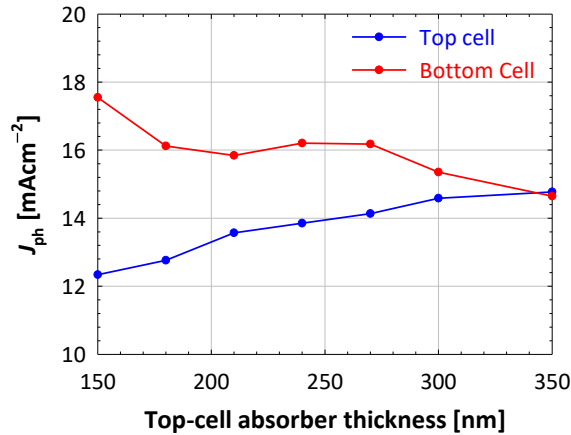


**Figure D.6.** Implied photocurrent density generated in top (a-Si:H) and bottom cell (nc-Si:H), as function of the top cell thickness ( $d_{\text{a-Si:H}} = 150 - 350$  nm). Good matching of the photocurrent density ( $J_{\text{ph,matched}} \approx 14.7 \text{ mAcm}^{-2}$ ) was achieved.

top cell absorber was gradually increased from a very thin 150 nm to 350 nm. It must be noted that, in manufactured devices, the top cell will suffer from the well-known light induced degradation (LID) phenomenon (i.e. the Staebler-Wronski effect) [239, 240]. For this reason, the initial value of photocurrent density in the top cell (a-Si:H) should be (slightly) higher than in the bottom junction. Additionally, the amorphous silicon junction should be made as thin as possible to reduce the degradation effect.

Results of the a-Si:H thickness sweep (fig. D.6) show that the top cell can produce more current than the nc-Si:H junction only if the top junction is at least 350 nm thick. Due to LID effects, it was decided not to investigate the performance of architectures with a thicker top cell. The values of the implied photocurrent that can be generated in the two junction in this configuration are  $15.0 \text{ mAcm}^{-2}$  in the a-Si:H cell ( $d_{\text{a-Si:H}} = 350$  nm) and  $14.7 \text{ mAcm}^{-2}$  in the nc-Si:H junction ( $d_{\text{nc-Si:H}} = 1600$  nm).

The final run of simulations is aimed at studying the effect of increasing the thickness of the bottom cell. The value of  $d_{\text{nc-Si:H}}$  was thus changed from 1600 nm up to 2500 nm, and investigated the impact on the implied photocurrent density generated in top and bottom junctions. The simulation results (fig. D.7) show that increasing the bottom cell thickness does not provide any additional benefit, since only the implied photocurrent density generated in the bottom cell increases. The performance of the top junction is not strongly affected, but the



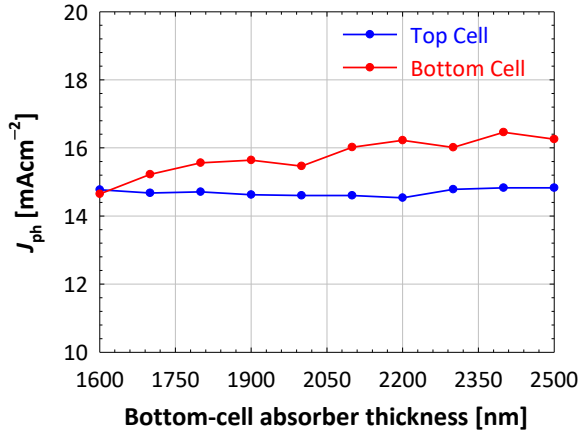


**Figure D.7.** Implied photocurrent density generated in top (a-Si:H) and bottom cell (nc-Si:H), as function of the bottom cell thickness ( $d_{\text{nc-Si:H}} = 1600 - 2500$  nm). Good matching of the photocurrent density ( $J_{\text{ph,matched}} \approx 14.7 \text{ mAcm}^{-2}$ ) was achieved.

extra absorption of the bottom cell is mostly lost due to current mismatch. For silicon devices, thinner absorbers can have better electrical properties (higher open-circuit voltage  $V_{\text{oc}}$  and fill factor  $FF$ ) with respect to thicker solar cells. Hence, the optimal design for the tandem device on 1-D periodic asymmetric triangular gratings is:

- Top-cell absorber:  $d_{\text{a-Si:H}} = 350$  nm
- Bottom-cell absorber:  $d_{\text{nc-Si:H}} = 1600$  nm
- Matched  $J_{\text{ph}} = 14.7 \text{ mAcm}^{-2}$

A recent publication by Tan *et al.* [39] showed that high-quality tandem micromorph device can be deposited on randomly textured substrates, achieving very good electrical properties:  $V_{\text{oc}} = 1.464 \text{ V}$  and  $FF = 0.759$ . The photocurrent density of that device is  $13.6 \text{ mAcm}^{-2}$ . The architecture modelled in this work showed the potential to achieve an even higher photocurrent density of  $14.7 \text{ mAcm}^{-2}$ . If such values of the external parameters could be obtained in the micromorph device on periodic symmetric triangular gratings, initial efficiency could be higher than 16%.

## Conclusions

In this chapter, the optical analysis of the performance of thin-film silicon solar cell on one-dimensional triangular asymmetric gratings was presented. First, it was shown that the asymmetry of gratings does not influence the direction of diffracted light. In fact, asymmetric structures scatter light in the same direction and symmetric ones. On the other hand, the intensity of light diffracted by asymmetric gratings is not symmetrically distributed. Same-order positive and negative diffracted modes have different intensity, and one propagation direction is predominant over the other. Second, single-junction a-Si:H and nc-Si:H cells were optimised. For the bottom cell (nc-Si:H), asymmetric gratings outperformed their symmetric counterparts, allowing for an implied photocurrent density gain of  $\sim 2 \text{ mAcm}^{-2}$ . For both cells a material optimisation was also performed, using highly transparent materials for the front TCO and *p*- and *n*-doped layers. The optimisation allowed for a further improvement of the optical performance ( $+ \sim 5 \text{ mAcm}^{-2}$ ). Finally, a current matching analysis was conducted, to achieve the highest possible efficiency. By adopting thickness values of 350 nm (top cell) and 1600 nm (bottom junction), a potential implied photocurrent density of  $14.7 \text{ mAcm}^{-2}$  was calculated. A real device that could generate this current and have good electrical properties (similar to similar devices manufactured within the PVMD group) has the potential to achieve a conversion efficiency above 16%.



---

# Bibliography

- [1] M. R. Allen *et al.*, in *Global Warming of 1.5° C. An IPCC Special Report on ...*, edited by V. Masson-Delmotte *et al.* (2018) Chap. 1.
- [2] O. Hoegh-Guldberg *et al.*, in *Global Warming of 1.5° C. An IPCC Special Report on ...*, edited by V. Masson-Delmotte *et al.* (2018) Chap. 3.
- [3] UN Treaty Collection, "PARIS AGREEMENT (English)," (2015).
- [4] "www.co2.earth," Accessed: 2020-05-29.
- [5] IRENA, "Global Energy Transformation: A Roadmap to 2050," (2018).
- [6] C. Le Quéré *et al.*, *Nature Climate Change* (2020).
- [7] P. Tans, NOAA/ESRL, "Trends in Atmospheric Carbon Dioxide," (2019).
- [8] M. Sato and G. Schmidt, "Forcings in GISS Climate Model," (2011), <http://data.giss.nasa.gov/modelforce/ghgases/>, accessed: 2020-05-29.
- [9] United Nations, Department of Economic and Social Affairs, Population Division, "World Population Prospects: The 2017 Revision, Key Findings and Advance Tables," (2017).
- [10] Berkeley Earth, "Data Overview - Land + Ocean (1850 - Recent)," <http://berkeleyearth.org/data/>, accessed: 2020-05-29.
- [11] IRENA, "Renewable Energy Statistics," (2020).
- [12] M. Willuhn, "Global PV market: 114 GW to be installed in 2019, with continued growth onwards," *PV Magazine* July 25, 2019.
- [13] IEA - PVPS, "Snapshot of global PV markets," (2020).
- [14] M. A. Green, *Progress in Energy* **1**, 013001 (2019).
- [15] R. Perez and M. Perez, *A fundamental look at supply side energy reserves for the planet*, Tech. Rep. (IEA, 2015).
- [16] IEA, "Global Energy & CO<sub>2</sub> Status Report," (2019).
- [17] M. Guarnieri, *IEEE Industrial Electronics Magazine* **9**, 58 (2015).
- [18] This Month in Physics History, "April 25, 1954: Bell Labs Demonstrates the First Practical Silicon Solar Cell", *APS News* **18** (2009).
- [19] R. M. Swanson, *Progress in Photovoltaics: Research and Applications* **14**, 443 (2006).
- [20] G. Carr, "Sunny Uplands," *The Economist* November 21, 2012.
- [21] Fraunhofer ISE, "Photovoltaics Report," Updated: September 16, 2020.

- [22] A. H. M. Smets, K. Jäger, O. Isabella, R. A. van Swaaij, and M. Zeman, *Solar Energy: The Physics and Engineering of Photovoltaic Conversion Technologies and Systems* (UIT Cambridge, 2016).
- [23] NREL, “Best Research-Cell Efficiencies,” <http://www.nrel.gov/pv/cell-efficiency.html>, accessed: 2020-05-29.
- [24] M. A. Green, E. D. Dunlop, J. Hohl-Ebinger, M. Yoshita, N. Kopidakis, and A. W. Ho-Baillie, *Progress in Photovoltaics: Research and Applications* **28**, 3 (2020).
- [25] K. Yamamoto, K. Yoshikawa, H. Uzu, and D. Adachi, *Japanese Journal of Applied Physics* **57**, 08RB20 (2018).
- [26] TRINA SOLAR, “Trina Solar Announces New Efficiency Record of 23.22% with n-type i-TOPCon Solar Cell on Cast-Mono Substrate,” Press release November 26, 2019.
- [27] P. Chiu *et al.*, in *Proceedings of the 40<sup>th</sup> IEEE Photovoltaic Specialist Conference (PVSC-40)* (IEEE, 2014).
- [28] K. A. W. Horowitz, T. Remo, B. Smith, and A. Ptak, *A Techno-Economic Analysis and Cost Reduction Roadmap for III-V Solar Cells*, Tech. Rep. (National Renewable Energy Laboratory, 2018).
- [29] S. Essig *et al.*, *Nature Energy* **2**, 17144 (2017).
- [30] M. Schnabel *et al.*, *Sustainable Energy Fuels* **4**, 549 (2020).
- [31] L. Meng *et al.*, *Science* **361**, 1094 (2018).
- [32] Helmholtz Zentrum Berlin, “World Record: Efficiency of perovskite silicon tandem solar cell jumps to 29.15 per cent,” Press release January 29, 2020.
- [33] H. Tan *et al.*, *Science* **355**, 722 (2017).
- [34] Z. Huang *et al.*, *ACS Energy Letters* **4**, 1521 (2019).
- [35] M. Liu *et al.*, *Nature* **570**, 96 (2019).
- [36] D. Dominé, P. Buehlmann, J. Bailat, A. Billet, A. Feltrin, and C. Ballif, *physica status solidi (RRL) - Rapid Research Letters* **2**, 163 (2008).
- [37] T. Matsui, K. Maejima, A. Bidiville, H. Sai, T. Koida, T. Suezaki, M. Matsumoto, K. Saito, I. Yoshida, and M. Kondo, *Japanese Journal of Applied Physics* **54**, 08KB10 (2015).
- [38] H. Sai, T. Matsui, H. Kumagai, and K. Matsubara, *Applied Physics Express* **11**, 022301 (2018).
- [39] H. Tan, E. Moulin, F. T. Si, J.-W. Schüttauf, M. Stuckelberger, O. Isabella, E.-J. Haug, C. Ballif, M. Zeman, and A. H. M. Smets, *Progress in Photovoltaics: Research and Applications* **23**, 949 (2015).

- [40] B. Yan, G. Yue, L. Sivec, J. Yang, S. Guha, and C.-S. Jiang, *Applied Physics Letters* **99**, 113512 (2011).
- [41] H. Sai, T. Matsui, , and K. Matsubara, *Applied Physics Letters* **109**, 183506 (2016).
- [42] B. Liu, L. Bai, T. Li, C. Wei, B. Li, Q. Huang, D. Zhang, G. Wang, Y. Zhao, and X. Zhang, *Energy & Environmental Science* **10**, 1134 (2017).
- [43] M. Konagai and R. Sasaki, *Progress in Photovoltaics: Research and Applications* **28**, 554 (2020).
- [44] F.-J. Haug and C. Ballif, *Energy & Environmental Science* **8**, 824 (2015).
- [45] S. Guha and J. Yang, *High-Efficiency Amorphous Silicon Alloy Based Solar Cells and Modules - Final Technical Progress Report*, Tech. Rep. (United Solar Ovonic Corporation, 2005).
- [46] K. Jäger, J. Lenssen, P. Veltman, and E. Hamers, in *Proceedings of the 28<sup>th</sup> European Photovoltaic Solar Energy Conference and Exhibition (28<sup>th</sup> EU PVSEC)* (2013) pp. 2164–2169.
- [47] K. Yamamoto *et al.*, *Progress in Photovoltaics: Research and Applications* **13**, 489 (2005).
- [48] M. Vetter, J. P. Borrajo, and J. Andreu, *physica status solidi c* **7**, 1101 (2010).
- [49] O. Gabriel, S. Kirner, C. Leendertz, M. Gerhardt, A. Heidelberg, H. Bloëß, R. Schlatmann, and B. Rech, *physica status solidi (c)* **8**, 2982 (2011).
- [50] SOLAR FRONTIER, “Solar frontier achieves world record thin-film solar cell efficiency of 23.35%,” Press release January 17, 2019.
- [51] FIRST SOLAR, “First solar achieves yet another cell conversion efficiency world record,” Press release February 23, 2016.
- [52] A. Rashedi and T. Khanam, *Environmental Science and Pollution Research* (2020).
- [53] O. Isabella, H. Sai, M. Kondo, and M. Zeman, *Progress in Photovoltaics: Research and Applications* **22**, 671 (2014).
- [54] M. A. Green, *Solar Energy Materials and Solar Cells* **92**, 1305 (2008).
- [55] P. Löper, M. Stuckelberger, B. Niesen, J. Werner, M. Filipič, S.-J. Moon, J.-H. Yum, M. Topič, S. De Wolf, and C. Ballif, *The Journal of Physical Chemistry Letters* **6**, 66 (2015).
- [56] R. E. Treharne, A. Seymour-Pierce, K. Durose, K. Hutchings, S. Roncallo, and D. Lane, *Journal of Physics: Conference Series* **286**, 012038 (2011).
- [57] G. E. Jellison, *Optical Materials* **1**, 151 (1992).
- [58] O. Isabella, J. Krč, and M. Zeman, *Applied Physics Letters* **97**, 101106 (2010).

- [59] A. Ingenito, O. Isabella, and M. Zeman, *Progress in Photovoltaics: Research and Applications* **23**, 1649 (2015).
- [60] F.-J. Haug, T. Söderström, O. Cubero, V. Terrazzoni-Daudrix, and C. Ballif, *Journal of Applied Physics* **106**, 044502 (2009).
- [61] Z. C. Holman, S. De Wolf, and C. Ballif, *Light: Science & Applications* **2**, e106 (2013).
- [62] E. Yablonovitch, *Journal of the Optical Society of America* **72**, 899 (1982).
- [63] T. Tiedje, E. Yablonovitch, G. D. Cody, and B. G. Brooks, *IEEE Transactions on electron devices* **31**, 711 (1984).
- [64] M. A. Green, *Progress in Photovoltaics: Research and Applications* **10**, 235 (2002).
- [65] W. Shockley and H. J. Queisser, *Journal of Applied Physics* **32**, 510 (1961).
- [66] PerkinElmer, "UV/Vis Spectroscopy," <https://www.perkinelmer.com/category/ultraviolet-uv-instruments>, accessed: 2020-05-29.
- [67] P. A. van Nijnatten, *Thin Solid Films* **442**, 74 (2003).
- [68] K. Jäger, O. Isabella, L. Zhao, and M. Zeman, *physica status solidi (c)* **7**, 945 (2010).
- [69] O. Isabella, *Light management in thin-film silicon solar cells*, Ph.D. thesis, Delft University of Technology (2013).
- [70] Woolam, "Ellipsometry Tutorial," <https://www.jawoollam.com/resources/ellipsometry-tutorial>, accessed: 2020-05-29.
- [71] Z. Remes, R. Vasudevan, K. Jarolimek, A. H. M. Smets, and M. Zeman, *Solid State Phenomena* **213**, 19 (2014).
- [72] J. Holovský, M. Schmid, M. Stuckelberger, M. Despeisse, C. Ballif, A. Poruba, and M. Vaněček, *Journal of Non-Crystalline Solids* **358**, 2035 (2012).
- [73] M. van Sebillie, R. A. Vasudevan, R. J. Lancee, R. A. C. M. M. van Swaaij, and M. Zeman, *Journal of Physics D: Applied Physics* **48**, 325302 (2015).
- [74] NREL, "Reference Solar Spectral Irradiance: Air Mass 1.5," <http://rredc.nrel.gov/solar//spectra/am1.5>, accessed: 2020-05-29.
- [75] ANSYS, "3D Electromagnetic Field Simulator for RF and Wireless Design," <http://www.ansys.com/Products/Electronics/ANSYS-HFSS>, accessed: 2020-05-29.
- [76] A. Yariv and P. Yeh, *Optical Waves in Crystals* (John Wiley & Sons, 1984).
- [77] W. Ritz, *Journal für die reine und angewandte Mathematik* **135**, 1 (1909).
- [78] K. Yee, *IEEE Transaction Antennas Propagation* **14**, 302 (1966).
- [79] T. Weiland, *Archiv Elektronik und Uebertragungstechnik* **31**, 116 (1977).

- [80] D. B. Davidson, *Computational electromagnetics for RF and microwave engineering* (Cambridge University Press, 2010).
- [81] O. Isabella, S. Solntsev, D. Caratelli, and M. Zeman, *Progress in Photo-voltaics: Research and Applications* **21**, 94 (2013).
- [82] I. Bardi, R. Remski, D. Perry, and Z. Cendes, *IEEE Transactions on Mag-netics* **38**, 641 (2002).
- [83] C. Lin and M. L. Povinelli, *Optics Express* **17**, 19371 (2009).
- [84] G. Demésy and J. Sajeew, *Journal of Applied Physics* **112**, 074326 (2012).
- [85] V. K. Narasimhan and Y. Cui, *Nanophotonics* **2**, 187 (2013).
- [86] J. Yoo, B.-M. Nguyen, I. H. Campbell, S. A. Dayeh, P. Schuele, D. Evans, and S. T. Picraux, *ACS Nano* **9**, 5154 (2015).
- [87] L. Cao, J. S. White, J.-S. Park, J. A. Schuller, B. M. Clemens, and M. L. Brongersma, *Nature Materials* **8**, 643 (2009).
- [88] L. Cao, P. Fan, A. P. Vasudev, J. S. White, Z. Yu, W. Cai, J. A. Schuller, S. Fan, and M. L. Brongersma, *Nano Letters* **10**, 439 (2010).
- [89] S.-K. Kim, K.-D. Song, T. J. Kempa, R. W. Day, C. M. Lieber, and H.-G. Park, *ACS Nano* **8**, 3707 (2014).
- [90] S.-K. Kim, R. W. Day, J. F. Cahoon, T. J. Kempa, K.-D. Song, H.-G. Park, and C. M. Lieber, *Nano Letters* **12**, 4971 (2012).
- [91] M. M. Adachi, M. P. Anantram, and K. S. Karim, *Scientific Reports* **3**, 1546 (2013).
- [92] Y. Kuang, M. Di Vece, J. K. Rath, L. van Dijk, and R. E. I. Schropp, *Reports on Progress in Physics* **76**, 106502 (2013).
- [93] R.-E. Nowak, M. Vehse, O. Sergeev, T. Voss, M. Seyfried, K. von Maydell, and C. Agert, *Advanced Optical Materials* **2**, 94 (2014).
- [94] L. Tsakalacos, J. Balch, J. Fronheiser, B. A. Korevaar, O. Sulima, and J. Rand, *Applied Physics Letters* **91**, 233117 (2007).
- [95] E. Garnett and P. Yang, *Nano Letters* **10**, 1082 (2010).
- [96] E. P. A. M. Bakkers, J. A. van Dam, S. De Franceschi, L. P. Kouwenhoven, M. Kaiser, M. Verheijen, H. Wondergem, and P. van der Sluis, *Nature Ma-terials* **3**, 769 (2004).
- [97] N. Anttu and H. Q. Xu, *Optics Express* **21**, A558 (2013).
- [98] C. Colombo, M. Heiß, M. Grätzel, and A. F. i. Morral, *Applied Physics Letters* **94**, 173108 (2009).
- [99] P. Krogstrup, H. I. Jorgensen, M. Heiss, O. Demichel, J. V. Holm, M. Aage-sen, J. Nygard, and A. Fontcuberta i Morral, *Nature Photonics* **7**, 306 (2013).



- [100] S. Geißendörfer, M. Vehse, T. Voss, J. P. Richters, B. Hanke, K. von Maydell, and C. Agert, *Solar Energy Materials and Solar Cells* **111**, 153 (2013).
- [101] A. Fontcuberta i Morral, J. Arbiol, J. D. Prades, A. Cirera, and J. â. Morante, *Advanced Materials* **19**, 1347 (2007).
- [102] B. Tian, X. Zheng, T. J. Kempa, Y. Fang, N. Yu, G. Yu, J. Huang, and C. M. Lieber, *Nature* **449**, 885 (2007).
- [103] E. C. Garnett and P. Yang, *Journal of the American Chemical Society* **130**, 9224 (2008).
- [104] T. Stelzner, M. Pietsch, G. Andrä, F. Falk, E. Ose, and S. Christiansen, *Nanotechnology* **19**, 295203 (2008).
- [105] V. Sivakov, G. Andrä, A. Gawlik, A. Berger, J. Plentz, F. Falk, and S. H. Christiansen, *Nano Letters* **9**, 1549 (2009).
- [106] E. C. Garnett, M. L. Brongersma, Y. Cui, and M. D. McGehee, *Annual Review of Materials Research* **41**, 269 (2011).
- [107] G. Jia, M. Steglich, I. Sill, and F. Falk, *Solar Energy Materials and Solar Cells* **96**, 226 (2012).
- [108] D. R. Kim, C. H. Lee, P. M. Rao, I. S. Cho, and X. Zheng, *Nano Letters* **11**, 2704 (2011).
- [109] K.-Q. Peng and S.-T. Lee, *Advanced Materials* **23**, 198 (2011).
- [110] M. Gharghi, E. Fathi, B. Kante, S. Sivoththaman, and X. Zhang, *Nano Letters* **12**, 6278 (2012).
- [111] G. Jia, B. Eisenhawer, J. Dellith, F. Falk, A. Thøgersen, and A. Ulyashin, *The Journal of Physical Chemistry C* **117**, 1091 (2013).
- [112] K. T. Li, X. Q. Wang, P. F. Lu, J. N. Ding, and N. Y. Yuan, *Nanoscale Research Letters* **8**, 396 (2013).
- [113] J. Zhu, Z. Yu, G. F. Burkhard, C.-M. Hsu, S. T. Connor, Y. Xu, Q. Wang, M. McGehee, S. Fan, and Y. Cui, *Nano Letters* **9**, 279 (2009).
- [114] J. Cho, B. O'Donnell, L. Yu, K.-H. Kim, I. Ngo, and P. R. Cabarrocas, *Progress in Photovoltaics: Research and Applications* **21**, 77 (2013).
- [115] L. W. Veldhuizen, Y. Kuang, and R. E. I. Schropp, *Solar Energy Materials and Solar Cells* **158**, 209 (2016).
- [116] M. J. Ashley, M. N. O'Brien, K. R. Hedderick, J. A. Mason, M. B. Ross, and C. A. Mirkin, *Journal of the American Chemical Society* **138**, 10096 (2016).
- [117] E. Lafalce, C. Zhang, Y. Zhai, D. Sun, and Z. V. Vardeny, *Journal of Applied Physics* **120**, 143101 (2016).
- [118] S. Z. Oener, P. Khoram, S. Brittman, S. A. Mann, Q. Zhang, Z. Fan, S. W. Boettcher, and E. C. Garnett, *Nano Letters* **17**, 6557 (2017).

- [119] A. Waleed, M. M. Tavakoli, L. Gu, Z. Wang, D. Zhang, A. Manikandan, Q. Zhang, R. Zhang, Y.-L. Chueh, and Z. Fan, *Nano Letters* **17**, 523 (2017).
- [120] A. Ingenito, *Opto-Electrical Surface Engineering of Wafer Based c-Si Solar Cells*, Ph.D. thesis, Delft University of Technology (2016).
- [121] H. Fujiwara and M. Kondo, *Physical Review B* **71**, 075109 (2005).
- [122] T. Koida, H. Fujiwara, and M. Kondo, *Japanese Journal of Applied Physics* **46**, L685 (2007).
- [123] T. Koida, H. Fujiwara, and M. Kondo, *Applied Physics Express* **1**, 041501 (2008).
- [124] A. Paduthol, M. K. Juhl, G. Nogay, P. Löper, and T. Trupke, *Progress in Photovoltaics: Research and Applications* **26**, 968 (2018).
- [125] Z. Yu, A. Raman, and S. Fan, *Proceedings of the National Academy of Sciences* **107**, 17491 (2010).
- [126] Z. Yu, A. Raman, and S. Fan, *Optics Express* **18**, A366 (2010).
- [127] H. A. Atwater and A. Polman, *Nature Materials* **9**, 205 (2010).
- [128] D. Fattal, J. Li, Z. Peng, M. Fiorentino, and R. G. Beausoleil, *Nature Photonics* **4**, 466 (2010).
- [129] B. W. H. Baugher, H. O. H. Churchill, Y. Yang, and P. Jarillo-Herrero, *Nature Nanotechnology* **9**, 262 (2014).
- [130] D. Lin, P. Fan, E. Hasman, and M. L. Brongersma, *Science* **345**, 298 (2014).
- [131] K. E. Chong *et al.*, *Nano Letters* **15**, 5369 (2015).
- [132] F. Aieta, M. A. Kats, P. Genevet, and F. Capasso, *Science* **347**, 1342 (2015).
- [133] P. Spinelli, M. A. Verschuuren, and A. Polman, *Nature Communications* **3**, 692 (2012).
- [134] A. Furasova, E. Calabró, E. Lamanna, E. Tiguntseva, E. Ushakova, E. Ubyivovk, V. Mikhailovskii, A. Zakhidov, S. Makarov, and A. Di Carlo, *Advanced Optical Materials* **6**, 1800576 (2018).
- [135] N. Odebo Länk, R. Verre, P. Johansson, and M. Käll, *Nano Letters* **17**, 3054 (2017).
- [136] V. G. Kravets *et al.*, *Nature Materials* **12**, 304 (2013).
- [137] M. Svedendahl, R. Verre, and M. Käll, *Light: Science & Applications* **3**, e220 (2014).
- [138] X. Liu, K. Fan, I. V. Shadrivov, and W. J. Padilla, *Optics Express* **25**, 191 (2017).
- [139] S. Zanotto, F. P. Mezzapesa, F. Bianco, G. Biasiol, L. Baldacci, M. S. Vitiello, L. Sorba, R. Colombelli, and A. Tredicucci, *Nature Physics* **10**, 830 (2014).
- [140] M. L. Brongersma, Y. Cui, and S. Fan, *Nature Materials* **13**, 451 (2014).

- [141] Y. Sun, Y. Sun, T. Zhang, G. Chen, F. Zhang, D. Liu, W. Cai, Y. Li, X. Yang, and C. Li, *Nanoscale* **8**, 10774 (2016).
- [142] M. Boccard, M. Despeisse, J. Escarré, X. Niquille, G. Bugnon, S. Hänni, M. Bonnet-Eymard, F. Meillaud, and C. Ballif, *IEEE Journal of Photovoltaics* **4**, 1368 (2014).
- [143] S. Hänni, M. Boccard, G. Bugnon, M. Despeisse, J.-W. Schüttauf, F.-J. Haug, F. Meillaud, and C. Ballif, *physica status solidi (a)* **212**, 840 (2015).
- [144] S. W. Glunz and F. Feldmann, *Solar Energy Materials and Solar Cells* **185**, 260 (2018).
- [145] LUMERICAL, “3D/2D Maxwell’s Solver for Nanophotonic Devices,” <http://www.lumerical.com/products/fdtd-solutions/>, accessed: 2020-05-29.
- [146] W. W. Salisbury, “Absorbent body for electromagnetic waves,” (1952), US Patent No. 2,599,944.
- [147] J. Springer, A. Poruba, L. Müllerova, M. Vaneček, O. Kluth, and B. Rech, *Journal of Applied Physics* **95**, 1427 (2004).
- [148] H. Tan, R. Santbergen, A. H. Smets, and M. Zeman, *Nano letters* **12**, 4070 (2012).
- [149] G. Yang, *High-efficient n-i-p thin-film silicon solar cells*, Ph.D. thesis, Delft University of Technology (2015).
- [150] T. Matsui, A. Bidiville, K. Maejima, H. Sai, T. Koida, T. Suezaki, M. Matsumoto, K. Saito, I. Yoshida, and M. Kondo, *Applied Physics Letters* **106**, 053901 (2015).
- [151] P. Grahn, A. Shevchenko, and M. Kaivola, *New Journal of Physics* **14**, 093033 (2012).
- [152] R. Verre, N. Odebo Länk, D. Andrén, H. Šípová, and M. Käll, *Advanced Optical Materials* **6**, 1701253 (2018).
- [153] H. Kakinuma, S. Nishikawa, and T. Watanabe, *Journal of Non-Crystalline Solids* **59**, 421 (1983).
- [154] S. Liu, M. B. Sinclair, S. Saravi, G. A. Keeler, Y. Yang, J. Reno, G. M. Peake, F. Setzpfandt, I. Staude, T. Pertsch, and I. Brener, *Nano Letters* **16**, 5426 (2016).
- [155] R. Camacho-Morales *et al.*, *Nano Letters* **16**, 7191 (2016).
- [156] E. Y. Tiguntseva, G. P. Zograf, F. E. Komissarenko, D. A. Zuev, A. A. Zakhidov, S. V. Makarov, and Y. S. Kivshar, *Nano Letters* **18**, 1185 (2018).
- [157] S. V. Makarov *et al.*, *ACS Photonics* **4**, 728 (2017).
- [158] A. E. Miroshnichenko, A. B. Evlyukhin, Y. F. Yu, R. M. Bakker,

- A. Chipouline, A. I. Kuznetsov, B. Luk'yanchuk, B. N. Chichkov, and Y. S. Kivshar, *Nature communications* **6**, 8069 (2015).
- [159] A. Kodigala, T. Lepetit, Q. Gu, B. Bahari, Y. Fainman, and B. Kanté, *Nature* **541**, 196 (2017).
- [160] P. Jackson, D. Hariskos, R. Wuerz, W. Wischmann, and M. Powalla, *Physica Status Solidi (RRL) - Rapid Research Letters* **8**, 219 (2014).
- [161] P. Jackson, D. Hariskos, R. Wuerz, O. Kiowski, A. Bauer, T. M. Friedlmeier, and M. Powalla, *Physica Status Solidi (RRL) - Rapid Research Letters* **9**, 28 (2015).
- [162] P. Jackson, R. Wuerz, D. Hariskos, E. Lotter, W. Witte, and M. Powalla, *Physica Status Solidi (RRL) - Rapid Research Letters* **10**, 583 (2016).
- [163] A. Chirilă *et al.*, *Nature Materials* **12**, 1107 (2013).
- [164] M. Gloeckler and J. R. Sites, *Journal of Applied Physics* **98**, 103703 (2005).
- [165] C. van Lare, G. Yin, A. Polman, and M. Schmid, *ACS Nano* **9**, 9603 (2015).
- [166] L. Aé, D. Kieven, J. Chen, R. Klenk, T. Rissom, Y. Tang, and M. C. Lux-Steiner, *Progress in Photovoltaics: Research and Applications* **18**, 209 (2010).
- [167] J. Malmström, in *Proceedings of the 3<sup>rd</sup> World Conference on Photovoltaic Energy Conversion (WCPEC-3)* (2003) pp. 344–347.
- [168] A. Čampa, J. Krč, J. Malmström, M. Edoff, F. Smole, and M. Topič, *Thin Solid Films* **515**, 5968 (2007).
- [169] C.-H. Liu *et al.*, *Nano Letters* **11**, 4443 (2011).
- [170] M. Schmid, R. Klenk, M. C. Lux-Steiner, M. Topič, and J. Krč, *Nanotechnology* **22**, 025204 (2011).
- [171] L. C. Andreani, P. A. Kowalczewski, C. I. Mura, M. Patrini, M. Acciarri, S. Binetti, A. Sassella, and S. Marchionna, in *Proceedings of the 27<sup>th</sup> European Photovoltaic Solar Energy Conference and Exhibition (27<sup>th</sup> EU PVSEC)* (2012) pp. 2334–2337.
- [172] W. Wang, S. Wu, R. J. Knize, K. Reinhardt, Y. Lu, and S. Chen, *Optics Express* **20**, 3733 (2012).
- [173] C. Colin *et al.*, in *Proceedings of SPIE OPTO*, Vol. 8620 (SPIE, 2013) p. 12.
- [174] J. Grandidier, R. A. Weitekamp, M. G. Deceglie, D. M. Callahan, C. Battaglia, C. R. Bukowsky, C. Ballif, R. H. Grubbs, and H. A. Atwater, *physica status solidi (a)* **210**, 255 (2012).
- [175] Y.-K. Liao *et al.*, *ACS Nano* **7**, 7318 (2013).
- [176] S.-U. Park, R. Sharma, J.-K. Sim, B. J. Baek, H.-K. Ahn, J. S. Kim, and C.-R. Lee, *Applied Surface Science* **280**, 757 (2013).

- [177] M. Schmid, J. Klaer, R. Klenk, M. Topič, and J. Krč, *Thin Solid Films* **527**, 308 (2013).
- [178] S.-C. Chen *et al.*, *ACS Nano* **8**, 9341 (2014).
- [179] W. Ohm, W. Riedel, U. Askünger, M. D. Heinemann, C. A. Kaufmann, J. L. Garcia, V. Izquierdo, X. Fontané, T. Goislard, M. C. Lux-Steiner, and S. Gledhill, *physica status solidi (a)* **212**, 76 (2014).
- [180] M. Xu, A. J. H. Wachtters, J. van Deelen, M. C. D. Mourad, and P. J. P. Buskens, *Optics Express* **22**, A425 (2014).
- [181] J. Goffard, A. Cattoni, F. Mollica, M. Jubault, C. Colin, J. F. Guillemoles, D. Lincot, N. Naghavi, and S. Collin, in *Proceedings of the 31<sup>st</sup> European Photovoltaic Solar Energy Conference and Exhibition (31<sup>st</sup> EU PVSEC)* (2015) pp. 1050–1052.
- [182] M.-J. Jeng, Z.-Y. Chen, Y.-L. Xiao, L.-B. Chang, J. Ao, Y. Sun, E. Popko, W. Jacak, and L. Chow, *Materials* **8** (2015).
- [183] Y.-C. Wang, H.-Y. Cheng, Y.-T. Yen, T.-T. Wu, C.-H. Hsu, H.-W. Tsai, C.-H. Shen, J.-M. Shieh, and Y.-L. Chueh, *ACS Nano* **9**, 3907 (2015).
- [184] G. Yin, A. Steigert, P. Andrae, M. Goebelt, M. Latzel, P. Manley, I. Lauer-mann, S. Christiansen, and M. Schmid, *Applied Surface Science* **355**, 800 (2015).
- [185] G. Yin, M. W. Knight, M.-C. van Lare, M. M. Solà Garcia, A. Polman, and M. Schmid, *Advanced Optical Materials* **5**, 1600637 (2016).
- [186] G. Yin, P. Manley, and M. Schmid, *Solar Energy Materials and Solar Cells* **153**, 124 (2016).
- [187] G. Yin, M. Song, S. Duan, P. Manley, D. Greiner, C. A. Kaufmann, and M. Schmid, *ACS Applied Materials & Interfaces* **8**, 31646 (2016).
- [188] N. Rezaei, O. Isabella, Z. Vroon, and M. Zeman, *Optics Express* **26**, A39 (2018).
- [189] G. Yin, P. Manley, and M. Schmid, *Solar Energy* **163**, 443 (2018).
- [190] N. Rezaei, O. Isabella, Z. Vroon, and M. Zeman, *Solar Energy* **177**, 59 (2019).
- [191] N. Rezaei, O. Isabella, P. Procel, Z. Vroon, and M. Zeman, *Optics Express* **27**, A269 (2019).
- [192] K. Söderström, J. Escarré, O. Cubero, F. J. Haug, S. Perregaux, and C. Ballif, *Progress in Photovoltaics: Research and Applications* **19**, 202 (2011).
- [193] T. Hara, T. Maekawa, S. Minoura, Y. Sago, S. Niki, and H. Fujiwara, *Physical Review Applied* **2**, 034012 (2014).

- [194] K. Jäger, D. N. P. Linssen, O. Isabella, and M. Zeman, *Optics Express* **23**, A1060 (2015).
- [195] H. Tan, E. Psomadaki, O. Isabella, M. Fischer, P. Babal, R. Vasudevan, M. Zeman, and A. H. M. Smets, *Applied Physics Letters* **103**, 173905 (2013).
- [196] H. Sai, K. Saito, and M. Kondo, *Applied Physics Letters* **101**, 173901 (2012).
- [197] K. Orgassa, H. W. Schock, and J. H. Werner, *Thin Solid Films* **431**, 387 (2003).
- [198] W. Shafarman and J. E. Philips, in *Proceedings of the 25<sup>th</sup> IEEE Photovoltaic Specialist Conference (PVSC-25)* (IEEE, 1996) pp. 917–919.
- [199] T. Wada, N. Kohara, T. Negami, and M. Nishitani, *Japanese Journal of Applied Physics* **35**, L1253 (1996).
- [200] R. Santbergen, H. Tan, M. Zeman, and A. H. M. Smets, *Optics express* **22**, A1023 (2014).
- [201] N. Allsop, R. Nürnberg, M. C. Lux-Steiner, and T. Schedel-Niedrig, *Applied Physics Letters* **95**, 122108 (2009).
- [202] Y. Fu, R. Sáez-Araoz, T. Köhler, M. Krüger, A. Steigert, I. Lauermann, M. C. Lux-Steiner, and C.-H. Fischer, *Solar Energy Materials and Solar Cells* **117**, 293 (2013).
- [203] B. Vermang, V. Fjällström, J. Pettersson, P. Salomé, and M. Edoff, *Solar Energy Materials and Solar Cells* **117**, 505 (2013).
- [204] B. Vermang, J. T. Wätjen, V. Fjällström, F. Rostvall, M. Edoff, R. Kotipalli, F. Henry, and D. Flandre, *Progress in Photovoltaics: Research and Applications* **22**, 1023 (2014).
- [205] P. Reinhard, B. Bissig, F. Pianezzi, H. Hagedorfer, G. Sozzi, R. Menozzi, C. Gretener, S. Nishiwaki, S. Buecheler, and A. N. Tiwari, *Nano Letters* **15**, 3334 (2015).
- [206] B. Vermang *et al.*, *Thin Solid Films* **582**, 300 (2015).
- [207] P. Casper, R. Hünig, G. Gomard, O. Kiowski, C. Reitz, U. Lemmer, M. Powalla, and M. Hetterich, *physica status solidi (RRL) - Rapid Research Letters* **10**, 376 (2016).
- [208] S. Krishnakumar and C. S. Menon, *Bulletin of Materials Science* **16**, 187 (1993).
- [209] D. J. L. Brémaud, *Investigation and Development of CIGS Solar Cells on Flexible Substrates and with Alternative Electrical Back Contacts*, Ph.D. thesis, ETH Zurich (2009).
- [210] J. Zhao, A. Wang, M. A. Green, and F. Ferrazza, *Applied Physics Letters* **73**, 1991 (1998).

- [211] K. Masuko, M. Shigematsu, T. Hashiguchi, D. Fujishima, M. Kai, N. Yoshimura, T. Yamaguchi, Y. Ichihashi, T. Mishima, and N. Matsubara, *IEEE Journal of Photovoltaics* **4**, 1433 (2014).
- [212] S. Glunz, F. Feldmann, A. Richter, M. Bivour, C. Reichel, H. Steinkemper, J. Benick, and M. Hermle, in *Proceedings of the 31<sup>st</sup> European Photovoltaic Solar Energy Conference and Exhibition (31<sup>st</sup> EU PVSEC)* (2015) pp. 259–263.
- [213] K. Yamamoto, in *Proceedings of the 25<sup>th</sup> International Photovoltaic Science and Engineering Conference (PVSEC-25)* (Busan, Korea, 2015).
- [214] C. Battaglia, A. Cuevas, and S. De Wolf, *Energy & Environmental Science* **9**, 1552 (2016).
- [215] K. Yoshikawa *et al.*, *Solar Energy Materials and Solar Cells* **173**, 37 (2017).
- [216] K. Yoshikawa, H. Kawasaki, W. Yoshida, T. Irie, K. Konishi, K. Nakano, T. Uto, D. Adachi, M. Kanematsu, and H. Uzu, *Nature Energy* **2**, 17032 (2017).
- [217] K. Söderström, G. Bugnon, R. Biron, C. Pahud, F. Meillaud, F.-J. Haug, and C. Ballif, *Journal of Applied Physics* **112**, 114503 (2012).
- [218] S. Kim, J.-W. Chung, H. Lee, J. Park, Y. Heo, and H.-M. Lee, *Solar Energy Materials and Solar Cells* **119**, 26 (2013).
- [219] B. Liu *et al.*, *Progress in Photovoltaics: Research and Applications* **23**, 1313 (2015).
- [220] W. S. Yang, J. H. Noh, N. J. Jeon, Y. C. Kim, S. Ryu, J. Seo, and S. I. Seok, *Science* **348**, 1234 (2015).
- [221] P. A. Basore, in *Proceedings of the 29<sup>th</sup> IEEE Photovoltaic Specialist Conference (PVSC-29)* (IEEE, 2002) pp. 49–52.
- [222] P. A. Basore, in *Proceedings of the 3<sup>rd</sup> World Conference on Photovoltaic Energy Conversion (WCPEC-3)*, Vol. 1 (2003) pp. 935–938.
- [223] M. A. Green *et al.*, *Solar Energy* **77**, 857 (2004).
- [224] M. A. Green, *Applied Physics A* **96**, 153 (2009).
- [225] S. Gall, C. Becker, K. Y. Lee, T. Sonthaimer, and B. Rech, *Journal of Crystal Growth* **312**, 1277 (2010).
- [226] D. Amkreutz, J. Haschke, S. Kühnappel, P. Sonntag, and B. Rech, *IEEE Journal of Photovoltaics* **4**, 1496 (2014).
- [227] T. Frijnts, S. Kühnappel, S. Ring, O. Gabriel, S. Calnan, J. Haschke, B. Stanowski, B. Rech, and R. Schlatmann, *Solar Energy Materials and Solar Cells* **143**, 457 (2015).
- [228] P. Sonntag, N. Preissler, M. Bokalič, M. Trahms, J. Haschke, R. Schlatmann, M. Topič, B. Rech, and D. Amkreutz, *Scientific Reports* **7**, 873 (2017).

- [229] C. T. Trinh, R. Schlatmann, B. Rech, and D. Amkreutz, *Solar Energy* **175**, 75 (2018).
- [230] C. Thi Trinh, N. Preissler, P. Sonntag, M. Muske, K. Jäger, M. Trahms, R. Schlatmann, B. Rech, and D. Amkreutz, *Solar Energy Materials and Solar Cells* **174**, 187 (2018).
- [231] E. R. Martins, J. Li, Y. Liu, V. Depauw, Z. Chen, J. Zhou, and T. F. Krauss, *Nature communications* **4**, 2665 (2012).
- [232] C. Pahud, O. Isabella, A. Naqavi, F.-J. Haug, M. Zeman, H. P. Herzig, and C. Ballif, *Optics express* **21**, A786 (2013).
- [233] M. Zeman, O. Isabella, S. Solntsev, and K. Jäd'ger, *Solar Energy Materials and Solar Cells* **119**, 94 (2013).
- [234] A. Ingenito, O. Isabella, and M. Zeman, *ACS Photonics* **1**, 270 (2014).
- [235] K. Jäger, C. Barth, M. Hammerschmidt, S. Herrmann, S. Burger, F. Schmidt, and C. Becker, *Optics Express* **24**, A569 (2016).
- [236] D. Eisenhauer, G. Köppel, K. Jäger, D. Chen, O. Shargaieva, P. Sonntag, D. Amkreutz, B. Rech, and C. Becker, *Scientific Reports* **7**, 2658 (2017).
- [237] O. Isabella, A. H. M. Smets, and M. Zeman, *Solar Energy Materials and Solar Cells* **129**, 82 (2014).
- [238] Z. C. Holman, A. Descoeurdes, S. De Wolf, and C. Ballif, *IEEE Journal of Photovoltaics* **3**, 1243 (2013).
- [239] D. L. Staebler and C. R. Wronski, *Applied Physics Letters* **31**, 292 (1977).
- [240] D. Staebler and C. R. Wronski, *Journal of Applied Physics* **51**, 3262 (1980).
- [241] T. Matsui, H. Sai, K. Saito, and M. Kondo, *Progress in Photovoltaics: Research and Applications* **21**, 1363 (2013).
- [242] M. Stuckelberger, M. Despeisse, G. Bugnon, J.-W. SchÄijttauf, F.-J. Haug, and C. Ballif, *Journal of Applied Physics* **114**, 154509 (2013).
- [243] J. Melskens, M. Schouten, A. Mannheim, A. S. Vullers, Y. Mohammadian, S. W. Eijt, H. Schut, T. Matsui, M. Zeman, and A. H. Smets, *IEEE Journal of Photovoltaics* **4**, 1331 (2014).
- [244] H. Sai, K. Saito, N. Hozuki, and M. Kondo, *Applied Physics Letters* **102**, 053509 (2013).
- [245] K. X. Wang, Z. Yu, V. Liu, Y. Cui, and S. Fan, *Nano Letters* **12**, 1616 (2012).
- [246] C. S. Schuster, A. Bozzola, L. C. Andreani, and T. F. Krauss, *Optics express* **22**, A542 (2014).
- [247] P. Kowalczewski and L. C. Andreani, *Solar Energy Materials and Solar Cells* **143**, 260 (2015).



- [248] S. L. Luxembourg, P. Spinelli, A. Ingenito, J. Liu, O. Isabella, M. Zeman, and A. W. Weeber, in *Proceedings of the 31<sup>st</sup> European Photovoltaic Solar Energy Conference and Exhibition (31<sup>st</sup> EU PVSEC)* (2015) pp. 972–975.
- [249] O. Isabella, S. Solntsev, D. Caratelli, and M. Zeman, in *MRS Proceedings*, Vol. 1426 (2012) pp. 149–154.
- [250] B. Lipovšek, M. Cvek, A. Čampa, J. Krč, and M. Topič, in *Proceedings of the 5<sup>th</sup> World Conference on Photovoltaic Energy Conversion (WCPEC-5)* (Valencia, Spain, 2010).
- [251] S. Solntsev, O. Isabella, D. Caratelli, and M. Zeman, *IEEE Journal of Photovoltaics* **3**, 46 (2013).
- [252] C. Ducros and H. Szabolics, “Method for producing a textured reflector for a thin-film photovoltaic cell, and resulting textured reflector,” US Patent No. 9952360B2.
- [253] H. Sai and M. Kondo, *Journal of Applied Physics* **105**, 094511 (2009).
- [254] H. Sai, H. Fujii, K. Arafune, Y. Ohshita, Y. Kanamori, H. Yugami, and M. Yamaguchi, *Japanese Journal of Applied Physics* **46**, 3333 (2007).
- [255] A. Naqavi, F.-J. Haug, K. Söderström, C. Battaglia, V. Paeder, T. Scharf, H. P. Herzig, and C. Ballif, *Progress in Photovoltaics: Research and Applications* **22**, 1147 (2014).
- [256] A. Ingenito, S. L. Luxembourg, P. Spinelli, J. Liu, J. C. Ortiz Lizcano, A. W. Weeber, O. Isabella, and M. Zeman, *IEEE Journal of Photovoltaics* **6**, 34 (2016).
- [257] H. Sai, T. Koida, T. Matsui, I. Yoshida, K. Saito, and M. Kondo, *Applied physics express* **6**, 104101 (2013).
- [258] V. Demontis, C. Sanna, J. Melskens, R. Santbergen, A. H. M. Smets, A. Damiano, and M. Zeman, *Journal of Applied Physics* **113**, 064508 (2013).
- [259] M. Boccard, C. Battaglia, S. Hänni, K. Söderström, J. Escarré, S. Nicolay, F. Meillaud, M. Despeisse, and C. Ballif, *Nano letters* **12**, 1344 (2012).
- [260] F. T. Si, D. Y. Kim, R. Santbergen, H. Tan, R. A. van Swaaij, A. H. Smets, O. Isabella, and M. Zeman, *Applied Physics Letters* **105**, 063902 (2014).
- [261] C. Battaglia, J. Escarré, K. Söderström, L. Erni, L. Ding, G. Bugnon, A. Billel, M. Boccard, L. Barraud, and S. De Wolf, *Nano letters* **11**, 661 (2011).
- [262] S. A. Shakir and A. F. Turner, *Applied Physics A* **29**, 151 (1982).
- [263] E. Anemogiannis, E. N. Glytsis, and T. K. Gaylord, *Journal of lightwave technology* **17**, 929 (1999).

- [264] A. Naqavi, F.-J. Haug, C. Ballif, T. Scharf, and H. P. Herzig, *Applied Physics Letters* **102**, 131113 (2013).
- [265] K. Morita, Y. Inomata, and T. Suemasu, *Thin Solid Films* **508**, 363 (2006).
- [266] S. Kishino, T. Imai, T. Iida, Y. Nakaishi, M. Shinada, Y. Takanashi, and N. Hamada, *Journal of Alloys and Compounds* **428**, 22 (2007).
- [267] D. B. Migas, V. L. Shaposhnikov, and V. E. Borisenko, *physica status solidi (b)* **244**, 2611 (2007).
- [268] K. Toh, T. Saito, and T. Suemasu, *Japanese Journal of Applied Physics* **50**, 068001 (2011).
- [269] N. A. A. Latiff, T. Yoneyama, T. Shibusami, K. Matsumaru, K. Toko, and T. Suemasu, *physica status solidi (c)* **10**, 1759 (2013).
- [270] M. Kumar, N. Umezawa, and N. Imai, *Applied Physics Express* **7**, 071203 (2014).
- [271] K. O. Hara, Y. Nakagawa, T. Suemasu, and N. Usami, *Procedia Engineering* **141**, 27 (2016).
- [272] M. Baba, K. Toh, K. Toko, N. Saito, N. Yoshizawa, K. Jiptner, T. Sekiguchi, K. O. Hara, N. Usami, and T. Suemasu, *Journal of Crystal Growth* **348**, 75 (2012).
- [273] M. Baba, K. Ito, W. Du, T. Sanai, K. Okamoto, K. Toko, S. Ueda, Y. Imai, A. Kimura, and T. Suemasu, *Journal of Applied Physics* **114**, 123702 (2013).
- [274] K. O. Hara, N. Usami, K. Nakamura, R. Takabe, M. Baba, K. Toko, and T. Suemasu, *Applied Physics Express* **6**, 112302 (2013).
- [275] G. B. Haxel, J. B. Hedrick, and G. J. Orris, "Rare earth-elements – critical resources for high technology," (2002), U.S. Geological Survey - Fact Sheet 087-02, <http://pubs.usgs.gov/fs/2002/fs087-02/>, accessed 2020-05-31.
- [276] R. Cariou, J. Benick, F. Feldmann, O. Höhn, H. Hauser, P. Beutel, N. Razek, M. Wimplinger, B. Bläsi, D. Lackner, M. Hermle, G. Siefer, S. W. Glunz, A. W. Bett, and F. Dimroth, *Nature Energy* **3**, 326 (2018).
- [277] M. Feifel, J. Ohlmann, J. Benick, M. Hermle, J. Belz, A. Beyer, K. Volz, T. Hannappel, A. W. Bett, D. Lackner, and F. Dimroth, *IEEE Journal of Photovoltaics* **8**, 1590 (2018).
- [278] OXFORD PV, "Oxford PV sets world record for perovskite solar cell," Press release June 25, 2018.
- [279] H. Sai, K. Maejima, T. Matsui, T. Koida, M. Kondo, S. Nakao, Y. Takeuchi, H. Katayama, and I. Yoshida, *Japanese Journal of Applied Physics* **54**, 08KB05 (2015).

- [280] M. A. Green, K. Emery, Y. Hishikawa, W. Warta, and E. D. Dunlop, *Progress in Photovoltaics: Research and Applications* **22**, 1 (2014).
- [281] M. A. Green, K. Emery, Y. Hishikawa, W. Warta, and E. D. Dunlop, *Progress in Photovoltaics: Research and Applications* **23**, 1 (2015).
- [282] M. A. Green, K. Emery, Y. Hishikawa, W. Warta, and E. D. Dunlop, *Progress in Photovoltaics: Research and Applications* **23**, 805 (2015).
- [283] M. A. Green, K. Emery, Y. Hishikawa, W. Warta, and E. D. Dunlop, *Progress in Photovoltaics: Research and Applications* **24**, 3 (2016).
- [284] J. Werner, C.-H. Weng, A. Walter, L. Fesquet, J. P. Seif, S. De Wolf, B. Niesen, and C. Ballif, *The Journal of Physical Chemistry Letters* **7**, 161 (2016).
- [285] M. Filipič, P. Löper, B. Niesen, S. De Wolf, J. Krč, C. Ballif, and M. Topič, *Optics Express* **23**, A263 (2015).
- [286] B. Hoex, S. B. S. Heil, E. Langereis, M. C. M. van de Sanden, and W. M. M. Kessels, *Applied Physics Letters* **89**, 042112 (2006).
- [287] S. Yachi, R. Takabe, H. Takeuchi, K. Toko, and T. Suemasu, *Applied Physics Letters* **109**, 072103 (2016).
- [288] Y. Tian, R. Vismara, S. van Doorene, P. Šutta, L. Vančo, M. Veselý, P. Vogrinčič, O. Isabella, and M. Zeman, *ACS Applied Energy Materials* **1**, 3267 (2018).
- [289] H. Tan, P. Babal, M. Zeman, and A. H. M. Smets, *Solar Energy Materials and Solar Cells* **132**, 597 (2015).
- [290] S. Fan, W. Suh, and J. D. Joannopoulos, *Journal of the Optical Society of America A* **20**, 569 (2003).
- [291] H. Ahmadpanahi, R. Vismara, O. Isabella, and M. Zeman, *Opt. Express* **26**, A737 (2018).
- [292] H. Ahmadpanahi, O. El Gawhary, R. Vismara, O. Isabella, and M. Zeman, *AIP Advances* **9**, 045001 (2019).
- [293] MathWorks, "MATLAB," <http://www.mathworks.com/products/matlab.html>, accessed: 2020-05-31.
- [294] P. B. Johnson and R. W. Christy, *Physical Review B* **6**, 4370 (1972).
- [295] O. Isabella, A. Campa, M. Heijna, W. Soppe, R. van Erven, R. Franken, H. Borg, and M. Zeman, in *Proceedings of the 23<sup>rd</sup> European Photovoltaic Solar Energy Conference and Exhibition (23<sup>rd</sup> EU PVSEC)* (2008) pp. 2320–2324.
- [296] C. Battaglia *et al.*, *ACS Nano* **6**, 2790 (2012).
- [297] C. Heine and R. H. Morf, *Applied Optics* **34**, 2476 (1995).

---

# Acknowledgements

At the end of this 4+ year journey – sitting in front of a computer screen (as usual) – I find myself looking back and trying to make sense of what happened, to understand how I manage to get here, to evaluate this great experience of becoming a PhD. Reaching this point has been a long, challenging and sometimes burdensome adventure, which I could not have embarked on alone. In fact, it would not have been possible to achieve what I have without the help of many colleagues, friends, and loved ones.

To begin, I would like to thank my promotor prof. dr. Miro Zeman – who offered me the great opportunity of carrying out my research in his group and who introduced me to the fantastic world of photovoltaics. At the beginning I had some doubts about my choice, but your vision, support and trust have been very important for me to complete this work – and I truly want to thank you for that. Moreover, I wish to express my deepest and sincerest gratitude to my other promotor and daily supervisor, dr. Olindo Isabella. *Olindo*, I could not have wished for a better person to supervise and guide me through these last years, from our very first encounter to discuss the AGATHA project and my M.Sc. thesis work, through the countless and often endless progress meetings, up to our most recent discussions about the final steps of this work. Not once I have felt you were unavailable or unwilling to help me when I needed it, and your constant belief and encouragement have been instrumental in achieving the results presented in this thesis. Throughout the entire duration of my stay at the PVMD, from the weekends in the office to the sleepless nights at conference hotels, from the comforts of the best resorts in Hawaii to the near-death experiences on the road in India, from the numerous scientific and research discussions to our amazing culinary food-related experiences (Shanghai, Phoenix, Catania, . . .), I met not only a great scientist, but someone I am grateful to call a mentor and friend. Even when I was dealing with serious personal matters you never failed to provide your honest and heartfelt support. So, there is only one thing I can say: *grazie di tutto!*

I also want to thank all the members of my thesis committee, for taking their time to read my thesis and provide useful and relevant feedback: thank you prof. Lucio Andreani, prof. Christiane Becker, dr. Benedikt Bläsi, prof. Albert Polman, prof. Elmar Eisemann, and prof. Peter Palenski.

The Photovoltaic Materials and Devices group has been my second home for the last years and I am really grateful for all the people that made me feel part of it. Right alongside prof. Miro Zeman and dr. Olindo Isabella, I wish to thank prof. Arno Smets, dr. René van Swaaij and prof. Arthur Weeber – whose passion and dedication to research and education were and are a constant source of motivation to carry out my work in the best possible way. I also want to thank the supporting staff of the ESE department, which was always available and extremely helpful: Carla, Diane, Ellen, Ilona, Laura, Margot, Mark, and Sharmila. The technical staff of the PVMD group has also been instrumental in completing the work presented in this manuscript, so a special thank you goes to Martijn, Remko and Stefaan. I am also thankful for having had the chance to collaborate with many great researchers from other groups: thank you to the AGATHA project partners dr. Oleksandr Astakhov, dr. Anna Battaglia, dr. Andrea Canino, dr. Louis Grenet, dr. David Joyce, and dr. Tsvetelina Merdzhanova – and thank you to dr. Nils Odebo Länk and dr. Ruggero Verre at Chalmers University for the collaboration on the metasurface work.

Over the years I have shared the office with many inspiring researchers, that never failed to help me when needed: thank you to dr. Lihao Han, Luca Locatelli, Vincenzo Maccaronio, dr. Mirjam Theelen, dr. Hamed Ahmadpanahi, dr. Hesam Ziar, Yilei Tian, Klaas Bakker, Arturo Martinez Lopez, and dr. Mirco Muttillio. I am also extremely grateful to have met so many great colleagues, some of whom I am lucky enough to call friends. Thank you Nasim, for being a true friend and the kindest person I know. Thank you Rita and Andres, for the many great nights and for the honest care and support. A special thank you to Dozie, Steve and Thomas: I had a great time supervising your M.Sc. thesis projects and your work contributed greatly to my thesis. And thank you to all the other past and present members of the PVMD group that I have met in the last years: dr. Zameer Ahmad, Johan Blanker, dr. Dimitris Deligiannis, dr. Yuan Gao, Can Han, dr. Andrea Illiberi, dr. Andrea Ingenito, dr. Gianluca Limodio, dr. Patrizio Manganiello, dr. Luana Mazzarella, Juan Camilo Ortiz Lizcano, dr. Engin Özkol, dr. Grégory Pandraud, dr. Paula Perez Rodriguez, dr. Silvio Pierro, dr. Paul Procel, dr. Carlos Ruiz Tobon, dr. Rudi Santbergen, Daniele Sciré, dr. Martijn van Sebille, dr. Fai Tong Si, Manvika Singh, dr. Hairen Tan, dr. Ravi Vasudevan, Maarten Verkou, dr. Malte Vogt, Thierry de Vrijer, Yudai Yamashita, dr. Guangtao Yang, Yifeng Zhao, Yilong Zhou. All of you have contributed in some way, big or small, to the success of my PhD career.

A big thank you also goes to the coffee/football Italian crew, which has made

many working days lighter and many nights memorable: grazie Anna e Gianluca, Annarita e Carmine, Chiara e Raffaele, Emma e Alferio, Fabrizio, Ghazaleh e Michele, Satoshi, Valeria e Luca. A special thank you goes to my long-time friends Davide e Manuel: anche se siamo lontani, il vostro supporto non mi è mai mancato. And another big thank you goes to the great beach-volleyball gang, for all the great times spent together: Daniel, Derk, Jessica, Julián, and Timo.

Finally, I will be forever grateful for all the love and support that my family has always been giving me. Hartstikke bedankt Oma, oom Bart, oom Leo en tante Petra, Sanne, Thomas, Joost, Gijs en Luuk. Grazie Bianca Vittoria – *amó* – per aver riempito la mia vita rendendola infinitamente più bella. Grazie Daya, per essere la sorella migliore che potessi sperare di avere. Grazie Mamma, per tutto ciò che hai fatto per me e per tutto l'amore e il supporto che mi hai sempre dato. E grazie papà, perché senza tutto quello che hai fatto per me, senza tutti i tuoi sacrifici, senza tutti i tuoi insegnamenti, non sarei diventato la persona che sono. Mi manchi.



---

# List of publications

## Peer-reviewed articles

M. Singh, R. Santbergen, L. Mazzarella, A. Madrampazakis, G. Yang, **R. Vismara**, Z. Remes, , A. Weeber, M. Zeman, and O. Isabella, "Optical characterization of poly-SiO<sub>x</sub> and poly-SiC<sub>x</sub> carrier-selective passivating contacts," *Solar Energy Materials and Solar Cells* **210**, 110507 (2020).

H. Ahmadpanahi, **R. Vismara**, O. Isabella, and M. Zeman, "Understanding the nano-photonics absorption limit in both front-side and front/rear-side textured slabs," *Optics Express* **27**(16), A1173-A1187 (2019).

**R. Vismara**, N. Odebo Länk, R. Verre, M. Käll, O. Isabella, and M. Zeman, "Solar harvesting based on all-dielectric perfect absorbing metasurfaces," *Optics Express* **27**(16), A967-A980 (2019).

H. Ahmadpanahi, O. El Gawhari, **R. Vismara**, O. Isabella, and M. Zeman, "Assessing light absorption contributions in thin periodically-textured silicon absorbers under oblique illumination," *AIP Advances* **9**(4), 045001 (2019).

**R. Vismara**, O. Isabella, A. Ingenito, F. T. Si, and M. Zeman, "Geometrical optimisation of core-shell nanowire array for enhanced absorption in thin crystalline silicon heterojunction solar cells," *Beilstein Journal of Nanotechnology* **10**, 322-331 (2019).

Y. Tian, **R. Vismara**, S. van Doorene, P. Šutta, L. Vančo, M. Veselý, P. Vogrinčič, O. Isabella, and M. Zeman, "Oxidation-Induced Structure Transformation: Thin-Film Synthesis and Interface Investigations of Barium Disilicide toward Potential Photovoltaic Applications," *ACS Applied Energy Materials* **1**(7), 3267-3276 (2018).

H. Ahmadpanahi, **R. Vismara**, O. Isabella, and M. Zeman, "Distinguishing Fabry-Perot from guided mode resonances in thin periodically-textured silicon absorbers," *Optics Express* **26**(18), A737-A749 (2018).

O. Isabella, **R. Vismara**, D. N. P. Linssen, K. X. Wang, S. Fan, and M. Zeman,



"Advanced light trapping scheme in decoupled front and rear textured thin-film silicon solar cells," *Solar Energy* **162**, 344-356 (2018).

**R. Vismara**, O. Isabella, and M. Zeman, "Back-contacted BaSi<sub>2</sub> solar cells: an optical study," *Optics Express* **25**(8), A402-A408 (2017).

O. Isabella, **R. Vismara**, A. Ingenito, N. Rezaei, and M. Zeman, "Decoupled front/back dielectric textures for flat ultra-thin c-Si solar cells," *Optics Express* **24**(6), A708-A719 (2016).

C. Onwudinanti, **R. Vismara**, O. Isabella, L. Grenet, F. Emieux, and M. Zeman, "Advanced light management based in periodic textures for Cu(In,Ga)Se<sub>2</sub> thin-film solar cells," *Optics Express* **24**(6), A693-A707 (2016).

## Conference presentations and proceedings

H. Ahmadpanahi, **R. Vismara**, O. Isabella, and M. Zeman, "Distinguishing Fabry-Perót from guided mode resonances in thin periodically textured silicon absorber," in *Light, Energy and the Environment*, OSA Technical digest (online), paper **OT5C.3**, November 5<sup>th</sup>-8<sup>th</sup> 2018, Singapore. *Oral presentation*

**R. Vismara**, D. N. P. Linssen, K. X. Wang, S. Fan, O. Isabella, and M. Zeman, "Decoupled textures for broadband absorption enhancement beyond Lambertian light trapping limit in thin-film silicon-based solar cells," in *Proceedings of the 7<sup>th</sup> World Conference on Photovoltaic Energy Conversion (WCPEC-7)*, pp. 3455-3459, June 10<sup>th</sup>-15<sup>th</sup> 2018, Waikoloa Village, HI (USA). *Oral presentation*

Y. Nakagawa, **R. Vismara**, T. Loef, K. Gotoh, Y. Kurokawa, O. Isabella, M. Zeman, and N. Usami, "Preparation of BaSi<sub>2</sub> thin films on micro-textured glass substrates and evaluation of the optical properties," the 65<sup>th</sup> Japan Society of Applied Physics (JSAP) Spring Meeting, March 17<sup>th</sup>-20<sup>th</sup> 2018, Tokyo (Japan). *Oral presentation*

**R. Vismara**, N. Odebo Länk, R. Verre, M. Käll, O. Isabella, and M. Zeman, "Thin-film amorphous silicon nanopillar solar cells: study of the optical potential," in *Light, Energy and the Environment*, OSA Technical digest (online), paper **PM3A.3**, November 6<sup>th</sup>-9<sup>th</sup> 2017, Boulder, CO (USA). *Oral presentation*

Y. Tian, **R. Vismara**, S. van Doorene, P. Šutta, L. Vančo, M. Veselý, P. Vogrinčič, O. Isabella, and M. Zeman, "Structural and optical analysis of sputtered BaSi<sub>2</sub> thin

---

films," 33<sup>rd</sup> European Photovoltaic Solar Energy Conference and Exhibition (33<sup>rd</sup> EU PVSEC), September 25<sup>th</sup>-29<sup>th</sup> 2017, Amsterdam (The Netherlands). *Poster presentation*

**R. Vismara**, O. Isabella, and M. Zeman, "Optical potential of BaSi<sub>2</sub> absorber material for thin-film PV applications," 33<sup>rd</sup> European Photovoltaic Solar Energy Conference and Exhibition (33<sup>rd</sup> EU PVSEC), September 25<sup>th</sup>-29<sup>th</sup> 2017, Amsterdam (The Netherlands). *Oral presentation*

**R. Vismara**, O. Isabella, L. Grenet, F. Emieux, and M. Zeman, "Light management based on periodic textures for Cu(In,Ga)Se<sub>2</sub> solar cells," 33<sup>rd</sup> European Photovoltaic Solar Energy Conference and Exhibition (33<sup>rd</sup> EU PVSEC), September 25<sup>th</sup>-29<sup>th</sup> 2017, Amsterdam (The Netherlands). *Oral presentation*

**R. Vismara**, O. Isabella, and M. Zeman, "Back contacted BaSi<sub>2</sub> thin-film solar cells: an optical analysis," in *Light, Energy and the Environment*, OSA Technical digest (online), paper **PM3B.4**, November 14<sup>th</sup>-17<sup>th</sup> 2016, Leipzig (Germany). *Oral presentation*

O. Isabella, **R. Vismara**, and M. Zeman, "BaSi<sub>2</sub> bottom absorber for double-junction thin-film solar cells," 26<sup>th</sup> International Photovoltaic Science and Engineering Conference (PVSEC-26), October 24<sup>th</sup>-28<sup>th</sup> 2016, Marina Bay (Singapore). *Poster presentation*

O. Isabella, **R. Vismara**, and M. Zeman, "Thin-film single- and double-junction solar cells based on barium-disilicide," 3<sup>rd</sup> Euroregional workshop on photovoltaics & nanophotonics (EUROREG-PV 2016), September 21<sup>st</sup>-23<sup>rd</sup> 2016, Ljubljana (Slovenia). *Oral presentation*

**R. Vismara**, O. Isabella, A. Ingenito, D. N. P. Linssen, and M. Zeman, "Nanophotonic approaches for high-efficiency silicon-based solar cells," NANOCITY 2016, June 21<sup>st</sup>, Amsterdam (The Netherlands). *Oral presentation*

**R. Vismara**, O. Isabella, and M. Zeman, "Organometallic halide perovskite/ barium di-silicide thin-film double-junction solar cells," in *Proceedings of SPIE 9898*, 9898J, SPIE Photonics Europe, April 4<sup>th</sup>-7<sup>th</sup> 2016, Brussels (Belgium). *Oral presentation*

**R. Vismara**, O. Isabella, and M. Zeman, "Exploring the optical potential of BaSi<sub>2</sub> as absorber in high-performance thin-film solar cells," 2016 MRS Spring Meeting

& Exhibit, March 28<sup>th</sup>-April 1<sup>st</sup> 2016, Phoenix, AZ (USA). *Poster presentation*

**R. Vismara**, C. Onwudinanti, L. Grenet, F. Emieux, O. Isabella, and M. Zeman, "Optical optimization of Cu(In,Ga)Se<sub>2</sub> solar cells on periodic gratings," MATH-EON Workshop - 9<sup>th</sup> Annual Meeting "Photonic Devices", March 3<sup>rd</sup>-4<sup>th</sup> 2016, Berlin (Germany). *Oral presentation*

O. Isabella, **R. Vismara**, A. Ingenito, and M. Zeman, "Decoupled front/back dielectric textures for flat ultrathin c-Si solar cells," in *Light, Energy and the Environment*, OSA Technical digest (online), paper **PTh2B.2**, November 2<sup>nd</sup>-5<sup>th</sup> 2015, Suzhou (China). *Oral presentation*

**R. Vismara**, C. Onwudinanti, L. Grenet, F. Emieux, O. Isabella, and M. Zeman, "Optical analysis of CIGS solar cells on periodic gratings," in *Light, Energy and the Environment*, OSA Technical digest (online), paper **PTu4B.5**, November 2<sup>nd</sup>-5<sup>th</sup> 2015, Suzhou (China). *Oral presentation*

**R. Vismara**, O. Isabella, and M. Zeman, "Optimization of thin-film silicon solar cells based on 1-D asymmetric periodic gratings," in *Proceedings of the 31<sup>st</sup> European Photovoltaic Solar Energy Conference and Exhibition (31<sup>th</sup> EU PVSEC)*, September 14<sup>th</sup>-18<sup>th</sup> 2015, Hamburg (Germany). *Poster presentation*

O. Isabella, A. Ingenito, F. T. Si, **R. Vismara**, and M. Zeman, "Radial heterojunction c-Si nanowire solar cells with 11.8% conversion efficiency," 2015 MRS Spring Meeting & Exhibit, April 6<sup>th</sup>-10<sup>st</sup> 2016, San Francisco, CA (USA). *Oral presentation*

O. Isabella, **R. Vismara**, A. Ingenito, F. T. Si, and M. Zeman, "Radial heterojunction c-Si nanowire solar cells with 11.8% conversion efficiency," in *Light, Energy and the Environment*, OSA Technical digest (online), paper **PW3C.3**, December 2<sup>nd</sup>-5<sup>th</sup> 2014, Canberra (Australia). *Oral presentation*

O. Isabella, A. Ingenito, F. T. Si, **R. Vismara**, and M. Zeman, "Radial heterojunction c-Si nanowire solar cells with 11.8% conversion efficiency," 6<sup>th</sup> World Conference on Photovoltaic Energy Conversion (WCPEC-6), November 23<sup>rd</sup>-27<sup>th</sup> 2014, Kyoto (Japan). *Oral presentation*

**R. Vismara**, A. Ingenito, O. Isabella, F. T. Si, and M. Zeman, "Radial heterojunction c-Si nanowire solar cells with 11.8% conversion efficiency," 2<sup>nd</sup> Euroregional workshop on photovoltaics (EUROREG-PV 2014), September 1<sup>st</sup>-3<sup>rd</sup> 2014, Ljubljana (Slovenia). *Oral presentation*

---

# Curriculum vitae

**Robin Vismara** was born in Torre de' Roveri (Italy) on December 17, 1990. In 2012 he received a B.Sc degree in Energy Engineering from Politecnico di Milano, while in 2014 he was awarded the M.Sc. degree in Sustainable Energy Technology by Delft University of Technology. In October 2014 he started to pursue a Ph.D. degree in the Photovoltaic Materials and Devices group, under the supervision of prof. Miro Zeman and dr. Olindo Isabella. During his Ph.D. trajectory, he focused on light management approaches for thin-film solar cells. The results of his research has led him to publish 11 scientific articles in peer-reviewed journals (6 of which as main contributing author) and have been presented at several national and international conferences, including: the 31<sup>st</sup> EU-PVSEC (Hamburg, Germany 2015), a first OSA-PV conference (Suzhou, China 2015), the MRS Spring Meeting (Phoenix AZ, U.S.A. 2016), the 33<sup>rd</sup> EU-PVSEC (Amsterdam, The Netherlands 2017), a second OSA-PV conference (Boulder CO, U.S.A. 2017), and the WCPEC-7 (Waikoloa Village HI, U.S.A. 2018). He also contributed to the online education offer of the Photovoltaic Materials and Devices group, by developing 2 professional education courses dedicated to the modelling of photovoltaic materials, devices and systems and 2 more professional education courses aimed at experimenting with photovoltaic system components in a virtual environment.

## Contact details

E-mail: [robin.vismara@gmail.com](mailto:robin.vismara@gmail.com)

Linkedin: [www.linkedin.com/in/robinvismara](http://www.linkedin.com/in/robinvismara)